5-3-2022

Light Management in III-V Thin-Film Photovoltaics and Micro-LEDs

Julia Rae D'Rozario
jrd4466@rit.edu

RIT

Light Management in III-V Thin-Film Photovoltaics and Micro-LEDs

by

Julia Rae D'Rozario

A dissertation submitted in partial fulfillment of the requirements
for the degree of Doctorate of Philosophy in Microsystems Engineering

Microsystems Engineering Program
Kate Gleason College of Engineering

Rochester Institute of Technology
Rochester, New York
May 3, 2022

Light Management in III-V Thin-Film Photovoltaics and Micro-LEDs
by
Julia Rae D'Rozario

Committee Approval:

We, the undersigned committee members, certify that we have advised and/or supervised the candidate on the work described in this dissertation. We further certify that we have reviewed the dissertation manuscript and approve it in partial fulfillment of the requirements of the degree of Doctorate of Philosophy in Microsystems Engineering.

Dr. Seth M. Hubbard — Date
Associate Professor, Physics and Microsystems Engineering

Dr. Mustafa A.G. Abushagur — Date
Professor, Microsystems Engineering

Dr. Parsian K. Mohseni — Date
Associate Professor, Electrical and Microelectronic Engineering

---

Dr. Stefan F. Preble — Date
Professor, Microsystems Engineering

Dr. Michael Zemcov — Date
Associate Professor, Physics and Astronomy

Certified by:

Dr. Stefan F. Preble — Date
Director, Microsystems Engineering Program

ABSTRACT

Kate Gleason College of Engineering
Rochester Institute of Technology

Degree: Doctorate of Philosophy **Program:** Microsystems Engineering
Author's Name: Julia Rae D'Rozario
Advisor's Name: Dr. Seth M. Hubbard
Dissertation Title: Light Management in III-V Thin-Film Photovoltaics and Micro-LEDs

Light management is essential to improve the performance of optoelectronic devices as they depend on the interaction between photons and device design. This research demonstrates novel approaches to enhance the light absorption in thin-film III-V photovoltaics (PV) and light emission from micrometer-scale light-emitting diodes (μLED).

The high power conversion efficiency (PCE) realized in III-V PV makes them attractive power generation sources, especially for off-the-grid space-related missions. Thin-film PV ($< 1\ \mu m$) offer great tolerance towards the inevitable radiation damage in the space environment as carrier collection is maintained compared to their optically thick counterparts (3-5 μm). To combat transmission loss of photons traveling through the thinned device, this work develops textured back surface reflectors (BSR) to increase the optical path length (OPL) of unabsorbed photons to generate electron-hole pairs. The textures are created via etching techniques and epitaxial regrowth and are characterized by surface imaging and reflectance (R) measurements. The textured BSR with high diffuse R increase the OPL, and the best-known design demonstrates over a four-fold increase in the OPL, which is two times greater than the planar BSR. This research delivers new analyses useful to the PV community, including the lifetime enhancement factor and free-carrier absorption modeling, which aim to improve the PCE in thin-film PV.

Modern display technology is constantly integrated into daily use to convey information and connect people worldwide. The next generation of wearable devices requires small-featured displays to achieve high resolution. The μLED delivers value to near-eye displays through low power consumption, long lifetime, high contrast, and increased resolution. As these devices reduce in size, surface states limit the light output power (LOP) at the roughened sidewalls, and the perimeter-to-area ratio must be considered. This research focuses on developing a fabrication process that improves LOP through sidewall treatments. The dry etch process is optimized to reduce surface roughness, and sidewall treatments via wet-chemical etching, in situ etching, and regrowth aim to improve the sidewall quality. Scanning electron microscopy on the LED sidewalls supports the optimized fabrication process. Luminescence characterization reveals that combinations of etching and regrowth suppress non-radiative recombination events. These techniques render pathways to enhance LOP in LEDs smaller than 25 μm x 25 μm.

This dissertation is dedicated to my parents,

who instilled the strength to pursue my passions.

Acknowledgments

I want to start by acknowledging my research advisor, Dr. Seth Hubbard, for his guidance and support throughout my graduate career. The opportunities he provided in the labs, networking experiences at conferences, and his trust in my research ideas allowed me to grow as a scientist and engineer. Thank you for these incredible opportunities that have prepared me for my future career. I also want to thank the Research Scientist in my group, Dr. Stephen Polly, who has provided substantial support and mentorship during my graduate studies. I am very fortunate to have five years of his guidance throughout my research and excellent life advice I'll continue to follow as I progress in my career.

I want to thank my entire committee for supporting my research studies. Dr. Stefan Preble, Dr. Parsian Mohseni, and Dr. Mustafa Abushagur, thank you for providing me with your excellent teachings during my time at RIT. You have all inspired me in numerous ways, and I consider myself lucky to have had you all as professors and mentors. Dr. Michael Zemcov, thank you for contributing to my research with an outside perspective that has allowed me to appreciate my work in a new light and see the bigger picture. Thank you to the US Air Force Research Laboratory for their support and funding under the SBIR FA9453-19-C-0592 and subcontract from BlueHalo under FA9453-14-D-0312 (SVAT)/TO 04. Thank you to my collaborators at MicroLink Devices, especially Dr. Rao Tatavarti, for fabrication and materials growth. Thank you to NanoPower Research Labs and my entire research group, past and present, for their help over the years, especially Dr. Zac Bittner, Dr. George Nelson, Dr. Elizabeth McClure, Dr. Brittany Smith, Dr. Yushuai Dai, Dr. Anastasiia Fedorenko, Salwan Omar, Brandon Bogner, Emily Kessler-Lewis, Katelynn Fleming, Andrew Sindermann, and Elijah Sacchitella. Thank you to colleagues outside my research group who have helped me in the clean room, including Venkatesh Deenadayalan, Matt Niekerk, Alireza Abrand, Bryan Melanson, Dr. Thomas Wilhelm, and Dr. Matt Hartensveld. Thank you to the NanoFab Cleanroom staff for years of technical support and education on cleanroom processes and equipment. Lisa Zimmerman and Elaine Lewis, thank you so much for the years of administrative support in my graduate studies. You made every milestone

and transition in the program manageable. Thank you, Ross Hisert, for helping with equipment in the labs. Thank you to everyone involved in the Microsystems Engineering Program that has helped me during my graduate career at RIT.

Thank you to my family and friends for their incredible support throughout my academic career. A special thank you to my parents, John and Kristen D'Rozario, for providing me with my fundamental roots. Dad, thank you for teaching me the power of endurance and pursuing my dreams, just like you did when you came to America as a teenager. Mom, thank you for teaching me the importance of self-confidence and respect and always being curious about the Universe. To my incredible boyfriend, Ethan Doe, I am so grateful for your love, support, care, and patience throughout my undergrad and graduate school studies. To my siblings, Erin, Jonathan, and my sister-in-law, Jordan, thank you for being such important role models. You have influenced my life in significant ways. Thank you to my niece Ayvah, who continues to keep me young at heart. I am proud of you and will be by your side as you continue to follow your own dreams. I was very fortunate to have my Beagle, Tycen, for nearly 20 years. Tycen provided comfort from grade school throughout my RIT studies, and I am so thankful for my time with him. Finally, I thank everyone not mentioned above who has impacted my life somehow. RIT is very special to me, and I am proud to be a member of this community.

Contents

List of Tables

List of Figures

Chapter 1

Dissertation Research Outline

1.1 Motivation

Optoelectronic devices are a substantial part of modern technology and are found in various specialized applications, including in the military, automatic control systems, telecommunications, power sources, biomedical, and display technology [1–5]. These devices manipulate the interaction between light and matter for use in specific material systems. The III-V compound semiconductor plays a crucial role in optoelectronic devices due to their fundamental properties and wide range in material selection, allowing them to be capable of sourcing, detecting, and controlling light [4, 5]. Some optoelectronic devices include photodiodes, photovoltaics (PV, also known as solar cells), light emitting diodes (LED), and laser diodes.

This dissertation research focuses on improving light absorption performance in thin-film III-V solar cells and light emission from micrometer-scale LEDs (μLED). New device designs have emerged as solar power generation and LED display technology advances. In solar power generation, conventional III-V solar cells are designed as "optically thick," where 3-5 μm of absorbing material ensures complete absorption of incident photons. For space-related PV applications, the solar cell efficiency declines after radiation exposure to highly energized particles

in the space environment as crystalline defects impact the carrier transport. Thinning the absorbing material to less than 1 μm reduces the distance carriers must travel to support power, making the thin-film design more tolerant to radiation degradation than their optically thick counterparts. Thin-film PV offers flexible and lightweight designs, favorable during space vehicle deployment. However, thinning the active solar cell region reduces the amount of photon absorption and limits the current generation in the solar cell. Therefore, light management is used to improve the photon absorption and result in an optically thick but physically thin solar cell design.

In the second application, the next generation of wearable devices requires small-featured LED displays to achieve high resolution. The μLED is valuable for near-eye display technology as it provides low power consumption, long lifetime, high contrast, and increased resolution, whereas the conventional millimeter-scale (mm) LED cannot achieve these goals. Instead, the mm-LED limits the resolution as these displays become closer to the eye. The μLED design proposes significantly improving the resolution of near-eye displays since they are over 10-times smaller than the mm-scale LED. However, the process development required to create a μLED damages the sidewalls and introduces defects, degrading the emitted light. Light management through sidewall passivation, surface cleaning, and regrowth techniques can be implemented to improve the light emitted from these devices.

The light management strategies in this work aim to reduce parasitic optical losses in the thin-film solar cell and the μLED to improve material quality and device performance. Part I of this dissertation focuses on the work to improve photon absorption in thin-film III-V solar cells to enable lightweight and highly efficient devices for space-related applications. Part II of this research focuses on improving the light emission in red-emitting μLED through sidewall passivation. The dissertation is organized as shown below.

1.2 Organization of Research

1.2.1 Part I: Light Management in Thin-Film III-V Photovoltaics

The first part of this dissertation focuses on light trapping development in thin-film III-V solar cells to maintain photon absorption and improve the radiation tolerance for space-related applications:

Chapter 2 introduces III-V PV technology and applications. Specifically, this chapter introduces the multijunction solar cell and the challenges of radiation damage in the space environment. The thin-film solar cell design is motivated as an approach to solving radiation damage issues and the light management required in thin-film solar cells to maintain photon absorption.

Chapter 3 provides details on various light trapping structures and the operation of solar cells.

Chapter 4 involves the design, growth, and fabrication process of conventional and thin-film solar cells.

Chapter 5 presents solution-based etching approaches for texture development to improve the photon absorption in gallium arsenide (GaAs) solar cells that are $< 1.1\ \mu m$ in thickness. Specifically, a photolithography-free wet chemical etching process referred to as the maskless etch is presented. The second technique uses inverse-progression metal-assisted chemical etching (I-MacEtch).

Chapter 6 involves modeling the absorption by free carriers in non-active layers of thin-film III-V solar cells. This analysis aims to reduce the optical loss due to this absorption mechanism and progress the performance of thin-film solar cells with light trapping structures.

Chapter 7 presents two favorable light trapping approaches, including dry etching and in situ etching. Optical characterization and dual-junction solar cell device results are presented.

Chapter 8 involves the optical and electrical device results for thin-film inverted metamorphic solar cells with various light trapping structures discussed in previous chapters. The results involve radiation modeling to validate integrating the developed textures in multijunction solar cells to achieve highly efficient, lightweight, and radiation tolerant space PV.

Chapter 9 concludes and highlights the light trapping and solar cell results.

1.2.2 Part II: Light Management in Micro-Light Emitting Diodes

The second part of this dissertation focuses on the process development, light management, and characterization of aluminum gallium indium phosphide (AlGaInP) μLEDs:

Chapter 10 introduces LED technology and its various applications. This chapter focuses on the use of red-emitting AlGaInP μLED for near-eye display technology.

Chapter 11 details the operation of the AlGaInP μLED and the integration of light management solutions through the use of sidewall passivation by wet-chemical etching and in situ etching, along with the overgrowth of wide bandgap materials.

Chapter 12 involves the experimental approaches towards optimizing a fabrication process for the AlGaInP μLED. This includes the mask development, ultraviolet photolithography, and dry etch processing. The surface cleaning consists of wet-chemical and in situ etching and the overgrowth of non-active wide band gap materials.

Chapter 13 involves the characterization of the μLEDs developed in this work.

Chapter 14 concludes the main highlights from the μLED research.

Chapter 15 lists the products as an outcome of this dissertation research.

Lastly, Appendix A provides additional detail on the solar and LED process development.

Part I

Light Management in Thin-Film III-V Photovoltaics

Chapter 2

Introduction to Photovoltaic Technology

2.1 Photovoltaic Technology and Applications

Solar power continues to emerge as a leading provider in sustainable power generation, and the various applications for PV technology require new device engineering and concepts according to the environment and application. For example, crystalline silicon (c-Si) PV is found in nearly 90% of terrestrial-related applications due to its abundance, cost-effective processing, and reliability [6,7]. For building-integrated PV, c-Si is a poor candidate since it is not inherently flexible and lightweight. Thinner materials such as amorphous Si (a-Si), cadmium telluride (CdTe), and copper indium gallium selenide (CIGS) are primarily used in applications requiring lightweight and flexible designs. Due to its low toxicity compared to CdTe, a-Si is used in consumer electronics such as calculators and watches [7]. The leading drawback when using a-Si over its crystalline counterpart is the reduced power conversion efficiency (PCE) from its discontinuous crystalline properties. While c-Si PV dominates the terrestrial market, the III-V compound semiconductor achieves unparalleled performance due to its excellent absorption properties. In addition, the III-V solar cell does not require as much material as c-Si, making them nearly 100x thinner and applicable where flexibility and weight restrictions apply. The main reason III-V solar technology is not as abundant in the terrestrial market is due to its

power generation cost near \$100-200 Watt^{-1}, which is orders of magnitude higher than c-Si technology near \$0.2-0.6 Watt^{-1} [8]. This difference requires dramatically reducing III-V PV processing costs to become a successful commercial terrestrial candidate.

There is an expanding market for sustainable power generation beyond terrestrial applications, specifically aerial and space-related missions. In these applications, weight and PCE are the primary factors to consider. For applications that require the deployment of aerial and space vehicles, the mounting area is much smaller than in terrestrial applications, so the solar cells must achieve high efficiency along with the minimal size and weight. The mass-specific power is a figure of merit to describe the efficiency output according to the system's weight. Si solar cells are thick in size compared to III-V materials and are approaching their theoretical efficiency limit of 29.8%, limiting their mass-specific power and integration into space-related missions [9, 10]. III-V PV experimentally demonstrates efficiencies greater than 32% with mass-specific power orders higher than Si, making them ideal for space power generation.

2.2 III-V Space Photovoltaics

2.2.1 Multijunction Solar Cells

III-V space PV are a leading power source for satellites, communication, scientific research, and outer-orbit space development [11]. For nearly sixty years, one of the leading providers in space PV, Spectrolab, has offered highly efficient and durable space solar arrays to customers, including the United States Air Force, Department of Defense, and National Aeronautics and Space Administration, to power spacecraft in missions operating in low and high Earth orbits as well as on Mars and lunar surfaces [12]. Another leading solar provider, SolAero, offers

high-efficiency space PV for various applications, including civil space exploration and observation, defense intelligence, and telecommunication [13]. The flexible PV arrays developed by MicroLink Devices power the High Altitude, Long Endurance (HALE) Unmanned Aerial Vehicle (UAV), enabling the craft to fly for months at a time for Earth surveillance, remote sensing, and resource management [14].

Space PV devices have one main similarity: they utilize the III-V multijunction solar cell (MJSC) design. The III-V compound semiconductor is an alloy consisting of group III and group V elements from the periodic table. Fundamentally, the III-V solar cell can absorb incident photons with energies greater than the energy gap, known as the band gap (E_g), for power generation. In a single-junction (SJ) III-V solar cell, such as GaAs, power generation is limited to photons with energy greater than its E_g, equivalent to 1.42 electronvolts (eV). The SJ solar cell cannot convert all photon energy into electrical work and suffers from thermalization and transmission losses. The III-V MJSC has achieved world record efficiencies because of its E_g tunability, targeting complementary parts of the solar spectrum and enabling broad photon absorption up to the semiconductor E_g in just a few μm of III-V absorbing thickness [6, 15]. State-of-the-art space solar cells consist of multiple solar absorbing materials with varying E_g energies that are monolithically stacked upon one another to utilize a broader range of the solar spectrum and minimize the thermalization and transmission losses prominent in the SJ solar cell design. The incident light strikes the widest E_g material capable of absorbing the high energy (UV-range) photons. Subsequent solar cells below this top-most absorbing region (referred to as a subcell in the MJSC) have narrow E_g energies to absorb the photons that transmit through the top subcell. Figure 2.1(a)-(b) displays the American Standard Extraterrestrial Spectrum (ASTM) Air-Mass zero (AM0) spectrum, which is the solar irradiance outside of Earth's atmosphere where (a) specifically shows the available energy to convert into electrical

work in a SJ GaAs solar cell and (b) shows the available energy for electrical work in the triple-junction inverted metamorphic (IMM) solar cell. The IMM triple-junction design consists of indium gallium phosphide (InGaP, E_g=1.8 eV) as the top-subcell, GaAs (E_g=1.42 eV) as the middle subcell, and indium gallium arsenide ($In_{0.3}Ga_{0.7}As$, E_g=1 eV) as the bottom subcell.

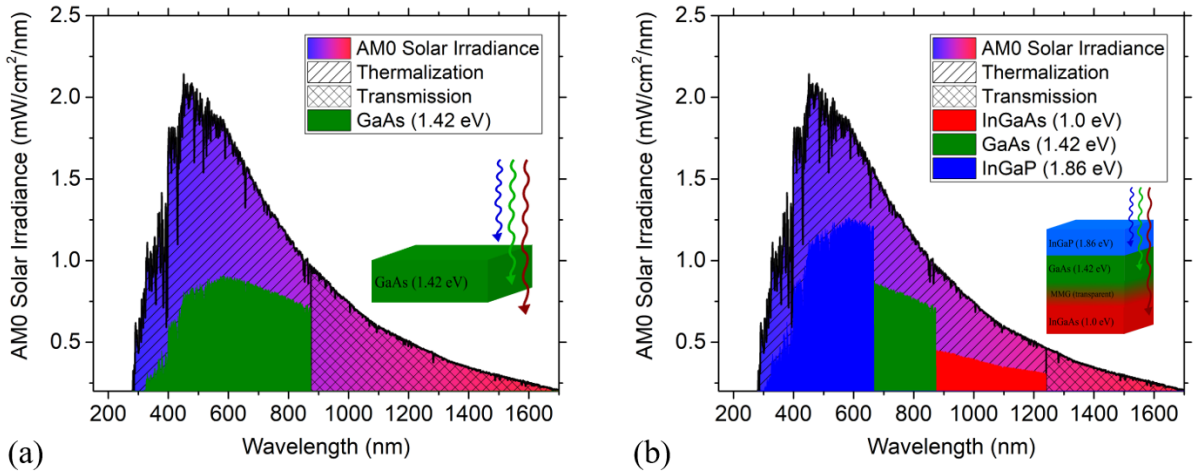

Figure 2.1: The American Standard Extraterrestrial Spectrum (ASTM) AM0 solar irradiance spectrum and energy losses for (a) single-junction GaAs solar cell (available energy in green) and (b) triple-junction IMM solar cell noting the available energy for the top InGaP subcell (blue), the middle GaAs subcell (green), and the bottom 1-eV InGaAs subcell (red). Both plots showcase the thermalization and transmission losses associated with each design.

In order to maintain a high-quality crystal between the semiconductors with varying E_g, the crystal lattice which describes the atomic placements across the unit cell in the semiconductor must be similar to avoid defects caused by free atomic bonds [16]. Figure 2.2(a) shows the IMM design, and Figure 2.2(b) shows the lattice-band gap chart with crossover points for each subcell. The top and middle subcells are lattice-matched near 5.642 Å, and the bottom InGaAs subcell with 30% In has a larger lattice constant near 5.767 Å. The bottom subcell has a band edge at 1 eV, which permits a broader range of the solar spectrum to be converted into electrical work. A metamorphic grade (MMG) consisting of multiple epitaxial growth steps with varying In% compositions is used to bridge the lattice constants between the middle and

bottom subcells.

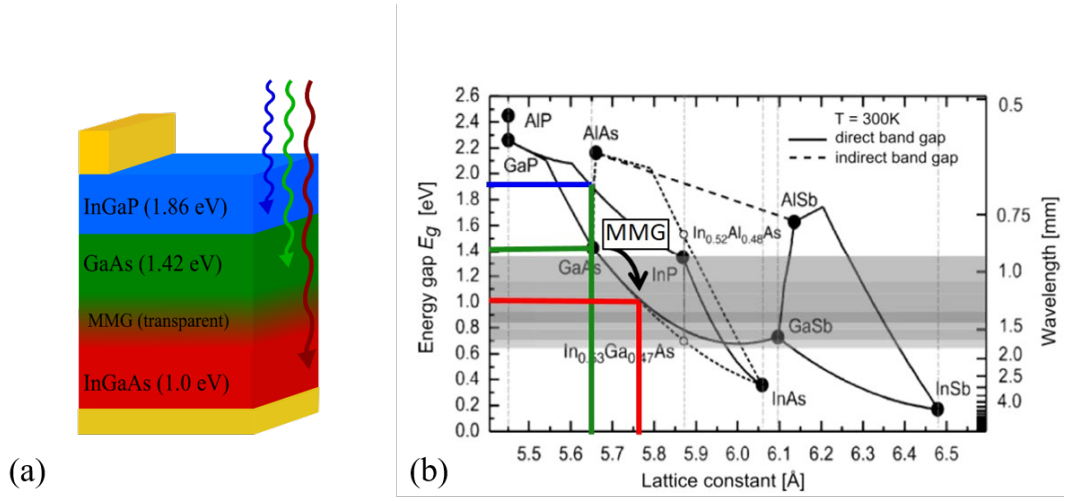

Figure 2.2: Plot (a) shows the IMM MJSC with the corresponding subcell band gaps. Plot (b) shows the lattice-band gap chart where the three subcells are depicted according to their respective band gaps and lattice constants.

Besides the IMM design, other high-efficiency MJSCs can be developed according to the lattice-band gap chart. SpectroLab and SolAero use a triple-junction design consisting of InGaP/GaAs/Germanium (Ge), lattice-matched to the Ge substrate. This MJSC has reached efficiency up to 32% under the AM0 spectrum. Another design from SolAero named the Z4J has a similar geometry but includes a fourth subcell to progress the PCE [13]. One main difference between the IMM design and the triple-junction grown on Ge substrate is the order of growth and detaching of the substrate in the IMM design. For the InGaP/GaAs/Ge solar cell, the InGaP top subcell is the last region grown since it will become the first material incident light initially strikes. This design remains intact with the Ge substrate, which is over 300 μm thick, leading to a robust and non-flexible design. The IMM design is grown inverted, meaning that the last epitaxial layer becomes the backside of the solar cell. MicroLink Devices utilizes their proprietary epitaxial lift-off (ELO) technology to detach the solar cell structure from the host substrate, rendering lightweight and flexible PV arrays. The IMM solar cell made by MicroLink

Devices is near 29% efficient under the AM0 spectrum and offers an areal mass density <350 g/m^2. The smaller areal mass density offers lightweight space PV arrays, making it easier to deploy spacecraft. More details on the design and transfer process used to develop the inverted solar cell and the epitaxial growth of III-V solar cells are discussed in Chapter 4.

2.2.2 Radiation Damage in Space Solar Cells

One main difference between solar power generation in terrestrial and space applications is the environment surrounding the device. Outside of Earth's atmosphere, the Van Allen radiation belts trap charged particles with energized electron fluxes up to 9x10^9 e$^-$/cm^2/s and protons up to 2x10^8 protons/cm^2/s [17–20]. Radiation damage occurs when the spacecraft with mounted solar arrays pass through the radiation belts, and energized particles constantly bombard the active absorbing region of the solar cell. This bombardment produces mid-E_g trapping centers for charge carriers, degrading the minority carrier diffusion length (MCDL). This degradation leads to a reduction in the beginning-of-life (BoL) efficiency. The atomic displacement from an incoming particle that breaks the atomic bond in the crystalline semiconductor and results in a trapping center for charge carriers [17]. Since this atomic displacement reduces the MCDL, the collection efficiency drops, and the performance at the end-of-life (EoL) is lower than the BoL performance.

The trapping centers from atomic damage in the solar cell affect the electronic properties by shortening the MCDL in the material. Each semiconductor has different damage coefficients as they respond differently to particles of different energies [18]. The radiation damage for different materials is explained through the empirical relationship correlating the radiation species, and the MCDL [21],

$$\frac{1}{L} = \frac{1}{L_0} + K_L \cdot \phi, \tag{2.1}$$

where L is the diffusion length after exposure, L_0 is the BoL diffusion length, K_L is the damage coefficient associated with the active region of the solar cell, and ϕ is the radiation fluence. Since the MJSC consists of subcells joined together in series by the top and bottom electrical contact, the overall current output is limited by the subcell producing the lowest current. At the same time, the voltage output is the summation across all subcells. The damage coefficients of the top InGaP subcell from electrons and protons with various fluences have previously been reported to be much less than the middle GaAs subcell and the bottom InGaAs subcell [22]. The bottom solar cell suffers the most from radiation damage in space and becomes the current-limiting cell (thus limiting the PCE) at EoL conditions.

2.2.3 Thin-Film Space Solar Cells for Radiation Hardness

One common approach to mitigate trap-assisted recombination and degradation of MCDL in the bottom subcell is to reduce the active region thickness [19, 23, 24]. Since the MCDL is a material property averaging how far carriers can diffuse before they recombine, thinning the active region will lessen the density of atomic displacement and allow carriers to travel a smaller mean-free path length to be collected at the external electrodes. Research has experimentally shown that thinning the active solar cell region maintains the current output in space PV [25]. Using Equation 2.1 with Technology Computer-Aided Design (TCAD) Synopsys Sentaurus Device, damage displacement modeling was performed in this work to compare the degradation in subcell performance for the optically thick (3.6 μm) and physically thin sub-µm (0.5 μm) devices. Sentaurus Device provides an electrical simulation of solar cells based on carrier transport, including drift of carriers in the presence of electric fields and diffusion of

carriers due to concentration gradients [22]. Based on the materials damage coefficient, this model renders predictive representations of the bottom subcells' electrical performance after radiation exposure. Nelson extensively developed the damage coefficients used in this work through various examples of experimental fitting [22]. Figure 2.3(a)-(b) presents the external quantum efficiency (EQE), which is an indication of the collected electron-hole pairs per incident photon at a specific wavelength. Figure 2.3(a) displays the EQE for the dual-junction (DJ) InGaP/GaAs solar cell Figure 2.3(b) displays the EQE for the IMM solar cell. For the optically thick design at BoL, a complete collection of photons is present up to the semiconductor band edge. After the exposure of 1 MeV electrons (e^-) at a fluence of $5x10^{15}$ e^-/cm^2, the collection reduces in the optically thick bottom subcells, especially evident near the band edge. Once the base region in the bottom subcell for both designs is thinned and the total absorber thickness is 0.5 μm, the current collection at EoL is maintained compared to the BoL current output. The remaining factor represents the ratio of current at EoL and BoL. The remaining factor is close to unity for the thinned subcell, whereas the optically thick absorber shows a significant drop in the remaining factor, as displayed in Table 2.1. The EoL performance is maintained for the sub-μm thick bottom subcell, indicating higher radiation tolerance.

Table 2.1: Bottom Subcell Remaining Factor

Bottom Subcell	BoL J_{SC} ($mA{\cdot}cm^{-2}$)	EoL J_{SC} ($mA{\cdot}cm^{-2}$)	Remaining Factor (EoL/BoL)
GaAs (3.6 µm)	12.87	11.07	0.86
GaAs (0.5 µm)	7.67	7.65	0.99
InGaAs (3.1 µm)	19.94	18.86	0.94
InGaAs (0.5 µm)	9.54	9.54	0.99

Both examples above show improved radiation tolerance in the bottom thinned subcells.

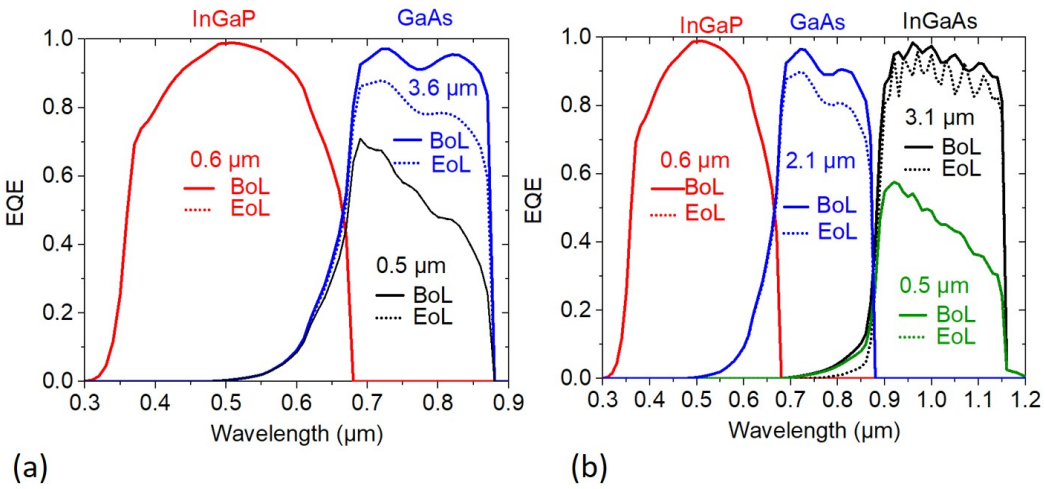

Figure 2.3: EQE and damage displacement modeling for a (a) dual-junction InGaP/GaAs and (b) IMM InGaP/GaAs/InGaAs solar cell design with different bottom subcell thicknesses.

However, it is evident that the reduction in absorber thickness minimizes the number of optically generated carriers and the PCE drops compared to the initial efficiency of the conventional, optically thick solar cell. The transmission loss of near band edge photons becomes the main issue when thinning the solar cell. Light trapping structures in thin-film solar cells grant the opportunity to increase photon absorption and maintain the current output realized in the optically thick device.

2.2.4 Light Management in Thin-Film Photovoltaics

Maintaining photon absorption in optically thin III-V MJSC can be accomplished by integrating back surface reflectors (BSR) to increase the photon path length inside the thin solar cell and enhance the photogenerated current. Recent research has proven the significance of light trapping designs in thin III-V solar cells with an increased photogenerated current collection comparable to conventional optically thick solar cells [26–30]. Since the low-energy photons near the band edge require extended absorption depth, the BSR is suitable for increasing photon optical path length (OPL). The ideal planar BSR will reflect unabsorbed photons after the

first pass back into the solar absorbing region. While a 2-fold path length enhancement effectively improves photon absorption, there is a limit to how thin the solar absorber can be while maintaining the current output realized in the optically thick design. Texturing the backside of the thin-film solar cell allows the incident photons to scatter in multiple directions. Once these photons strike the internal front surface of the solar cell, they have a higher probability of experiencing total internal reflection (TIR) to achieve a path length greater than two. The highly diffuse textured BSR renders a pathway for radiation-tolerant, lightweight thin-film solar cells, and its benefits are further described in Chapter 3.

Figure 2.4 portrays the DJ InGaP/GaAs and the inverted metamorphic (IMM) InGaP/GaAs/InGaAs design employed in this work. This figure compares the optically thick and physically thin bottom subcells where the incorporation of light management can increase the OPL by reflecting unabsorbed photons into the active region. Although the leading providers in space PV all utilize the triple-junction (or more junction) designs, the DJ solar cell has been shown to provide high efficiencies approaching 30% under the AM1.5G spectrum [31]. By integrating light trapping structures into the solar cell design, it is possible to maintain the photon absorption in the thinned DJ solar cell to match the current expected from the optically thick design. This design also presents a highly efficient solar cell at EoL with less material consumption, achieving high mass-specific power and radiation tolerance. Furthermore, improving the radiation tolerance in the bottom subcell for an IMM design will render flexible and lightweight PV with high efficiency at EoL, providing the opportunity to surpass the performance of conventionally thick MJSC at EoL.

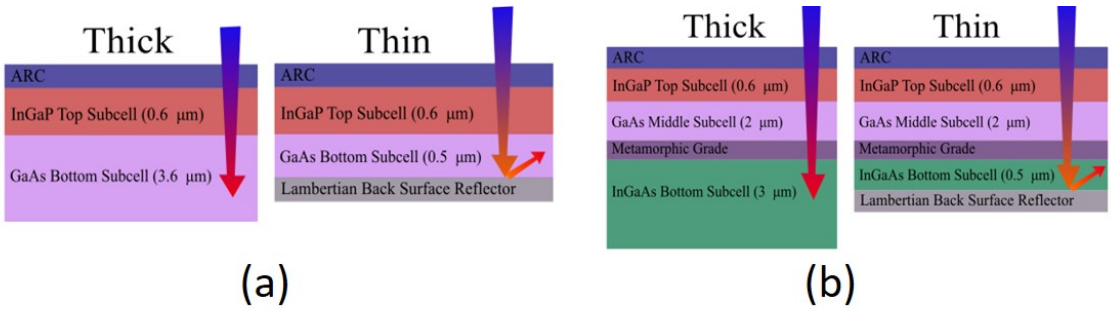

Figure 2.4: The case of optically thick bottom subcells to the thinned subcell with a back surface reflector for the (a) dual-junction design and (b) the triple-junction IMM design.

Currently, the III-V photovoltaic community has extended light trapping schemes using photonic crystals and gratings, distributed Bragg reflectors (DBR), solution-based chemical etching, ultraviolet photolithography, and nanoimprint lithography techniques in ultrathin solar cells [29, 30, 32–39]. These methods are sufficient to increase the OPL in ultrathin absorbers; however, they may not be cost-effective for already-established production. For space PV, it is essential to keep the cost of device production low, so the light management solutions should not require multiple steps, long processing times, or have increased material costs. The DBR and planar backside mirrors are used for space-manufactured solar cells but limit the path length enhancement and thus the current output in ultrathin (sub-μm) solar cells. Therefore, this dissertation research focuses on simple processes to develop diffuse textured BSR through novel solution-based etching, in situ etching, and regrowth techniques. The benefits of employing diffusely textured BSR in thin-film space PV are motivated in Chapter 3.

Chapter 3

Light Management and Photovoltaic Operation

3.1 Introduction

This chapter is dedicated to light management concepts and impacts on device operation of III-V solar cells. The progress in III-V light management stems from the evolution of light trapping in Si-based PV research. However, many fundamental differences exist between the E_g of Si and most III-V semiconductors, leading to different light trapping influences on III-V solar cell performance. For example, when light management is introduced to the III-V solar cell operating in the radiative limit, both current and voltage output are impacted depending on the light trapping structure. While the inevitable material degradation in thin-film space PV reduces the potential benefits from photon recycling, light trapping structures can maintain the photogenerated current and motivate using textured BSRs. Increasing the TIR using low-index interlayers presents an opportunity to design highly effective light trapping structures, and these techniques are used throughout this work.

3.2 Evolution of Light Management

Emerging light management designs in current thin-film III-V PV stem from the considerable light trapping efforts and progress in silicon PV. In the 1960s, the highest recorded Si cell

terrestrial efficiency remained at 14.5% for several years due to proper engineering of the active region [40]. The following phase in solar cell advancement that employed photon management finally broke this record by more than 2% through anti-reflection coatings (ARC) and textured surfaces [40]. In 1975, the dramatic efficiency boost from the termed "non-reflecting" Si solar cell was partly a result of the textured front surface. Created by a solution-based crystallographic etch, the three-dimensional pyramidal surface texture reduced surface reflectivity and amplified light absorption within the active region [40]. The aspect ratios of the pyramidal surface texture, produced by the potassium hydroxide (KOH) etchant, can be tailored according to the etchant conditions. The change in the aspect ratio of the features on the surface of the solar cell increases the wide angle of incident photon collection by gradually changing the index of refraction between air (low index) and the bulk silicon (high index). These structures randomly scatter and increase the OPL inside the absorbing region and the PCE [41–43]. One current solar cell design that uses this light scattering technique is the passivated emitter, rear locally diffused (PERL) design. Due to simple development, other modern Si solar cells still use this texture at both the front and back surfaces of the solar cell to enhance the photon absorption and current output [44–47]. The PERL solar cell design has achieved one of the highest terrestrial SJ Si-based solar cell efficiencies equal to 25.5% [40].

3.3 Solar Cell Operation

The fundamental difference in the absorption coefficient (α_c) between Si and most III-V semiconductors is the E_g. In a direct E_g semiconductor, the conservation of momentum is met since the maximum of the valence band (E_V) lines up with the minimum of the conduction band (E_C). This alignment means that the optical absorption of a photon and corresponding excitation and generation of an electron-hole pair only requires that the incident photon have

energy greater than the E_g itself. The generation of an electron-hole pair in the indirect E_g semiconductor, such as c-Si, depends not only on the optical absorption of a photon but also on the assistance of phonon, or lattice vibration, to conserve momentum since the minimum E_C and maximum E_V do not line up. The α_c of the indirect E_g, therefore, is lower than the direct E_g semiconductor as it is proportional to the E_g and the phonon energy (E_{ph}) [48]. The energy bands, shown in the energy (E) - momentum (k) diagrams in Figure 3.1, portray the necessary processes to support the generation of an electron-hole pair. The direct E_g has a higher α_c as it relies only on the photon absorption with sufficient energy.

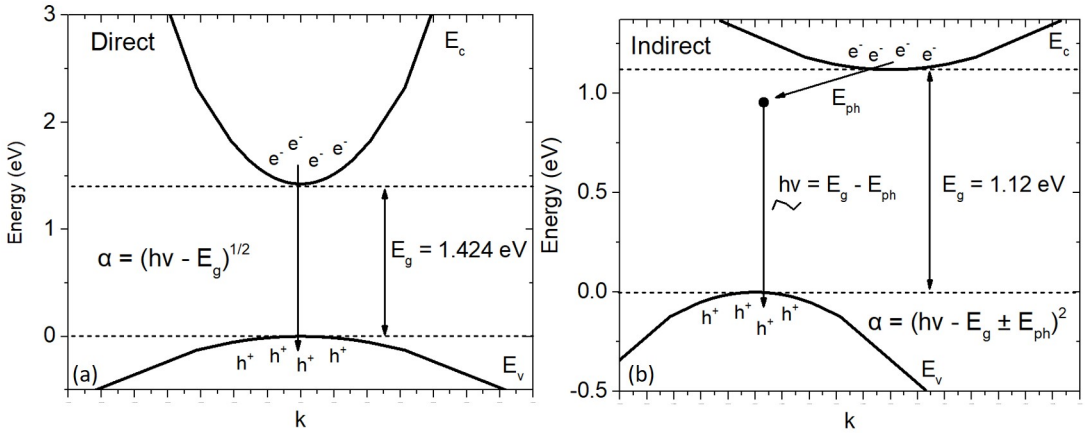

Figure 3.1: Energy-momentum (E-k) diagrams to compare the optical absorption in direct and indirect E_g semiconductors.

Direct E_g semiconductors have a sharp cut-off in absorption near their energy band edge, whereas c-Si with its indirect E_g gradually reduces in absorption at longer wavelengths. This difference allows the III-V solar cell to be over 100-times thinner than Si without mitigating photoabsorption loss of available photons above the E_g. The α_c near the E_g of GaAs around 1.42 eV shown in Figure 3.2 is much sharper compared to the indirect E_g of c-Si. This figure shows the α_c for the various materials used in this work. The right y-axis in Figure 3.2 shows the absorption depth ($1/\alpha_c$), which is the required material thickness to absorb the available photons at a particular wavelength. For Si with a E_g around 1.12 eV, the required optical

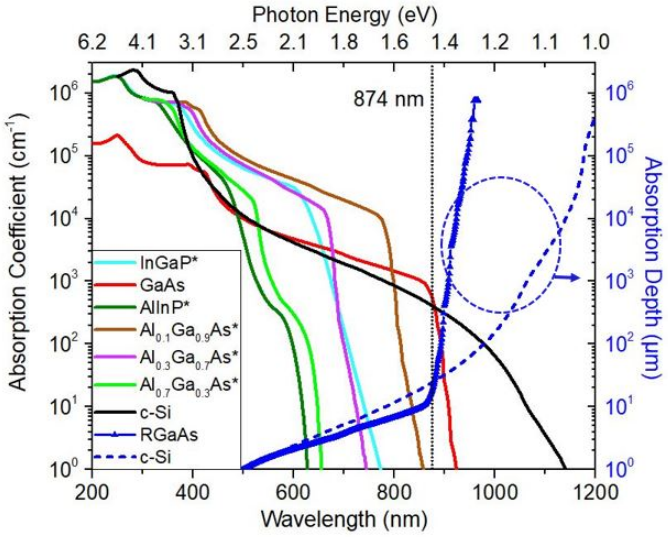

Figure 3.2: Absorption coefficients for commonly used materials in this research. The materials indicated by (*) are RIT grown materials that were measured using variable angle spectroscopic ellipsometry (VASE). The measured data is fit using a Cauchy oscillator to extract the index of refraction and extinction coefficient for each material between 200 nm and 1700 nm. Since GaAs is a well-developed material, the absorption coefficient specifications are from the Woollam Database, and the Si specifications, as recorded by Green [49] were used.

thickness is on the order of a few hundred micrometers thick, whereas GaAs only requires approximately 4 μm absorber thickness.

The solar cell is a two-terminal device asymmetrically connected to an external circuit and operates like a diode in the dark and generates a photovoltage under the presence of light [1]. Placing two semiconductor regions with foreign atoms, also known as impurities or dopants, which have either one less (holes) or one more valence electron than the host material, results in a diffusion of carriers and creates a junction. The electrons diffuse to the positive side, where a positively ionized donor atom is left behind, and the holes diffuse to the negative side, leaving a negatively ionized acceptor atom resulting in the space charge region (SCR) at the positive-negative (PN) junction [1]. Due to the diffusion current of electrons and holes, the built-in electric field across the PN junction results in a potential difference that determines the voltage at open-circuit conditions. An incident photon can transfer its energy to excite the bound

electron into the conduction band as long as the energy is the same or higher in magnitude than the bandgap [50]. This process is the first step to a photogenerated current where the hole is an empty site in the valence band once the electron liberates into the conduction band [1]. When there is an external light bias, the total current will be influenced by the sum of the photogenerated current, J_L, and the dark current as,

$$J(V) = J_L - J_{01}(e^{\frac{q(V-JR_S)}{n_1 kT}} - 1) - J_{02}(e^{\frac{q(V-JR_S)}{n_2 kT}} - 1) - \frac{V - JR_S}{R_{SH}}, \tag{3.1}$$

where J_{01} is the dark recombination current density in the quasi-neutral regions (outside of the junction) and J_{02} is the dark recombination current density in the SCR. The ideality factors, n_1 and n_2, are associated to each dark diode, k is Boltzmann's constant, V is the voltage across the cell terminals, and T is the temperature of the solar cell. The terms R_S and R_{SH} relate to the series resistance and the shunt resistance, respectively, which are two parasitic losses in the non-ideal diode case. The ideal case would have an infinite shunt resistance so that current cannot flow in parallel to the diode, and the series resistance, ideally, would be close to zero. This ideality will make the last term in Equation 3.1 negligible. Additionally, the ideal solar cell would not have recombination within the SCR associated with trapping centers for minority carriers. When modeling realistic solar cell performance, the double-diode equation represents different recombination events where SCR recombination current density usually dominates at low voltages, and bulk effects outside this region take over at high voltage [22]. At short-circuit conditions where no voltage is present, the photogenerated current output is known as the short-circuit current density (J_{SC}). The current density is the current output normalized to the active area of the solar cell, which is important when comparing solar cells of different active areas. When light is not present, the dark current density, J_D, across the PN junction is represented by Equation 3.1 with $J_L = 0$. Figure 3.3(a) represents the equivalent

solar cell circuit under a light bias, and the region within the dotted circle relates to the diode and dark current density. This equivalent circuit only shows the single-diode. The second diode would parallel the first diode and the R_{SH} path.

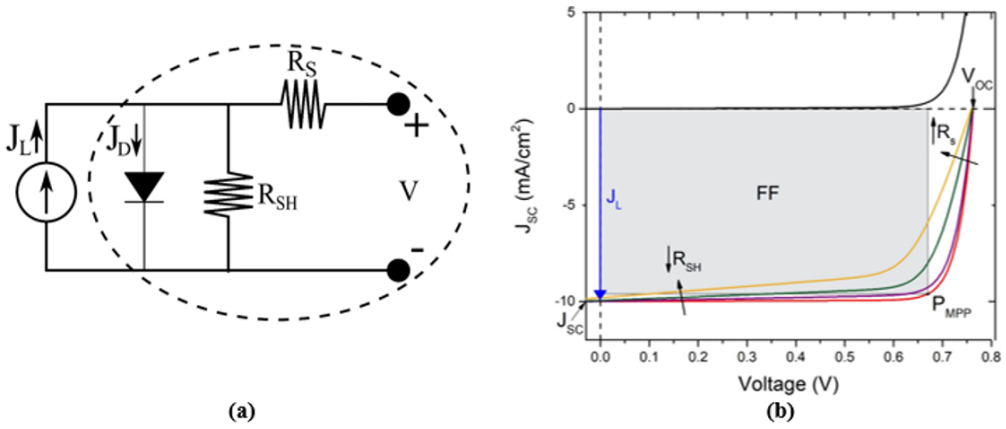

Figure 3.3: (a) Equivalent circuit of a solar cell where the region within the dotted circle is the diode in the dark, and the entire circuit relates to the solar cell under light bias. (b) J-V curves for the solar cell in the dark (black curve) and under light bias with the impact of resistive losses, P_{mpp}, FF, V_{OC}, and J_{SC}.

The corresponding performance of the diode, both with and without the influence of light, is represented by the current density–voltage (J-V) curves shown in Figure 3.3(b). The J-V curves have been modeled using an implicit fit of the diode Equation 3.1 using Matlab's computer programming language. For the solar cell measured in the darkness where $J_L = 0$ (black curve), the current through the diode is small at low applied voltages and increases with voltage. Under a light bias, when a photogenerated current is present, the J-V shifts downward by a factor of J_L, and the red curve models the ideal scenario. Here, J_{SC} is shown where the bias is zero. The diode current balances the photogenerated current with increasing forward bias until the net current through the diode is zero at open-circuit conditions, resulting in the open-circuit voltage (V_{OC}) on the J-V curve. For the ideal red curve where no resistance losses

are present, the maximum power point (P_{mpp}) is the highest. As the series resistance increases and the shunt resistance reduces, the P_{mpp} reduces. The series resistance from the most ideal J-V curve (red) to the least ideal J-V curve (yellow) increase by 5 $\Omega{\cdot}cm^2$ starting at 0 $\Omega{\cdot}cm^2$, and R_{SH} reduce from 1x10^5 $\Omega{\cdot}cm^2$ down to 80 $\Omega{\cdot}cm^2$. The series resistance includes any resistive loss that carriers flow throughout the cell, including lateral movement in the emitter or other lateral conduction layers, movement across the junction, and metal/semiconductor contact resistance and affects the slope near V_{OC}. The shunt resistance is related to leakage currents throughout the diode, including trap-assisted tunneling, recombination events, poor material quality in the bulk region, at the edges, or interfaces of the solar cell, and affects J_{SC}. For the ideal solar cell with the smallest resistance losses, there will be the largest rectangular area under the J-V curve. The grayed region represents the fill factor (FF) in Figure 3.3b, which is a ratio of the P_{mpp} on the J-V curve divided by the product of J_{SC} and V_{OC},

$$FF = \frac{P_{mpp}}{J_{SC} * V_{OC}} = \frac{V_{mpp} * J_{mpp}}{J_{SC} * V_{OC}}. \tag{3.2}$$

The power conversion efficiency, η, of the solar cell depends on the FF and is the ratio of the total maximum generated power to the incident illumination power,

$$\eta = \frac{P_{mpp}}{P_{in}}, \tag{3.3}$$

where P_{in} is the total illumination power incident on the solar cell. This illumination power depends on the solar spectrum incident on the solar cell. Conventionally, the illuminated J-V curve is plotted in the first quadrant, referred to as the power quadrant.

3.4 Influence on Device Operation with Light Trapping Geometries

3.4.1 Enhanced Open-Circuit Voltage by Photon Recycling

When the BSR is integrated behind optically thick solar cells, the behavior and operation of a solar cell remain the same. However, once the solar cell active region is thinned and no longer optically thick, light trapping mechanisms will affect J_{SC} and V_{OC}. The BSR can be designed in many ways, including a planar mirror to achieve a twofold photon path length [35, 51], a textured surface to increase TIR [52–54] or nanostructures to excite optical modes within the cavity of the active region [55–58]. For the optical designs displayed in Figure 3.4, the GaAs absorbing region in green is intended to be optically thin. Design (a) shows the GaAs solar cell on an absorbing substrate where low-energy photons not easily absorbed at the front of the solar cell will be parasitically absorbed due to transmission loss after an OPL of one pass. Design (b) displays a parasitic backside mirror that does not adequately reflect light into the absorbing region. Designs (c) shows a highly reflective planar BSR and (d) displays a highly reflective and textured BSR. In Designs (c)-(d), the triangle represents the escape cone, as discussed in further detail below, and the reflective properties directly impact the voltage or current output in thin-film solar cells.

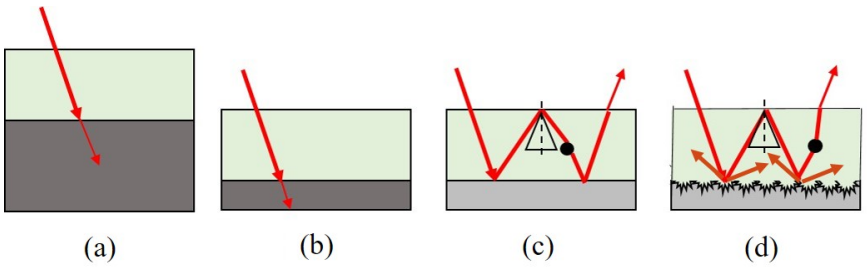

Figure 3.4: Different photon management structures for a thin GaAs absorber: (a) GaAs on an absorbing substrate, (b) GaAs with an absorbing back mirror/surface, (c) GaAs with a good planar mirror, and (d) GaAs with a good, textured mirror and a planar front surface.

For SJ GaAs solar cells, it has been determined that high-quality material and photon management will assist in reaching the upper detailed balance efficiency [59–61]. The internal luminescence efficiency (η_{int}) indicates the material quality and is described by,

$$\eta_{int} = \frac{U_{rad}}{U_{rad} + U_{nr}}, \tag{3.4}$$

where U_{rad} and U_{nr} are the radiative and non-radiative recombination rates, respectively [62]. The η_{int} is based on the material quality of the semiconductor, including bulk, interface, and perimeter recombination effects. High material quality is associated with negligible U_{nr}, where U_r is the only recombination mechanism, leading to η_{int} or internal radiative efficiency (IRE) at unity. For an ideal direct E_g material, band-to-band or radiative recombination of an electron-hole pair is the theoretical limiting recombination event. For indirect E_g, such as Si, the domination of the non-radiative Auger recombination limits its internal luminescence $< 20\%$ [63]. Auger recombination is described as a subsequent excitation of charge carriers into higher energy states, leading to energy loss from heat within the crystal. In high-quality GaAs, the probability of internal photon emission from radiative recombination has been experimentally determined to be 99.7%, which is close to the ideal case where η_{int} is at unity [64]. Shockley-Read-Hall (SRH) recombination may occur for both material systems, which describes the trap-assisted recombination of electron-hole pairs due to defects in the crystal. Overall, for direct E_g, the radiative band-to-band recombination events yield a higher probability of enhancing the GaAs solar cell's luminescence efficiency.

Light trapping structures can be tailored such that the ongoing cycle of internally generated photons increases the OPL and results in an increase in the photogenerated current. These structures can also be designed to increase the external luminescence efficiency (η_{ext}), which is the external emission of photons from the front of the device and impact the voltage output

at open-circuit conditions. With high material quality, radiative recombination will be the dominant mechanism in a solar cell with high η_{int}. The absorption of the reflected photon from a BSR can lead to radiative recombination of an electron-hole pair, leading to another photon emission event. This process is known as photon recycling and creates a build-up of internally generated photons at open-circuit conditions, yielding a higher voltage output [64, 65]. When the material quality and luminescence efficiency is low, incoming photons that create electron-hole pairs do not radiatively recombine, and the benefits from photon recycling break down. With high material quality, the reflective back mirror in Figure 3.4(c) allows these re-absorption/emission events to continue. The parallel-plane geometry can emit a large amount of internally generated photons, indicative of higher carrier density build-up and V_{OC}. By considering the mass action law, at open-circuit conditions, the voltage output is related to the generated carrier densities [65].

$$np = n_0 p_0 exp(\frac{qVoc}{kT}). \tag{3.5}$$

Due to reciprocity, thermodynamics reveals that light absorption and emission must be proportional and is part of a necessary equilibrium process, much like in the LED [64]. Therefore, the build-up of generated carriers must be at equilibrium and balanced by the act of carrier recombination. So under open-circuit conditions, the high density of re-emission events must lead to external luminescence efficiency. The re-absorption/emission in high-quality GaAs makes it a suitable material to improve photon recycling and V_{OC} while approaching the efficiency limit. The η_{ext} dependence on V_{OC} can be written as [66],

$$V_{OC} = V_{OC}^{ideal} + \frac{kT}{q} ln(\eta_{\text{ext}}). \tag{3.6}$$

For a GaAs solar cell to operate in the radiative limit, the SRH and Auger lifetimes must be longer than the radiative lifetime, equivalent to 5 nanoseconds (ns), to reach V_{OC} of 1.12 V [66, 67]. Referring back to Figure 3.4, Design (c) will limit current output for ultrathin GaAs absorbing regions since the increase in OPL is twofold for normal incident light; however, the voltage output will increase as the increased external luminescence due to the planar front surface. Therefore, if the goal of the light trapping structure is the improve the current output, a textured back mirror as shown in Figure 3.4(d) is required to promote an increase in OPL. This is discussed in detail in Section 3.4.2.

The relationship between V_{OC} and the planar mirror's reflectivity in high-quality GaAs solar cells has been reported throughout literature [64, 68] where the slightest drop in reflectivity reduces the voltage output. Figure 3.5 displays the impacts on V_{OC} according to a planar mirror's reflectivity for a GaAs solar cell with high material quality. The highly reflective mirror close to unity is crucial to enhance the solar cell's luminescence efficiency since repeated attempts are created for internally generated photons to escape through the emission angle. The impacts on parasitic absorption mechanisms that degrade the mirror reflectivity is investigated in Chapter 6.

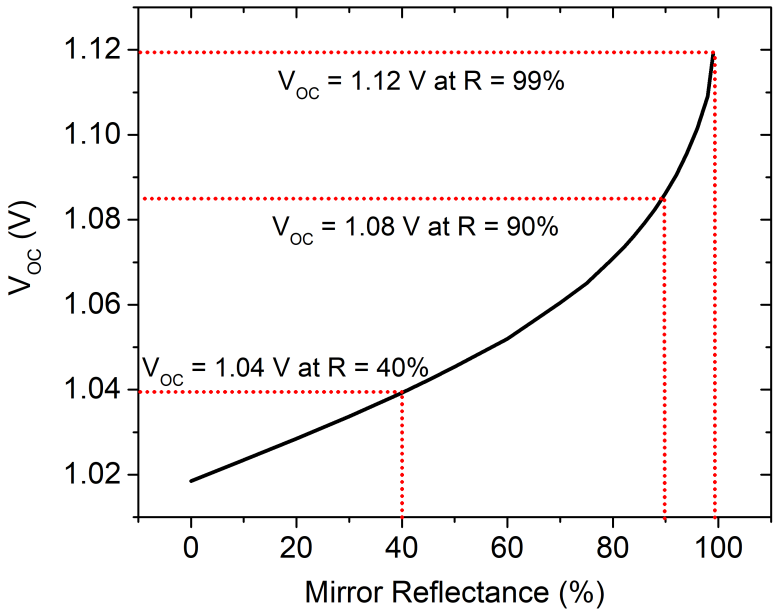

Figure 3.5: Significance of a highly reflective backside mirror (»90% reflectivity) for a GaAs solar cell with high material quality.

In certain cases, the benefits of photon recycling and high external luminescence on voltage output are not as valuable. One example is outer orbit space PV technology, where the atomic displacement in the crystal from radiation damage introduces numerous defects that acts as traps and enhance non-radiative recombination. This reduces the η_{int} shown in Equation 3.4 since the U_{nr} increases. There may be scenarios, though, where atomic displacement may not fully impact the photon recycling, such as in ultrathin GaAs solar cells (<100 nm thick) in low-orbit missions where radiation damage is not as detrimental to the crystal properties. Although photon recycling is primarily not valuable for space-related PV, light management is still profitable to heighten the photon absorption by increasing the OPL in ultrathin solar cells, which is the ultimate goal of this work.

3.4.2 Enhanced Short-Circuit Current Density by Optical Path Length

The Beer-Lambert Law describes the amount of incident light absorption passing through an absorbing medium. For ultrathin GaAs absorbers, the output intensity will be much higher than the optically thick absorber. The Beer-Lambert law shows the dependence of the thickness and absorption coefficient of the absorbing medium and is written as,

$$I = I_0 e^{-\alpha \cdot l}, \tag{3.7}$$

where α is the absorption coefficient of the solar absorbing material, l is the thickness of the absorbing material, I_0 is the incident intensity of the illumination source, and I is the output intensity after traveling through the absorbing material. The absorption can be calculated at different wavelengths for various absorbing thicknesses by setting the incident intensity to unity. This was done for different thicknesses of a GaAs absorbing region ranging from 0.1 μm thickness to 3.6 μm thickness, as shown in Figure 3.6. In this figure, the absorption for the 3.6 μm GaAs absorber is near 100% to the GaAs band edge at 870 nm in wavelength (equivalent to E_g of 1.42 eV). This complete absorption shows that the output intensity will be close to zero. As the absorber is thinned, the near band edge photons transmit through the backside and reduce the absorption.

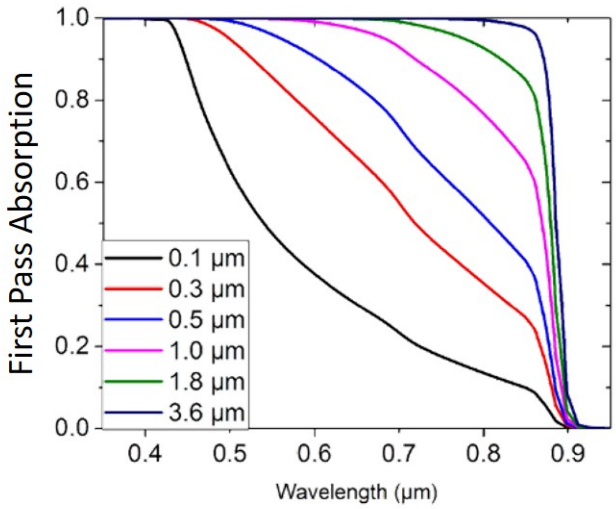

Figure 3.6: First pass absorption through a GaAs absorbing region with different thicknesses.

By integrating the absorption, $A(\lambda)$, in the optically thick GaAs with the AM0 spectrum intensity, $E(\lambda)$, over the wavelength range from 350 nm to 870 nm, the generated current density is,

$$J_{\mathrm{SC}} = \frac{q}{hc} \int_{\lambda_1}^{\lambda_2} \lambda E_{AM0}(\lambda)\, A(\lambda)\, d\lambda, \tag{3.8}$$

where q is the electronic charge, h is Planck's constant, and c is the speed of light. For the 3.6 μm GaAs absorber, the J_{SC} is calculated to be 35 mA·cm^{-2}. Once the solar cell is thinned, the absorption reduces, and the J_{SC} drops from this ideal current output.

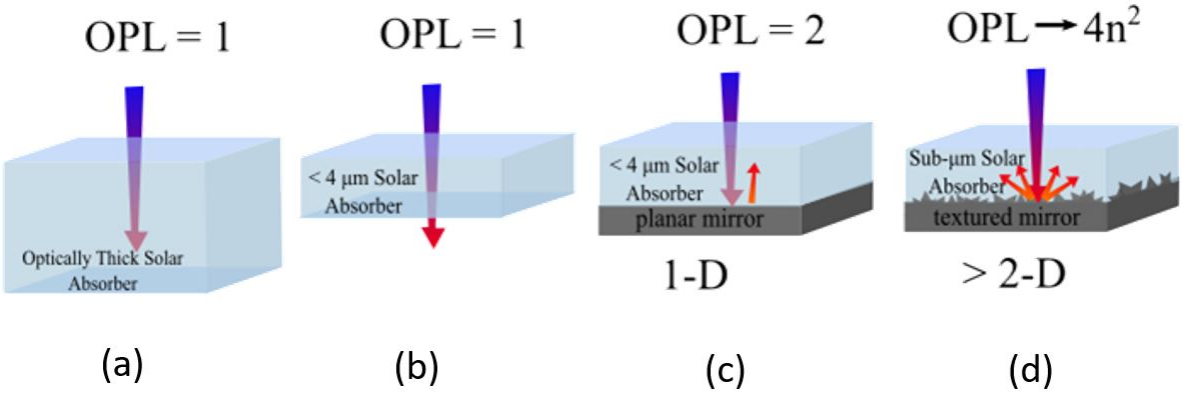

Figure 3.7: Schematic diagrams showing optical path length enhancement for (a) an optically thick absorber, (b) an optically thin absorber, (c) an optically thin absorber with a planar back mirror, and (d) an optically thin absorber with a textured back surface reflector.

Figure 3.7(a) represents an optically thick absorbing region with the arrow indicating photon path length. If this absorbing region reduces in thickness, as shown in Figure 3.7(b), the near band edge photons transmit through the backside due to inadequate attenuation of the long wavelength photons. The BSR increases the OPL and near band edge photon absorption. The planar mirror reflects unabsorbed photons for a 2-fold increase in the OPL, as shown in Figure 3.7(c). Notably, if the BSR is introduced to an optically thick solar cell, the light trapping structure will have no optical benefits since the photon absorption is complete after one pass. As the absorber thickness approaches the sub-μm scale, a BSR with more than 1-dimension must be used to increase the photon scattering at the backside of the solar cell. Creating a highly diffuse, or Lambertian surface, will raise the OPL towards the $4n^2$ limit, where n is the index of refraction of the absorbing material, as shown in Figure 3.7(d). The Lambertian $4n^2$ limit is based on statistical derivations of a Lambertian surface where high scattering properties intensify the internal angular distribution of light and increase photon absorption within the semiconductor [69]. For GaAs, this gives an absorption enhancement of 51, which analogously

describes the OPL enhancement. In the PV light trapping community, demonstrating a $4n^2$ increase in the OPL remains the threshold for diffuse light trapping structures.

Developing a highly diffuse texture to enhance the OPL depends on the geometry and escape cone angle at the front surface of the solar cell. In the case of a textured BSR and a planar front surface, the angle of reflected light from the rear must be large enough to ensure TIR at the front surface by avoiding light loss through the escape cone. According to Snell's law, under the condition of TIR and depending on the materials index of refraction,

$$sin(\theta_c) = \frac{1}{2}, \tag{3.9}$$

where θ_c is the critical angle. For GaAs, this angle is 16°. As long as the reflected light is outside the escape cone, the light will experience TIR and continue to propagate in the GaAs region. In order to guarantee photon scattering, the backside texture must have an angle greater than half of 16° (the escape cone angle). This angular reflection is especially important for incident photons within the first couple of interactions with the surface to ensure light propagation and enhance TIR [69]. The backside texture must then have a departing angle that follows the equation below,

$$\theta > \frac{1}{2} arcsin(\frac{1}{n}). \tag{3.10}$$

The departing angle must be $> 8°$ for GaAs, which agrees with the calculated escape cone angle in GaAs. For ultrathin absorbers less than 0.5 μm thick, the geometry of the light trapping design must be scaled down to the thickness of the absorbing region to achieve optimum distribution for the photon wavelengths of interest. Realistically, the backside metal is not an ideal reflector, meaning it does not reflect 100% of the photons. Commonly used metals

for reflective surfaces, adhesion layers, or ohmic contacts have reflectance properties ranging between 60%-95%. The most common metals used as the backside mirror for GaAs solar cells are Au and Ag due to their high reflectivity [29, 35, 60, 65, 66, 70, 71]. Figure 3.8 displays the reflectance properties of highly reflective and highly absorbing metals. Au and Ag achieve reflectance above 94% at both the GaAs and InGaAs solar cell bandgap, while Cr and Ti absorb a significant amount of incident photons. The peak reflectance at the GaAs band edge for Cr and Ti is less than 65%. Although Cr and Ti may be sufficient adhesion layers, they parasitically absorb incident photons near the band edges of the solar cell and therefore are not used at the backside of the solar cells in this research.

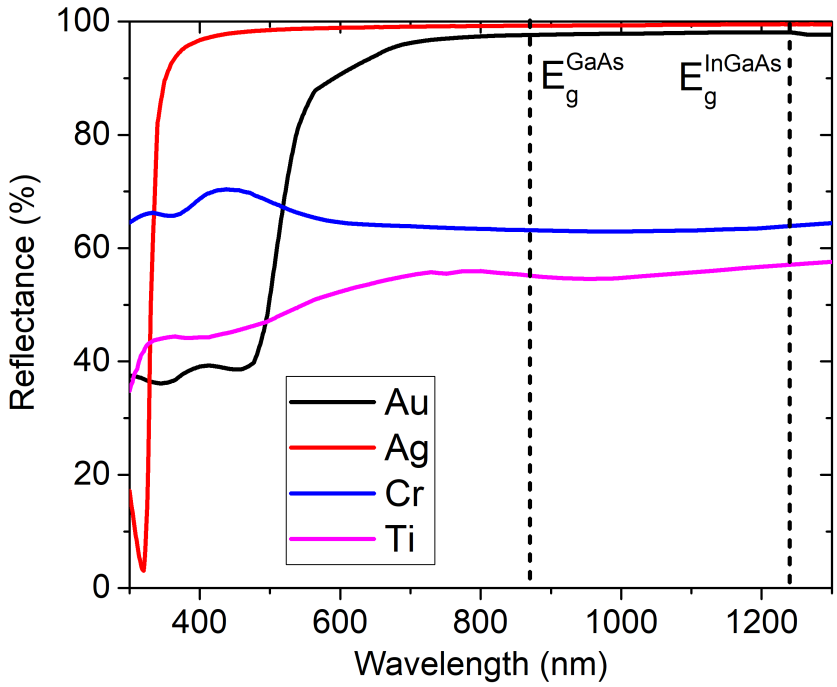

Figure 3.8: Reflectance of commonly used metals as adhesion layers, contacts, and reflective backside mirrors.

Metals like Au or Ag are not 100% reflective and suffer from parasitic absorption loss at the

semiconductor/metal interface due to the excitation of surface plasmons into the metal [72–74]. Utilizing dielectric interlayers between the back mirror-semiconductor interface can increase the amount of TIR and reduce the excitation and propagation of localized surface plasmons into the metal [72, 75, 76]. Figure 3.9(a)-(b) display the different planar back reflector geometries with and without the silicon dioxide (SiO_2) interlayer. Figure 3.9(a) shows the metal-semiconductor interface, which leads to the generation of surface plasmons for a wide range of angles outside the critical angle. Figure 3.9(b) displays the addition of SiO_2 with 500 nm thickness between the semiconductor and the metal where absorption in the metal is suppressed by minimizing the penetration of evanescent fields [72].

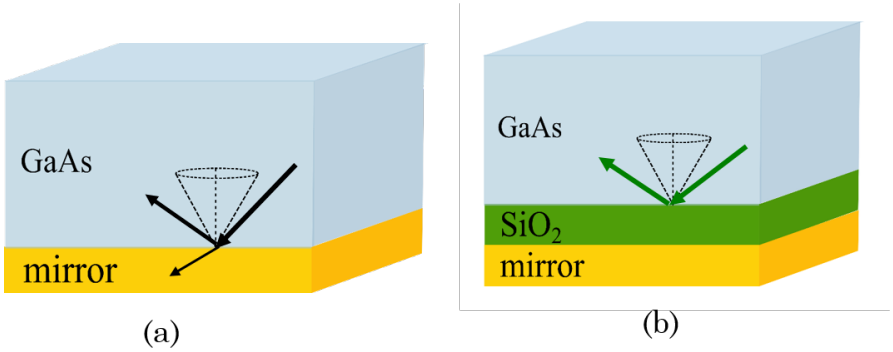

Figure 3.9: Plot (a) displays the metal-semiconductor interface and plot (b) displays the SiO_2 interlayer to suppress absorption of incident photons in the metal.

Figure 3.10 presents the transfer matrix method (TMM) results showcasing the reflective benefits using a low-index TIR layer between a GaAs absorber and the Au mirror. In this figure, the black curve represents the backside reflectance as a function of the incident angle. The colored curves present increasing thickness of SiO_2 between the semiconductor and Au mirror where TIR occurs for angles greater than 60°. The reflectance increases to 100%, indicating an increase in OPL compared to the semiconductor/metal design.

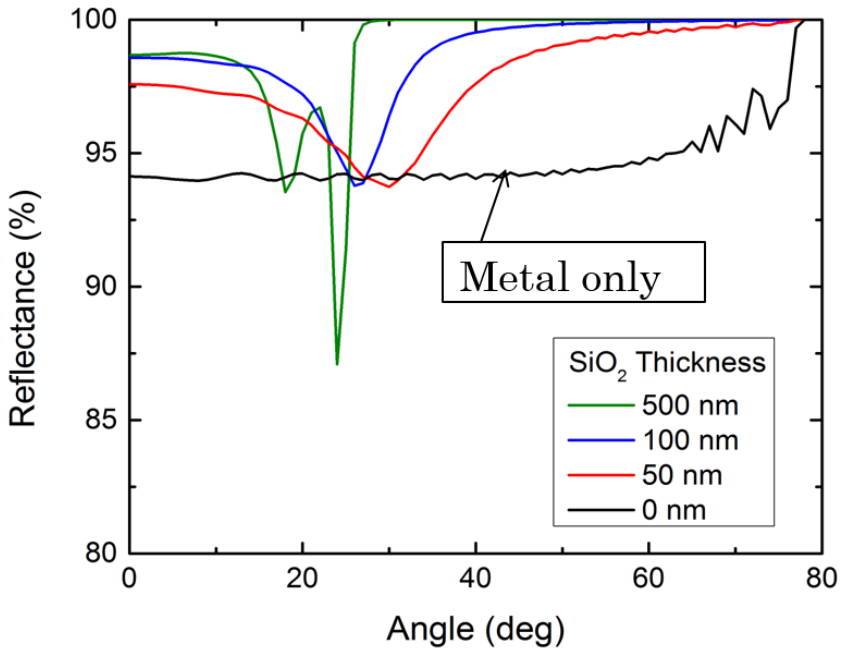

Figure 3.10: Total internal reflection using a low-index interlayer between the Au mirror and the GaAs solar cell.

The texture development throughout this research requires a transparent material to remove band-to-band absorption after photons pass through the thin-film solar cell. The $Al_xGa_{1-x}As$ ternary alloy remains close to lattice-matched with GaAs for the Al values (x) spanning between its binary components, GaAs and AlAs, which allows the electrical and optical properties to change as a function of the Al composition and can be tuned for specific applications [77]. This material is used in several optoelectronic devices due to its tunable nature in material properties, including LEDs, DBRs, and laser diodes [78–81]. For the case of ultrathin, sub-μm thick solar cells, varying the Al composition allows this material to become transparent at the backside of the solar cell so that unabsorbed photons can travel through without being absorbed. Table 3.1 displays the increased bandgap with Al composition.

Relating to the first pass absorption in the GaAs plot (see Figure 3.6), the absorption for the thinned absorbers falls from unity at longer wavelengths, so increasing the Al composition

Table 3.1: Bandgap energies for $Al_xGa_{1-x}As$

Al Composition	Bandgap (eV)	Wavelength (nm)
10%	1.55	800
30%	1.80	689
50%	2.00	620
70%	2.05	605
90%	2.11	588

is necessary to remove parasitic absorption loss. The bandgap of $Al_xGa_{1-x}As$ transitions from a direct to indirect bandgap near x=0.55, so the absorption near its band edge is lower than the case for a direct bandgap (see Figure 3.1). Four main texturing methods are introduced in this research, including solution-based etching, in situ etching, and regrowth techniques. All textures aim to increase the surface roughness and angle of incidence of photons to be greater than 8° to improve TIR. Since the Al composition must increase as the solar cells reduce in thickness, the etching properties and textured morphology change between GaAs and AlAs-based crystal structures. The experimental results on the etching properties across the different texturing methods are presented and discussed throughout Part I of this dissertation.

3.5 Chapter Summary

This chapter motivates the importance of light management in PV technology and describes the fundamental differences between light trapping benefits in Si and GaAs PV. In the GaAs solar cell, there are many benefits of the BSR, including higher radiative efficiencies, which lead to an enhancement of V_{OC} (through photon recycling) as well as J_{SC} (through OPL enhancement). While it is essential to realize the benefits of photon recycling in high-quality GaAs, for space-PV, increasing the photoabsorption in the bottom subcell for current-matching at EoL is the primary goal. With the thinned absorber, transmission loss after the first pass reduces the photogenerated current and efficiency. Integrating a textured BSR will enhance

the photogenerated current through a higher degree of the angular distribution of reflected and scattered light. Improving the backside mirror reflectivity using low-index interlayers will increase the TIR. For textured BSRs, the wide E_g material, known as aluminum gallium arsenide (AlGaAs), removes band-to-band absorption loss for photons that transmit to the back mirror and is used as the textured layer. The AlGaAs layer is textured using methods described in the upcoming chapters and aims to improve the angular photon scattering at the backside of the thin-film solar cells. These concepts are used for the experimental BSR demonstrated throughout this work.

Chapter 4

Design, Growth, and Fabrication

4.1 Introduction

This chapter is dedicated to the growth, design, and fabrication of thin-film III-V solar cells with backside light trapping structures. The main differences between the design and growth of conventional solar cells attached to the host substrate and thin-film solar cells are presented. Thin-film solar cells require an inverted growth sequence compared to solar cells that remain attached to the host substrate. The current state-of-the-art fabrication process is ELO and emerging concepts for substrate removal are discussed. Integrating textured BSRs with the thin-film fabrication process presents new challenges with creating sufficient backside contact for electrical transport. One approach investigates a top-top contact design where the electrical components of the thin-film solar cell are separated from the optical benefits of the BSR. This design has many optical benefits compared to the conventional top-bottom contact approach, where localized ohmic contacts are required for carrier transport to the external electrode. One main drawback is the thickness and high doping concentration required in the lateral conduction layer for the top-top contact design, which inevitably leads to increased material consumption and parasitic photon absorption by free carriers. Finally, the trade-offs between the top-top and top-bottom contact designs are employed in the thin-film solar cells.

4.2 Upright and Inverted Solar Cell Growths

For the III-V solar cell grown by metalorganic vapor phase epitaxy (MOVPE), a host substrate with similar lattice constants to the epitaxial layers is required. The conventional solar cell is grown in an "upright" direction, where the first epitaxial layers grown on the substrate become the backside of the solar cell. The last epitaxial layer becomes the front-most region where incident light enters the solar cell. The solar cells in this research follow a similar layer structure consisting of a front contact layer for carrier collection. Next is the front surface field (FSF), which has a wider bandgap than the active PN junction, so photons transmit while influencing the minority carriers to travel towards the junction. The active absorbing region consists of the emitter and base regions, forming the PN junction. The back surface field (BSF) behaves similarly to the FSF but is situated behind the solar cell base to passivate the backside from interface recombination. The backside contact layer is behind the BSF. Since electrons naturally have a higher carrier diffusion length, the dopant profile suitable for the space environment is the *N-on-P*, so the minority carriers in the thick base region have a greater probability of traveling to the PN junction. Finally, the diagram of the *N-on-P* solar cell structure, which is used for all solar cells investigated in this work, is shown in Figure 4.1. Finally, the layer specifications, including material composition, doping concentration, and layer thickness, are provided in the following chapters for the GaAs solar cells (Chapters 5) and DJ solar cells (Chapter 7).

For the conventional solar cell following the layer structure shown in Figure 4.1, the p-type region is first grown on the substrate. Therefore, the substrate must also be p-type to promote carrier transport through the bulk substrate material. The growth sequence for the upright solar cell is shown in Figure 4.2(a), and the last upright solar cell with front and backside metal contacts are shown in Figure 4.2(b).

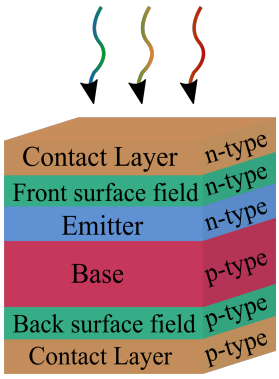

Figure 4.1: Diagram of the *N-on-P* layer structure and doping profile for the solar cells in this research.

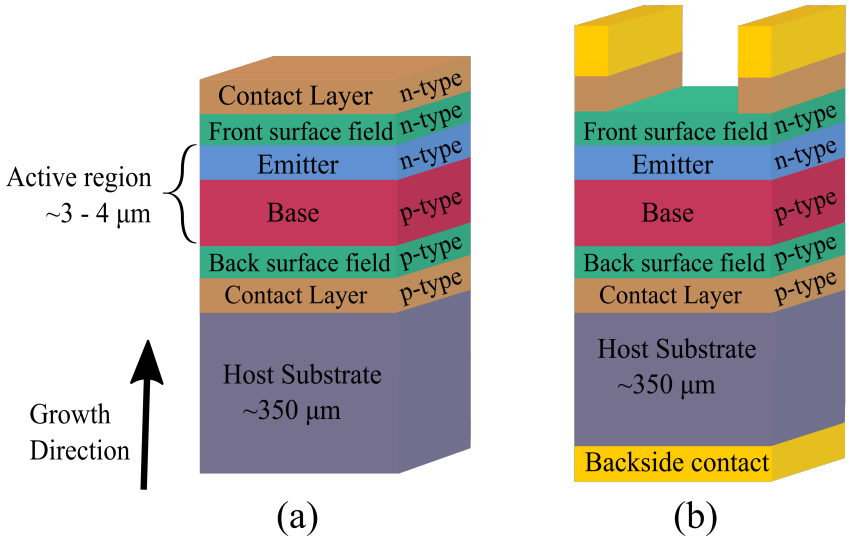

Figure 4.2: (a) upright growth sequence for an optically thick solar cell on a host substrate and (b) completed fabrication of the upright solar cell.

One main difference between a conventional and thin-film solar cell is that the final structure is detached from the substrate. Removing the substrate reduces the weight and overall thickness, making a flexible and lightweight design. The primary method to detach the substrate from the solar cell structure is ELO. This process requires bonding, in which the thin-film layers are attached to a secondary carrier handle. If the *N-on-P* design is the goal and the layer structure were grown in the same manner as the conventional solar cell, the final device would be flipped, making the p-type region the top-most part of the device where incident light enters. Therefore, thin-film solar cells require an "inverted" growth sequence where the first epitaxial layers are grown close to the host substrate and become the top-most layers in the completed device. For the *N-on-P* design, the last epitaxial layers grown are p-type. The growth sequence and ELO process are displayed in Figure 4.3(a)-(c) where (a) displays the "inverted" growth on the host substrate, (b) displays the ELO process where the solar cell is flipped over and bonded to a support handle, and (c) displays the completed thin-film solar cell with the substrate removed and contacts intact. The fabrication process for inverted solar cells is described in further detail in the following section.

4.3 Fabrication of Thin-Film Solar Cells

4.3.1 Epitaxial Lift-Off and Substrate Removal

The support handle is necessary for the inverted growth and thin-film design during the substrate removal process. The thin epitaxial layers are not robust enough to survive the remainder of III-V processing, fabrication, and device characterization without device tearing. The support handle can be temporary or permanent, depending on the bonding materials used. Flexible handles can also be used, provided they remain inert to any wet-chemical etching

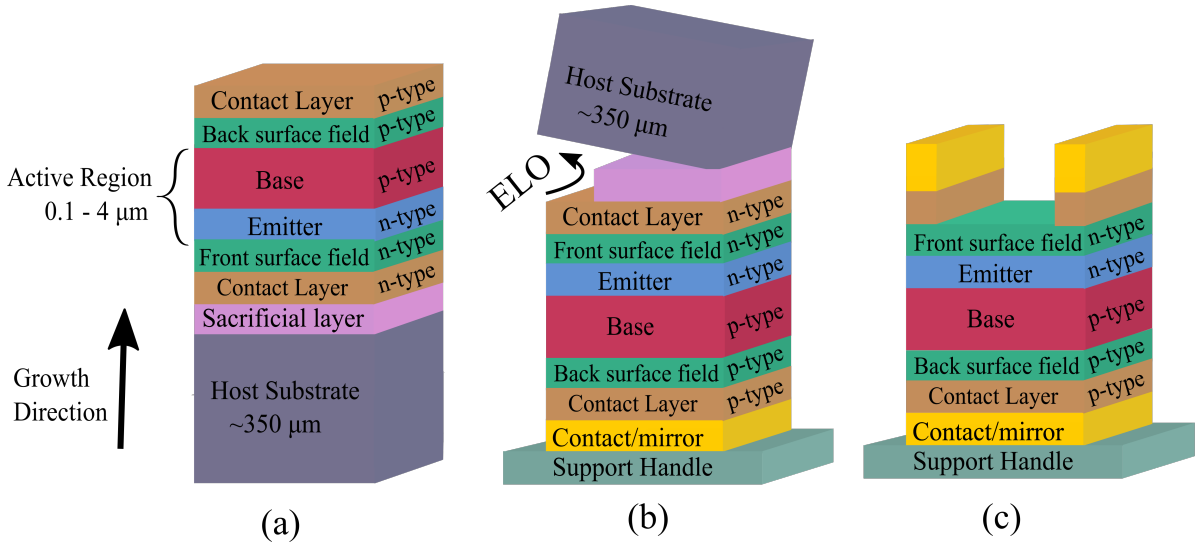

Figure 4.3: (a) inverted growth sequence for the thin-film solar cell, (b) ELO removing the sacrificial layer and bonding the solar cell to a support handle, and (c) the final thin-film solar cell with front and backside contacts.

associated with the solar cell processing. Figure 4.3(b) shows the sacrificial layer between the GaAs substrate and the solar cell layers. This layer is crucial in the transfer process. Detaching a thin-film III-V solar cell from the host substrate was first presented in 1978 and referred to as the Peeled Film Technology, originally developed as a cost-effective approach to reducing the overall cost associated with III-V solar cells [35, 82]. This transfer method incorporated the idea of employing a sacrificial layer as the first layer grown in the device layer stack that would selectively etch away from the active solar cell region, safely separating the solar cell from the host substrate. As described above, this post-growth separation technique is currently known as ELO and is widely used throughout industry, and research development [35, 80, 83]. The ELO flow process used by MicroLink Devices to invert the IMM triple-junction design is used for the thin-film IMM solar cells discussed in Chapter 8.

The flow begins with a release layer grown on the host substrate, and for the GaAs solar cell, MicroLink Devices uses aluminum arsenide (AlAs) as the sacrificial layer due to its selectively etch in hydrofluoric (HF) acid. Once the solar cell structure is grown, the backside metal is

deposited, and the structure is bonded to a carrier handle for support. The AlAs sacrificial layer is removed in HF, separating the epitaxial layers from the host substrate. The host substrate is then re-polished for subsequent growths. Other research that uses the ELO process may vary regarding the sacrificial layer material and etch processes, but the flow sequence remains consistent [35, 80]. Using chemo-mechanical polishing of the GaAs substrate post-ELO to remove the surface contamination enables the same substrate to be used 15-20 times [84]. However, ELO has a drawback, where the multiple steps required to re-polish the GaAs substrate before performing another solar cell growth [84]. Recently, a promising sacrificial layer using the water-dissolvable NaCl that is only 0.2% lattice-mismatched to GaAs presents the opportunity to reduce material costs and develop high-quality GaAs solar cells while removing the need for etching in acids as well as the extra steps to re-polish the GaAs substrate before reuse [85]. Another drawback is the hours-long etch of the sacrificial AlAs layer, which not only adds processing time but expands the time operators work with HF, which is a lethal and highly corrosive acid [80]. Other modern techniques that reduce either ELO duration or cost include surface tension-assisted ELO (STA-ELO) and spalling. These techniques provide alternative approaches that do not depend on long etch times and offer a high throughput lift-off technique. STA-ELO works fast by maximizing the lateral etch rate along the <100> direction in the sacrificial layer and spalling relies on fracture mechanics and a stabilized cleavage plane within a tensile-stressed sacrificial film [80, 86]. Lastly, substrate removal may be considered the most straightforward transfer technique since it only relies on a vertical wet chemical etch through the GaAs substrate until the etch stop layer is exposed, consisting of a material that will not etch away the same chemistry as the substrate. The issue with substrate removal is that it completely dissociates the substrate and results in high material waste. The ELO process remains the primary transfer process for III-V-based solar cells throughout the industry,

and emerging transfer methods aim to lower the processing cost associated with substrate re-polishing and working with corrosive acids.

4.3.2 Backside Contact and BSR Development

Provided that there are many transfer methods, they all require that the active solar cell region follows the inverted epitaxial growth sequence. Over the past few decades, when light trapping in III-V solar cells emerged, the inverted growth process allowed backside texturing to be possible before the transfer process. As backside light trapping structures evolved in III-V solar cells, adding the low-index dielectric interlayer became crucial to improve the TIR and reduce parasitic absorption in the metal reflector. Compared to the conventional upright-grown solar cell, where the highly doped substrate serves as the pathway for charge carriers to travel to the backside metal, the dielectric interlayer at the backside of the thin-film solar cell presents an issue creating ohmic backside contacts. A common approach for sufficient contact at the semiconductor/dielectric interface is to use holes, or vias, throughout the dielectric layer to provide an ohmic pathway to the metal for carriers to travel [29,30,35,58,87,88]. However, vias cumulatively result in an optical percent loss provided by the BSR, and it has previously been reported that vias have as high as 5% coverage [29]. The accumulation of vias degrades the mirror and light trapping properties from the textured BSR, reducing both the photoabsorption by an impaired path length enhancement as well as the V_{OC} due to a decreased probability in photon recycling [68,89]. Therefore, to investigate the optical properties of the textured BSR, a top-top contact design was developed in this research to avoid the use of vias throughout the dielectric interlayer where the full optical benefits of the BSR can be employed.

Apart from the conventional top-bottom contact design, a top-top contact design uses a highly doped and thick back layer for sufficient lateral carrier movement and collection situated

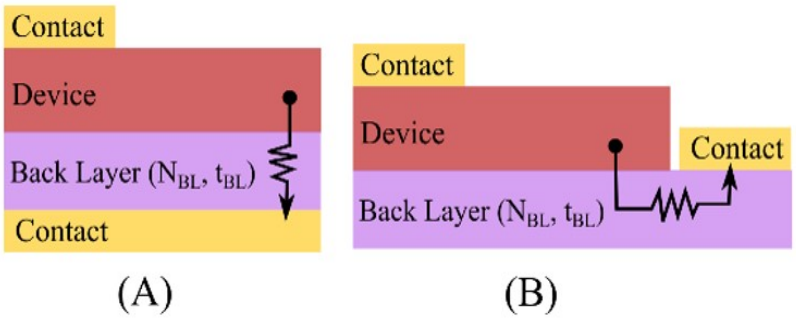

Figure 4.4: Backside contact for (a) a conventional top-bottom vertical back contact design and (b) a top-top lateral back contact design.

at the side of the solar cell. The difference between the two backside contacts is shown in Figure 4.4(a)-(b), where plot (a) shows the vertical carrier flow in the top-bottom design and plot (b) shows a top-top contact where the backside metal is at the side, avoiding the use of vias throughout the backside light trapping structure. The top-bottom design is used for conventional solar cells or thin-film solar cells where dielectric interlayers are not used. The main benefit of the top-top contact design is the removal of localized ohmic contacts in the dielectric layer. However, there are issues with using a top-top contact design since the lateral carrier movement highly depends on the doping concentration and thickness of this layer, which must be scaled for larger-area devices without suffering from carrier collection.

The top-top contact design incorporates the textured-transparent-conductive (TTC) layer, a multipurpose layer situated at the backside of the device, and separates the circuit from the textured semiconductor, a low-index interlayer, and a reflective mirror. This separation provides optical access to the light trapping structure and preserves ohmic backside contact. Figure 4.5(a) displays a top-top contact design with experimental doping and thickness parameters used as one of the thin-film GaAs solar cells, as discussed in Chapter 5. The SiO_2 and insulating encapsulant are separated from the active region of the solar cell. The backside contact resides on the top of the TTC layer away from the solar cell's perimeter to avoid shunting. Figure

4.5(b) is a schematic top-down view of the solar cell (green) area and the exposed TTC layer (red), which serves as the separating region between the backside metal and the perimeter of the solar cell. This top-down view shows the spacing between back grid fingers, S, the length of the solar cell, X_1, and the length of the exposed TTC layer, X_2.

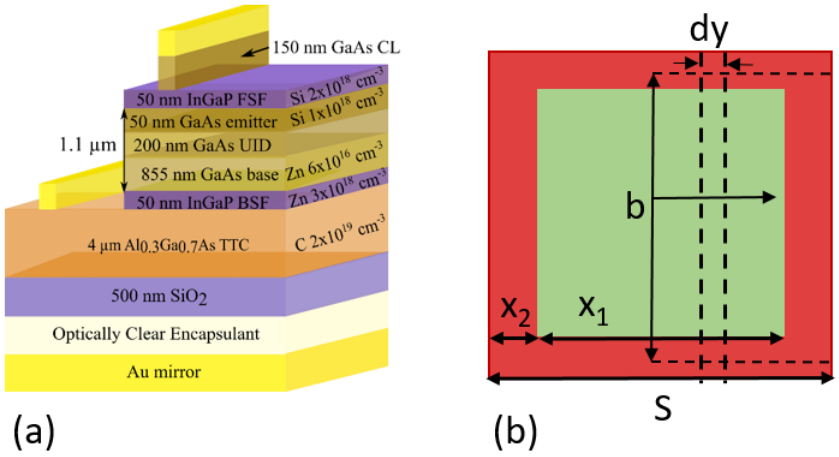

Figure 4.5: (a) Diagram of the thin GaAs solar cell with the top-top contact design and planar BSR. For the maskless BSR (further described in Chapter 5), the texture resides at the TTC/SiO_2 interface. (b) top-down view of the solar cell (green) area and the perimeter of the TTC region (red), which serves as a separation region between the perimeter of the solar cell walls and the backside contact.

The TTC layer is designed as a lateral conduction layer (LCL) where both doping concentration and thickness are optimized for sufficient majority carrier collection resulting in a small fractional power loss at the maximum power point (P_{mpp}), as discussed by Green [90]. The analysis uses the sheet resistivity from the LCL and the spacing between the grid fingers to determine the fractional power loss. The sheet resistivity, ρ_s, is known as,

$$\rho_s = \frac{1}{q\mu N t}, \tag{4.1}$$

which depends on the thickness, t, of the layer along with the mobility of the majority carriers (μ) and the doping concentration (N). The integrated area, dy, contains the region

from the center of the solar cell to the inside perimeter of the deposited metal contact since this would be the maximum distance a carrier would need to travel to the contact. From this, the resistive power loss (I^2dR) from the lateral current flow and ρ_s can be calculated from the gradual power loss within the section *dy*. Since *dR* is the resistive loss within the integrated region, it is equal to $\rho_s dy/b$. Here, *I* is equal to *Jby* where the current density increases linearly from zero at the midpoint of the solar cell to its maximum at the contact. The total power loss is the integral of all losses [90].

$$P_{\text{loss}} = \int_0^{\frac{S}{2}} I^2 dR = \frac{J^2 b^2 y^2 \rho_s}{b}\, dy = \frac{J^2 b S^3 \rho_s}{24}. \tag{4.2}$$

The maximum power point, which is the highest generated power measured within the transport length S/2, can be determined by,

$$P_{mpp} = V_{mpp} J_{mpp} b \frac{S}{2}, \tag{4.3}$$

where the maximum voltage point (V_{mpp}) and the maximum current density point (J_{mpp}) are the highest values that make up the P_{mpp} in the illuminated J-V curve. Now, the fractional power loss from the incremental resistance from carriers traveling to the contact can be determined:

$$p = \frac{P_{\text{loss}}}{P_{\text{mpp}}} = \frac{\rho_s S^2 J_{\text{mpp}}}{12 V_{\text{mpp}}}. \tag{4.4}$$

The values of the V_{mpp} (0.89 V) and the J_{mpp} (22 mA/cm^2) were based on previous experimental values obtained from a GaAs solar cell without an anti-reflection coating. To find the ρ_s, the TTC material in the solar cell design was grown separately and consists of $Al_xGa_{1-x}As$ doped with carbon at a concentration of $2x10^{19}$ cm^{-3}. The Hall effect includes a four-point probe

measurement that injects current diagonally across a 1 cm^2 square sample area, and from a constant and perpendicular applied magnetic field, the voltage measured across the remaining opposite corners of the square sample area is used to determine the ρ_s. The resistivity and the ρ_s were calculated to be 4.35x10^{-3} Ω·cm and 31 Ω/sq, respectively. For the largest active area used in this work of 1 cm^2, this results in a fractional power loss at P_{mpp} of 2.3%. For the smallest area device of 0.06 cm^2, the fractional power loss is 0.14%. Since the thickness of the layer is inversely proportional to ρ_s, a thicker TTC layer will result in a smaller power loss for larger-area devices. This work set the TTC layer thickness limit to 5 μm considering practical epitaxial growth parameters. Appendix A provides detail for the three-level top-top contact design, which is used during the fabrication process outlined below. Pictures of fabricated solar cells using the top-top contact design are shown in Appendix A.

4.3.3 Substrate Removal and Device Fabrication

The solar cells are grown on 2-inch GaAs wafers on the (100) plane with a 2° offcut toward the <110>, using a 3x2" Aixtron close-couple showerhead MOVPE reactor. Both arsine and phosphine are used for the group-V gas sources and trimethyl-gallium and trimethyl-indium group-III precursors. The thin-film solar cells are grown inverted and bonded to the metal-coated support handle with the low-index Dow Corning Sylgard 184 (see Chapter 5, Section 5.2.1). For the textured BSR discussed in the following chapters, the texturing takes place before bonding. Rather than using ELO as described above, substrate removal is used to detach the substrate from the epitaxial structure after bonding to a support handle. This process is similar to the process flow shown in Figure 4.3 but instead of removing the sacrificial layer first. The substrate is removed by wet-chemical etching using 1:2 NH_4OH:H_2O_2 until the sacrificial layer is exposed. The sacrificial layer consists of InGaP, which is selective to the NH_4OH etchant.

The InGaP etch stop is removed using concentrated HCl. The solar cells undergo three rounds of photolithography: top metal contact, area isolation, and backside metal contact onto the $Al_{0.3}Ga_{0.7}As$ TTC layer. After the active area isolation, the TTC layer is exposed and the entire perimeter of the cells is protected by photoresist, and backside metal was electroplated. Both Au top and back contacts were electroplated with approximately 1 μm thicknesses. The active areas across each wafer include 1 cm^2, 0.2 cm^2, and 0.06 cm^2, with grid finger shadowing of 4%, 4.5%, and 10%, respectively. In subsequent chapters, the growth design parameters are presented to clarify the layer structure in each experiment.

4.4 Chapter Summary

This chapter describes the design and growth differences between upright and inverted thin-film solar cells and the fabrication process required for both designs. The trade-offs between BSR optical improvement and carrier collection using top-top contact design is discussed. Using the top-top contact design removes the use of localized ohmic contacts at the backside of the device, which reduces parasitic absorption at the semiconductor/ohmic contact interfaces. However, the required thickness and doping concentration in the TTC layer leads to an enhancement in free-carrier absorption in the backside non-active layer, as investigated in Chapter 6. Potential applications using the top-top contact design include low-light indoor PV applications where using a TTC layer can be optically advantageous, and photon recycling benefits can be exploited to improve the efficiency of mm-scale GaAs devices [91–93]. This design is primarily applicable for small-area PV; however, the textured BSRs discussed in the following chapters are not confined to this design and can be scaled for large-area PV designs, provided that vias are implemented. Overall, trade-offs occur for both top-top and vertical contact designs, and both are explored for various solar cells throughout this research.

Chapter 5

Thin-Film Single-Junction GaAs Solar Cells with Light Management

5.1 Introduction

This chapter involves the development and characterization of thinned GaAs solar cells with textured BSRs produced by a maskless solution-based chemical etch as well as I-MacEtch. The main goal is to render wavelength-specific (WS) light trapping structures for thin GaAs solar cells that provide straightforward and inexpensive processing and is accessible for large-scale manufacturing. For the maskless etching, the formation of the pyramidal-like structures relies on a chilled solution-based etchant of NH_4OH:H_2O_2 that enters a reaction-controlled regime and increases the lateral etch rate along the diagonal crystallographic planes in the face-centered-cubic (FCC) based GaAs crystal structure. The EQE from the 1.1 μm GaAs solar cell with the maskless BSR achieves a photogenerated current 0.7 mA less than the 3.6 μm optically thick GaAs control near the band edge. The 80% haze in reflectance measured on the I-MacEtch BSR indicates high diffused photon scattering, and the EQE from the 0.5 μm GaAs solar cell shows a 38% enhancement in the photogenerated carrier collection from the base of the solar cell when compared to the modeled thin absorber without the BSR. The fundamental properties of

the Fabry-Pérot (FP) cavity have been applied to the thin GaAs solar cells to determine the path length enhancement caused by the textured BSRs. The maskless BSR increased the path length up to 4.3 while the I-MacEtch BSR increased the path length up to 5.7 passes. Since the I-MacEtch BSR was integrated behind a 0.5 μm GaAs solar cell, the light trapping effects are more prominent and result in a greater path length enhancement than the maskless BSR. Both solution-based texturing approaches in this chapter validate their use in thin-film multijunction solar cells.

5.2 Textured BSR Development

5.2.1 Optical Performance of a Planar Reflector

Before introducing texture to the BSR, the optical performance from the planar BSR using a top-top contact design, as discussed in Chapter 4, was evaluated to ensure high reflectance by combining the highly reflective Au mirror and the low-index SiO_2 interlayer. One challenge with the Au/SiO_2 interface is the poor adhesion, mainly due to oxidation at the interface [94]. A seed layer can be used for better adhesion before evaporating the metal mirror. Popular materials consist of chrome and titanium; however, these materials have a reflectance less than 65% and would degrade the back mirror's quality.

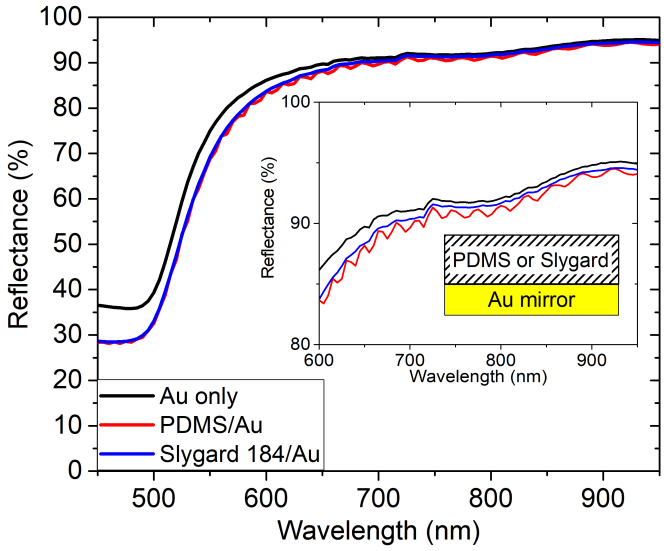

Figure 5.1: Reflectance at normal incidence to test optically clear adhesives.

This work investigates two optically clear and well-known silicone-based adhesives, polydimethylsiloxane (PDMS) and Dow Corning Sylgard 184, as the adhesion layer to connect an Au-coated Si handle and the SiO_2 interlayer. Both adhesives were applied to the Au-coated Si handle, and the reflectance at normal incidence was measured and compared to the Au-coated Si handle alone. As shown in Figure 5.1, the difference in reflectance varies more at high energy photons where the GaAs solar cell will be less absorbing. Additionally, Sylgard 184 is a low-index material that will assist TIR at the backside mirror. In the GaAs absorbing region between 650 nm and 950 nm, the average specular reflectance difference between Au alone and Au with Sylgard 184 is less than 0.5%. Even though the PDMS and Sylgard 184 resulted in high reflectance, the Sylgard 184 was used moving forward as the viscosity was more favorable to work with when bonding the solar cell to the handle.

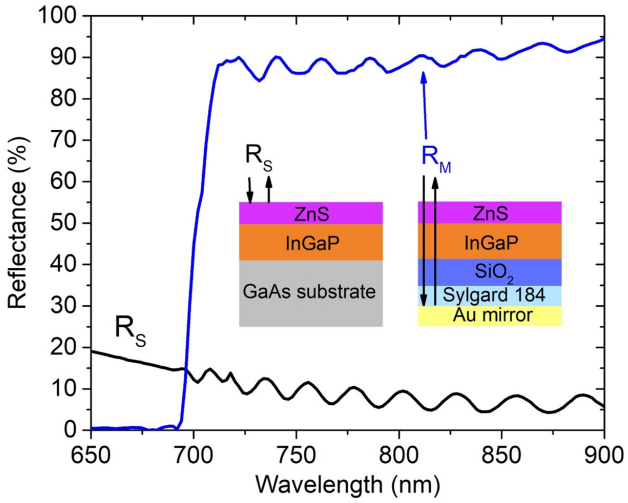

Figure 5.2: Reflectance at normal incidence to measure mirror reflectance for the flat BSR.

The mirror reflectance for the Au mirror with SiO_2 and Sylgard 184 was investigated by following a similar procedure as discussed by Bauhuis et al. [71]. The test structure grown by MOVPE consists of 3 μm of InGaP on GaAs substrates. The SiO_2 was deposited by plasma-enhanced chemical vapor deposition (PECVD), and the structure was bonded to the Au-coated handle using Sylgard 184. The GaAs substrate was removed using substrate removal until the InGaP layer was exposed, and 85 nm of ZnS was evaporated on top to reduce the reflection at the surface. The InGaP layer has a similar index of refraction to GaAs and will remain transparent to the photons near the GaAs band edge. This transparency will allow the photons to travel through a similar index material before coming in contact with the BSR. As explained by Bauhuis et al. [71], the mirror reflectance is calculated from the total reflectance using the equation,

$$R_{\mathrm{m}} = \frac{R_{\mathrm{total}} - R_{\mathrm{S}}}{1 - R_{\mathrm{S}}}. \tag{5.1}$$

The surface reflectance, R_S, was measured from a test structure consisting of ZnS on 3 μm

of InGaP on a GaAs substrate. Figure 5.2 displays the specular mirror reflectance between 85% and 95% for the wavelength range from 700 nm to 950 nm. The Au mirror achieves a peak reflectance of 94% near the GaAs band edge and provides high reflectance for unabsorbed photons in the thin GaAs solar cell. Relating to the reflectance vs. V_{OC} plot in Chapter 3 (see Figure 3.5), will reduce the V_{OC} approximately 15 mV from the case of perfect reflectance for a high material quality GaAs solar cell. While the goal is to achieve backside reflectance as close to unity as possible, Section 5.4 discusses the use of Ag as the back mirror, achieving higher reflectance of 96% for the planar BSR.

5.2.2 Wet-Chemical Maskless Etching

The chilled solution-based maskless etch can produce three-dimensional pyramidal structures in GaAs by exposing and etching the diagonal crystallographic planes in the FCC-based crystal structure. The solution consists of H_2O_2 as the oxidizer and NH_4OH as the dissolution agent. This etch has experimentally been demonstrated in GaAs using 1:4:80 NH_4OH:H_2O_2:H_2O at 5°C [95]. In this work, it is important to use a transparent material with a band gap higher than $E_{g\text{-}GaAs}$ as the TTC layer, so $Al_xGa_{1-x}As$ with a varying Al composition has been employed. The crystallographic etch has successfully been developed in $Al_{0.1}Ga_{0.9}As$ using 1:4:40 NH_4OH:H_2O_2:H_2O at 2.5°C ± 0.5°C for 5 minutes, and provided good uniformity over a 2-inch wafer with 5% specular reflectance and a standard deviation less than 9% at 870 nm wavelength [96]. The top-down SEM image shown in Figure 5.3(a) displays the exposed $Al_xGa_{1-x}As$ diagonal planes. In Figure 5.3(a), one region of the top-down SEM image magnifies the specified diagonal crystal planes. At 2.5°C ± 0.5°C, the vertical etch rate (VER) was measured to be less than 1 nm/second, outperforming the faster lateral etch rate (LER). The high LER at low temperatures confers that the lateral diffusion-oxidation process

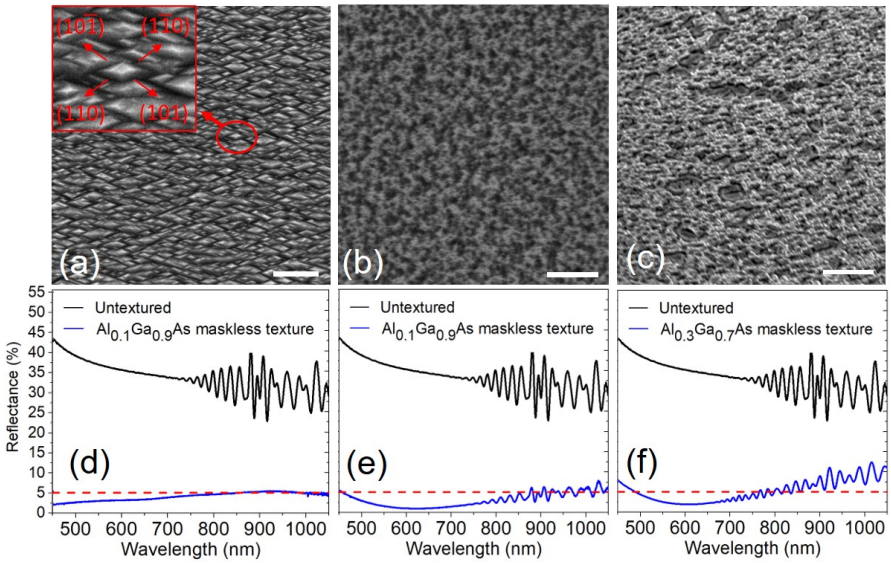

Figure 5.3: Top-down SEM and reflectance at normal incidence on three maskless etch textures produced in (a)(d) low Zn doped $Al_{0.1}Ga_{0.9}As$, (b)(e) highly C-doped $Al_{0.1}Ga_{0.9}As$, and (c)(f) highly C-doped $Al_{0.3}Ga_{0.7}As$. The scale bars represent 10 μm. Below each SEM image are the respective reflectance at normal incidence from air to the textured semiconductor.

is energetically favorable along the diagonal GaAs planes. The resulting specular reflectance for this texture displayed in Figure 5.3(d) is lower than 5% in the GaAs absorbing region from 550 nm to 950 nm in wavelength. The untextured $Al_{0.1}Ga_{0.9}As$ shown by the black curve in Figure 5.3(d),(e), and (f) are presented to show the reduction in reflectance from all of the textured surfaces.

Next, the $Al_{0.1}Ga_{0.9}As$ is doped with carbon (C) to ensure sufficient carrier transport, as discussed in Chapter 4. The top-down SEM in Figure 5.3(b) shows that under the same etching conditions described above, the surface morphology did not replicate the pyramidal structures. Since the chilled etch is sensitive to changes in the crystal structure, the carbon incorporation during epitaxial growth obstructs the diagonal etch at low temperatures. During the $Al_xGa_{1-x}As$ growth, the C atoms replace the Ga sites, and the Al-C bond is energetically higher than the C-Ga bond [97]. The crystallographic etch depends on the Ga-As bond along the (110) planes and is susceptible to change once the strong Al-C bonds form at the Ga

sites. Although introducing carbon to the crystal lattice did not result in the etching along diagonal crystal planes, the surface roughness contributed to specular reflectance below 5% for the carbon-doped $Al_{0.1}Ga_{0.9}As$ in Figure 5.3(e).

The maskless etch was then tested in carbon-doped $Al_{0.3}Ga_{0.7}As$, which serves as the TTC layer for the 1.1 μm GaAs solar cells studied in this work. The surface remained specular with the same etch conditions mentioned above, proving that increasing the Al composition affects the etch rates along the various crystal planes. In GaAs, the addition of NH_4OH to H_2O_2 expedites the reaction rate as it creates a higher amount of soluble compounds with oxidized Ga and As elements [98]. Increasing the Al during epitaxial growth allowed stronger Al-C bonds to form while replacing the Ga sites, so the low NH_4OH concentration in the 1:4:40 ratio limited oxidative species on the surface, and the dissolution rate reduced at low temperatures. A new ratio consisting of 2:1:40 concentration was attempted for the carbon-doped $Al_{0.3}Ga_{0.7}As$. Figure 5.3(c) shows successful roughening of the surface under these etch conditions. Although the surface morphology did not expose crystallographic planes, the etch pattern is similar to the carbon-doped $Al_{0.1}Ga_{0.9}As$, and the specular reflectance, as shown in Figure 5.3(f), was lower than 8% near the GaAs band edge at 870 nm in wavelength. These maskless textures are scalable to larger areas, provided that there is no fluctuation in the etchant temperature.

The entire BSR component in this top-top contact design consists of the $Al_{0.3}Ga_{0.7}As$ layer (with or without texturing), a low-index material, an adhesion layer, and the Au-coated support handle. To achieve high reflectivity at the mirror's surface, the incident medium that the light travels through should have a low-index to avoid the propagation and excitation of plasmonic modes in the metal while being thick enough to suppress frustrated TIR within the low-index material [22, 75]. Previous studies show that 0.5 μm of SiO_2 at the $Al_{0.3}Ga_{0.7}As$/Au interface lessens surface plasmon generation while enhancing the TIR of incident photons past the critical

angle in GaAs [22, 54] and is used as the thickness of the low-index layer in this work. Since poor adhesion occurs due to oxidation at the Au/SiO_2 interface [94], the optically transparent Dow Corning silicone-based encapsulant, Sylgard 184, is used as dual-purpose adhesion and low-index layer at the Au/SiO_2 interface.

Before integrating the BSR into the GaAs device, the reflectance properties of the entire BSR are investigated. To imitate the interaction between the incident photons at the BSR for the reflectance measurements, test structures using the high E_g material, InGaP, which remains transparent to photons near the GaAs band edge, were created. This material also has a comparable index of refraction to GaAs; thus, the photons are expected to travel similarly within the GaAs solar cell. The test structures grown by MOVPE consist of 2 μm $Al_{0.3}Ga_{0.7}As$ on 0.5 μm InGaP on GaAs substrates. For the maskless BSR structure, the maskless etch was performed on the $Al_{0.3}Ga_{0.7}As$ surface. Then, 0.5 μm of SiO_2 was deposited by PECVD on the maskless etched and flat test structures, and the structures were separately bonded to the Au-coated handle using the Sylgard encapsulant. For each structure, the GaAs substrate was removed using 1:2 NH_4OH:H_2O_2 until the InGaP layer was exposed, and 85 nm of ZnS was evaporated to reduce surface reflection. To confirm high reflectance with the Sylgard, another flat BSR structure that does not have the low-index materials was created by evaporating Au at the $Al_{0.3}Ga_{0.7}As$ surface before the sample was bonded to a support handle for substrate removal. The three sample structures are referred to as the (1) Au BSR (no low-index materials), (2) flat BSR, and (3) maskless BSR, and the diagram in Figure 5.4(a) shows the layer structure for the flat BSR.

The total and diffuse reflectance were measured for these three samples using a Shimadzu Spectrophotometer UV-Vis attached to an integrating sphere. The goal is to observe high total reflectance from the flat BSR with the low-index materials and high diffuse scattering properties

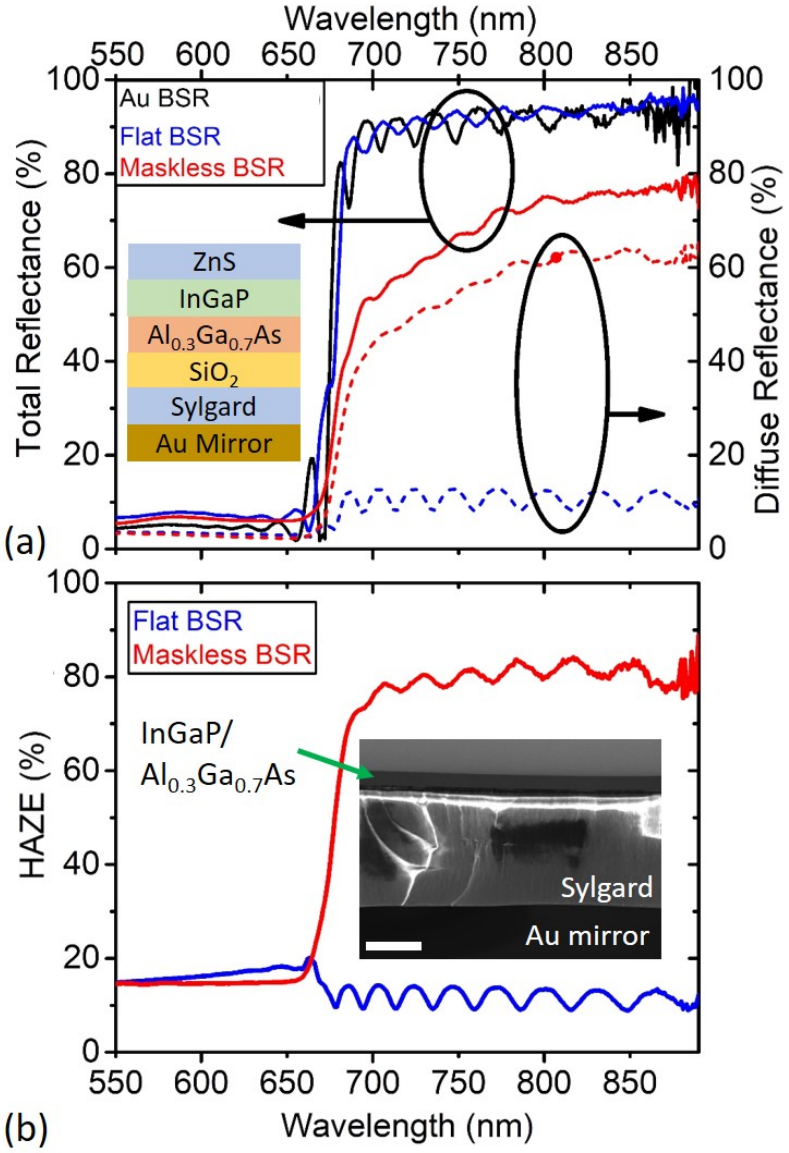

Figure 5.4: (a) Total and diffuse reflectance for the BSR structures. The Au BSR does not have low-index materials. The inset diagram (not representative of the layer thicknesses) displays the layer order. Plot (b) shows the haze in reflectance for the flat and maskless BSR structures. The inset cross-sectional SEM image (white scale bar is 10 μm) was taken from the flat BSR structure to display the non-planar characteristic within the Sylgard region.

once the maskless textured $Al_{0.3}Ga_{0.7}As$ is introduced. Figure 5.4(a) displays the total (left y-axis) and diffuse (right y-axis) reflectance for the three structures. The total reflectance of the flat BSR has a peak reflectance at 94% near the GaAs band edge, which is slightly higher than the Au BSR, which has a peak reflectance of 93%. The distinct diffuse scattering from the maskless BSR is near 60% at the GaAs band edge. For an ideal planar reflector, the diffuse properties should be near zero; however, this is not observed with the low-index materials. The cross-sectional SEM in Figure 5.4(b) was taken after the reflectance measurements on the flat BSR structure. From this image, the non-planar behavior within the Sylgard layer is apparent, likely leading to the increased diffuse reflectance.

The haze in reflectance, defined as the ratio of the diffuse and the total reflectance, reveals the degree of angular scattering from a roughened surface and is often used within light trapping research [53, 99, 100]. For a near-Lambertian surface, the diffuse light will be much higher than the specular light, resulting in a higher haze in reflectance. Figure 5.4(b) shows the haze in reflectance for the BSR structures, which oscillates between 10-15% for the flat BSR, mainly due to the non-planar behavior of the Sylgard layer. The maskless BSR sample shows the highest haze near 80% at the GaAs band edge, more than 6-times greater than the flat BSR structure, which exceeds the scattering capabilities of the flat BSR.

5.2.3 Inverse Progression Metal-Assisted Chemical Etching

Metal-assisted chemical etching (MacEtch) is a low-cost and straightforward texturing process that offers isotropic features and does not require low-pressure vacuum systems or hazardous gases associated with dry etching [101, 102]. Forward progression MacEtch was first discovered in Si, where hole injection from a noble metal takes place at the metal-semiconductor interface. The semiconductor beneath the catalyst etches at a faster vertical rate than the

semiconductor unexposed to the metal catalyst [101, 103, 104]. In return, the metal isotropically sinks into the semiconductor and produces the same metal catalyst dimensions. Recently, inverse-progression metal-assisted chemical etching (I-MacEtch) was successfully demonstrated in $Al_xGa_{1-x}As$ with Al composition ranging between $0.55 < x < 0.7$, where hole injection from the metal into the semiconductor increases the oxidation-dissolution etch around the metal catalyst as the oxidized material underneath the metal is not immediately dissolved [77]. The injected holes can diffuse around to the off-metal regions, which subsequently are etched away first [77]. The model presented by Wilhelm et al. presents the I-MacEtch behavior using Au catalysts in unintentionally doped (UID) $Al_xGa_{1-x}As$ with Al composition ranging from $0.55 < x < 0.7$ [77]. In this theory, the I-MacEtch mechanism requires that the semiconductor's ionization potential have higher energy than the redox potential of the metal such that it is closer to the vacuum level, and hole injection can occur [77]. The hole injection from the Au catalyst into the semiconductor increases the number of oxidative species where dissolution around the metal catalysts occurs rather than below the metal-semiconductor interface. From this, Wilhelm determined that the Al composition alters the reduction-oxidation potential and changes the LER and VER of the Au-patterned nanopillars arrays for temperatures ranging from 55°C to 75°C [77]. Additionally, the increase in etchant temperature increases the catalytic oxidation since the number of thermally activated holes increases as the H_2O_2 decomposition enhances hole diffusion [77].

For sub-μm GaAs solar cells, creating back textures on the same scale as the absorber thickness is essential to scatter the photons of interest to reflect into the solar cell. Patterned I-MacEtch allows specific dimensions to be developed according to the Au catalyst dimensions. I-MacEtch in high Al composition $Al_xGa_{1-x}As$ ($x > 0.55$) serves as an alternative approach for texturing at the backside of thinned solar cells. As well, I-MacEtch in carbon-doped

$Al_{0.7}Ga_{0.3}As$ provides a transparent textured material in terms of band-to-band absorption, which is required to reduce parasitic absorption loss at the backside of the sub-μm GaAs solar cell.

To prepare for the I-MacEtch, the Au catalyst was patterned with a 1.5 μm diameter and 1.5 μm pitch array across the surface of the wafer. The pattern was created using a laser direct-write in a positive photoresist. After the pattern was developed, the circular pattern was cleaned with HCl to provide an oxide-free surface before the Au was deposited. The Au was electroplated at a current density of 1 mA/cm^2 for 10 seconds with an anticipated thickness between 60-100 nm. The cartoon diagram in Figure 5.5(a) displays the dimensions of the direct write mask for the circular Au-patterned array, and Figure 5.5(b) is a nomarski image of the Au-patterned semiconductor. The approximate Au thickness was less than 50 nm according to a previous deposition rate of 2.5 nm/sec in Au. The I-MacEtch solution consists of (1:1) citric acid and DI, which was heated to 50 °C and mixed for 30 minutes to ensure complete dissolution. The oxidizing agent, H_2O_2, was added to the solution using a (5:1) ratio. The etch solution remained at 50 °C, and the patterned surface was submerged face up.

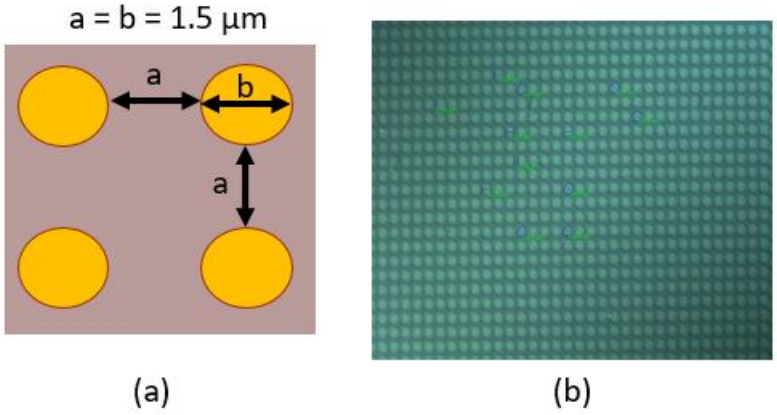

Figure 5.5: Plot (a) cartoon diagram of the Au circle patterned on $Al_{0.7}Ga_{0.3}As$ with 1.5 μm diameter and 1.5 μm pitch, and plot (b) of the nomarski image for the Au-electroplated array.

The etch duration was one hour, and the tilted SEM at 35° of the surface texture can be seen in Figure 5.6. From the SEM image, the spherical structures did not appear like the nanopillar arrays reported by Wilhelm [77]. The LER and VER for the p-type $Al_{0.7}Ga_{0.3}As$ changed, even under similar etchant conditions described by Wilhelm, suggesting that the introduction of acceptors into the semiconductor changes the energy potential differences and hole injection in the semiconductor-metal system and alters the I-MacEtch process. The nanopillar arrays reported by Wilhelm show a planar top surface directly at the Au/$Al_{0.7}Ga_{0.3}As$ interface [77], whereas the carbon-doped $Al_{0.7}Ga_{0.3}As$ in Figure 5.6 resulted in rounded tops. For the carbon-doped $Al_{0.7}Ga_{0.3}As$, the increased LER produces spherical dome-like structures, mainly due to a fast lateral etch close to the Au before the underlying semiconductor is exposed.

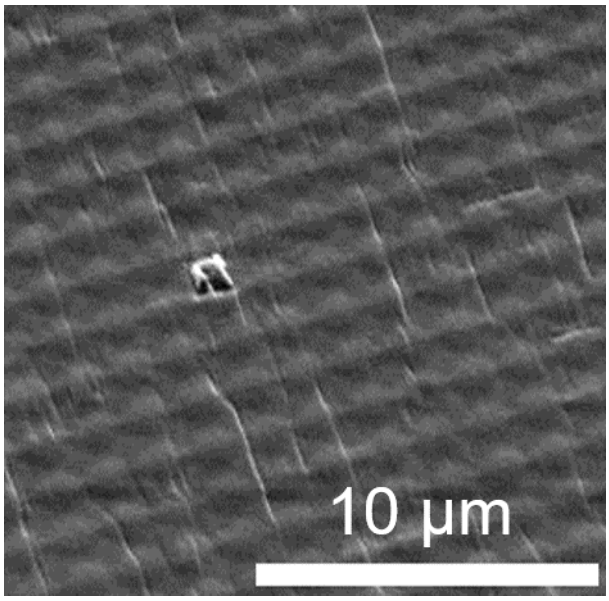

Figure 5.6: Tilted 35° SEM of the MacEtch textured surface on Al0.7Ga0.3As. The scale bar represents 10 μm and the image was scanned at 10 kV and 5 kx magnitude.

As the contact area between the metal and semiconductor reduces, the catalytic reaction slows and limits the amount of hole injection into the semiconductor. This limitation may also be the cause of the reduced VER since the spheres are no more than 200 nm high, as seen in

the atomic force microscopy (AFM) image shown in Figure 5.7. The high root mean square (RMS) roughness equal to 79 nm relates to increased diffuse scattering properties.

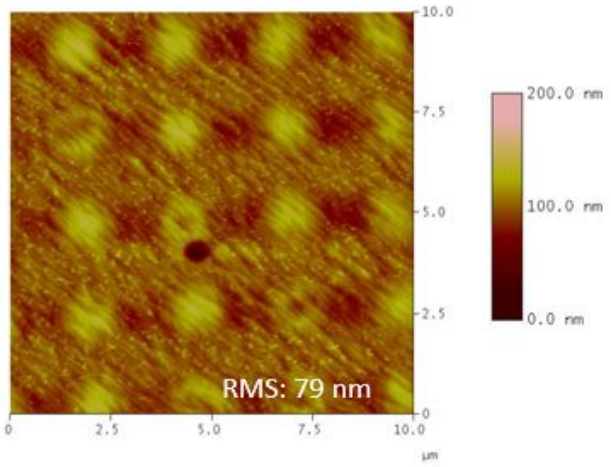

Figure 5.7: AFM on the I-MacEtch texture.

Since the valence band edge (VBE) of $Al_{0.7}Ga_{0.3}As$ is similar to AlAs, the catalytic oxidation for the $Au/Al_{0.7}Ga_{0.3}As$ will result in lower etch rates, consistent with the slow VER calculated to be around 5.8 nm/min. This VER is nearly half of what was expected for the $Al_{0.7}Ga_{0.3}As$ I-MacEtch process under 50 °C for the citric-H_2O_2 etch conditions. According to the LER of nearly 20 nm/min at 50 °C for the UID $Al_{0.7}Ga_{0.3}As$ [77], it would take 75 minutes for the 1.5 μm diameter Au catalyst to detach from the semiconductor for the carbon-doped $Al_{0.7}Ga_{0.3}As$.

Although the carbon doping appears to be the main difference leading to the different surface texture morphology, the spherical structures present a promising texture since the heights are the same order as the thickness of the GaAs solar cell absorbing region. The WS dimensions allow the unabsorbed photons to scatter as desired rather than pass through the textured semiconductor. The reflectance measurements on the I-MacEtch BSR using similar optical test structures as the maskless BSR structures (see Chapter 5) are performed. The flat reflector utilized Ag as the back mirror, which is more reflective than the Au mirror previously used.

The total reflectance is near 96% for the Ag BSR, close to the ideal planar reflector. Figure 5.8 displays the measured haze in reflectance for the flat and I-MacEtch BSR, which significantly increases for the I-MacEtch BSR due to the enhanced diffused reflectance. The flat Ag BSR is expected to have no haze in reflectance; however, the fringing between 5% and 10% appears caused by inherent roughness at the Ag mirror. This will increase the effective OPL from 2 times enhancement as the diffused mirror properties are heightened.

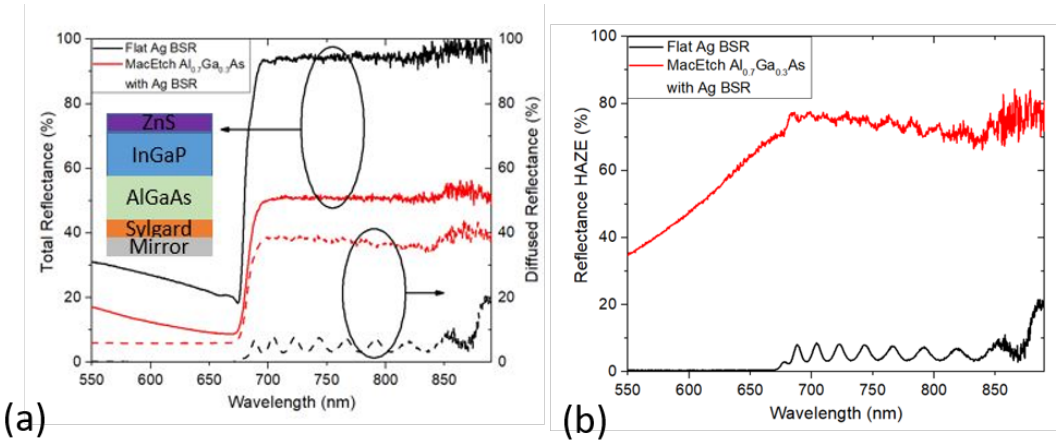

Figure 5.8: (a) The measured total and diffused reflectance from the flat Ag BSR and the MacEtch BSR. The textured MacEtch region resides at the AlGaAs/Sylgard interface, (b) haze in reflectance measured from the flat Ag BSR and the MacEtch BSR test structures.

5.3 GaAs Solar Cells with a Maskless BSR

5.3.1 Device Growth and Fabrication

As described in Chapter 4, the method of detaching the host substrate in this research includes substrate removal by wet-chemical etching. The 1.1 μm-thick GaAs solar cells follow the growth sequence shown in Table 5.1 where the growth sequence starts at the GaAs substrate. The substrate is UID since it is removed after the bonding process. Above the InGaP etch stop

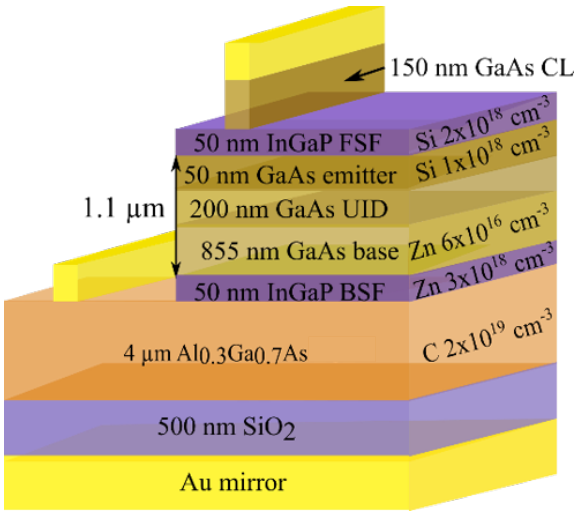

Figure 5.9: Diagram of the thin GaAs solar cell with a top-top contact design and flat BSR. For the maskless BSR, the texture resides at the TTC/SiO_2 interface.

Table 5.1: Growth design for 1.1 μm-thick GaAs solar cells.

Layer	Material	Thickness (nm)	Doping (cm^{-3})
TTC	p-$Al_{0.3}Ga_{0.7}As$	4000	$2x10^{19}$ (C)
Window	p-InGaP	50	$3x10^{18}$ (Zn)
Base	p-GaAs	855	$6x10^{16}$ (Zn)
Intrinsic	GaAs	200	UID
Emitter	n-GaAs	50	$1x10^{18}$ (Si)
Window	n-InGaP	50	$2x10^{18}$ (Si)
Contact	n-GaAs	100	$3x10^{18}$ (Si)
Contact	n-GaAs	50	$2x10^{19}$ (Te)
Barrier	n-GaAs	10	$3x10^{18}$ (Si)
Etch Stop	n-InGaP	150	$3x10^{18}$ (Si)
Substrate	GaAs	350 μm	UID

is a GaAs:Si barrier to reduce the dopant diffusion from the GaAs:Te contact layer. These devices have a base thickness of 855 nm, intrinsic region of 200 nm, and an emitter equal to 50 nm. In total, the active region is 1.1 μm. The last layer grown is the TTC layer, which is 4000 nm thick for texture development and sufficient carrier transport using the top-top contact design.

The TTC layer, shown in Figure 5.9, consists of 1.8 eV $Al_{0.3}Ga_{0.7}As$ to remain transparent for the unabsorbed low-energy photons passing through the GaAs solar cell. The carbon-doped

$Al_{0.3}Ga_{0.7}As$ was grown by MOVPE on a GaAs substrate. From the Hall effect, the resistivity of the calibration sample was measured to be 4.35x10^{-3} Ω·cm at a doping concentration of 4.17x10^{19} cm^{-3}. Specifically, for the 4 μm thick TTC layer, this translates to a fractional power loss at P_{mpp} of 2.3% and 0.14% for the 1 cm^2 and 0.06 cm^2 area devices, respectively [90]. The three solar cells include the 2.25 μm GaAs control grown upright on the GaAs substrate and the 1.1 μm GaAs thin cells with the flat and maskless BSR. The GaAs control has the same epitaxial layer structure with a thicker base region. These solar cells were fabricated using the top-top contact mask and three-level photolithography process, as discussed in Chapter 4. The final version of the thin-film solar cell with the flat BSR is displayed in Figure 5.9, and for the maskless BSR, the texture resides between the TTC layer and the SiO_2.

5.3.2 Electrical Device Results and Discussion

This section refers to the thin 1.1 μm solar cells as the "flat BSR device" and the "maskless BSR device." The 2.25 μm GaAs control on the substrate is referred to as the "GaAs control." The illuminated J-V measurements were conducted using a TS Space Systems dual-source 18 kW solar simulator filtered for the AM0 spectrum. Following the calibration process discussed in detail by Polly [105], the ultraviolet-visible part of the spectrum, created from a mercury halide arc bulb, was calibrated using a standard SJ InGaP solar cell. The infrared region, created from the quartz tungsten halogen bulb, was calibrated using a standard SJ GaAs solar cell. A silicon monitor cell varied ± 0.03 $mA{\cdot}cm^{-2}$ across the measurements taken, showing temporal stability in the lamps. The calibrations and measurements were performed at 25°C.

Table 5.2 displays the illuminated J-V figures of merit for the best-performing cells and the standard deviation across the measured cells from each device. Even though the absorbing thickness of the maskless BSR device is half of the GaAs control, the short-circuit current

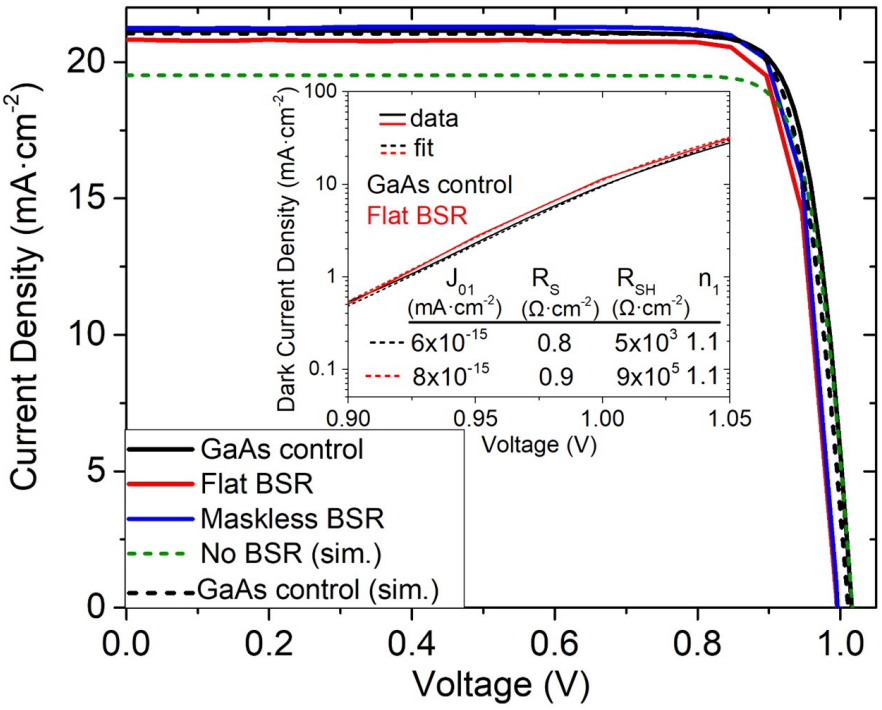

Figure 5.10: Illuminated AM0 J-V measurements of the flat and maskless BSR devices compared to the GaAs control. The two dashed curves represent the modeled GaAs control (black) and the thin GaAs device without a BSR (green). The inset diagram is dark J-V measurements with fitting.

density, J_{SC}, agrees between the two devices within the experimental error. The maskless BSR device shows an approximate 0.4 mA improvement in J_{SC} compared to the flat BSR device. This increase is consistent with the difference in the integrated J_{SC} between the flat and maskless BSR devices from the EQE shown in Figure 5.11(a)-(b). The *FF* produced by the BSR devices confirms good carrier collection in the TTC layer since there is no significant reduction at P_{mpp}. The inset diagram in Figure 5.10 shows the dark J-V measurements (solid

Table 5.2: Solar Cell 1-Sun AM0 Characteristics

Device	J_{SC} (mA·cm^{-2})	V_{OC} (V)	*FF* (%)	η (%)
GaAs control	21.16 ± 0.15	1.013 ± 0.002	84.4 ± 0.8	13.3 ± 0.2
Flat BSR	20.82 ± 0.31	0.996 ± 0.005	84.6 ± 0.8	12.9 ± 0.3
Maskless BSR	21.25 ± 0.29	0.996 ± 0.005	85.1 ± 1.3	13.2 ± 0.4
No BSR (sim.)	19.51	1.017	84.6	12.3
GaAs control (sim.)	21.06	1.012	84.2	13.2

lines) for the GaAs control and flat BSR device, which were fit (dotted lines) using the diode Equation 3.1. The recombination current, J_{01}, and ideality, n_1, are in agreement between both devices, and the R_S is low in each device. The shunt resistance in the GaAs control is lower than the flat BSR device due to the increased active area. The V_{OC} from the flat and maskless BSR devices was reduced by 17 mV, indicating the loss is mainly associated with the inversion process rather than the texture exposure. Although the V_{OC} from the maskless BSR device is less than the GaAs control, the current output and FF maintained the device efficiency. With an improved ELO process and a wide E_g front surface field (FSF), the BSR device efficiency is expected to approach 20% under 1-Sun AM0.

Figure 5.10 also shows two modeled curves of the GaAs control on the substrate and a thinned 1.1 μm solar cell with no BSR mainly to indicate the anticipated baseline current output for the thinned solar cell with no path length enhancement. The corresponding figures of merit for the modeled devices are shown in Table 5.2. The GaAs control electrical diode modeling was performed using the well-established Synopsys Sentaurus Device with III-V electrical parameters extensively used in the Sentaurus database, discussed in further detail by Nelson [22]. The minority carrier electron lifetime and mobility in the base are $1x10^{-7}$ s and $5.9x10^3$ cm^2/Vs, respectively, while the MC hole lifetime and mobility in the emitter are $1x10^{-6}$ s and 163 cm^2/Vs, respectively. The modeled surface recombination velocity (SRV) is $5x10^5$ cm/s. The Hovel/Woodall model based on the carrier transport equations was also used to represent the current collection from the front accurately [17, 106]. Both models used experimental absorption data from in-house MOVPE-grown materials measured by spectroscopic ellipsometry. In Figure 5.10, the two-dimensional model accounted for the 4% grid finger shadowing on the GaAs control, and the modeled J_{SC} is in agreement with the experimental result. The V_{OC}, FF, and efficiency are also within the measurement variation for the GaAs control. The modeled

GaAs control absorbing region was reduced to 1.1 μm, and the 4% grid finger shadowing was included. Both the flat and maskless BSR produce a higher J_{SC} when compared to the thinned device model, showing that the light trapping structures are indeed improving the photoabsorption within the active region. The EQE in Figure 5.11(a)-(b) was taken on regions with no grid finger shadowing. Thus, the integrated J_{SC} is slightly higher compared to the illuminated J-V measurements across all devices. The modeled EQE of the thinned device with no BSR shows a limited collection of low-energy photons due to transmission loss at the backside of the absorber. From the integrated J_{SC} between 350 nm to 950 nm, the current gained back by the flat BSR, and maskless BSR devices are approximately 1.6 mA and 2 mA, respectively. This recovered current in the base region is due to the increased reflection of the low-energy photons from the light trapping structures, and both BSR devices follow the same trend in EQE as the GaAs control. Between 700 nm and 950 nm, the maskless BSR provides a 19.7% increase in the integrated J_{SC} compared to the modeled thin absorber without a BSR. The flat and maskless BSR devices have a slightly higher front side collection, possibly due to different FSF thicknesses during epitaxial growth.

The photon lifetime enhancement factor (LEF) within the flat and maskless BSR cavities was derived using the FP oscillations, as seen in Figure 5.12 near the GaAs band edge where light is not fully attenuated. Figure 5.12 shows the relationship between the FP fringes depicted in the EQE according to the multiple resonance reflections at the front surface and the backside mirror.

In the typical characterization of the FP cavity, as discussed in more detail by Verdeyen and Thyagarajan et al. [3, 107], the quality factor, Q, is an important parameter that describes the energy dissipating from the cavity and is dependent on the mirror's reflectivity. The photon lifetime within the cavity, referred to as the light-trapping photon lifetime ($\tau_{ph}^{trapping}$) is derived

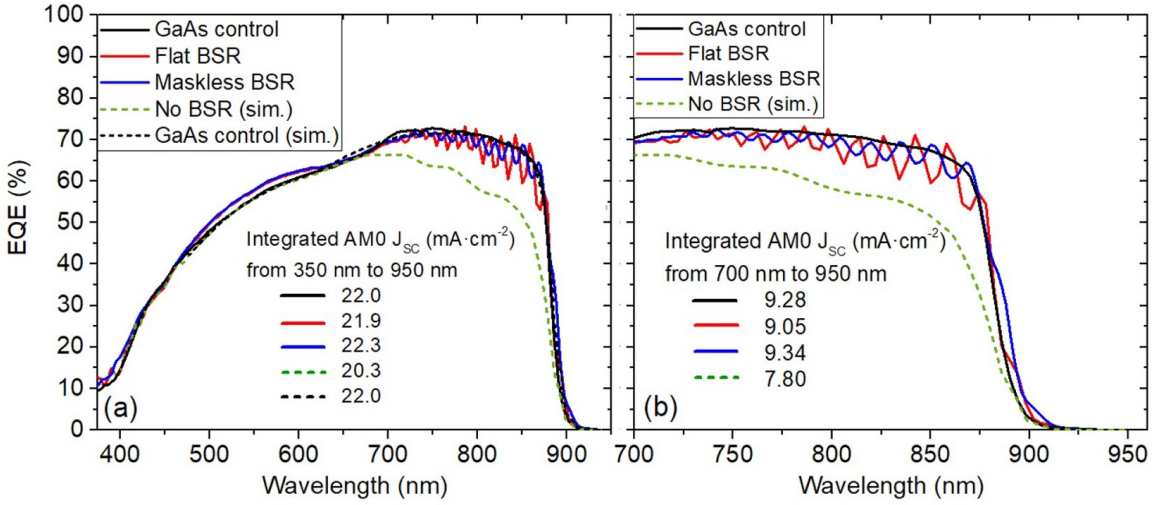

Figure 5.11: External quantum efficiency of the GaAs control, flat and maskless BSR devices, and modeled GaAs absorber with no BSR for (a) the full spectrum and (b) near the band edge. The inset diagram represents the Fabry-Pérot fringes caused by the reflection of photons at the front surface and BSR.

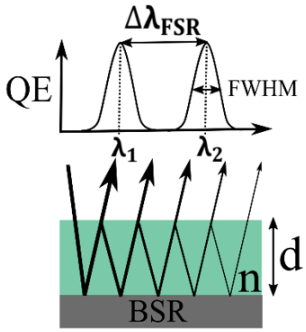

Figure 5.12: Diagram to display the correlation between thin-film oscillations measured in QE measurements and the reflectance in the thin-film solar cell with a BSR.

from Q. This lifetime is compared to the single-pass photon lifetime (τ_{ph}^{single}), which is the case where no light management is present. For the τ_{ph}^{single}, the thickness, d, of the flat and maskless BSR cavities is determined from the Free Spectral Range (FSR), as depicted in Figure 5.11(b). The FSR in wavelength space, ($\triangle\lambda_{FSR}$) is the distance between the last two consecutive resonance peaks at their maxima and is inversely proportional to the cavity thickness. Since the index of refraction, n, of the absorbing material is known, the total thickness of the optical cavity is determined using the relationship,

$$\triangle\lambda_{FSR} = \frac{-\lambda_{\mathrm{p}}^2}{2nd}, \tag{5.2}$$

where λ_p is the peak wavelength at the maximum EQE value from the last FP oscillation. This relationship results in a cavity thickness of 5.98 μm for the flat BSR device and 5.47 μm for the maskless BSR device. The maskless BSR device has a thinner cavity since a portion of the $Al_{0.3}Ga_{0.7}As$ was removed during the maskless etch. For both BSR devices, the total cavity thickness includes the GaAs absorbing region, the $Al_{0.3}Ga_{0.7}As$ TTC layer, SiO_2, and the Sylgard encapsulant. The τ_{ph}^{single} is measured, knowing that time is the ratio between the measured thickness of the BSR cavity and the speed of light. This results in a τ_{ph}^{single} for the flat and maskless BSR devices to be 19.9 femtoseconds (fs) and 18.3 fs, respectively. Since the cavity is thinner from the maskless etching, the τ_{ph}^{single} is shorter in the maskless BSR device.

Q is determined from the ratio between λ_p and the full-width half max (FWHM) from the last EQE fringe. The calculated value of Q for the flat and maskless BSR devices is 153.3 and 170.2, respectively. With highly effective light trapping structures, $\tau_{ph}^{trapping}$ will increase as Q improves. The $\tau_{ph}^{trapping}$ is calculated by,

$$\tau_{ph}^{trapping} = \frac{Q}{2\pi c}\lambda_p, \tag{5.3}$$

where c is the speed of light. The $\tau_{ph}^{trapping}$ for the flat and maskless BSR devices are 71.1 fs and 78.4 fs, respectively. The LEF within the cavity is determined by taking the ratio between the light-trapping and single-pass photon lifetimes.

$$LEF = \frac{\tau_{ph}^{trapping}}{\tau_{ph}^{single}} = \frac{\frac{Q}{2\pi c}\lambda_p}{\frac{d}{c}} = \frac{Q}{2\pi d}\lambda_p. \tag{5.4}$$

Using this relationship, the LEF for the flat and maskless BSR devices is 3.5 and 4.3,

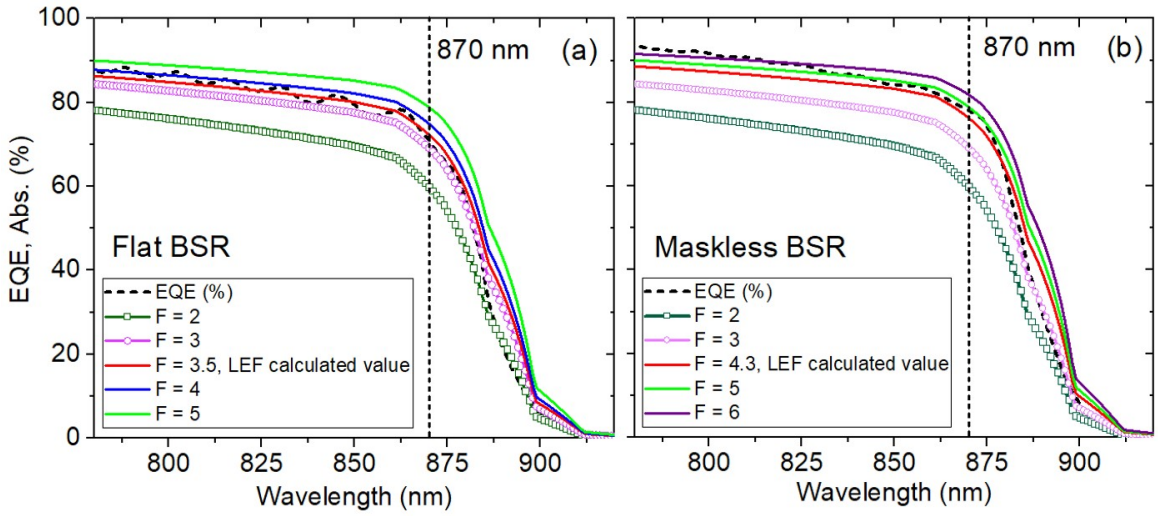

Figure 5.13: The light path enhancement factor, F, for the (a) flat BSR device and the (b) maskless BSR device. The EQE is measured data from each solar cell with an ARC. The absorption is based on the propagation model for thin absorbers with reflectors from reference [47]. The LEF calculated value was used for the F factor, as shown by the red curves.

respectively. These values correspond to the extended photon lifetime within the cavity, directly related to the light trapping properties. The LEF is similar to the Finesse of a cavity as it is related to Q. The Finesse increases as the FWHM of the oscillation fringe decreases, or in other words, as the oscillation becomes sharper. The benefit of the LEF is it considers the single-pass photon lifetime where no light management is present, which allows the path length enhancement to be known. The LEF can also be compared to the optical characterization techniques performed in this work. For example, the LEF for the maskless BSR device is related to the increased haze in reflectance near 80% at the GaAs band edge, depicted in Figure 5.4(b). This diffuse reflectance indicates a higher degree of internal photon scattering. Additionally, the dampened FP fringes and higher photoabsorption in the base region of the maskless BSR device all support the increased LEF compared to the flat BSR device. The LEF and increased photoabsorption from a maskless BSR are expected to become more noticeable in absorbers less than 1.1 µm thick where the active region does not become optically thick within a 4-fold increase in the photon path length. The calculated optical parameters for the

BSR devices are displayed in Table 5.3.

Table 5.3: Optical cavity parameters calculated for the BSR devices

BSR	Flat	Maskless
FSR (nm)	17.5	19.1
d (μm)	5.98	5.47
FWHM (nm)	5.7	5.1
λ_p (nm)	873.9	868.1
Q	153.3	170.2
$\tau_{ph}^{trapping}$ (fs)	71.1	78.4
τ_{ph}^{single} (fs)	19.9	18.3
LEF	3.5	4.3

Another method to calculate the light path enhancement factor, F, described by Gaucher et al. [47] was applied to the BSR devices in this work. An ARC consisting of 53 nm of ZnS and 100 nm of MgF_2 was evaporated on the solar cells to analyze the F factor. From the EQE with an ARC, the analytical propagation model describes the absorption enhancement based on varying the F factor [10,47]. The model uses the weakly absorbing region of the EQE, where light is not fully attenuated. The absorption is expressed as

$$A(\lambda) = \frac{\alpha d}{\alpha d + \frac{1}{F}}, \tag{5.5}$$

where α is the wavelength-dependent absorption coefficient in GaAs, and d is the absorber thickness of 1.1 μm. Figure 5.13(a)-(b) displays the change in the absorption model with various F factors that are adjusted to match the EQE from the GaAs solar cell with the flat and maskless BSR. For the double pass where F equals 2, the EQE is much higher, revealing an increase in photon scattering and carrier collection. This increased collection is valid not only for the maskless BSR device in Figure 5.13(b), but also for the flat BSR device in Figure 5.13(a). The increased F factor in the flat BSR device correlates to the observed 10-15% haze in reflectance, shown in Figure 5.4(b), near the GaAs band edge, and supports a higher degree

of light scattering. The inset cross-sectional SEM in Figure 5.4(b) shows the Sylgard does not have a perfectly flat interface between the epitaxial layers and the mirror, implying that the light path varies from the scenario of an ideal flat reflector. As the F factor increases from 2, the fit matches the experimental EQE measurement near the GaAs band edge. The red solid curves on each plot show that the calculated LEF values agree the most with the EQE. This agreement supports the validity of the LEF optical analysis, obtained from the FP oscillations in the measured EQE, as a technique to determine the performance of light trapping structures in terms of the photon lifetime enhancement.

The integrated J_{SC} taken on the ARC-coated devices resulted in 30.7, 29.6, and 31.3 mA·cm^{-2} for the GaAs control, flat BSR, and maskless BSR device, respectively. Due to complications with the ARC deposited on the front side metal contacts, the four-point probe measurements from the illuminated J-V measurements for the thin solar cells are not shown, but it is expected that the maskless BSR device can produce an efficiency of 19.7% under 1-Sun AM0 given this increased current output along with an improved ELO process and highly transparent FSF. For light trapping devices with an ARC, the band edge shift in the IQE, as described by Steiner et al. [62], is caused by the measured backside reflectance and increases the apparent carrier collection. Due to this artifact, it is more accurate to use the EQE measurement when using the LEF analysis for thin-film solar cells with backside light trapping structures.

5.3.3 Conclusions

The maskless etch has successfully increased the surface roughness as demonstrated in $Al_xGa_{1-x}As$ with Al composition ranging between $0.1<x<0.3$ at different carbon doping concentrations. For the 1.1 μm GaAs solar cell, the maskless texture resulted in a haze in reflectance

near 80% at the GaAs band edge, enabling a J_{SC} comparable to the GaAs control, which is twice the absorbing thickness. The maskless BSR device also provides an integrated J_{SC} in the base region that is nearly 20% higher than the modeled thin absorber without a BSR. These results relate to the maskless BSR developed under the specific conditions used in this work; however, the broad range of etchant parameters in ratio, temperature, and duration presents an opportunity to produce distinct maskless textures tailored for high diffuse reflectance in different parts of the spectrum. The LEF, derived from the FP optical characterization, was calculated to be 3.5 and 4.3 for the flat and maskless BSR devices. The LEF greater than 2 for the flat BSR device is explained by the haze in reflectance between 10-15% at the GaAs band edge and is caused by the non-planar behavior in the Sylgard region, suggesting that the light path varies from the case of an ideal flat reflector. The LEF in the maskless BSR device correlates to the increased haze in reflectance, dampened FP oscillations, and improved photoabsorption shown in the EQE near the band edge. The LEF values agree with the F factor determined by the propagation model and verify using this new technique to define the enhanced photon lifetime in thin solar cells with light management.

5.4 GaAs Solar Cells with I-MacEtch BSR

5.4.1 Device Growth and Fabrication

The active region of the GaAs solar cell is 0.5 μm thick and is fabricated similarly to the solar cells explained in Chapter 4. The growth design is shown in Table 5.4 and the structure of these solar cells is shown in Figure 5.14, where a top-top contact design was utilized. The Sylgard 184 adhesion layer has a low index of refraction near 1 and serves as the TIR layer. In these structures, only the Sylgard 184 is used as the low-index layer to remove the additional

step to deposit SiO_2 as a low-index TIR layer.

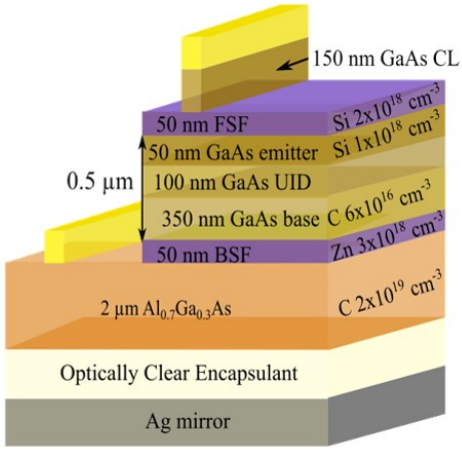

Figure 5.14: Solar cell design for a 0.5 μm GaAs solar cell with a BSR using a top-top contact design.

Table 5.4: Growth design for 0.5 μm-thick GaAs solar cells.

Layer	Material	Thickness (nm)	Doping (cm^{-3})
TTC	p-$Al_{0.3}Ga_{0.7}As$	2000	2x10^{19} (C)
Window	p-InGaP	50	3x10^{18} (Zn)
Base	p-GaAs	350	6x10^{16} (C)
Intrinsic	GaAs	100	UID
Emitter	n-GaAs	50	1x10^{18} (Si)
Window	n-InGaP	50	2x10^{18} (Si)
Contact	n-GaAs	100	3x10^{18} (Si)
Contact	n-GaAs	50	2x10^{19} (Te)
Barrier	n-GaAs	10	3x10^{18} (Si)
Etch Stop	n-InGaP	150	3x10^{18} (Si)
Substrate	GaAs	350 μm	UID

5.4.2 Electrical Device Results and Discussion

Figure 5.15 displays the measured EQE obtained from the optically thick GaAs control and the sub-μm thick GaAs solar cells with the flat and MacEtch BSR, and Table 5.5 displays the full spectrum and near band edge integrated J_{SC}. The EQE spectrum obtained from a GaAs control with a 2.25 μm absorbing region shows the reduction in carrier collection in the base region compared to the optically thick 3.6 μm GaAs control. To compare the thin solar cells with the BSR to a thin absorber scenario in the absence of light trapping structures, the Hovel/Woodall model was used.

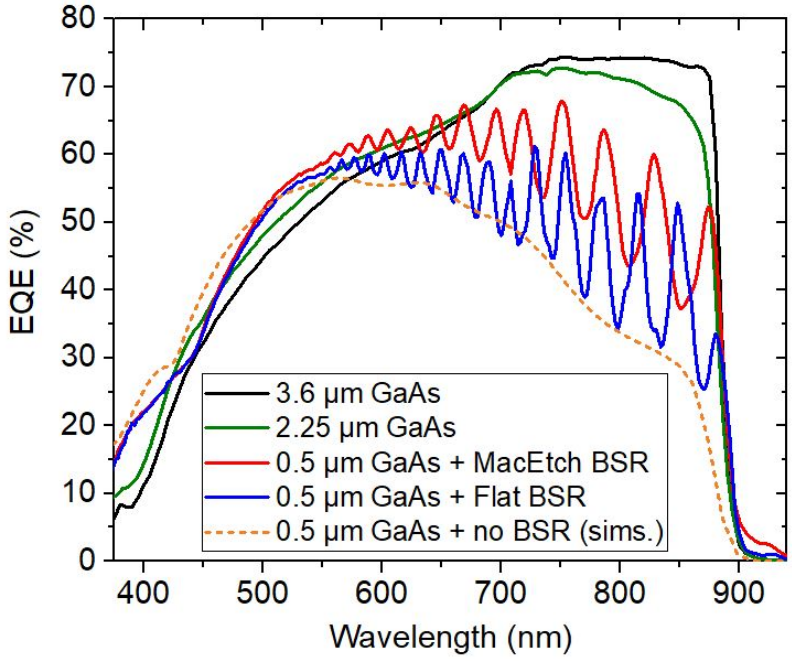

Figure 5.15: External quantum efficiency for the optically thick GaAs control and the thin GaAs solar cells with the flat and MacEtch BSR. The 500 nm GaAs solar cell with no light trapping structures was modeled as shown by the orange dotted curve.

The simulated 500 nm GaAs device without a BSR, as shown by the orange dotted curve in Figure 5.15, displays the transmission loss from low energy photons as current collection is

Table 5.5: Integrated J_{SC} from the EQE spectra

Device	Full Spectrum J_{SC} (mA·cm^{-2})	Band Edge J_{SC} (mA·cm^{-2})
GaAs control 3.6 um	34	19.5
GaAs control 2.25 um	22	12.1
Flat BSR	20.7	10.2
I-MacEtch BSR	18.6	8.6
No BSR (sim.)	16.9	6.9

limited in the base region. The recovered current is apparent in the flat and I-MacEtch BSR devices, as shown by the FP fringing of low-energy photons reflected off the back mirror that begins around 600 nm. The Ag mirror indicates a suitable reflector, and the I-MacEtch texture results in a higher degree of photon scattering as the fringes become broader and more current is collected. Based on the integrated J_{SC} from 650 nm to 950 nm, the I-MacEtch BSR device regains 17% and 38% of the current loss from the flat BSR device and the simulated no BSR device, respectively. Although the I-MacEtch BSR current collection in the base region is not as prominent as the optically thick GaAs control, the improved absorption proves that the textured BSR efficiently improves the photogenerated carrier collection. Furthermore, different I-MacEtch textures created by changing the catalyst dimensions or etching conditions can outperform the spherical dome texture, further improving photoabsorption to reach the current output realized in the optically thick solar cell.

The LEF described in Chapter 5 is applied to the thinned GaAs solar cells with the BSR to evaluate the increase in photon lifetime within the optical cavity due to the light trapping structures [96]. The LEF is calculated from the FP fringes in the EQE near the band edge for each device, and the corresponding values are displayed in Table 5.6. The thickness of the cavity in the flat BSR device is larger than the I-MacEtch BSR device since the texturing process removed an amount of the $Al_{0.7}Ga_{0.3}As$. The higher Q factor in the I-MacEtch BSR device reveals that the near band edge photons remain inside the cavity for a longer duration than the

flat BSR device. For the I-MacEtch BSR device, this results in a longer light-trapping photon lifetime, $\tau_{ph}^{trapping}$, and the single-pass photon lifetime, τ_{ph}^{single}, is shorter since the cavity is thinner. The LEF was calculated to be 5.7 for the MacEtch BSR device from these two factors. With an anti-reflection coating, the photoabsorption for near band edge photons is expected to increase by this value. The flat BSR device resulted in a LEF of 3.4, which is similar to what was seen for the previous planar BSR device discussed in Chapter 5. Referring back to the haze in reflectance in Figure 5.15, the diffused scattering for near band edge photons in the flat BSR device is around 10%. The flat BSR device is expected to be completely specular; however, the haze in reflectance shows that some photon scattering at the back interfaces is involved. The low index encapsulant, Sylgard 184, may not be completely flat and uniform below the GaAs solar cell.

Table 5.6: Optical cavity parameters calculated for the BSR devices

BSR	Flat	I-MacEtch
FSR (nm)	32	47
d (μm)	3.361	2.257
FWHM (nm)	10.8	9.5
λ_p (nm)	880	874
Q	81.5	92
$\tau_{ph}^{trapping}$ (fs)	38	42.7
τ_{ph}^{single} (fs)	11.2	7.5
LEF	3.4	5.7

5.4.3 Conclusions

Based on previous reports in the literature for I-MacEtch in $Al_xGa_{1-x}As$ [77], the patterned 1.5 μm diameter array of Au catalysts was performed as a first approach to create a periodic texture with similar dimensions compared to the thickness of the GaAs solar cell. The spherical arrays in carbon-doped AlGaAs developed from the I-MacEtch showed high diffuse scattering abilities. This texture was incorporated into 0.5 μm GaAs solar cells and the EQE and lifetime

enhancement factor within the cavity show that the I-MacEtch BSR improves photoabsorption, especially near the band edge of the GaAs solar cell. Notably, the I-MacEtch process can be tuned to produce nanostructures with higher diffuse reflectance to further improve current collection in sub-μm thick GaAs solar cells.

5.5 Chapter Summary

The two textures developed in this work include a maskless etching approach where no photolithography is required to produce a 3-dimensional crystal structure. The second texture utilizes I-MacEtch to produce a periodic dome-like structure. There are benefits and trade-offs to both approaches. The maskless etch requires fewer steps since no patterning is required. However, the size of the pyramidal structures and morphology is limited to the random nature of this etch technique. On the other hand, the I-MacEtch can be produced both randomly and through a pattern. The pattern adds additional steps but is capable of improving photon absorption in the sub-μm thick GaAs solar cells. Combining the maskless texture with the 94% reflective flat mirror enhanced the photogenerated carrier collection in the 1.1 μm GaAs solar cell by 1.6% when compared to the 2.25 μm GaAs control on the GaAs substrate. The LEF analysis was developed to define the extended cavity photon lifetime due to efficient BSR light trapping properties. The LEF for the maskless and I-MacEtch BSR devices was measured to be 4.3 and 5.7 times greater than the single-pass photon lifetime. This enhanced OPL validates the application of these texturing approaches to maintain absorption in thin-film multijunction solar cells.

Chapter 6

Free-Carrier Absorption in Thin-Film GaAs Solar Cells

6.1 Introduction

Optical modeling has become a well-established and integral part of demonstrating the efficacy of light trapping structures as ultrathin III-V solar cells continue to push towards their maximum achievable efficiency. In particular, researchers have rendered potential pathways to reach higher voltage and current output in ultrathin GaAs solar cells [35, 38, 54, 54, 56, 58, 60, 61, 108]. All parasitic optical losses must be accounted for when modeling ultrathin GaAs solar cells, including absorption loss in the back mirror and non-active layers behind the photoactive region of the device. Absorption in the metal can be suppressed by using a low-index spacer to improve TIR [29, 54, 58, 66, 72] and using wide bandgap materials for non-active back layers removes band-to-band absorption loss [35, 51, 57]. This back layer is called "non-active" since it is outside the photoactive region and does not proactively generate photocurrent but requires an elevated doping concentration for carrier transport to the external electrodes. This elevated doping concentration in the back layer may lead to the absorption mechanism known as free-carrier absorption (FCA). FCA is a parasitic optical process that occurs in heavily doped

semiconductors where free carriers reduce the intensity of light passing through an absorbing medium but do not generate electron-hole pairs [109, 110]. In photovoltaics, FCA is mainly considered in silicon solar cells due to its indirect E_g [10, 42, 109–111] or in heavily doped and thick III-V substrates [26, 95]. Intuitively, FCA is ignored when modeling III-V solar cells since the non-active layers are ultrathin and have a direct E_g. This premise changes when the solar cell optical cavity is related to a laser cavity where FCA must be considered as a design constraint due to the optical enhancement within these systems [112–117]. Moreover, light trapping development requires the non-active back layers to be thick enough for texturing and must preserve electrical contact using a high doping concentration [35, 51]. These factors reveal the situation where absorption by free carriers may be present in the non-active back layers, initially designed for light management and carrier transport. In particular, transmitted photons after the first pass through the ultrathin GaAs solar cell will slowly attenuate in the non-active back layer due to FCA, eliminating the light trapping structure's potential current and voltage enhancement benefits. For these reasons, it is crucial to include the parasitic loss from FCA in non-active layers when modeling the optical performance of light trapping structures in ultrathin III-V solar cells.

This study primarily focuses on the optical modeling of ultrathin GaAs solar cells with different BSR designs, as seen in Figure 6.1, to investigate trends in the FCA based on the doping concentration and thickness of non-active layers behind the photoactive GaAs region. This study investigates GaAs solar cells operating under the terrestrial AM1.5G spectrum, but can easily be performed under the AM0 solar irradiance for space applications. The electrical performance of the diode is assumed to remain consistent across all simulations, while the change in doping concentration in the back layer impacts the series resistance. A thorough investigation to determine an optimal doping concentration in the back layer targeting low

series resistance for sufficient carrier transport and minimal FCA is necessary for device-specific designs. Focusing on the optical modeling, the light trapping geometries investigated in this work include a planar reflector and three cylindrical geometries. These designs are modeled using a rigorous coupled-wave analysis (RCWA) included in the open-source Python 3 extension, RayFlare [118]. The free-carrier absorption coefficient used in the back layer is determined according to classical Drude theory as discussed in Section 6.2.2. By combining Drude theory to describe the absorption by free carriers in the back layer with RCWA, we show that the FCA increases as the thickness and doping concentration of the back layer increases. From these trends, we extract the reduction in the J_{SC} and the V_{OC} from ideal conditions where FCA is not considered. The results indicate that FCA in non-active layers should not be underestimated as the reduction in device efficiency may be substantial in these devices.

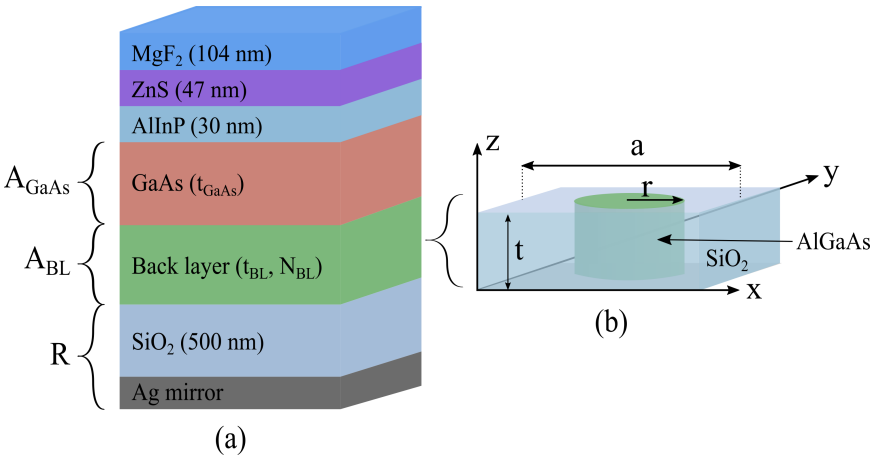

Figure 6.1: Plot (a) illustrates the GaAs solar cell with a planar Ag mirror and a SiO_2 interlayer. The three main parameters including the absorptance in the GaAs solar cell (A_{GaAs}), absorptance in the back layer due the FCA (A_{BL}), and the backside reflectance (R) are displayed to correlate these processes to the regions in which they occur. Plot (b) shows a unit cell of the cylindrical gratings, further discussed in Section 6.3.3. The AlGaAs radius (r), SiO_2 pitch (a), and height (t_{BL}) change according to each grating design.

6.2 Methods

6.2.1 Solar Cell Design and Light Trapping Geometries

The first BSR investigated is a planar geometry, capable of achieving a twofold increase in the OPL as transmitted photons reflect off the back mirror into the optically thin GaAs solar cell. Figure 6.1(a) represents the GaAs solar cell with a planar reflector and a bi-layer ARC of MgF_2 and ZnS. Below the ARC is the wide E_g front surface window, AlInP. These three layers assist in reducing the front surface reflection of incident light. The GaAs absorber has a photoactive region with thickness indicated by t_{GaAs}. For the planar BSR, three values of t_{GaAs} are investigated: 100 nm, 300 nm, and 500 nm. Behind the GaAs region is the non-active back layer where absorption by free carriers is studied, dependent on the thickness (t_{BL}) and doping concentration (N_{BL}) of the back layer. Behind the back layer is a 500 nm-thick low-index SiO_2 spacer and a highly reflective Ag mirror. In this design, the *n-i-p* polarity is considered to investigate the worst-case scenario of FCA in the p-type back layer. Further discussed in Section 6.2.2, holes naturally have a lower mobility and result in a higher FCA than electrons [112]. Due to its wide E_g with increasing Al composition, $Al_xGa_{1-x}As$ is chosen as the material for the non-active p-type back layer. Additionally, $Al_xGa_{1-x}As$ (hereafter, referred to as AlGaAs) is a common material used in GaAs solar cells due to its E_g tunability, texturing and doping capabilities, and the fact that it can be grown nearly lattice-matched to GaAs [29, 53, 66]. The AlGaAs back layer varies in t_{BL} and N_{BL}, and combinations between these factors with t_{GaAs} are modeled to find trends in FCA. Figure 6.1(a) also displays the specific regions of interest where absorptance and the backside reflectance (R) occur. Specifically shown are the absorptance in the photoactive GaAs solar cell (A_{GaAs}) which aids in proactive photogenerated current, and the parasitic absorptance in the back layer (A_{BL}) due to FCA. Lastly, R is the

measured amount of reflected photons, which is dependent on t_{GaAs}, t_{BL}, and N_{BL}. Section 6.2.2 discusses the computation to find A_{GaAs}, A_{BL}, and R.

Apart from the planar geometry, three cylindrical gratings consisting of AlGaAs cylinders embedded in SiO_2 are investigated. Figure 6.1(b) displays a unit cell of the cylindrical gratings with AlGaAs radius (r), SiO_2 pitch (a), and height (t_{BL}). In this design, the unit cell repeats periodically in the xy plane and replaces the back layer. This substitution is the only difference compared to the planar BSR design in Figure 6.1(a). For the cylindrical geometry, the 300 nm-thick GaAs solar cell is the main focus since, under ideal Lambertian circumstances, it can absorb 98% of the available photons in the radiative limit [58]. The optical constants used in the model were measured on in-house grown or deposited non-active layers (MgF_2, ZnS, AlInP, and SiO_2) using a spectroscopic ellipsometer (RC2, J.A. Woollam Co., Inc.) and appropriate fits were performed using the CompleteEASE software. Since GaAs is a widely understood material, the optical constants were taken from the J.A. Woollam CompleteEase database. The optical constants for the materials used in the model are displayed in Appendix A. This study ignores band-to-band absorption in the AlGaAs layer since FCA is the main focus. Instead, the extinction coefficient in the AlGaAs layer is dependent on the modeled free-carrier absorption coefficient, as discussed in Section 6.2.2. This assumption in the model is reasonable considering that in experimental designs that use AlGaAs as a textured backside layer, the Al fraction is high enough to make it transparent in terms of band-to-band absorption [52, 53, 58].

6.2.2 Modeling Free-Carrier Absorption in the Back Layer

The classical Drude model, which is extensively used to calculate the free-carrier absorption coefficient (α_{FCA}) in laser cavities [112, 119–121], is used to describe the FCA in the AlGaAs

layer. The α_{FCA} is calculated by,

$$\alpha_{\mathrm{FCA}} = \frac{q^3 \lambda^2 N}{4\pi^2 \mu m^2 n \varepsilon_0 c^3}, \tag{6.1}$$

where q is the electron charge, λ is the emission wavelength, N is the carrier concentration, ε_0 is the electric constant, n is the index of refraction, and μ and m are the mobility and effective mass of the charge carriers, respectively. In this expression, absorption by free carriers is dependent on the carrier concentration and mobility and will be greater in a p-doped semiconductor since the mobility is nearly two orders of magnitude lower than in an n-type semiconductor at the same doping concentration [121]. As the FCA is studied at different doping levels, the mobility to determine α_{FCA} must change, too. This is accomplished by using the low-field empirical mobility model to calculate the mobility of p-type carriers [122]. The mobility at 25 °C is defined by,

$$\mu = \mu_{min} + \frac{\mu_{max} - \mu_{min}}{1 + (\frac{N}{N_{ref}})^{\lambda}}, \tag{6.2}$$

where μ_{min}, μ_{min}, N_{ref}, and λ are fitting parameters specific to the carrier type and semiconductor [122]. To validate the mobility model against experimental measurements, multiple $Al_{0.3}Ga_{0.7}As$ films were grown on 2-inch (100) GaAs wafers with a 2-degree offcut <110> via MOVPE and measured using Hall to determine N and μ. Figure 6.2(a) displays the experimental results plotted against the mobility model using the fitting parameters described by Sotoodeh et al. [122]. The agreement between the experimental Hall measurements validates the use of the mobility model to determine μ in Equation 6.1. The remaining parameters in Equation 6.1 are based on values in literature, such as the effective mass of holes in AlGaAs as determined by Adachi [123], which remains constant for a given Al composition. Values for

n are determined by spectroscopic ellipsometry and appropriate fits on $Al_{0.3}Ga_{0.7}As$. Figure 6.2(b) shows the α_{FCA} of AlGaAs at doping concentrations between 5x10^{18} cm^{-3} and 4x10^{19} cm^{-3}, which is the range used in the modeled structures. In this plot, the doping concentration has a direct influence on FCA, especially at longer wavelengths. The modeled FCA results in this work are based on Equation 6.1 and are performed at standard temperature at 25 °C. Notably, if the solar cells are designed for extreme temperature conditions, then the low-field mobility model including temperature must be applied to calculate the change in mobility as a function of temperature [122].

Integrated in Rayflare, the Pol method established in the Stanford Stratified Structure Solver (S^4) was used in the RCWA computations [118,124] to study the impacts of FCA in the AlGaAs layer (simply referred to as the back layer, hereafter) behind the ultrathin GaAs solar cells. The four main factors contributing to the change in transmitted photons during each pass through the solar cell cavity include t_{GaAs}, α_{GaAs}, t_{BL}, and α_{FCA}. With the RCWA methods and absorption coefficients determined in the GaAs absorber and back layer, various combinations

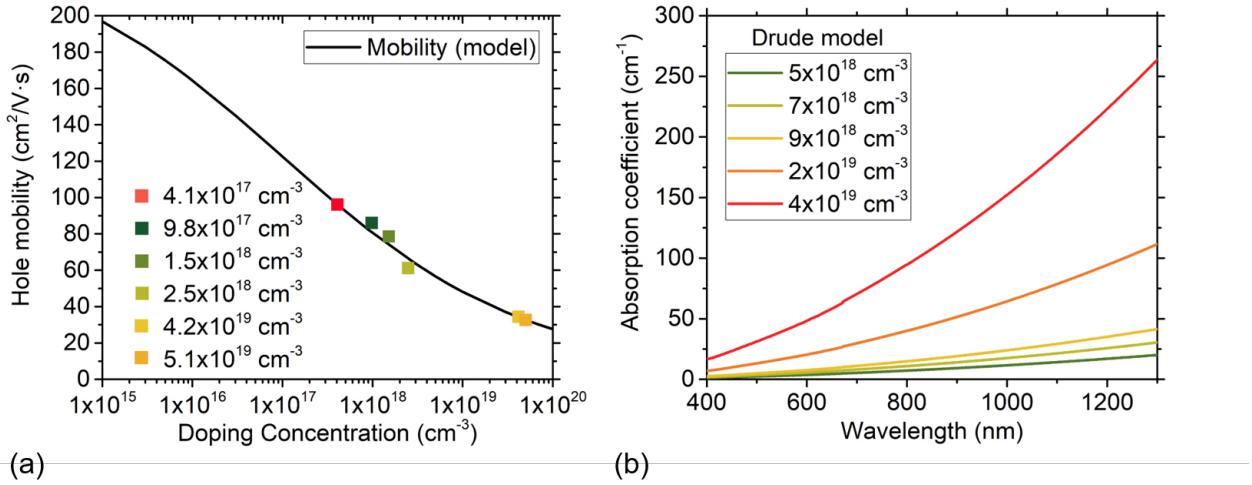

Figure 6.2: Plot (a) shows experimental Hall results taken on p-type AlGaAs samples compared to the mobility model. Plot (b) shows the α_{FCA} calculated by the Drude model, which is integrated with the mobility model.

depending on the thicknesses of each layer are simulated to determine the variation in FCA. The total reflectance (R), absorptance (A), and transmittance (T) between 350 nm - 900 nm at normal incidence are computed as follows:

$$RAT = reflectance + transmittance + A_{GaAs} + A_{BL}, \tag{6.3}$$

where A_{GaAs} and A_{BL} present the absorptance in the GaAs and back layer based on their absorption coefficients, respectively. The fractional R, T, A_{GaAs} and A_{BL} are determined separately by normalizing each parameter to the total RAT computation. Additionally, the summation of each fractional parameter always equals unity. In the ideal case where FCA is not present, A_{BL} is ignored so that all absorption occurs within the GaAs solar cell. Initially, the ideal conditions are computed without including FCA in the back layer. By introducing the α_{FCA} to find A_{BL} in the back layer, the total RAT changes where some level of FCA occurs in the back layer. This absorption takes away from potential photogenerated current in the GaAs absorbing region. The fractional free carrier absorption (FFCA) in the back layer is extracted by normalizing A_{BL} to the RAT computation and is used to describe the loss in current and voltage output compared to ideal conditions, as discussed in Section 6.3.

Due to the three-dimensional nature of the cylindrical gratings, convergence tests were conducted to find accuracy in the RCWA computation. The number of Fourier orders increased in the xy plane of the grating layer, and the two main responses including the J_{SC} and FFCA in the back layer converge at higher Fourier orders. The maximum deviation for J_{SC} and FFCA between 169 orders and 225 orders is less than 0.01% and 0.05%, respectively. To accommodate for computation time, 169 Fourier orders was used, resulting in nearly a 3x reduction in computation time. The convergence results are shown in Appendix A.

6.3 Results and Discussion

6.3.1 Current Loss due to Free-Carrier Absorption with a Planar BSR

An example of the reduction in absorptance in a 300 nm-thick GaAs solar cell with a planar BSR, as depicted in Figure 6.1(a), when FCA is present in a 800 nm-thick back AlGaAs layer is shown in Figure 6.3. Specifically, Figure 6.3(a)shows the reduction in A_{GaAs} and increase in A_{BL} as N_{BL} increases in the non-active back layer. Focusing on Figure 6.3(a), the shortest wavelengths are easily absorbed towards the front of the optically thin GaAs solar cell (blue curves) during the first pass. Around 500 nm in wavelength, the absorption drops in the GaAs solar cell and the thin-film interference patterns are observed in the GaAs absorber and the back layer due to reflection from the mirror. As N_{BL} increases in the back layer, the photon absorption by free carriers in the back layer increases, too (green curves). This absorption in the back layer is especially noticeable towards the longer wavelengths as N_{BL} increases. This increased FCA is especially limiting to the absorption of near band-edge photons not easily absorbed during the first pass in the GaAs solar cell. In Figure 6.3(b), the reduction in R from the planar BSR is observed as N_{BL} increases in the back layer and is more pronounced at longer wavelengths. In the ideal case where FCA is not present, the backside reflectance is above 98% near 900 nm in wavelength (dark brown curve) and the reflected photons experience a twofold path length enhancement through the GaAs absorber. The photons that reflect off the mirror will experience a path length enhancement in the back layer before reaching the GaAs region again. Therefore, when N_{BL} and the associated FCA is considered, this immediate path length enhancement in the back layer will reduce the measured R as photons parasitically absorb in the back layer. For example, at N_{BL} equal to 4x10^{19} cm^{-3}, the backside R is measured to be 86% near 900 nm in wavelength (light pink curve), indicating a significant loss of photons due

to the absorption by free carriers. This observation is especially detrimental not only to the J_{SC}, but also the V_{OC}, as discussed in Section 6.3.2.

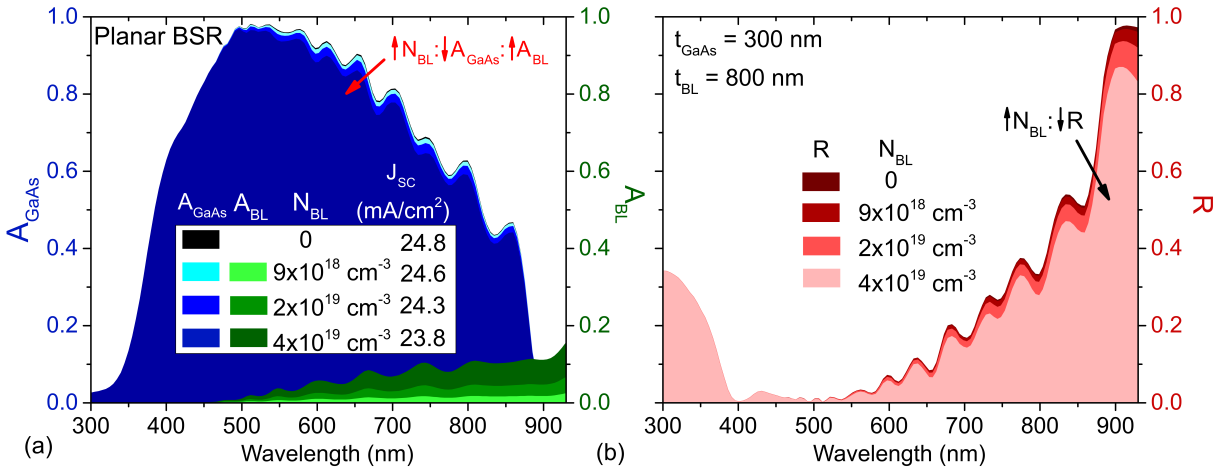

Figure 6.3: The plots above show the change in absorptance in a 300 nm-thick GaAs solar cell (A_{GaAs}) and in a 800 nm-thick back layer (A_{BL}) along with the change in backside reflectance (R) of a planar Ag mirror as a function of N_{BL}. Specifically, plot (a) shows the reduced absorption in the GaAs solar cell (blue curves) and the increased absorption in the back layer (green curves) as N_{BL} increases. Plot (b) shows reduction in backside reflectance as N_{BL} increases in the back layer.

The example explained above provides a glimpse of the negative impacts due to FCA. However, there are various combinations of the t_{GaAs}, t_{BL}, and N_{BL} available to explore. First, the ideal absorption for the three GaAs solar cells with t_{GaAs} of 100 nm, 300 nm, and 500 nm are determined without including FCA in the back layer. The solar cells are modeled in the radiative limit and A_{GaAs} is used to determine the EQE where $A_{GaAs}(\lambda) = \mathrm{EQE}(\lambda)$. From this absorption, the ideal J_{SC} ($J_{SC}{}^{ideal}$) is found by integrating the GaAs absorption against AM1.5G reference spectrum, E(λ),

$$J_{SC}^{ideal} = \frac{q}{hc}\int_{\lambda_1}^{\lambda_2} \lambda E_{AM1.5G}(\lambda)\, EQE(\lambda)\, d\lambda, \tag{6.4}$$

where q is the electronic charge, h is Planck's constant, and c is the speed of light. Across

the wavelength range from 350 nm to 900 nm, the J_{SC}^{ideal} for the 100 nm, 300 nm, and 500 nm-thick GaAs solar cells with the planar geometry are 16.2, 24.8, and 27.8 mA·cm^{-2}, respectively. When the α_{FCA} is included in the back layer, A_{BL} will reduce absorption in the GaAs region depending on the back layer thickness and doping concentration. The FFCA determines the loss in J_{SC} in the GaAs absorber as shown by,

$$J_{SC}^{loss} = J_{SC}^{ideal} \cdot FFCA. \tag{6.5}$$

This computation is performed for various combinations of t_{BL} and N_{BL}, and contour maps of the J_{SC}^{loss} for the three ultrathin GaAs solar cells are shown in Figure 6.4(a)-(c). The N_{BL} between 5x10^{18} cm^{-3} and 4x10^{19} cm^{-3} and the t_{BL} between 0.2 μm to 3 μm are investigated. These ranges are common for sufficient carrier transport and texturing capabilities as reported in literature [52–54, 66].

The scale bar to the right displays the J_{SC}^{loss} and the contour lines display the FFCA at the specified conditions. In all cases, the most detrimental current loss occurs as the back layer thickness and doping concentration increase. Intuitively, this is expected to occur as the attenuation of photons in the back layer increases at high doping levels. Comparing the FFCA contour lines in plots a, b, and c, the rise in J_{SC}^{loss} is more prominent in the 100 nm-thick GaAs absorber since the transmitted photons after the first pass through GaAs have a higher intensity compared to the thicker absorbers. At the maximum values investigated for t_{BL} and N_{BL}, the FFCA over 25% results in nearly 5 mA/cm^2 current loss for the 100 nm-thick GaAs device. Any transmitted photons that survive the first pass through the back layer and reflect off the planar mirror experience a twofold increase in OPL through the back layer. Figure 6.4(d) displays the reduction in J_{SC} with increasing back layer thickness at three specific doping concentrations for the three GaAs solar cells under investigation. For each doping concentration, the slope is

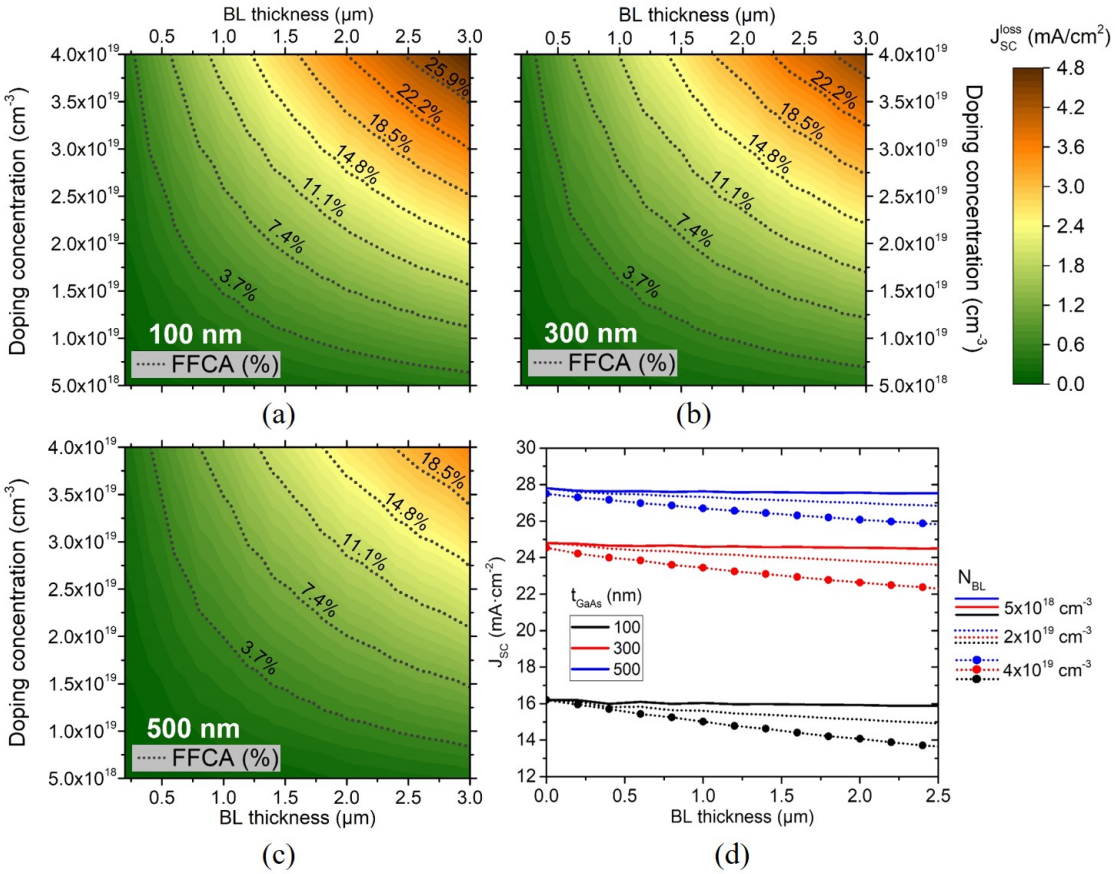

Figure 6.4: Contour maps displaying the J_{SC}^{loss} in GaAs solar cells with a planar BSR at various combinations between the back layer doping concentration (N_{BL}) and back layer thickness (t_{BL}). Specifically, plot (a) represents t_{GaAs} = 100 nm, (b) t_{GaAs} = 300 nm, and (c) t_{GaAs} = 500 nm. The contour lines display the FFCA corresponding to specific back layer conditions. Plot (d) displays the reduction in J_{SC} in the GaAs solar cells from ideal conditions vs. t_{BL} at three doping concentrations.

greater in the 100 nm-thick GaAs solar cell as t_{BL} increases from 0 μm to 2.5 μm. This trend illustrates the significance of GaAs absorber thickness with the loss of photons due to FCA after the first pass.

6.3.2 Voltage Loss due to Free-Carrier Absorption with a Planar BSR

Along with improved current output, light trapping structures in ultrathin GaAs solar cells allow an enhancement in the V_{OC} to occur and numerous studies have shown increased voltage output by introducing highly reflective mirrors [60,66,68]. The voltage enhancement is

especially noticeable in high-quality ultrathin GaAs solar cells where radiative recombination dominates and the internal luminescent efficiency (η_{int}) is close to or at unity [125]. The η_{int} is represented by,

$$\eta_{int} = \frac{U_{rad}}{U_{rad} + U_{nr}}, \tag{6.6}$$

where U_{rad} and U_{nr} are the radiative and nonradiative recombination rates, respectively. For GaAs solar cells operating in the radiative limit, an ideal reflector allows internally emitted photons to cycle within the active region and increase the external luminescent efficiency (η_{ext}), which in return, increases V_{OC}. Embedded in η_{ext} are optical properties, which can be changed according to the efficacy of the light trapping geometry. V_{OC} can be expressed in terms of the ideal open-circuit voltage, (V_{OC}^{ideal}), as calculated using detailed-balance [60,64,68,125], and η_{ext} as

$$V_{OC} = V_{OC}^{ideal} + \frac{kT}{q} ln(\eta_{ext}). \tag{6.7}$$

In this equation, η_{ext} is determined by the η_{int} and the photons probability of escape ($\overline{P}_{esc}$) and absorption ($\overline{P}_{abs}$):

$$\eta_{ext} = \frac{\eta_{int}\overline{P}_{esc}}{1 - \eta_{int}\overline{P}_{abs}}. \tag{6.8}$$

These probabilities depend on the front (R_f) and backside reflectance (R_b) and their expressions are further explained by Steiner et al. [68]. In these probabilities, R_f is calculated from the solar cell escape cone and R_b is calculated from the backside reflectance. In an ideal design, both η_{int} and R_b are equal to 1, which allows η_{ext} to reach unity and sets the measured V_{OC} to equal the ideal V_{OC} in Equation 6.7.

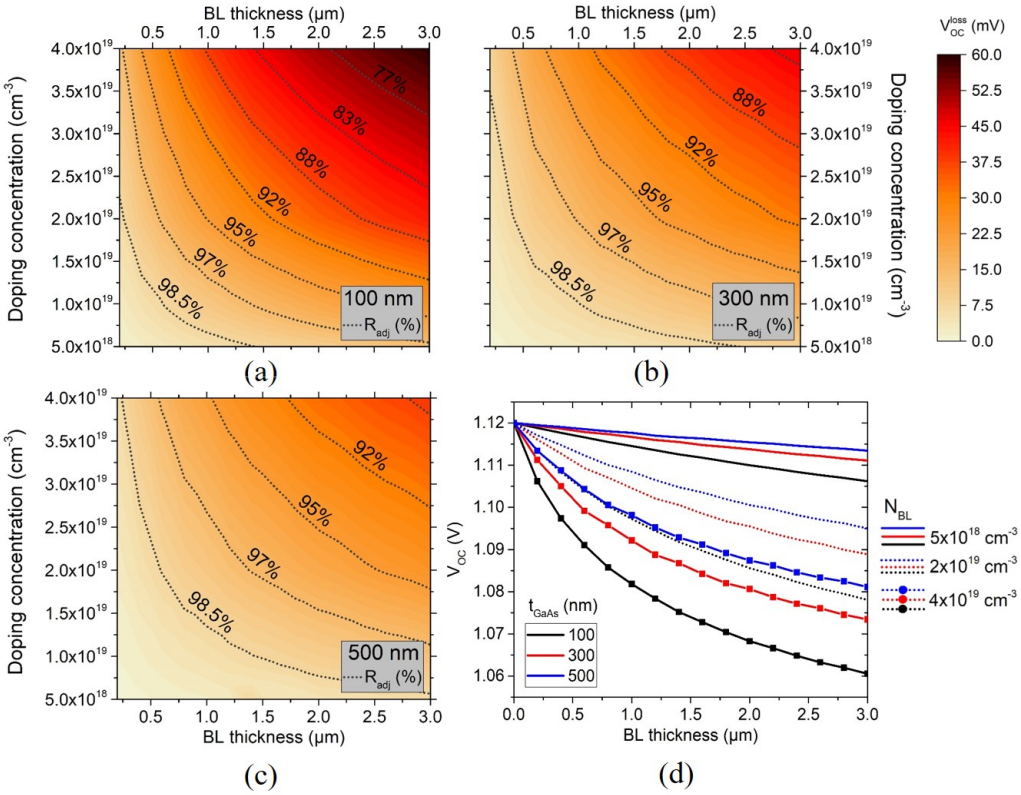

Figure 6.5: Contour maps displaying V_{OC}^{loss} in GaAs solar cells with a planar BSR at various combinations between the back layer doping concentration (N_{BL}) and back layer thickness (t_{BL}). Specifically, plot (a) represents t_{GaAs} = 100 nm, (b) t_{GaAs} = 300 nm, and (c) t_{GaAs} = 500 nm. The contour lines display the R_{adj} corresponding to specific back layer conditions. Plot (d) displays the reduction in V_{OC} from ideal conditions in the GaAs solar cells vs. t_{BL} at three doping concentrations.

When FCA is considered in the back layer, the ideal conditions diminish as R_b reduces. Building on the work of Steiner et al., an adjusted back reflectance (R_{adj}) that now considers the FFCA in the back layer is introduced into the model. The R_{adj} is calculated by,

$$R_{adj} = R_b - FFCA, \tag{6.9}$$

where R_b is set to 1 to represent an ideal reflector and FFCA is determined using the same methods described in Section 6.2.2. For all combinations of N_{BL} and t_{BL}, the R_{adj} determines the loss in V_{OC} using Equations (6.7)-(6.8). In all calculations, the η_{int} is set to unity to model

the GaAs cell operating in the radiative limit. The R_f is set to 96% which considers the escape cone in GaAs [69]. Under the detailed-balance limit for a 3 μm-thick GaAs cell, 1.12 V is used for V_{OC}^{ideal} in Equation 6.7 [64].

The contour maps in Figure 6.5(a)-(c) display the loss in voltage from V_{OC}^{ideal} for GaAs solar cells with t_{GaAs} equal to (a) 100 nm, (b) 300 nm, and (c) 500 nm. The contour lines display the R_{adj} at the specified back layer parameters to represent the reduced reflectance from the ideal R_b. The scale bar represents the voltage loss from V_{OC}^{ideal}, where a thicker and highly doped back layer results in a larger voltage drop from ideal conditions. The voltage loss is less extreme in the 500 nm-thick GaAs solar cell since there are less transmitted photons after the first pass through the absorbing region. For the 100 nm-thick GaAs solar cell, the higher amount of transmitted photons result in a larger voltage loss as more photons are parasitically absorbed by free carriers in the back layer. At the maximum conditions explored for t_{BL} and N_{BL}, the voltage loss approaches 60 mV in the 100 nm-thick design. For each solar cell, the reduction in V_{OC} as the back layer thickness increases at three values of N_{BL} are seen Figure 6.5(d). The decay in voltage is greater in the 100 nm-thick GaAs solar cell as t_{BL} increases from 0 μm to 3 μm. Across all solar cells, the drop in V_{OC} is more prominent at higher doping concentrations. The three ultrathin absorbers require near 100% reflected photons at the band edge for maximum voltage benefits to occur, and the parasitic FFCA in the back layer removes any chance of achieving V_{OC}^{ideal}. In realistic planar BSR designs, achieving a backside reflectance equal to 100% is complex, and experimental results found in literature have shown mirrors performing with a 98-99% peak reflectance [114, 116, 117]. The realistic peak mirror reflectance reduces R_b in Equation 6.9, ultimately dropping R_{adj} even further. Therefore, the expected R_b for specific BSR designs must be accounted for when measuring the adjusted reflectance.

6.3.3 Free-Carrier Absorption in Back Cylindrical Gratings

Besides the planar BSR design, cylindrical gratings consisting of AlGaAs embedded in SiO_2, as shown in Figure 6.1(d), are also considered in this study. This geometry is quite attractive for light trapping in ultrathin GaAs solar cells given the contrast in index of refraction between the two materials, making it suitable to enhance resonance modes and photogenerated current. Recently, Buencuerpo et al. demonstrated strategies to obtain an optically thick, but physically thin 300 nm-thick GaAs solar cell using these materials in a backside nanostructured layer [58]. In experimental designs, some method of backside carrier transport and collection is required and one approach includes using a top-bottom contact design with highly doped AlGaAs cylinders to serve as ohmic pathways, or vias, to the metal mirror. Based on the promising results in Buencuerpo's optimized nanostructured design, three similar designs are investigated for a 300 nm-thick GaAs solar cell operating in the radiative limit while considering different doping concentrations in the AlGaAs cylinders. In this design, the SiO_2 spacer above the Ag mirror reduces parasitic absorption in the mirror, but blocks carrier transport. To explore similar designs to Buencuerpo et al. with maximum reflectance from the backside metal, the SiO_2 spacer remains in these simulations. In realistic design, a top-top contact approach with the TTC layer allows the SiO_2 space to remain intact, but will increase FCA as the TTC requires a high doping concentration and its thickness must scale with increasing solar cell active area to reduce sheet resistance [52]. For researchers interested in using the top-top contact design with light trapping structures, optimization must be made between the thickness and doping concentration in the TTC to minimize FCA while providing sufficient carrier transport.

In the top-bottom contact design, highly doped AlGaAs cylinders with larger radii may provide adequate carrier transport, but also increase FCA as the doped semiconductor coverage

Table 6.1: Cylindrical grating unit cell specifications and J_{SC}^{ideal} without FCA

Grating label	t (nm)	r (nm)	a (nm)	AlGaAs coverage (%)	SiO_2 coverage (%)	J_{SC}^{ideal} (mA/cm^2)
A	200	105	300	38.5	61.5	27.8
B	350	200	520	46.5	53.5	28.7
C	500	250	550	64.9	35.1	27.9

scales up. Grating B refers to the optimized light trapping structure while Grating A and C look at a low and higher AlGaAs coverage, respectively. For each grating, the AlGaAs percent coverage varied across the unit cell by adjusting the radius of the cylinder and changing the pitch, as shown in Figure 6.1(d). Each grating achieves J_{SC}^{ideal} that is 3-4 mA above the planar BSR design (refer to Section 6.3.1). Table 6.1 shows the grating specifications labeled A, B, and C, with percent coverage and J_{SC}^{ideal} where FCA is not considered.

An example of the absorptance in the 300 nm-thick GaAs solar cell with Grating B is shown in Figure 6.6(a) where A_{BL} now represents the absorption in the AlGaAs cylinders within Grating B. Similar trends to the planar BSR design show that higher values of N_{BL} reduces the overall absorption in the GaAs solar cell. At wavelengths below 500 nm, A_{GaAs} at

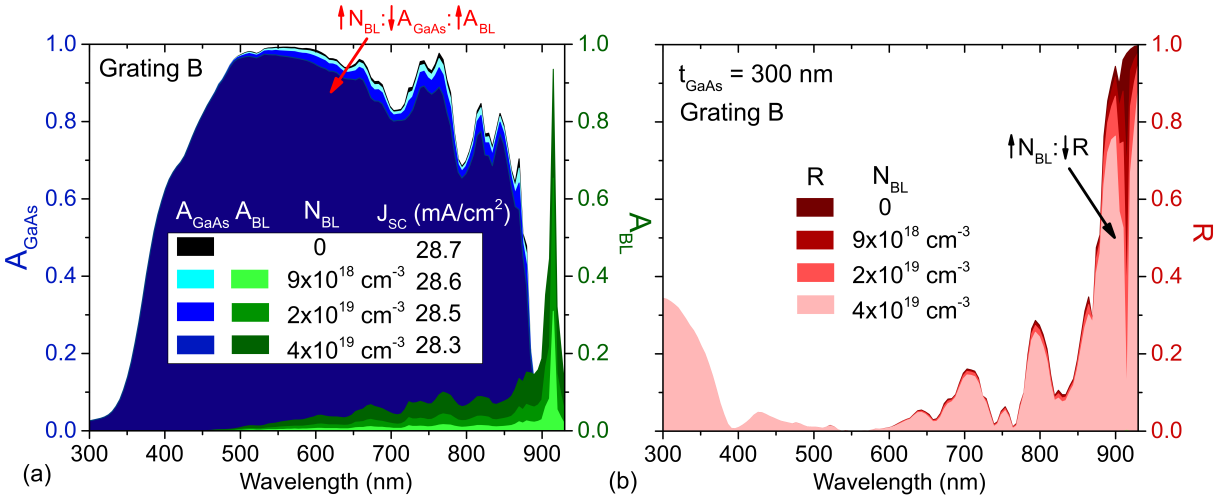

Figure 6.6: The plots above show the change in absorptance in a 300 nm-thick GaAs solar cell (A_{GaAs}) and the in AlGaAs regions of Grating B (A_{BL}) along with the change in backside reflectance (R) as a function of N_{BL}. Specifically, plot (a) shows the reduced A_{GaAs} (blue curves) and the increased A_{BL} (green curves) as N_{BL} increases. Plot (b) shows reduction in R as N_{BL} increases in the AlGaAs regions in Grating B.

the different N_{BL} remains the same. After this point, transmitted photons interact with the nanostructured layer and as the doping concentration increases, the A_{GaAs} decreases. Due to the nature of propagating light in nanostructured designs, the FCA can be higher at specific wavelengths and a dramatic spike in A_{BL} is evident near 900 nm in wavelength, near the band edge of GaAs. Figure 6.6(b) displays the reduction in backside reflectance as the N_{BL} increases in Grating B. At N_{BL} equal to 4x10^{19} cm^{-3}, the backside reflectance dramatically drops below 85% from the peak reflectance in the ideal case.

Each grating is tested in the ideal case where no FCA is present in the AlGaAs regions, and again for AlGaAs at the same doping concentrations modeled with the planar BSR. The ideal J_{SC} values are recorded in Table 6.1. Figure 6.7(a) shows the reduction in J_{SC} from the ideal geometry in each grating design as N_{BL} increases. When FCA is not considered, Grating C outperforms Grating A in terms of J_{SC}. However, once the FCA is included in the model, Grating C significantly reduces the amount of photogenerated current in the GaAs solar cell at N_{BL} greater than 1x10^{19} cm^{-3} due to the increased AlGaAs coverage. The normalized J_{SC} plot in Figure 6.7(b) highlights the significant reduction in photogenerated current as AlGaAs coverage increases across the designs. As a result, Grating A becomes more effective as a light trapping structure than Grating C at doping concentrations greater than 1x10^{19} cm^{-3}.

The same method to determine the reduction in V_{OC} as described in Section 6.3.2 is done for the grating geometries by changing R_{adj} based on the FFCA. As shown in Figure 6.7(c), similar trends to the loss in J_{SC} are observed, and Grating C results in the largest voltage loss. The solar cell efficiency is calculated using AM1.5 conditions with a total irradiance of 100 mW/cm^2, and a realistic fill factor of 84% for GaAs solar cells [108]. Figure 6.7(d) shows the drop in efficiency as N_{BL} increases in each grating geometry. Noticeably, Grating A degrades the least as N_{BL} increases since it has the lowest doped semiconductor coverage.

At low doping concentrations, Grating B remains as the optimized light trapping design. At doping concentrations greater than 2.7x10^{19} cm^{-3}, Grating A outperforms Gratings B and C due to its steady decline in efficiency, allowing it to become the favored light trapping design. At 4x10^{19} cm^{-3}, Grating B and C lose an absolute efficiency of 1.8% (6.9% relative) and 2.9% (11.5% relative), respectively, while grating A losses an absolute efficiency less than 0.6% (2.2% relative), making it the better light trapping structure at higher doping concentrations. This study suggests that when designing nanostructured geometries for light trapping, the doped semiconductor regions should lean towards smaller unit cell dimensions to reduce the absorption by free carriers. While increased doped semiconductor coverage leads to improved carrier transport in a top-bottom contact design, the optical benefits of the light trapping structure will reduce at high doping concentrations. Therefore, an optimal point between sufficient carrier transport and effective light trapping must be found in device-specific designs as research aims to improve the efficiency in ultrathin III-V solar cells.

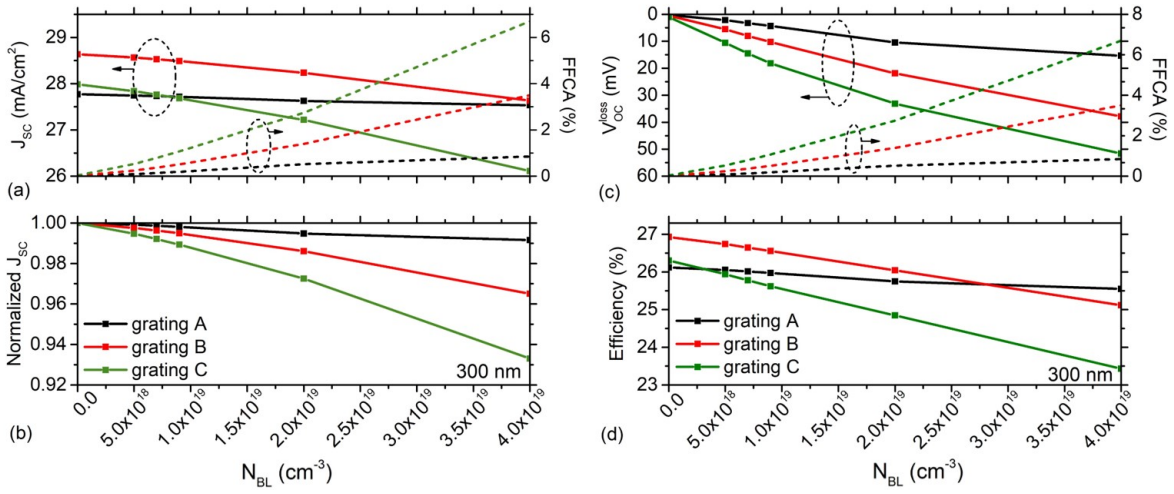

Figure 6.7: Plot (a) displays the reduction in J_{SC} and increase in FFCA and plot (b) displays the normalized J_{SC} as N_{BL} increases in the AlGaAs regions of the three gratings behind a 300 nm-thick GaAs solar cell. Plot (c) displays the voltage loss from $V_{OC}{}^{ideal}$ with associated FFCA and plot (d) displays the decrease in efficiency as N_{BL} increases.

6.4 Chapter Summary

This research focuses on the optical modeling of FCA in non-active layers behind ultrathin GaAs solar cells with planar and nanostructured grating designs. The results show that FCA increases as the thickness and doping concentration of the back layer increase. The FCA is more noticeable as the GaAs absorber thickness reduces since more transmitted photons after the first pass interact with free carriers. The FCA optical loss reduces the light trapping benefits in terms of reduced J_{SC} and V_{OC} from ideal conditions, and in return, reduces the device efficiency. When designing nanostructured gratings, the doped semiconductor region must be optimized to balance minimal FCA and sufficient carrier transport to external electrodes. Recognizing the potential optical loss by FCA in non-active layers will help set guidelines for careful material selection when designing ultrathin III-V solar cells with light trapping structures and will support these devices in reaching their maximum efficiency based on the detailed-balance limit.

Chapter 7

Thin-Film Dual-Junction Solar Cells with Light Management

7.1 Introduction

This chapter involves the development of inverted DJ solar cells with novel texturing approaches. The first texturing approach uses reactive-ion etching (RIE) to damage the last non-active epitaxial layer physically. When a wide E_g material is regrown on its surface, the epi material inherently grows roughened. The second texturing approach renders a promising new technique to texture the last epitaxial layer grown in the MOVPE reactor directly after solar cell growth. The RIE and in situ etch are integrated into the inverted DJ solar cells. The DJ design is optimized first by focusing on the bottom GaAs subcell, and design changes to the FSF and PN junction are made to improve the device's photon absorption and electrical performance, respectively. The device results indicate that the in situ BSR can improve base collection in the thinned bottom subcell and achieve 100% diffuse scattering near 700 nm in wavelength. In addition, the base collection in the 800 nm-thick GaAs subcell matches the current output in the control device, indicating a 4-fold increase in the OPL. Finally, this chapter discusses future work for the inverted DJ design, growth, and fabrication, to achieve highly

efficient and thin-film solar cells with the RIE and in situ textured BSRs.

7.2 Optimized GaAs Subcell Design

Modeling the FCA in non-active textured layers, as described in Chapter 6, guides the textured layer design for the inverted DJ solar cell. The bottom GaAs subcell is also optimized to target higher voltage output and maintain photon absorption as expected in an optically thick design. This goal is accomplished by changing the material selection and growth and utilizing the heterojunction design. First, the dopants used in the PN junction were carefully considered. The p-type Zn dopant used in the GaAs base has a high diffusion coefficient, so during epitaxial growth, it diffuses outside of the base region and creates a gradual doping profile rather than an abrupt profile at the PN junction interface. This reduced doping concentration will limit the voltage output at open-circuit conditions and was previously determined to be less than 1.0 V. Another p-type dopant source available is carbon using the precursor carbon tetrachloride (CCl_4). CCl_4 has a significantly lower diffusion coefficient than Zn and allows an abrupt profile to form at the PN junction [126]. Before experimenting with a solar cell, numerous calibrations were performed to understand the growth rate, surface morphology, and carbon incorporation in GaAs. These test structures were characterized through microscopic imaging and Hall measurements. Once the growth conditions were established to target a doping concentration of $5x10^{16}$ cm^{-3}, different upright GaAs solar cells were grown and fabricated to analyze the improved device performance. Different front surface windows were investigated with the switch to using carbon in the p-type base to improve front surface collection. The devices grown and tested are shown in Figure 7.1(a)-(c).

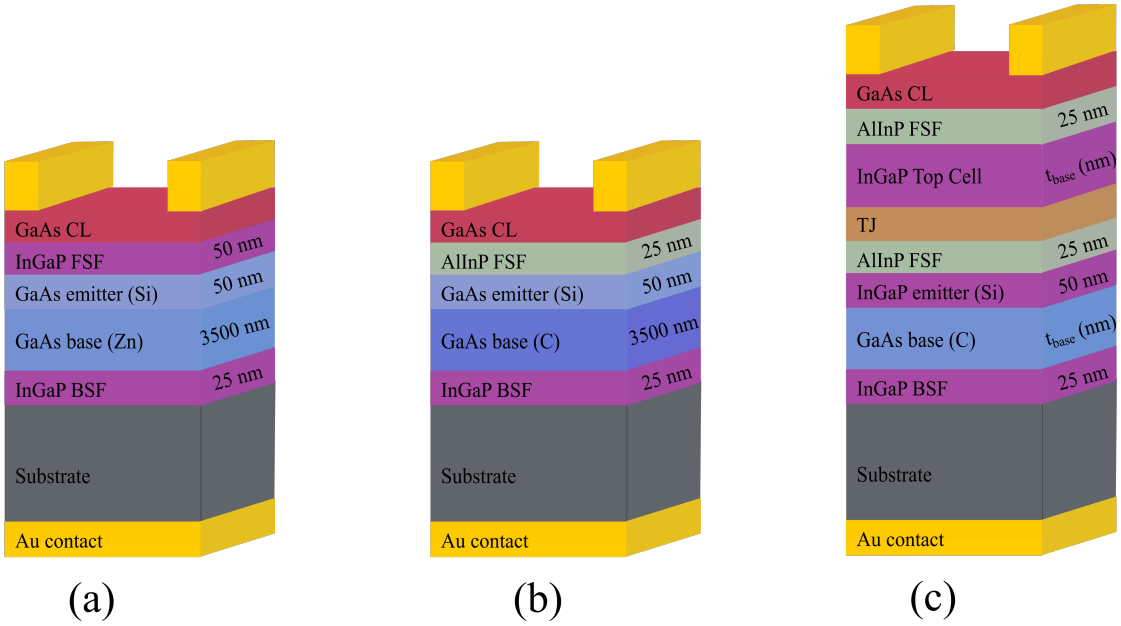

Figure 7.1: Diagrams of the optimized GaAs solar cells with (a) InGaP FSF and Zn base, (b) AlInP FSF and C base, and (c) AlInP FSF and a heterojunction with an InGaP emitter and GaAs:C base.

The electrical results for the GaAs solar cells with different front surface windows and base dopants are shown in Figure 7.2(a)-(b) where plot (a) shows the illuminated J-V curves and plot (b) shows the EQE curves. In the J-V curves, nearly 5 mA of current is recovered replacing the InGaP window with a wider E_g semiconductor. Also, the V_{OC} increases over 20 mV, and the *FF* increases by an absolute 5%. These figures of merit lead to an absolute 4% increase in efficiency. Plot (b) displays the EQE where the collection at the front of the device with the AlInP FSF is significantly higher.

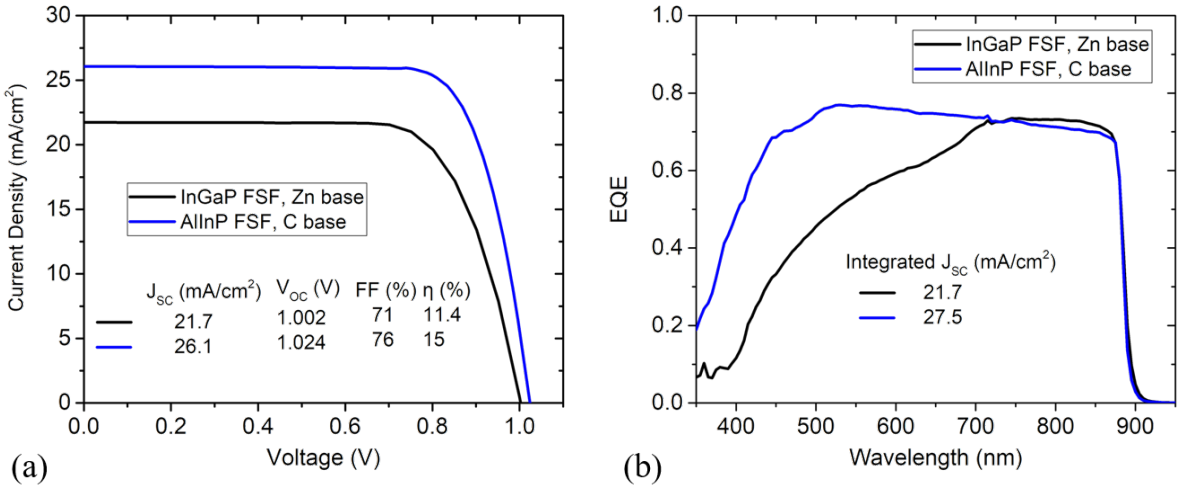

Figure 7.2: Diagrams of the optimized GaAs solar cells (without an ARC) to investigate impacts using carbon as the p-type dopant in the base and different front surface windows.

Next, the homojunction was replaced with a heterojunction design where two semiconductors with dissimilar E_g are used to form the PN junction. The emitter was changed to InGaP, which has a wider E_g than GaAs and promoted an increase in V_{OC} from the bottom subcell. Changing the FSF and the p-type dopant concentration in the GaAs base resulted in significant improvement in J_{SC} and V_{OC} for the single-junction GaAs solar cell without degrading fill factor.

7.3 Dual-Junction Solar Cell Design

The DJ design includes the bottom heterojunction GaAs subcell described above and a standard top InGaP subcell. The InGaP top subcell is based on previous research and was used for the solar cell structures in this work. The diagram of the design is shown in Figure 7.1(c), and the growth design is shown in Table 7.1 where layers marked with "top" refer to the top InGaP subcell and layers marked with "bottom" refer to the bottom GaAs subcell. The

Table 7.1: Growth design for the upright DJ solar cell.

Layer	Material	Thickness (nm)	Doping (cm^{-3})
Top Contact	n-GaAs	50	$2x10^{19}$ (Te)
Top Contact	n-GaAs	100	$5x10^{18}$ (Si)
Top Window	n-AlInP	20	$8x10^{17}$ (Si)
Top Emitter	n-InGaP	70	$2x10^{18}$ (Si)
Top Intrinsic	InGaP	10	UID
Top Base	p-InGaP	390	$5x10^{16}$ (Zn)
Top Window	p-AlGaInP	100	$2x10^{18}$ (Zn)
Tunnel	p-$Al_{0.3}Ga_{0.7}As$	10	$2x10^{19}$ (C)
Tunnel	n-GaAs	10	$2x10^{19}$ (Te)
Bottom Window	n-AlInP	25	$8x10^{17}$ (Si)
Bottom Emitter	n-InGaP	50	$2x10^{18}$ (Si)
Bottom Intrinsic	GaAs	200	UID
Bottom Base	p-GaAs	3500	$1x10^{17}$ (C)
Bottom Window	p-InGaP	50	$2x10^{18}$ (Zn)
Substrate	GaAs	350 μm	$5x10^{18}$ (Zn)

averaged J-V measurement figures of merit across twelve samples for this device are reported in Table 7.2. The V_{OC} is the summation of the top and bottom subcells and leads to AM0 efficiency equal to 18.3%. Additionally, the current output is near 12 mA/cm^2 due to the dual-junction design where current is limited by the subcell producing the smaller amount of current. This current output is reasonable for a DJ design and is the new target to match in the thin-film bottom heterojunction solar cells, indicating increased photon path length from the textured BSRs.

The solar cells shown above are all upright and attached to the host substrate. With textured BSRs, the substrate is removed, and the solar cell is grown inverted, as discussed in Chapter 4. Figure 7.3(a) shows the inverted growth of the DJ solar cell, and Figure 7.3(b) shows the completed DJ solar cell detached from the substrate and with the textured BSR. Table 7.3 displays the layer structure for the inverted DJ solar cell, which is the same as the upright device other than the switch in the growth sequence. The following section discusses two new light trapping structures and their application in the DJ solar cell.

Table 7.2: Figures of Merit for the original and optimized DJ solar cell

Device	J_{SC} (mA·cm^{-2})	V_{OC} (V)	FF (%)	η (%)
DJ solar cell	12.13 ± 0.33	2.352 ± 0.011	87.7 ± 0.9	18.3 ± 0.4

Table 7.3: Growth design for the inverted thin-film DJ solar cell.

Layer	Material	Thickness (nm)	Doping (cm^{-3})
TTC	p-$Al_{0.3}Ga_{0.7}As$	1500	2x10^{19} (C)
Bottom Window	p-InGaP	50	2x10^{18} (Zn)
Bottom Base	p-GaAs	390-3500	1x10^{17} (C)
Bottom Intrinsic	GaAs	100	UID
Bottom Emitter	n-InGaP	50	2x10^{18} (Si)
Bottom Window	n-AlInP	25	8x10^{17} (Si)
Tunnel	n-GaAs	10	2x10^{19} (Te)
Tunnel	p-$Al_{0.3}Ga_{0.7}As$	10	2x10^{19} (C)
Top Window	p-AlGaInP	100	2x10^{18} (Zn)
Top Base	p-InGaP	390	5x10^{16} (Zn)
Top Intrinsic	InGaP	10	UID
Top Emitter	n-InGaP	70	2x10^{18} (Si)
Top Window	n-AlInP	20	8x10^{17} (Si)
Top Contact	n-GaAs	100	5x10^{18} (Si)
Top Contact	n-GaAs	50	2x10^{19} (Te)
Barrier	n-GaAs	10	3x10^{18} (Si)
Etch Stop	n-InGaP	150	3x10^{18} (Si)
Substrate	GaAs	350 μm	UID

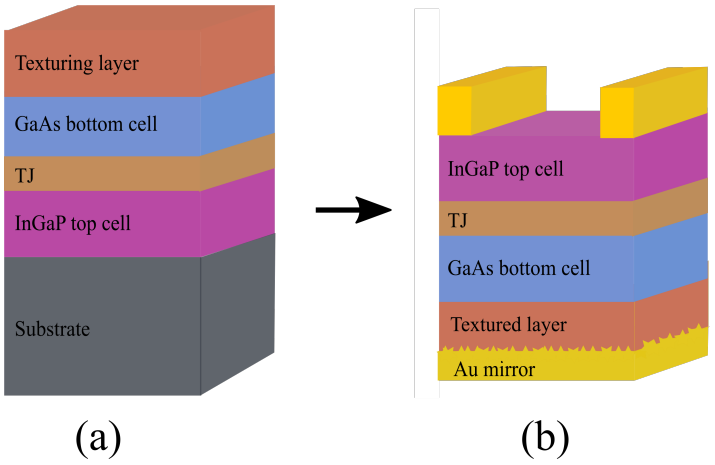

Figure 7.3: Diagram of (a) inverted DJ after growth and (b) completed DJ solar cell with textured layer and Au mirror.

7.4 Texture Development

7.4.1 Surface Treatment using Reactive-Ion Etching

The previous solution-based textures in Chapter 5 display promising results using the mask-less etch and I-MacEtch to achieve three-dimensional structures and recover photogenerated current in the thin-film GaAs solar cell. While these approaches show promising results as textured BSRs, new texturing approaches that do not require additional time associated with lab bench processing were investigated. The RIE surface treatment involves exposing the last non-active epitaxial layer to a fluorine-based plasma to damage the crystal without removing the III-V material. The carbon tetrafluoride (CF_4) was generated with the inductively-coupled plasma (ICP) power and directed towards the III-V solar cell at a controlled forward bias (RF). These conditions allowed the ions from the plasma to bombard the top non-active III-V layer without etching the material. The process is shown in Figure 7.4(a)-(b).

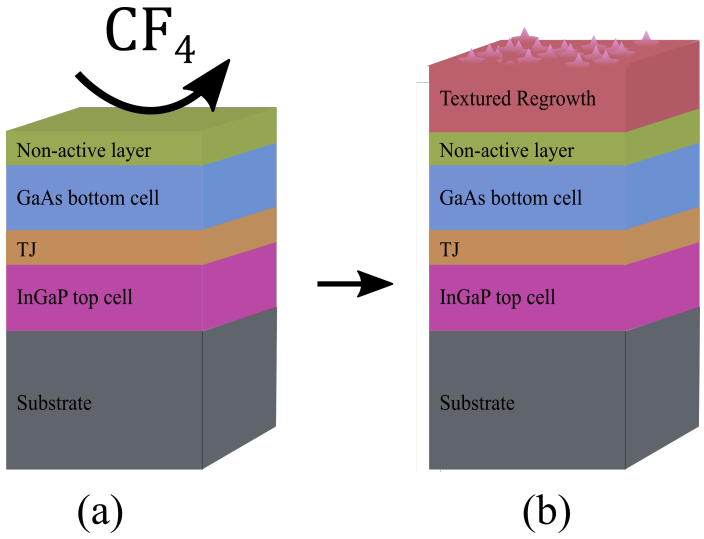

Figure 7.4: Flow sequence using the RIE surface treatment for epitaxial texturing where (a) presents the RIE treatment using ICP-RIE and (b) presents the regrowth of a wide bandgap $Al_{0.7}Ga_{0.3}As$ layer once the RIE-treated solar cell is back in the MOVPE reactor.

This treatment has a wide processing window where conditions such as the RF and ICP power, chamber pressure, etch duration, and gases used for plasma generation. Adjusting these conditions and testing the electrical performance between the overgrown textured semiconductor and the metal contacts can determine a target range between roughened textured surface and effective electrical properties, which otherwise are degraded at the textured semiconductor/metal interface. The RIE process in this work used CF_4 at 50 sccm, an ICP power equal to 100 W, RF power equal to 50 W, and a chamber pressure of 35 mTorr. After the RIE treatment, the wafers were placed back into the MOVPE reactor to overgrow the wide E_g p-type $Al_{0.7}Ga_{0.3}As$ layer. For the DJ solar cell with the thinned bottom GaAs subcell, high Al composition is required for unabsorbed photons to interact with the textured region rather than parasitically absorb, as discussed in Chapter 3. The deposited epitaxial material grew rough as the crystal surface was no longer atomically smooth.

Figure 7.5(a)-(b) displays the RIE-roughened $Al_{0.7}Ga_{0.3}As$ layer through (a) AFM and (b) SEM. The final AlGaAs:C layer was nearly 500 nm thick, and Figure 7.5(a) shows the increased surface roughness above 60 nm due to the RIE process and roughened surface morphology. The surface is more than six times rougher than the pre-textured solar cell.

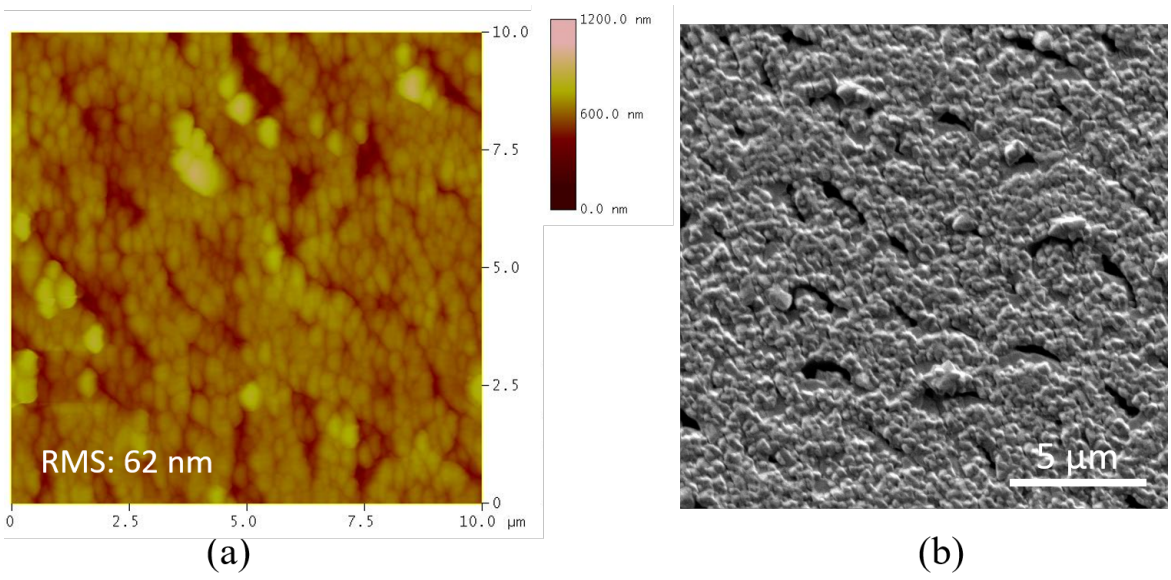

Figure 7.5: Surface characterization on RIE treated and regrowth of $Al_{0.7}Ga_{0.3}As$ showing (a) 10x10 μm AFM scan and (b) 10 μm top-down SEM scan.

The haze in reflectance measurements, as described in Chapter 5, are performed on the RIE treated $Al_{0.7}Ga_{0.3}As$ structures. The structures use InGaP as a transparent material, which is also suitable for substrate removal. Substrate removal is required on the test structures to remove the parasitic absorption in the GaAs substrate. After the RIE treatment and regrowth, the Au mirror was evaporated on the semiconductor, and the structure was bonded to a silicon handle for substrate removal. An ARC consisting of ZnS and MgF_2 was deposited to suppress front surface reflection.

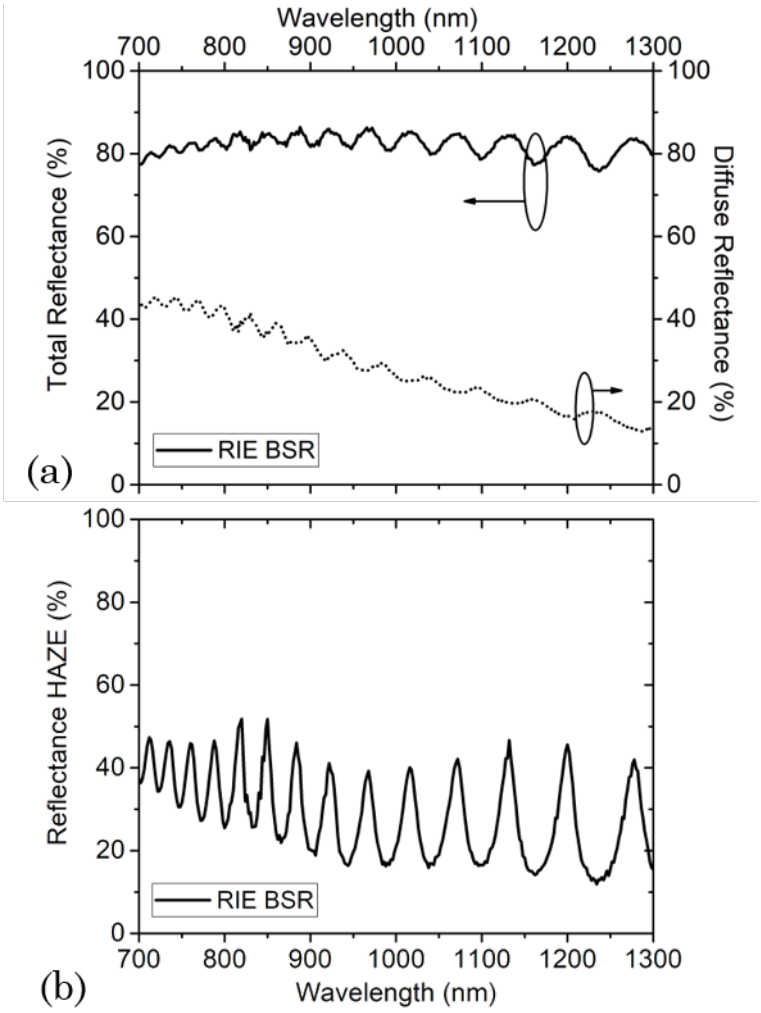

Figure 7.6: Reflectance measurements on the RIE BSR with and without a SiO_2 interlayer, namely the (a) total and diffuse reflectance and (b) haze in reflectance.

Figure 7.6(a)-(b) shows the total and diffuse reflectance measurements and haze in reflectance. In Figure 7.6(a), the RIE texture increases the diffuse reflectance up to 40% for wavelengths near the GaAs band edge at 870 nm. For wavelengths beyond 900 nm, the diffuse reflectance drops by 20%. This drop in diffuse scattering is especially noticeable near the InGaAs band edge at 1240 nm in wavelength. The reason is mainly because there is minimal interaction between the longer wavelengths and the textured surface. Surface dimensions on

the same order as the wavelength are required to promote angular photon scattering. Figure 7.6(b) shows the haze in reflectance for the RIE-textured BSR. For this particular texture, the haze is limited since the diffuse reflectance is below 50%. The surface roughness and haze in reflectance can be improved by changing the process conditions during the RIE step as well as by changing the growth conditions of the regrowth material.

7.4.2 In Situ Etching using Halomethane Compounds

In III-V semiconductors, halomethane compounds are mainly used as a p-type dopant rather than a tool for semiconductor texturing. Throughout literature, CCl_4 has been known to reduce the growth rate of III-V materials as the Cl atoms replace surface sites available for group III elements, such as Al, Ga, and In, to bond with [127–129]. This research investigates a method of texturing III-V semiconductors using halomethane compounds by MOVPE in a semiconductor light absorbing device structure for improved photon absorption. The texturing method is described using CCl_4 but can be achieved using other halomethane gas sources such as carbon tetrabromide (CBr_4). The texturing method does not rely on a pre-existing surface texture or roughness for textured epitaxial overgrowth. Instead, the in situ texturing method relies on the etching mechanism of group III elements (such as Al, Ga, and In).

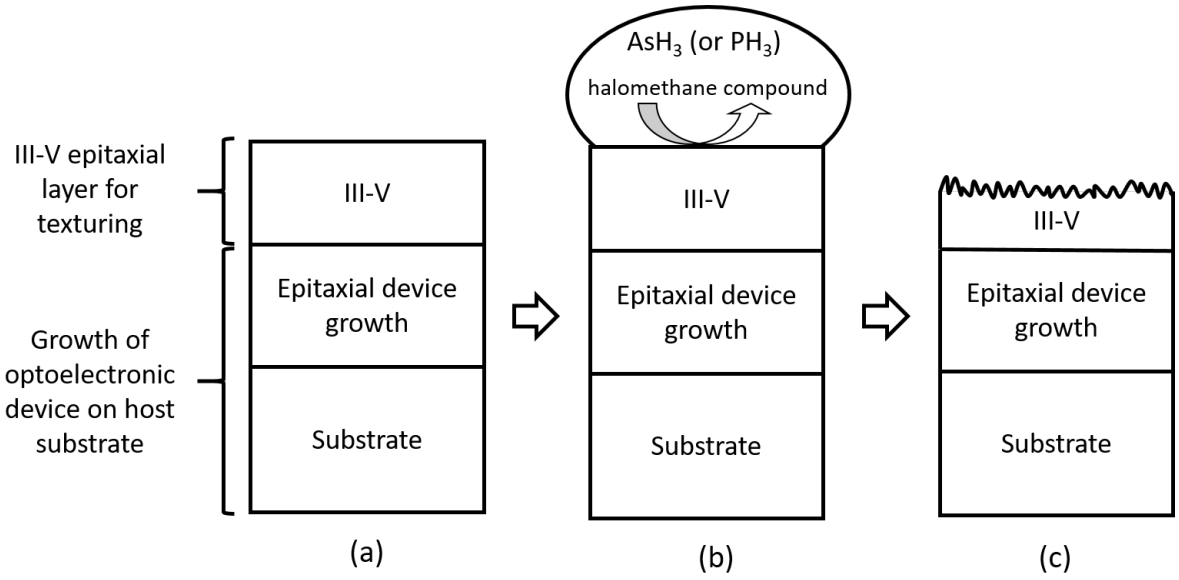

Figure 7.7: Process flow of in situ etching where (a) displays the grow of the last layer for texturing, (b) displays the etch-back and (c) displays the final structure once the etch-back is complete.

Figure 7.7(a)-(c) displays the in situ texturing method where (a) presents the first step growing a transparent III-V material for texturing. Figure 7.7(b) displays the etch-back where during this process, thermally decomposed chlorine radicals from the CCl_4 gas react with the group III elements in the top-most layer and creates volatile byproducts released from the semiconductor surface. The texturing method is achieved by flowing CCl_4 with an overpressure consisting of arsine (AsH_3) or phosphine (PH_3), depending on the group V element in the top-most epitaxial layer to exploit volatile Cl-III byproducts [126]. This step continues until the desired thickness and surface roughness are met, as shown in Figure 7.7(c). The texturing method can be applied at the surface, interfaces, or a combination thereof during the epitaxial growth of the III-V device structure. The etch-back is monitored with an in situ metrology system where etch rates are determined according to the epitaxial growth parameters, including

reactor pressure, molar flow, V/III ratio, and sample temperature. In return, the amount of material etched away is controlled to target specific surface roughness of the pseudo-random surface morphology and layer thickness.

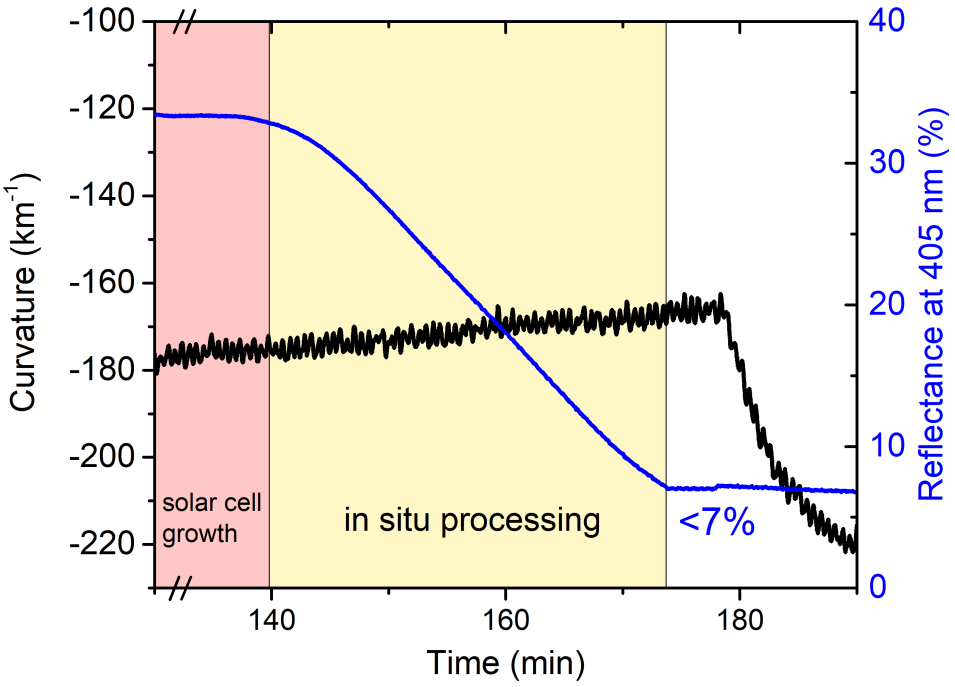

Figure 7.8: epiTT during the in situ etching of 70% AlGaAs.

This process was conducted on multiple samples to target a slow etch rate. The in situ texturing method in $Al_{0.7}Ga_{0.3}As$ requires an AsH_3 overpressure with a partial pressure equal to 0.826 mbar. The reactor pressure was 100 mbar, and the AsH_3 and H_2 carrier gas molar flows are $1.02x10^{-3}$ mol/min and $1.22x10^{-1}$ mol/min, respectively. An internal metrology system to monitor the etch rate and reduction in surface reflectance is beneficial for calibrating the texturing process for specific III-V materials. Monitoring the drop in surface reflectance during the etch-back step seen in Figure 7.8 indicates increased surface roughness and photon scattering. Promisingly, the surface reflectance drops below 7% at the end of the growth. The

curvature also shows a gradual evolution of stress during the etch-back. This step continues to meet the desired thickness of the transparent textured layer. Finally, the AFM shows a surface roughness of 126 nm, over 100 times greater than the pre-textured semiconductor with surface roughness less than 10 nm. The SEM in Figure 7.9(b) displays the three-dimensional pyramidal structure across the AlGaAs layer.

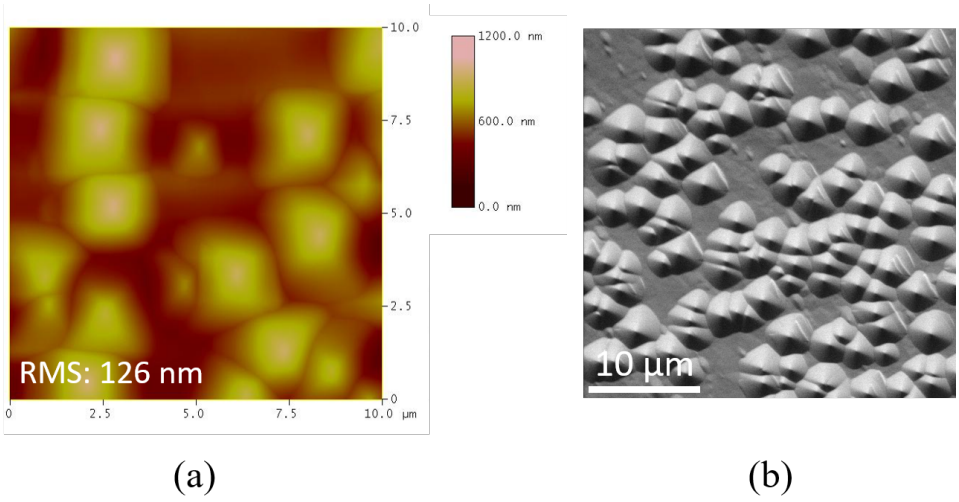

Figure 7.9: Surface characterization of the in situ textured AlGaAs showing (a) AFM and (b) top-down SEM.

Figure 7.9(a)-(b) shows the surface characterization on the in situ textured $Al_{0.7}Ga_{0.3}As$ using (a) AFM and (b) top-down SEM. The height of the pyramidal structures extracted from the AFM is near 1200 nm, and the surface roughness is greater than 120 nm. This surface roughness is the greatest achieved across all textures developed in this research. The top-down SEM in plot (b) shows the pyramidal structures, and the sides were determined to be the (111) crystal planes. The sides of the pyramids rise at an angle much greater than 8°, making this texture suitable to promote TIR after the second and third pass through the solar cell, as discussed in Chapter 3.

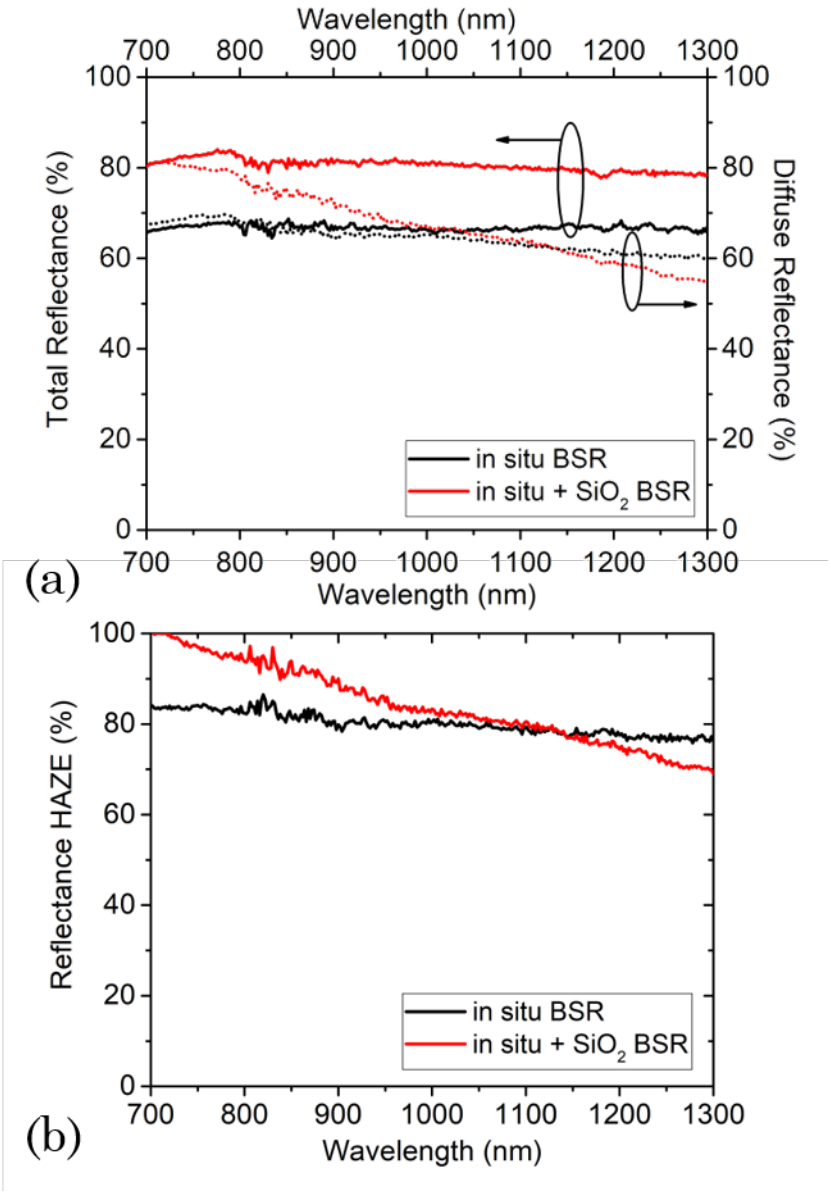

Figure 7.10: Reflectance measurements on the in situ BSR with and without a SiO_2 interlayer, namely (a) total and diffuse reflectance and (b) haze in reflectance.

Haze in reflectance measurements were performed for the in situ textured BSR. One of the test structures includes a 500 nm-thick TIR layer of SiO_2, which is deposited before the Au mirror. The purpose of the TIR interlayer to improve reflection at the textured interface is discussed in detail in Chapter 3 and Chapter 5. Figure 7.10(a) displays the total and diffuse

reflectance from the in situ BSR with and without the SiO_2 interlayer. The addition of the SiO_2 interlayer increases the total reflectance by about 10%, and the diffuse reflectance increases at wavelengths between 800 nm and 950 nm. Interestingly, the SiO_2 structure drops in diffuse reflectance at wavelengths longer than 1000 nm. This reduction in diffuse reflectance may be due to the thickness of the TIR layer, which may need to increase to remove frustrated TIR associated with the longer wavelengths [72]. Figure 7.10(b) shows the haze in reflectance for both in situ BSR structures. Promisingly, the in situ BSR with the SiO_2 interlayer achieves haze in reflectance equal to 100% at 700 nm in wavelength. This result indicates complete diffuse scattering at this wavelength since it equals the total reflectance. Since these pyramidal structures are wavelength specific according to their base and height dimensions, the diffuse reflectance drops as the wavelength increases. The haze in reflectance also decreases to 75% at wavelengths beyond 1200 nm. Overall, both in situ test structures achieve the greatest haze in reflectance out of the different textures developed in this research, indicating a high degree of angular photon scattering and effective at improving photon absorption in sub-μm thick solar cells.

7.5 Design, Growth and Fabrication

The DJ solar cells were grown following the same growth conditions as discussed in Chapter 4. The upright control DJ solar cell consists of the optically thick top and bottom subcells to ensure total photon absorption. In the control device, the bottom GaAs subcell is 3.6 μm thick. In the inverted thin-film designs, the bottom GaAs subcell base thickness equals 800 nm and is nearly four times thinner than the optically thick design. These devices were designed without including a low-index TIR layer to confirm if beneficial light trapping can occur without the additional fabrication steps associated with the low-index layer. For this reason, a top-bottom

contact design was used. The first step for the thin-film solar cells was to develop the BSR using the RIE and in situ texturing approaches discussed above. Then, the backside Au mirror, which also serves as the contact, was evaporated. Substrate removal and fabrication were performed using the processes discussed in Chapter 4.

7.6 Electrical Device Results and Discussion

Illuminated J-V measurements were taken across the various inverted DJ solar cells and compared to the upright DJ solar cell design. Figure 7.11 displays the illuminated J-V curves from the solar cells. First, the inverted DJ solar cells (blue) do not perform at the same level as the upright DJ solar cells design (red). Specifically, the loss in V_{OC} by nearly 300 mV provides evidence of material degradation in the active region of the solar cell. The J_{SC} is limited to approximately 9 mA/cm^2. Since this device is optically thick, the J_{SC} should be near 12.5 mA/cm^2. The fact that it is nearly 3.5 mA lower than the upright DJ solar cell validates material degradation most likely due to the inverted growth. As discussed previously, the inverted growth and removing the substrate from the epitaxial layers brings forward complex processing challenges. One main issue is the growth sequence between P and As-based layers, which is opposite between the upright and the inverted growths [130–132]. The growth sequence was not optimized in this research and resulted in negative impacts on the device performance. Therefore, progress on the device performance depends on future work to optimize the DJ inverted growth.

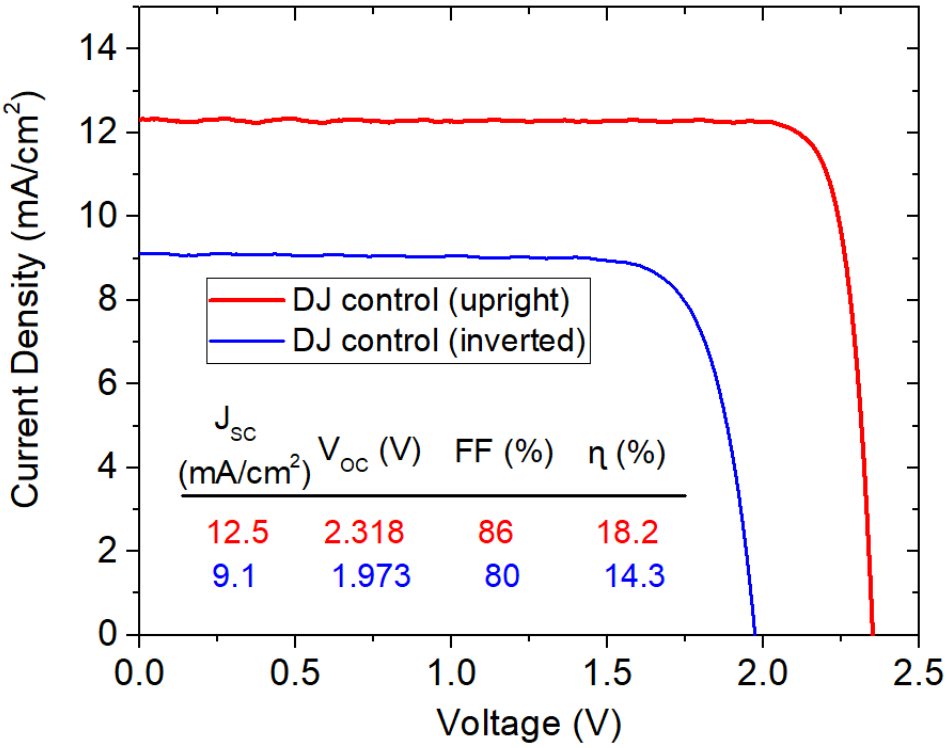

Figure 7.11: Illuminated J-V measurements comparing the optically thick upright and inverted DJ solar cells.

While it is important to optimize the inverted growth of the control sample in future work, the textured BSRs were integrated into similar structures as the inverted control to provide a glimpse into the potential light trapping benefits using the current inverted DJ solar cell design. Therefore, EQE measurements are compared between the inverted DJ solar cell and the inverted thin-film solar cells with the RIE and in situ BSRs. Figure 7.12 displays the EQE measurements on the inverted control and BSR devices. The three BSR devices include a flat, RIE, and in situ texture. These three devices have an active region thickness of 800 nm, which is over 4 times thinner than the optically thick design. The EQE in the top InGaP subcell varies across the different devices. Promisingly, the bottom GaAs subcell with the in situ BSR has the same base collection as the control. This result indicates complete photon collection in

the 800 nm thick base, highlighting that the increased diffuse reflectance from the in situ BSR can improve photon absorption and the photon path length near 4 passes provided it is four times thinner than the control.

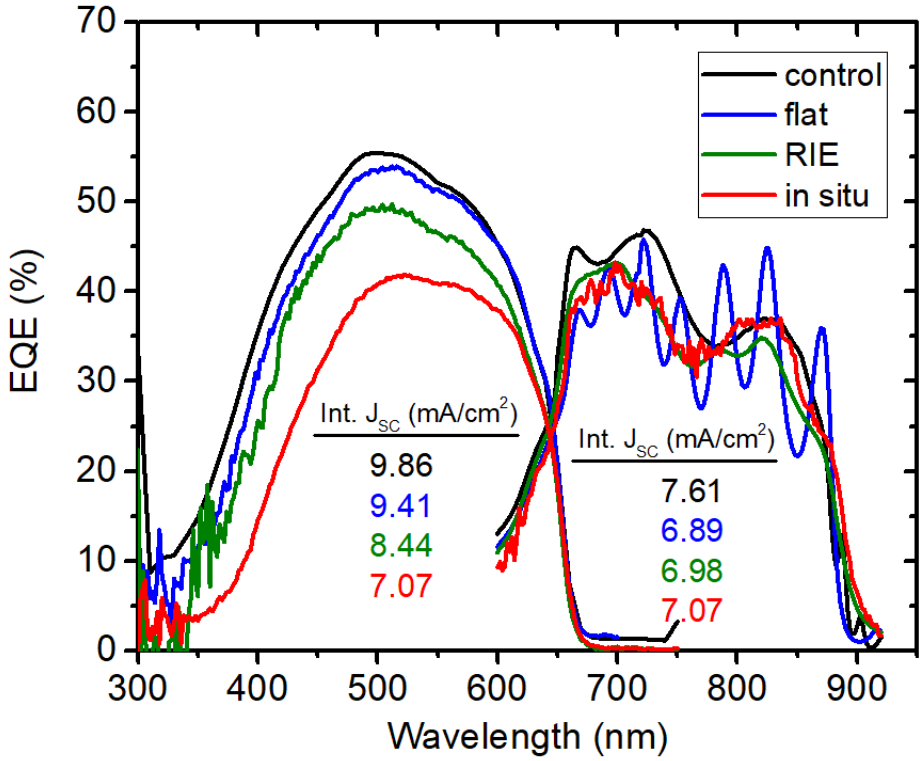

Figure 7.12: EQE measurements on the control DJ solar cell and the inverted DJ solar cell with various BSRs.

Figure 7.13 shows the EQE on the bottom GaAs subcell. The integrated J_{SC} under the curve describes the base region collection between 750 nm to 920 nm in wavelength. The FP fringes from the flat BSR start in the emitter range near 650 nm in wavelength. These fringes become more pronounced towards the band edge, highlighting the optical performance of the flat mirror. Designing the textured layers to be less than 500 nm in thickness with p-type doping concentration less than 1x10^{19} cm^{-3} confirms that the absorption by free carriers is negligible and does not affect the back reflectance. The RIE BSR achieves a slightly lower current output

than the planar mirror, indicating that the surface treatment must be optimized to promote increased surface roughness. This low current output aligns with the low degree of haze in reflectance for this specific RIE-textured BSR.

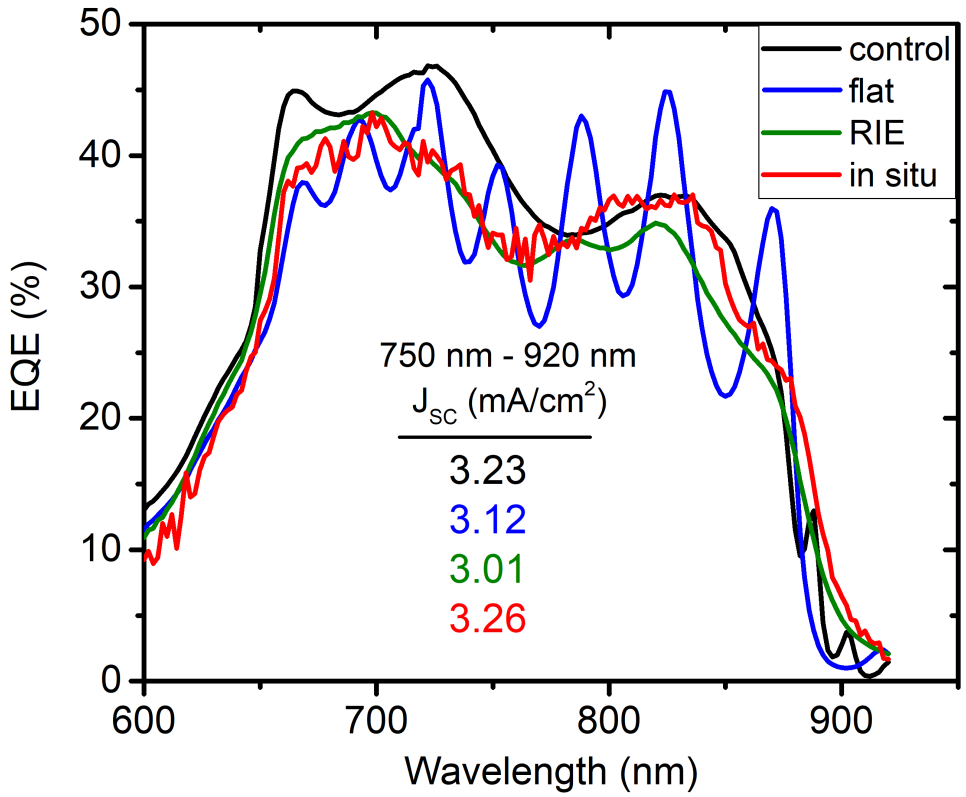

Figure 7.13: EQE measurements on the bottom GaAs subcells with various BSRs.

The in situ BSR performs the best out of the different light trapping geometries and shows a higher base current collection than the control. This result is due to interface enhancement, also known as Urbach tailing effects, where absorption occurs past the band edge of the GaAs solar cell. The thin-film solar cell with the in situ BSR achieves numerous passes, indicating multiple chances for interface enhancement. Additionally, the current output in the in situ BSR design indicates a path length enhancement greater than 4 passes. The collapsed FP cavity, increase

in RMS roughness from AFM, and haze in reflectance near unity all support the enhancement base current collection from the in situ texture.

7.7 Chapter Summary

This chapter presents promising results using the RIE surface treatment and the in situ texturing processes for BSR development in thin-film DJ solar cells. The in situ texturing method can produce highly diffuse light scattering surfaces without adding multiple processing steps, applicable for a wide range of optoelectronic device applications that require textured interfaces or surfaces for angular photon scattering. The pyramidal structures' dimensions are similar to the wavelengths near the GaAs band edge, making the diffuse reflectance greater than 80% in the GaAs base wavelength absorbing region. The haze in reflectance for the in situ texture is near unity at 700 nm in wavelength and signifies complete diffuse scattering and dampened specular reflectance of incident photons interacting with the BSR. Additionally, the surface roughness from the in situ textured AlGaAs extracted from AFM is above 120 nm, which is the best result from the textured semiconductors developed in this work. The three-dimensional pyramids are much like the Si-based KOH texture discussed in Chapter 3, are a favored feature to achieve high OPL, and can be integrated into various thin-film MJSC designs. While the inverted growth and fabrication require optimization to produce highly efficient solar cells, the EQE measurements display enough information to support using the RIE and in situ textured BSRs in future multijunction solar cells. Specifically, the in situ BSR achieves a higher current output in the base region than the optically thick baseline. The RIE texture has room for improvement as many variables in the ICP-RIE processing and the epitaxial regrowth can induce a higher degree of surface roughening. These textured BSRs are further investigated in a thin-film IMM design, as discussed in Chapter 8.

Chapter 8

Thin-Film Inverted Metamorphic Solar Cells with Light Management

8.1 Introduction

This chapter involves the integration of the RIE and in situ BSRs in thin-film IMM solar cells. The first approach was to demonstrate improved J_{SC} in SJ InGaAs solar cells experimentally compared to the thin-film geometries with no light trapping. The surface roughness extracted from AFM shows increased diffuse scattering properties for the textured layers compared to the planar geometry. These devices maintain V_{OC} and improve J_{SC}, which merits further characterization of the triple-junction IMM design with the RIE and in situ BSRs to study light trapping properties and radiation tolerance experimentally. Thin-film IMM devices with base thicknesses of 600 nm and 1200 nm were compared to the control device with base thickness equal to 3000 nm. The highlighted results show that all BSR devices improve photon absorption and current output compared to the thin-film geometries with no light management or a planar BSR. The EQE shows base and band edge photon collection within 1 mA of the control, which suggests considerable path length enhancement from sufficient light trapping in

the thin-film devices. By using a well-established damage displacement dose model, the remaining factor provided trends in the reduced current and efficiency as these devices become damaged from 1 MeV electrons. The trends show that, for both current and efficiency, the baseline device has the largest reduction in performance. Three of the four BSR devices surpass the IMM control in terms of J_{SC}. Specifically, the 1300 nm + RIE BSR device outperforms the control at the lowest electron fluence equal to 1.5x10^{14} e^{-}/cm^{2}, the 700 nm + in situ BSR surpasses the control at 6x10^{14} e^{-}/cm^{2}, and the 1300 nm + in situ BSR device surpasses the control near 9x10^{14} e^{-}/cm^{2}. In terms of mass-specific power, since the 700 nm-thick devices are much lighter in weight, their mass-dependent efficiency surpasses the control beyond an electron fluence of 4x10^{14} e^{-}/cm^{2}. As well, at 2x10^{15} e^{-}/cm^{2}, the 700 nm + in situ device achieves a mass-specific power that is 157 W/kg greater than the baseline. This is a significant result as it indicates that the 700 nm-thick device is radiation tolerant, and the textured BSRs can produce higher mass-specific power compared to the conventional design. These results validate the use of the RIE and in situ processing for space PV manufacturing and matches the light trapping goals outlined in this research.

8.1.1 Texture Development

The two texturing methods reported in Chapter 7 resulted in favorable light trapping in the thinned GaAs bottom subcell and encouraged the use of the simple texturing approaches for the IMM devices. The first approach uses the RIE surface treatment to damage the top epitaxial layer where the subsequent overgrowth of a wide E_g material inherently grows roughened due to the RIE treatment. The second approach is an in situ etching process on the last non-active epitaxial layer directly after the growth of the solar cell. For both treatments, GaAs was chosen as the material for texture development since its E_g is wider than the 1-eV InGaAs solar cell.

These textures were initially investigated with SJ 1-eV InGaAs solar cells to reduce the material and growth costs associated with the triple-junction IMM device.

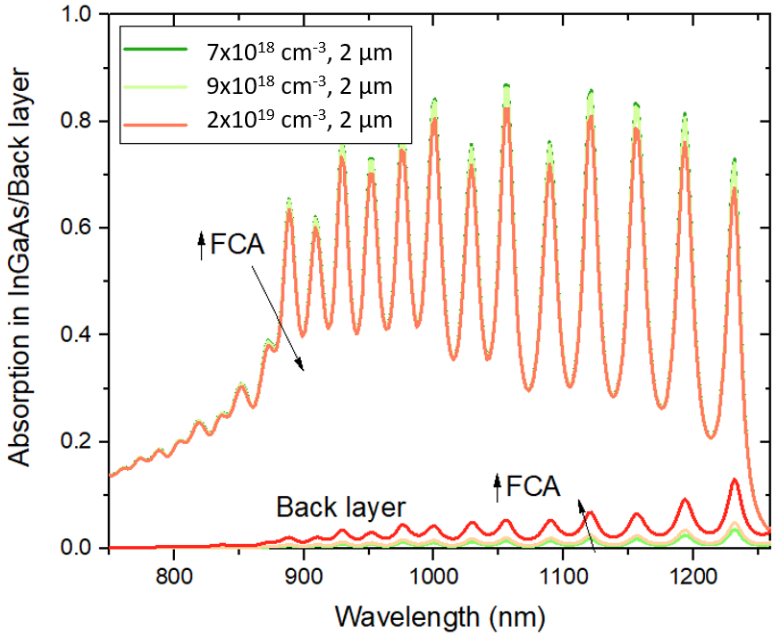

Figure 8.1: Absorption in a 600 nm-thick InGaAs solar cell according to different doping concentrations in a 2 μm thick backside GaAs layer. Behind the GaAs layer is a planar Au mirror.

The study on FCA in the backside textured layer, as discussed in Chapter 8, led to the first design optimization for the InGaAs solar cells. Modeling the FCA in the p-type GaAs textured layer helped guide the design and reduced the parasitic absorption by free carriers. In particular, various p-type doping concentrations were modeled in the bottom GaAs layer to predict the absorption loss due to FCA and target a feasible doping concentration. The photons that transmit through the InGaAs absorbing region will have an immediate 2-fold increase in the OPL in the textured back layer as they reflect from the mirror. Therefore, the first two passes are crucial to reducing parasitic absorption by free carriers. Originally, the GaAs layer had a doping concentration equal to 2x10^{19} cm^{-3} and a thickness equal to 2 μm for proper texture development. Figure 8.1 displays the absorption in the 600 nm-thick InGaAs solar cell

and the textured GaAs back layer with doping concentrations of 7x10^{18} cm^{-3}, 9x10^{18} cm^{-3}, and 2x10^{19} cm^{-3}. As the doping concentration increases, the absorption by free carriers of near-band edge photons does, too. This absorption loss reduces the number of reflected photons from the Au mirror and degrades the absorption in the InGaAs solar cell. This result is observed as the thin-film interference patterns reduce with increasing doping concentration. At the doping concentration of 1x10^{19} cm^{-3}, the layer must be no more than 500 nm in thickness to achieve sufficient carrier transport while minimizing FCA.

The same RIE process described in Chapter 7 was used at a controlled forward bias to bombard the last-grown GaAs layer without etching the material. After the RIE treatment, the treated wafers were brought back to the MOVPE reactor to overgrow the wide E_g p-type GaAs layer. The deposited epitaxial material grew rough as the crystal was no longer atomically smooth. The GaAs layer was monitored using a LayTec EpicurveTT metrology system until the 405 nm surface reflectance dropped below 20%, as displayed in Figure 8.2.

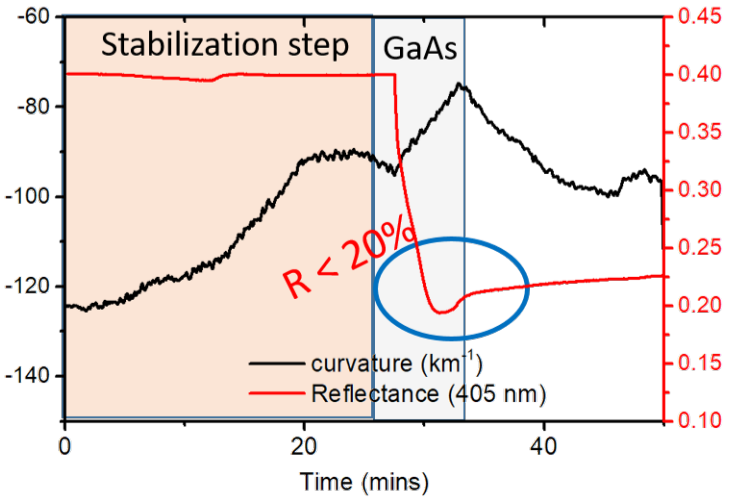

Figure 8.2: EpiTT curvature and surface reflectance (405 nm) during the regrowth of GaAs:C on the RIE-treated InGaAs solar cell.

Figure 8.3(a) presents the AFM scan from the pre-textured InGaAs solar cell with extracted surface roughness before the texture development to use as a baseline. The surface roughness

around 7 nm is slightly rougher than an epi-ready surface because of the metamorphic grade in these devices. However, it is still low enough not to produce a high diffuse reflectance without additional texture development. Figure 8.3(b) displays the RIE-roughened GaAs layer, highlighting nearly a 3-fold increase in surface roughness compared to the pre-textured InGaAs solar cell.

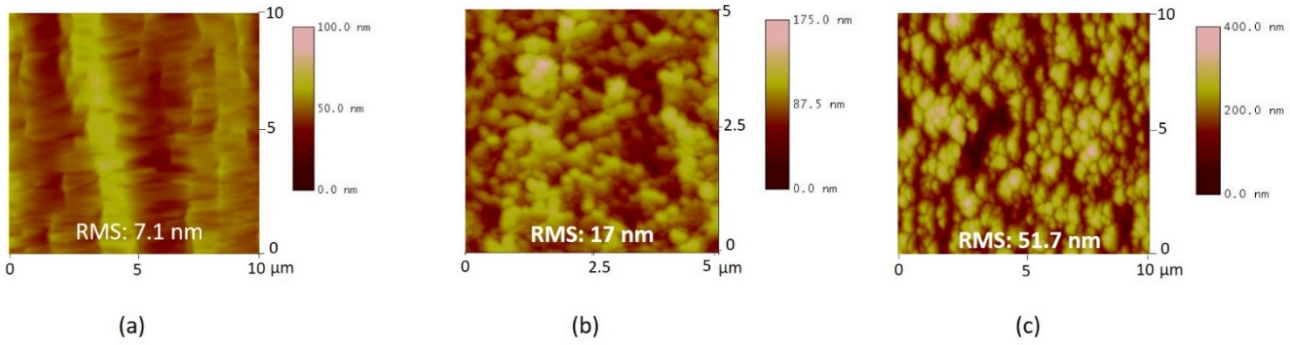

Figure 8.3: AFM with surface roughness on (a) pre-textured InGaAs solar cell, (b) RIE textured GaAs and (c) in situ textured GaAs.

The in situ texturing process shown in Figure 8.4 used the same etch-back conditions in Chapter 7 to slowly remove and texture the GaAs layer. Calibration runs were developed to achieve high surface roughness and low in situ surface reflectance while targeting a GaAs layer less than 500 nm in thickness. The final process starts with the growth of a 1500 nm-thick GaAs layer, and the etch-back with an etch rate near 3 nm/min is performed until approximately 300 nm of textured GaAs is left.

From the in situ process, the final GaAs:C layer was 500 nm thick and Figure 8.3(c) shows the increased surface roughness from the in situ process and roughened surface morphology. The surface roughness is more than six times that of the pre-textured solar cell. The drop in surface reflectance during the etch-back step is seen in Figure 8.5 and indicates a higher degree of photon scattering and is related to the increased RMS characterized by AFM. The curvature shows an increase in film stress during the etching procedure and is likely associated

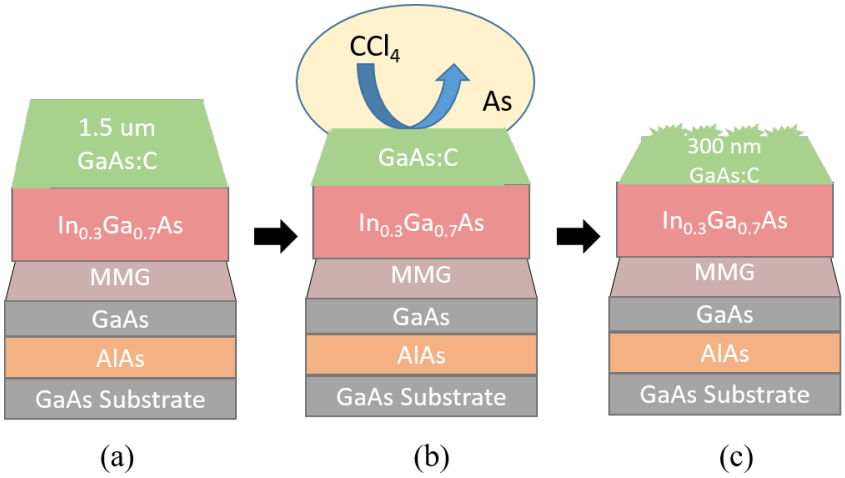

Figure 8.4: The in situ texturing process where (a) displays the growth step of the Gaas:C layer, (b) displays the etch back using CCl_4, and (c) displays the final textured GaAs layer on the inverted SJ InGaAs solar cell.

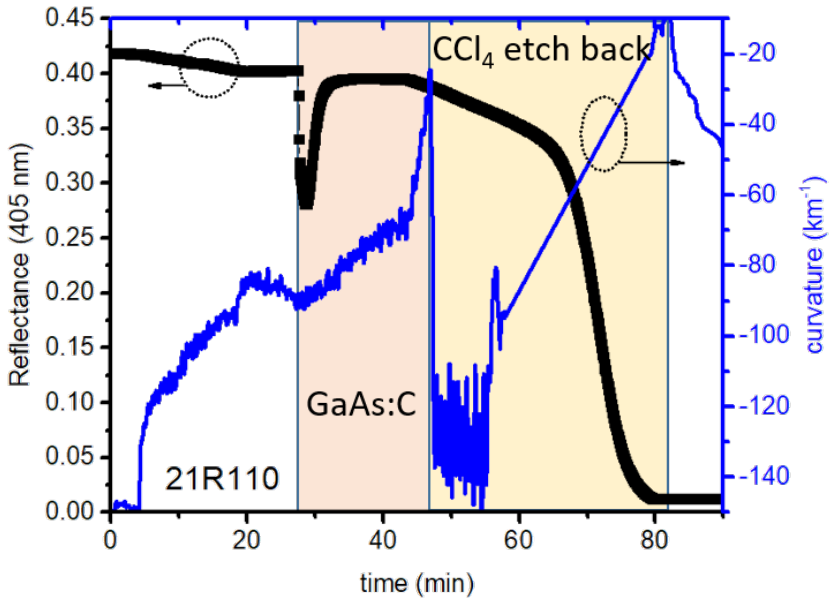

Figure 8.5: EpiTT surface reflectance and curvature during the growth of 1500 nm thick GaAs (orange region) and the in situ etch-back of the GaAs layer (yellow region).

with breaking crystalline bonds as the group III elements are removed from the surface.

8.2 Single-Junction 1-eV InGaAs Solar Cells

8.2.1 Device Characterization

The four BSR designs include an absorbing mirror with a Cr interlayer, a planar mirror, the RIE-roughened texture, and the in situ texture. All BSRs use a reflective Au mirror, which also serves as the backside contact. The Au was thermally evaporated with a final thickness of 500 nm. The 1-eV InGaAs solar cells were grown by MicroLink Devices and fabricated using ELO, as dsicussed in Chapter 4. An ARC consisting of MgF_2/ZnS was deposited on the completed devices, followed by characterization and analysis. The final devices are shown in Figure 8.6. The InGaAs solar cells have an n-type 100 nm emitter and a p-type 500 nm-thick base, resulting in a total active region thickness of 600 nm. This thickness is nearly five times thinner than its optically thick counterpart.

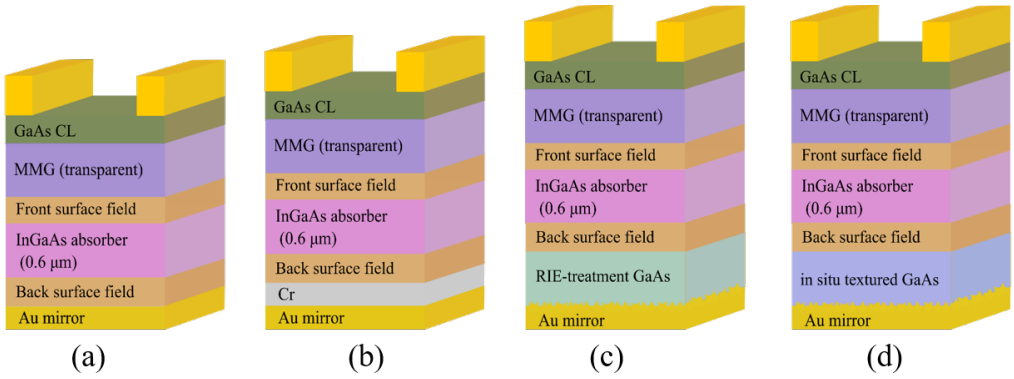

Figure 8.6: Diagrams of the thin-film 1-eV InGaAs solar cells with (a) planar Au BSR, (b) absorbing BSR, (c) RIE-textured BSR, and (d) in situ textured BSR.

Illuminated J-V measurements were taken on the ARC-coated, optically thin 1-eV InGaAs solar cells with the absorbing, planar, RIE, and in situ BSR designs. For each device, ten samples were measured at 25°C using a TS Space Systems dual-source 18 kW solar simulator filtered for the AM0 spectrum. Figure 8.7 displays the J-V curve from the best-performing

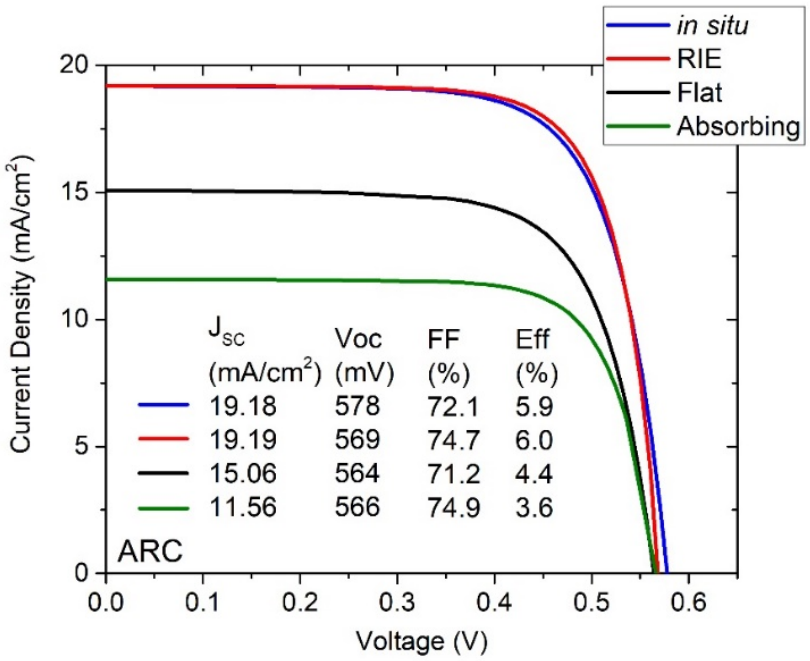

Figure 8.7: Illuminated J-V results with an ARC for the 1-eV InGaAs solar cells with various back surface reflectors.

cells. The first improvement was made by removing the Cr adhesion layer, which recovered 3.5 mA of the current collection between the absorbing BSR device (green) and planar BSR device (black). Promisingly, the InGaAs solar cells with the RIE and in situ BSR enhance the J_{SC} by more than 25% compared to the planar BSR. The RIE and in situ BSR devices have a band gap voltage offset, W_{OC}, equal to 431 mV and 422 mV, respectively. These values are similar to the voltage offset reported by NREL for a 1-eV solar cell, which was reported to be 400 mV [134]. The texture procedures do not appear to interfere with backside carrier collection, as seen from the maintained V_{OC} and FF while enforcing angular photon scattering within the cell to improve the J_{SC}. Both textured BSR devices improve the J_{SC} compared to the absorbing and planar mirror.

The EQE and reflectance results from the BSR devices are displayed in Figure 8.8, and the integrated J_{SC} results are reported in a bar chart in Figure 8.9. Similar to the illuminated

J-V, the current output in the textured BSRs is greater than the planar mirror, and the Cr adhesion layer significantly reduces the photon absorption across the entire solar cell. The RIE and in situ BSRs demonstrate a 20% and 28% increase in the integrated J_{SC}, respectively, compared to the planar BSR. Additionally, the reflectance drops after the InGaAs band edge in the textured BSR designs, indicating a higher degree of photon scattering. The FP thin-film oscillations are evident in the planar BSR device starting around 900 nm in wavelength but dampen in the RIE BSR and disappear in the in situ BSR designs.

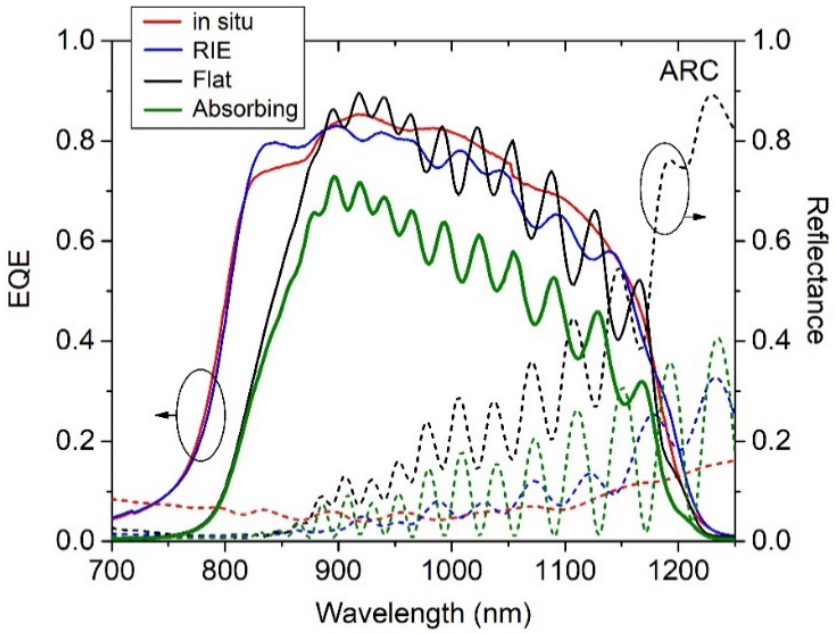

Figure 8.8: EQE and reflectance ARC for the 1-eV InGaAs solar cells with various back surface reflectors.

Based on the FP cavity behavior and using the LEF analysis [52], the extended photon lifetime inside the solar cell is calculated to determine the photon path length. The planar and RIE BSR result in a LEF of 2.4 and 3.6, respectively. The LEF near two for the planar BSR is expected as a planar mirror can only improve the path length by two passes. The LEF

is slightly higher than two in the planar BSR device, most likely due to the inherently rough properties of the metamorphic material. The increased LEF from the RIE BSR demonstrates an enhanced path length inside the solar cell, corresponding to the improved J_{SC} and low specular reflectance after the InGaAs band edge. The in situ BSR does not show FP cavity behavior, so the LEF analysis cannot be applied. However, due to the in situ processing, the collapsed FP cavity is promising since it indicates a high degree of photon scattering.

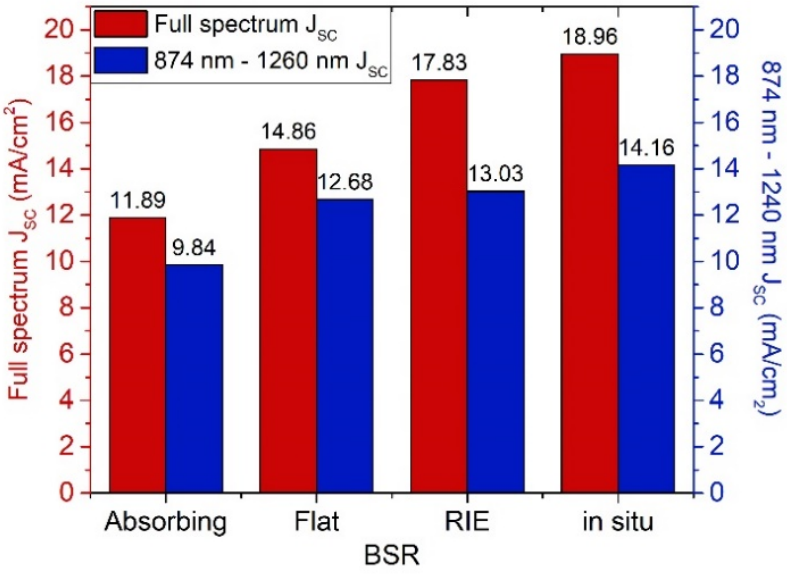

Figure 8.9: Integrated AM0 J_{SC} measured from the BSR devices, full-spectrum and expected J_{SC} when integrated into a full IMM device.

The difference in EQE at the front side of the planar and textured BSRs is due to the different thicknesses of the GaAs contact layer. The optically thick InGaAs subcell in an IMM design achieves a current output of 16.7 mA/cm^2 [83,135], and results show that both textured BSRs have J_{SC} greater than this value. This result is because the SJ InGaAs solar cell can convert the high-energy photons into a photogenerated current since the middle GaAs subcell

is not present. For this reason, the integrated AM0 J_{SC} between 870 nm and 1240 nm was also determined provided that in the triple-junction device, the middle GaAs subcell will absorb photons up to its band edge near 870 nm. The expected J_{SC} for the RIE and in situ BSR are calculated as 13.03 mA/cm^2 and 14.16 mA/cm^2, respectively. The in situ BSR device results in a J_{SC} that is nearly 2.5 mA lower than the optically thick design, potentially due to other parasitic absorption mechanisms such as absorption in the mirror. Incorporating a low-index interlayer, as shown with the SJ GaAs solar cell results in Chapter 5, will help improve the backside reflectance but also introduces a more complex fabrication process since a top-top contact design or backside vias are required for carrier transport. This approach was not experimentally realized in this work. Instead, the triple-junction IMM devices with slightly thicker absorbing regions were developed. The goal of slightly increasing the base thickness in the bottom InGaAs subcell is to reduce the current loss and reach the photogenerated current output expected from the IMM control while achieving a higher mass-specific power. The following section involves the experimental results and discussion of this approach.

8.3 Triple-Junction Inverted Metamorphic Solar Cells

8.3.1 Device Characterization

The promising experimental results using the RIE treatment and the in situ texturing approaches in the SJ 600 nm-thick InGaAs solar cells projected the integration of these light trapping structures into the triple-junction IMM solar cell with the thinned bottom InGaAs subcell. The IMM devices were grown by collaborators at MicroLink Devices using the inverted growth and ELO process explained in Chapter 4. Figure 8.10 is a diagram of the IMM device with a top InGaP subcell, middle GaAs subcell, and thin-film InGaAs subcell. As mentioned

above, instead of developing a more complicated fabrication process by incorporating a low-index interlayer, the bottom InGaAs subcell base region thickness was increased to help improve the current output. Originally, the SJ solar cell base region thickness was 500 nm. Two new base thicknesses were explored for the triple-junction devices, namely 600 nm and 1200 nm, to improve the current output and mass-specific power. The top and middle subcell have the same design across all devices and are based on MicroLink Devices solar cell structure. These triple-junction solar cells were combined with another research project studying multiple quantum wells (MQW) and a DBR between the middle and bottom subcells. The MQWs are embedded in the middle GaAs subcell and do not impact the photon collection in the base of the bottom subcell. The DBR consists of an alternating material stack between AlInP and InGaP and is based on previous work [136, 137]. Four thin-film designs with combinations of the RIE or in situ texture are paired with the Au reflective mirror. All devices have a 100 nm-thick emitter. Therefore, the active region thicknesses for the control and thin-film devices are 3100 nm, 1300 nm, and 700 nm, respectively. These devices are referenced according to the InGaAs active region thickness and the BSR. For example, the 600 nm thick InGaAs base design with the RIE texture is denoted as "700 nm + RIE," while the 1200 nm thick base design with the in situ texture is referred to as "1300 nm + in situ." The names of the four light trapping devices include, "700 nm + RIE", "1300 nm + RIE," "700 nm + in situ," and "1300 nm + in situ." These four devices are compared to the optically thick design, which has a 3000 nm-thick InGaAs base region and is referred to as the "IMM Control."

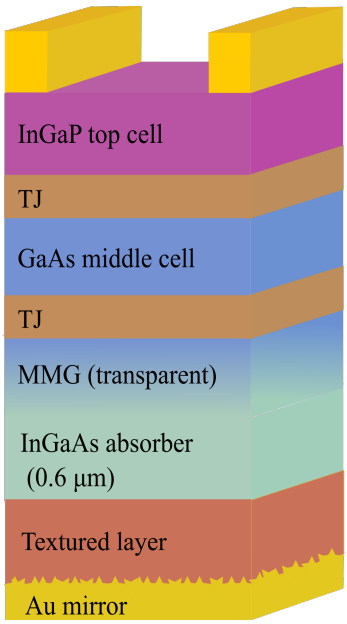

Figure 8.10: Diagram of the triple-junction IMM device with a top InGaP cell, middle GaAs cell, and the thin-film InGaAs cell with a textured mirror.

Illuminated J-V measurements were taken on ten different samples across each BSR device. Out of the ten samples, one cell has an active region of 1 cm^2, while the rest have a smaller active region of 0.25 cm^2. The best-performing J-V measurements across the four BSR devices are shown in Figure 8.11. The V_{OC} in all devices is about 250 mV less than the IMM control device reported in literature. This voltage loss may be associated with the nanostructured MQW region in the middle GaAs subcell, which is known to increase nonradiative recombination in solar cells [138]. To understand this loss in V_{OC}, devices without the MQW are required. Overall, all samples have a BoL efficiency greater than 24% along with J_{SC} that is 1.5-2 mA greater than the SJ InGaAs solar cells reported in Section 8.2.

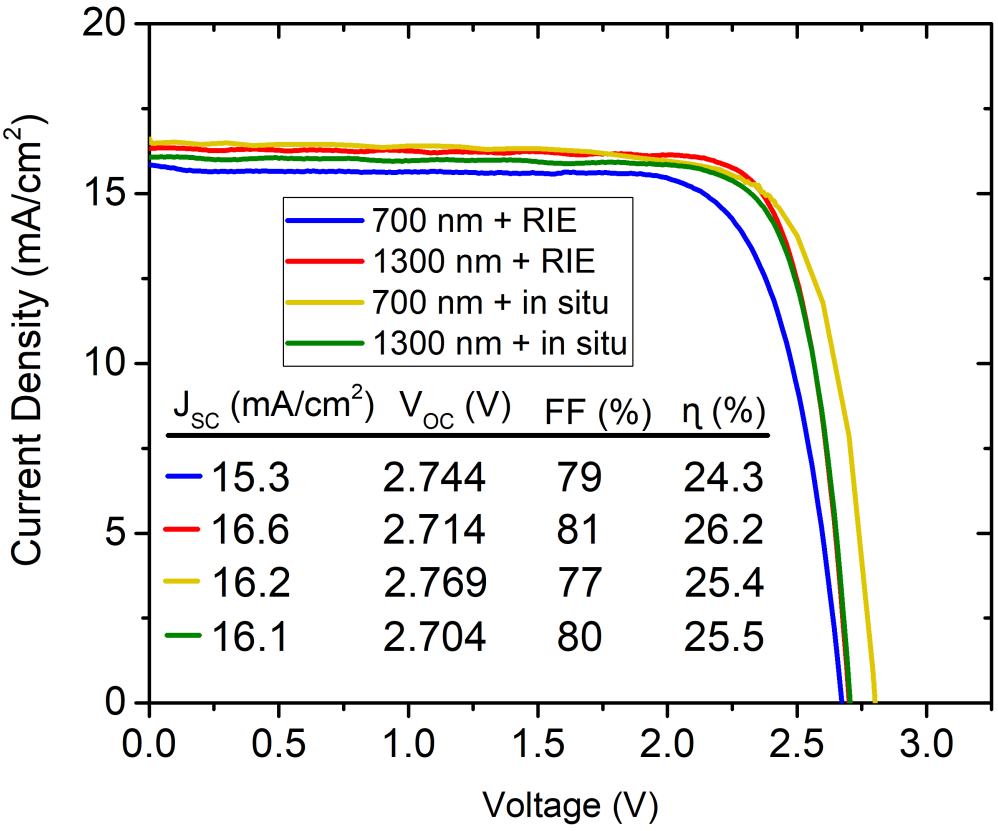

Figure 8.11: Illuminated J-V measurements for IMM device with various BSR designs and InGaAs base thicknesses.

Figure 8.12 displays the measured EQE from the BSR devices compared to the IMM control. Across all samples, the top InGaP cell has the same photon collection and indicates high uniformity in growth and fabrication. The middle GaAs cell has oscillation peaks due to the reflectance between the DBR and the top of the cell, with similar J_{SC} across all BSR devices. Compared to the control (black), the base collection in the GaAs middle subcells and the front side collection in the InGaAs bottom subcells are slightly low. This result is explained when considering the DBR reflectance as shown by the black dotted line. The DBR aims to reflect high-energy photons into the middle subcell but parasitically absorbs photons near

the reflectance peak at 900 nm in wavelength. Therefore, the collection in the bottom InGaAs subcells between 870 nm and 975 nm is lower for the BSR devices. The full spectrum integrated J_{SC} is reported for the bottom subcells, and the 2 mA difference in J_{SC} can be explained by the DBR reflectance. The influence from the light trapping structures is evident in the base region and near the band edge of the bottom InGaAs subcells. The thin-film interference patterns differ across each sample due to the difference in absorbing thickness and light trapping effects.

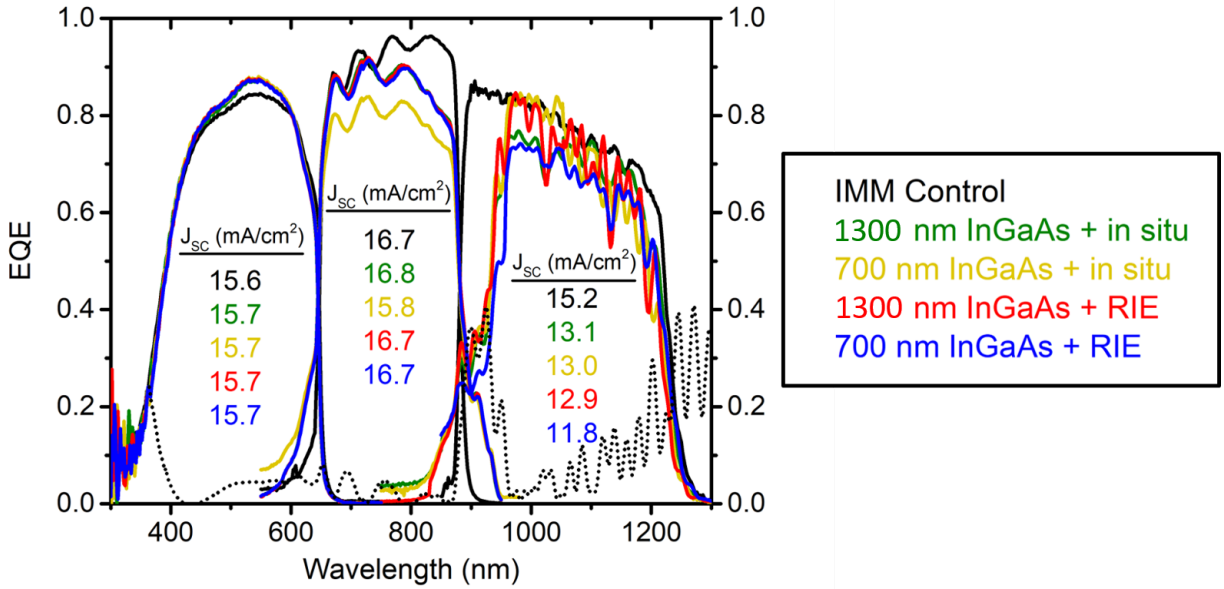

Figure 8.12: EQE on the IMM devices with different BSRs and InGaAs base thicknesses.

The bottom InGaAs subcell is plotted separately in Figure 8.13. The bottom InGaAs subcell has numerous oscillations due to the change in photon incidence from the top and middle subcells, the thin-film nature of the bottom cell, and the backside reflectance from the BSR. A better comparison between the IMM control and the BSR devices considering the reflectance loss from the DBR is shown in this plot, and the integrated J_{SC} between 975 nm to 1300 nm in wavelength is reported. The IMM control achieves the most significant base and

band edge photon collection. The 1300 nm + RIE (green) and 700 nm + in situ (yellow) curves show the greatest improvement in the J_{SC} and are within 1 mA of the control sample.

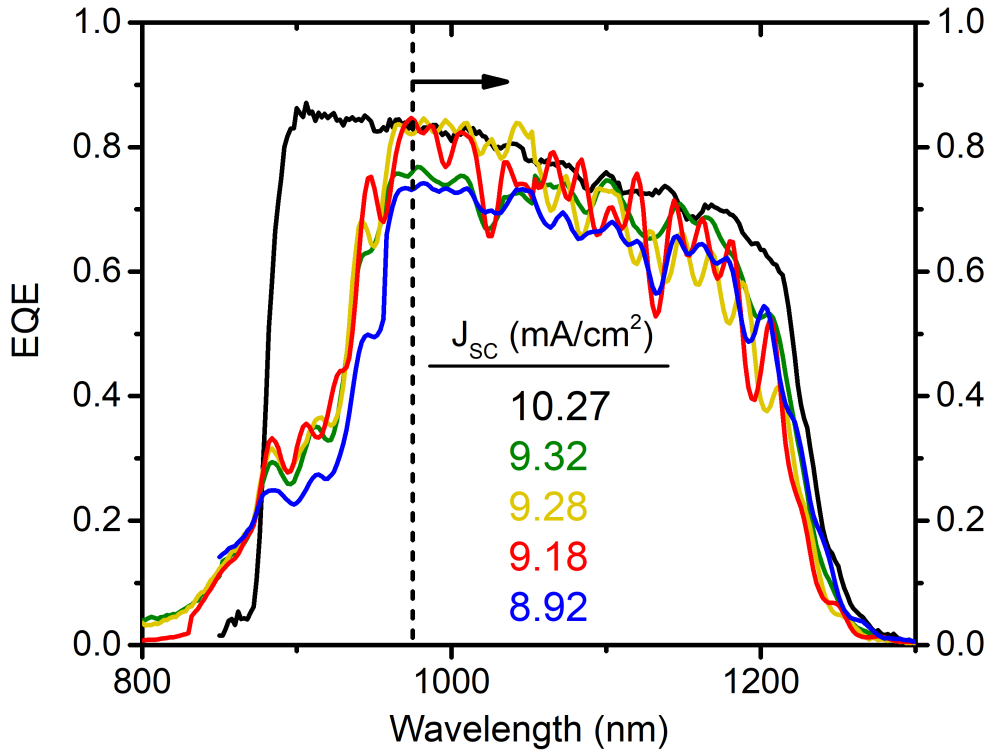

Figure 8.13: EQE on the bottom InGaAs subcell across all BSR devices.

The thin-film IMM devices with light trapping structures show that the current output is greater than the designs without light management. However, the best-performing BSRs are within 1 mA of the control device. These figures of merit are true at BoL performance before exposure to radiative particles. Therefore, damage displacement modeling using TCAD Sentaurus Device and established material coefficients for the InGaP, GaAs, and InGaAs subcells, as discussed in Chapter 2, is performed on these samples. First, the remaining factor was determined for the InGaAs devices with a base thickness of 3000 nm (control), 1200 nm (thin-film), and 600 nm (thin-film, sub-μm regime). Figure 8.14(a) shows the remaining factor for these

three thicknesses where the control (black) reduces its current collection to 91% at an electron fluence equal to 2x10^{15} e^{-}/cm^{2}. This value is significant since it represents the radiation damage after a 15-year mission in Geosynchronous Earth orbit (GEO). Notably, the remaining factor for the 600 nm-thick base device is 99% of its BoL current output at EoL. These trends are used to calculate the remaining factor using the experimentally measured J_{SC} across the BSR devices. Specifically, the BoL J_{SC} from the best-performing devices, as shown in Figure 8.11, are used for the thin-film IMM devices. For the IMM control, the reported BoL J_{SC} value equal to 16.7 mA/cm^{2} is used [135]. Figure 8.14(b) displays the calculated J_{SC} vs. electron fluence for the BSR devices compared to the IMM control. At BoL, the BSR devices achieve a lower J_{SC} than the IMM control. Promisingly, the 1300 nm + RIE BSR device produces a current within 0.2 mA of the IMM control. Since the IMM control has poor radiation tolerance, this device loses more than 1.5 mA of current at EoL conditions. Promisingly, three out of the four BSR devices surpass the IMM control in terms of J_{SC}. Specifically, the 1300 nm + RIE BSR device outperforms the control at the lowest electron fluence equal to 1.5x10^{14} e^{-}/cm^{2}, the 700 nm + in situ BSR surpasses the control 6x10^{14} e^{-}/cm^{2}, and the 1300 nm + in situ BSR device surpasses the control near 9x10^{14} e^{-}/cm^{2}.

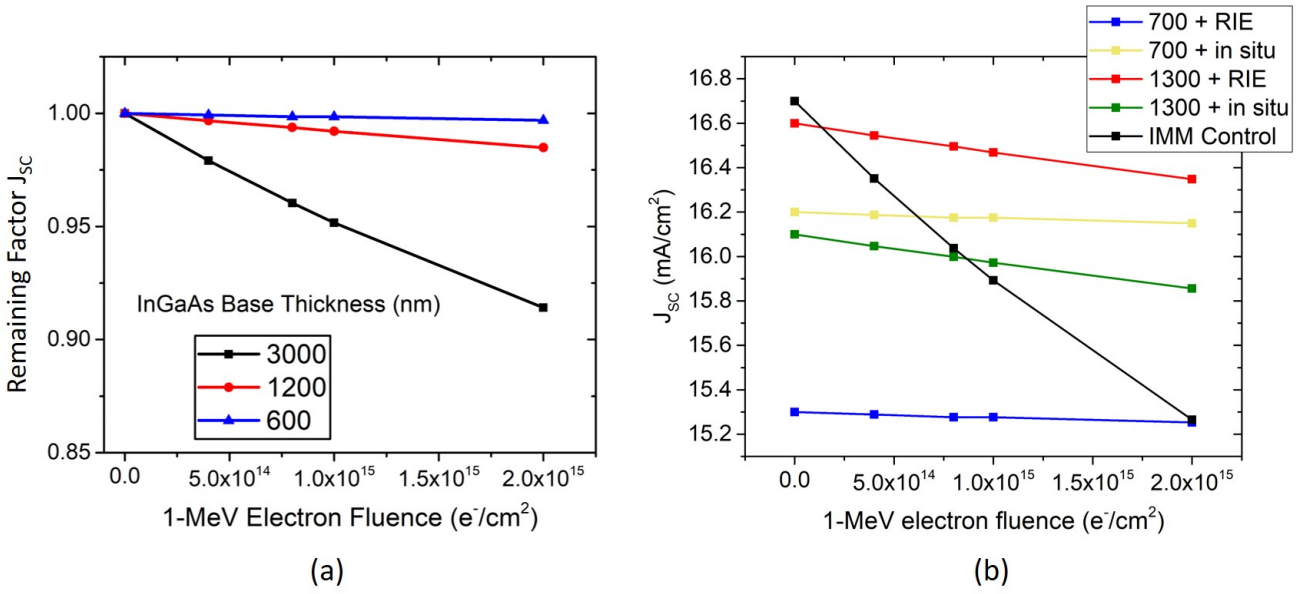

Figure 8.14: Radiation modeling based on the experimental J_{SC} from the thin-film IMM device with the in situ BSR (a) remaining factor in J_{SC} and (b) trend in J_{SC} based on measured values.

Rather than considering the J_{SC} vs. electron fluence alone, the AM0 efficiency extracted from the BSR devices is also investigated in terms of the remaining factor at EoL. The same method described for the remaining factor in J_{SC} is performed using the AM0 efficiency from the best-performing devices. For reference, the BoL efficiency values are displayed in Figure 8.11. Figure 8.15(a) displays the remaining factor in efficiency across the three InGaAs solar cells with different base thicknesses. In particular, the IMM control shows the highest efficiency degradation and can maintain only 67% of its BoL efficiency. At the same time, the thin-film device has less degradation and can maintain 78% of the BoL efficiency at EoL conditions. Figure 8.15(b) shows the calculated AM0 efficiency across the IMM + BSR devices and IMM control. At EoL, the IMM control achieves the highest efficiency, equivalent to 20.4%. The 700 nm + in situ BSR device achieves the second highest efficiency, equivalent to 19.8%.

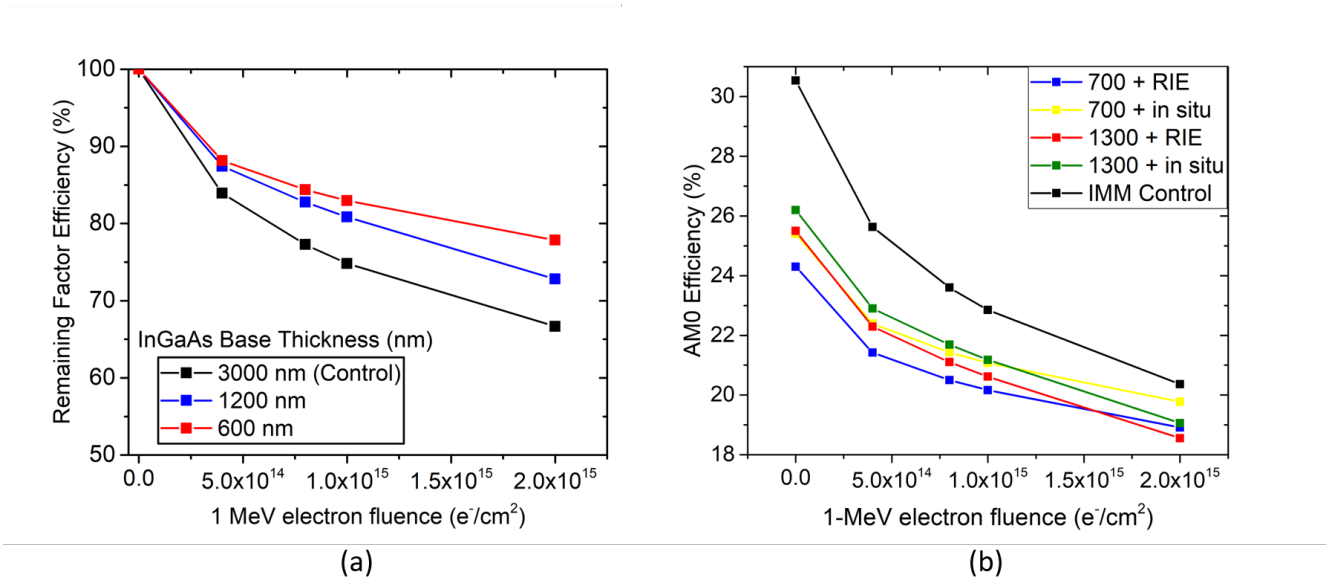

Figure 8.15: Plot (a) displays radiation modeling of the AM0 efficiency of the IMM devices with three base thickness of 3000 nm (black), 1200 nm (blue), and 600 nm (red). Plot (b) displays the AM0 efficiency vs. electron fluence using the experimentally measured BoL efficiency and trends in the remaining factor from plot (a).

While the thin-film BSR devices do not surpass the efficiency of the IMM control at EoL conditions, there are further observations to examine. The first is the trend in efficiency. If the model continued past 2x10^{15} e^{-}/cm^{2}, there is a clear cross-over point in efficiency between the BSR devices and the IMM control. This is applicable for deep-space missions where the electron fluence is higher than 2x10^{15} e^{-}/cm^{2}. Secondly, it is important to consider the mass-specific power vs. electron fluence for each of these designs. As discussed in Chapter 2, the mass-specific power of the solar cell is its efficiency normalized to its weight. This metric can be calculated at the cell or array scale. For the cell size, the material densities of each subcell and the thickness of the overall device are considered. The cell-size mass-specific power is considered and calculated using the material densities for InGaP, GaAs, and InGaAs as 4.47, 5.317, and

5.68 g/cm^3, respectively. The total thickness of triple-junction device varies according to the thickness of the bottom InGaAs subcell. The control, thin, and ultrathin IMM devices lead to weight/area values of 2.04x10^{-5} kg/cm^2, 1.75x10^{-5} kg/cm^2, 1.7x10^{-5} kg/cm^2, respectively. Using these values as the weight of the device and the calculated efficiencies reported in Figure 8.15(b), the mass-specific power vs. electron fluence is determined.

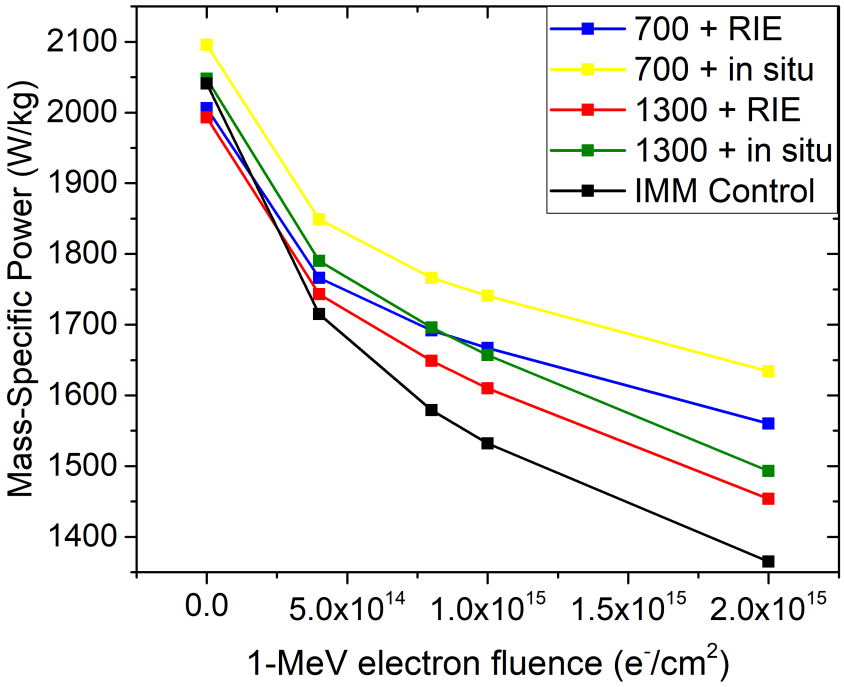

Figure 8.16: Plot of the calculated mass-specific power for the BSR devices and IMM control.

Figure 8.16 displays the calculated mass-specific power for the IMM + BSR devices compared to the IMM control. The mass-specific power for the IMM control reduces over 670 W/kg at EoL due to its radiation intolerance. Since both of the 1300 nm + BSR devices have similar trends in the remaining factor of efficiency, the mass-specific power trends are also similar. Although all BSR devices have a lower BoL efficiency than the IMM control, they outperform the control after electron radiation. In particular, all thin-film BSR devices surpass the IMM

control before 5x10^{14} e^{-}/cm^{2}. The 700 nm + RIE BSR device and the 700 nm + in situ BSR device achieve a mass-specific power at EoL that is 195 W/kg and 269 W/kg greater than the IMM control, respectively. The 600 nm-thick IMM devices achieve the greatest mass-specific power at EoL due to their maintained collection of photogenerated carriers, even after radiation damage. This result is significant since, at BoL, the 600 nm-thick + BSR devices are not the favored candidate, provided their absolute efficiency is approximately 4% less than the IMM control. However, their resilience to radiation damage allows them to prevail in the harsh space environment and makes them a better candidate for EoL conditions. Through careful material selection, texture development, modeling, and characterization, the goal to increase radiation hardness and mass-specific power was accomplished in this work. These light trapping results support the use of the RIE and in situ textured BSRs in space PV technology and provide the opportunity to extend the mission lifetime for space vehicles.

8.4 Chapter Summary

The RIE-surface treatment and in situ processing techniques provide inexpensive methods for texturing III-V semiconductors applicable at the backside of thin-film MJSC for space applications. The first approach was to demonstrate improved J_{SC} in SJ InGaAs solar cells compared to the thin-film devices with no light trapping structures. The surface roughness extracted from AFM shows increased diffuse scattering properties from the textured layers compared to the planar geometry. The textured BSR devices maintained V_{OC} and improved J_{SC}, which merits further investigation in the triple-junction IMM device. The highlighted results from the triple-junction IMM devices show that all BSR devices improve photon absorption and current output compared to the thin-film geometries with no light management or a planar BSR. The

EQE shows base and band edge photon collection within 1 mA of the IMM control, which suggests path length enhancement from adequate light trapping in the thin-film devices. Since the 700 nm-thick devices are much lighter in weight, their mass-dependent efficiency surpasses the baseline after an electron fluence of $4x10^{14}$ e^{-}/cm^{2}. This is a significant result as it indicates the 700 nm-thick devices are radiation tolerant, and the in situ BSR is capable of maintaining current and producing higher mass-specific power compared to the conventional design. These results validate using this simple processed texture for space PV manufacturing and match the goals outlined in this research.

Chapter 9

Conclusions and Future Work

The first part of this dissertation describes the work investigating the integration of light trapping structures in the form of BSRs behind thin-film III-V photovoltaics. The goal is to realize optically thick but physically thin device architectures capable of improving radiation tolerance while maintaining device efficiency at EoL conditions. Various techniques were developed to texture III-V semiconductors and achieve highly diffuse scattering surfaces through simple processes. Simple processing is vital to reduce the time and cost of the III-V solar cell system and make the texturing methods adaptable to already-established PV manufacturing. The bulk of the texture development is performed in SJ solar cells, namely the GaAs and 1-eV InGaAs solar cells, before integrating them into their respective multijunction designs. The texture development was developed in transparent semiconductors with band gaps wider than the solar cell. A top-top contact design was also developed to characterize the optical benefits of the BSRs with low-index interlayers without the use of localized contacts. The favorable candidates for texture development include the solution-based maskless etch, I-MacEtch, RIE, and in situ texturing. Using RIE as a surface treatment introduced a broad parameter space for semiconductor texturing, which can be expanded to other III-V materials. The in situ etching of III-V semiconductors using halomethane compounds became the leading texturing process due to its ability to create three-dimensional structures directly after solar cell growth. The

in situ method removes the additional steps required with the other texturing processes and immediately allows for solar cell fabrication once removed from the MOVPE reactor.

Novel methods and approaches to characterize the textured BSRs and thin-film devices were developed in this work. First, the haze in reflectance measurements using a transparent semiconductor and substrate removal presented the opportunity to experimentally observe the interaction of incident photons with the textured BSRs. The total and diffuse reflectance measurements provided detail behind the scattering properties. The best-performing textured BSRs present highly diffuse reflectance, indicating a reduction in the specular reflectance and a high degree of photon scattering. The in situ BSR with the TIR layer achieved 100% haze in reflectance at 700 nm in wavelength, and the SEM images revealed pyramidal structures developed in $Al_{0.7}Ga_{0.3}As$ from this in situ etch-back technique. These results demonstrate a Lambertian scattering surface near the GaAs band edge as the angular dimensions of the pyramids improve the path length enhancement beyond three passes. At the GaAs band edge, the in situ BSR achieves the highest haze in reflectance near 90%. The second novel characterization technique relies on experimentally measured EQE from the thin-film solar cells to extract the quality factor and the photon lifetime. By comparing the extended photon lifetime, based on the measured quality factor, and comparing it to the single-pass photon lifetime, the increased lifetime due to effective light trapping is determined [52]. This analysis is valuable when quantitatively representing the path length enhancement in thin-film solar cells. Additionally, a unique modeling analysis focusing on the FCA in non-active backside layers has progressed the understanding of light interaction with semiconductor layers due to optical enhancement from light trapping. The FCA analysis shows that careful material selection and design must be considered to reduce the absorption by free carriers while maintaining sufficient carrier transport through doping concentration and layer thickness. This analysis investigates a well-known

mechanism that occurs in semiconductors, but one that is often overlooked when modeling the performance of solar cells [139].

These analyses are carried through the device design for the SJ GaAs, thin-film DJ, and IMM solar cells. The experimental results show that all textured BSRs promote photogenerated current in the base of the bottom subcell as a direct impact of increased LEF and OPL. For the SJ GaAs solar cells, the textured BSR devices demonstrate a significant improvement in J_{SC} and path length enhancement compared to the devices with no light management or a planar BSR. The main result from the DJ solar cells shows that the in situ textured BSR is capable of maintaining the base and near band edge photon collection as the trends in EQE aligned with the optically thick control. Since the DJ solar cell with the in situ BSR is 4-times thinner than the control, the similarities in EQE provide evidence that the in situ texture enhanced the OPL up to 4 passes. The IMM solar cells with the in situ and RIE textured BSRs showed minimal degradation to the V_{OC} and FF across the IMM solar cells with texture development. The radiation modeling of the IMM devices shows that, although the BoL J_{SC} is slightly lower than the optically thick IMM devices, they achieve 99% of photogenerated current at EoL performance. Namely, for 1 MeV electrons, the thin-film IMM device with the in situ BSR outperforms the baseline with a mass-specific power of 269 W/kg greater than the IMM control. The novel and compelling results, both through device modeling and experimental measurements, promote the direction of incorporating these textured BSRs into thin-film space PV and meet the overall goal of achieving high radiation tolerance and EoL device performance.

Part II

Light Management in Micro-Light Emitting Diodes

Chapter 10

Introduction

10.1 LED Technology and Applications

The LED is a light source consisting of semiconducting materials that emit photons through current injection. The photon emission from the LED depends on the direct E_g of the semiconductor and has allowed them to emerge in various applications, including the arts, sensing, medical therapy, automotive parts, indoor lighting, and display technology [2, 140–144]. In the ultraviolet and blue-wavelength range, LEDs are used in biomedical devices [144]. The development of short-wavelength LEDs progressed antimicrobial research, including the demonstration of inactivating pathogens that absorb and react with the emitted visible violet and blue light [144]. Additional research in short-wavelength LEDs has demonstrated the potential application to produce Vitamin D3 in the human skin, water sterilization, and immunotherapy [141, 145]. On the other hand, infrared (IR)-wavelength LEDs are used for communications, sensing, and monitoring. These LEDs have emerged in applications for motion sensors where the emitted light reflects from an object and is detected using a photosensor, which is valuable in portable device applications [146].

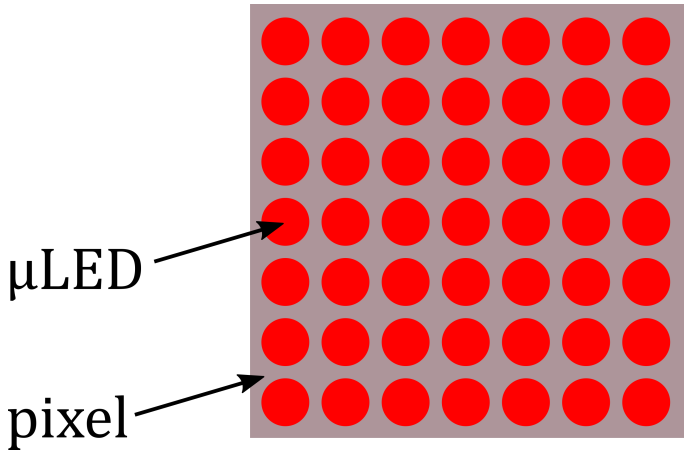

Figure 10.1: Display of the scale of μLEDs embedded into single pixels as red, green, and blue light sources.

LEDs have many benefits in display technology due to their low power consumption, long lifetime, high brightness, and contrast ratio. Current advancements in modern display technology include virtual reality (VR), augmented reality (AR), smart glasses, and other wearable products. These products provide a new form of connection and interaction between people worldwide. The main characteristic of these displays is their close proximity to the human eye. This distance requires more pixels within a unit cell area to achieve a higher resolution in the digital display. The millimeter-sized LED pixel limits the resolution depending on its size. Therefore, small-area μLEDs less than 100 micrometers are required to achieve this goal. There are many benefits using these devices compared to conventional organic LEDs and liquid crystal displays (LCD) [140, 147]. One main benefit of using μLEDs in displays is integrating multiple self-emitting light sources into a single pixel, as seen in Figure 10.1. This kind of display is known as a self-emitting display, and its development is crucial to the VR/AR and other wearable device applications to obtain a high resolution with miniature pixel size [2, 147].

10.2 Red-Emitting AlGaInP Micro-LEDs

With self-emitting technology, the μm-scale pixels are addressed separately to improve the quality and contrast of the picture. In 2000, the first blue-emitting μLED array was demonstrated and consisted of gallium nitride (GaN) with indium gallium nitride (InGaN) QWs [147, 148]. The success of this display projected research to improve blue and explore green LED technology using the same material system. For proper color contrast and image quality, red-green-blue (RGB) displays are required, which launched new exploration using GaN structures for red-emitting LEDs. However, many complications surfaced in the development of red-emitting GaN LEDs due to the increased non-radiative recombination with increasing indium composition in the QWs, which is necessary to red-shift the emission [149]. Developing red light emission has been challenging in nitride-based LEDs and compelled new investigations with other material sources. On the other hand, the mm-sized AlGaInP LED has demonstrated controllable red light emission, driving research to explore this material system rather than GaN-based μLEDs [147, 150, 151].

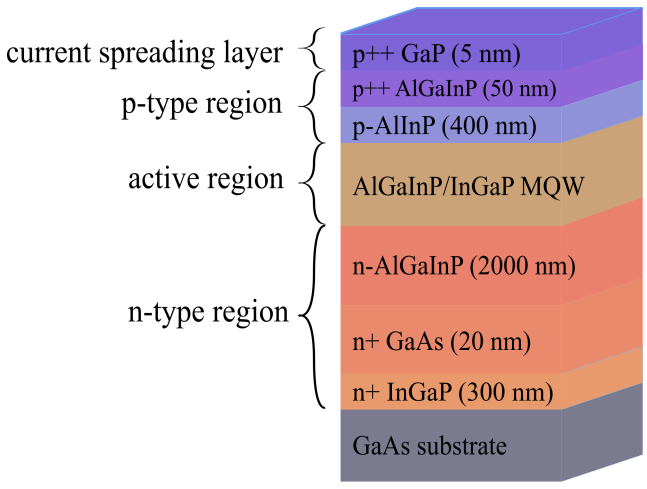

Figure 10.2: Structure of the AlGaInP LED with confinement and active layers.

Figure 10.2 displays the red-emitting AlGaInP LED, consisting of a PN junction and InGaP QWs between the different doped AlGaInP confinement regions. The intrinsic region is not doped with excess carriers. Instead, the narrow E_g material compared to AlGaInP is introduced to increase carrier concentration and radiative recombination, as discussed in more detail in Chapter 11. The AlGaInP barriers have a wide E_g and are lattice matched to the QW region, which reduces threading dislocations throughout the active region. The diode voltage is equivalent to the E_g of the QWs, which is near 2.0 eV. This energy is equivalent to 620 nm, the targeted emission wavelength. The band structure near the active region of the AlGaInP LED is shown in Figure 10.3. The active region refers to the intrinsic region at the junction where five repeating InGaP QWs are placed to promote carrier confinement under a positive bias.

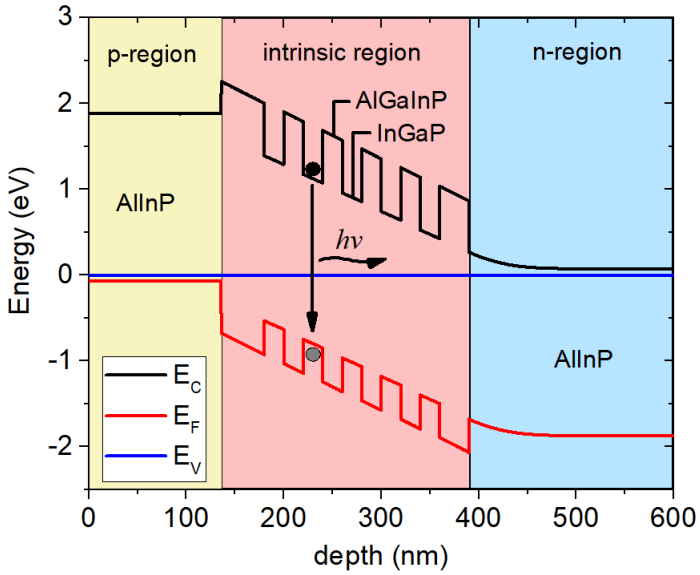

Figure 10.3: The band diagram of a MQW structure.

As the size of the AlGaInP LED continues to reduce, the sidewall perimeter-to-area ratio increases, and the device efficiency dramatically depends on the etched sidewall quality. The low efficiency in AlGaInP μLEDs can be attributed to the sidewall damage from dry etching. The etched sidewalls lead to increased roughness and dangling bonds that trap charge carriers,

allowing non-radiative recombination to increase. Since the LED depends on radiative recombination of electron-hole pairs in the active region, sidewall treatments must be included to passivate the sidewalls to combat parasitic carrier loss.

10.3 Light Management in AlGaInP Micro-LEDs

Ideal LED operation occurs when electrons and holes in the semiconductor recombine radiatively, accompanied by the emission of a photon according to the semiconductor E_g. Preferably, all electron-hole pairs emit a photon, but in practical device operation, several scenarios will increase non-radiative recombination events. For example, deep-level traps from native defects within the crystal lattice allow liberated electrons to fall to lower energy levels between the conduction and valence bands. High-quality semiconductor materials and proper device design mitigate native defects. However, one main non-radiative recombination site that is unavoidable as the LED continues to shrink in size is the surface recombination at the sidewalls of the LED. Any surface of a semiconductor device disrupts the periodicity of the crystal lattice, and the dangling bonds increase the electronic energy states in the forbidden gap [140]. The significance of surface states on radiative recombination as a function of LED size is shown in Figure 10.4. At the surfaces, carriers rapidly recombine in forbidden energy levels and are lost in parasitic recombination events. Minimizing surface states is crucial in maximizing radiative recombination to achieve high optical power output.

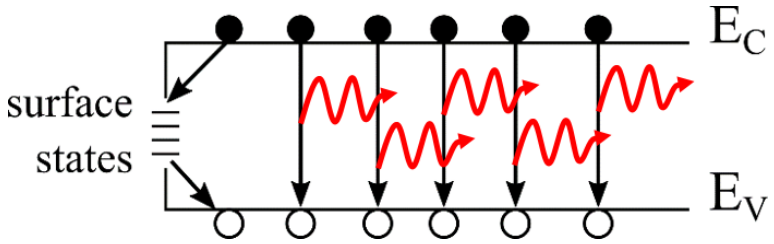

Figure 10.4: Representation of surface states reducing radiative recombination events.

Light management in LEDs comes in several forms, and this research focuses on improving light emission by reducing non-radiative recombination at the sidewalls of the μLED. The dry etch process required to isolate the μLEDs leads to dangling bonds at the surface and forms trapping centers. One approach is to deposit a transparent dielectric material on the sidewalls to passivate dangling bonds [152]. Usually, atomic layer deposition (ALD) or PECVD is used to deposit a dielectric material that is not electrically active. One issue with Al-containing semiconductors is the oxidation of Al when exposed to air, which occurs between the dry etch and passivation processing steps. This is a crucial parameter for Al-containing materials since Al slowly reacts with oxygen over time [153, 154]. An intermediate step includes wet-chemical etching to slightly remove the damaged and oxidized regions at the LED sidewalls [155–158]. After the wet-chemical treatment, the LEDs are exposed to air before the sidewalls are protected by depositing a non-active material. Another approach to passivate the sides of the LED is by overgrowing wide E_g semiconductors through MOVPE. This passivation is similar to conventional methods of depositing dielectric materials via ALD or PECVD. The benefit to MOVPE overgrowth is that the III-V material growth morphology can be controlled according to the growth parameters. Furthermore, the use of halomethane compounds that slowly etch III-V materials during MOVPE can be used to slightly remove the sidewall material before regrowth of the passivation layer. This approach can improve sidewall morphology and passivation. This research focuses on engineering proper sidewall treatments through wet-chemical etching and in situ etching, along with the overgrowth of non-active wide E_g materials through MOVPE to improve the sidewall quality and the radiative recombination inside the active region of the red-emitting μLEDs. With passivated μLEDs, the light output power (LOP) will significantly improve and result in high quality displays with high resolution, color contrast, and brightness.

Chapter 11

Light Management and LED Operation

11.1 Introduction

This chapter is dedicated to the concepts of light management and its impact on the device operation of AlGaInP μLEDs. Specifically, sidewall treatments promote radiative recombination in the active region by reducing sidewall damage and midgap energy states, which are essential for high optical power output. The sidewall cleaning treatments include wet chemical and in situ etching to remove nanometers of material from the sidewalls. The wide E_g regrowth and surface cleaning techniques are characterized through SEM to determine suitable combinations that result in uniform coverage and smooth LED mesa profiles. The fabrication process is outlined along with approaches to improve the LOP at the front side of the LEDs.

11.2 LED Operation and Light Management

11.2.1 LED Design and Radiative Recombination

Much like the solar cell described in Chapter 3, the LED is a two-terminal diode that allows current to flow in one direction. The LED utilizes a heterojunction design to promote radiative recombination of electron-hole pairs. The heterojunction design introduces a narrow

E_g material between the wide E_g material, and as the width of the narrow E_g material reduces, charge carrier movement becomes restricted and discrete energy levels form where carriers may exist [140]. The carrier confinement in the QW leads to a high concentration in the active region, increasing the radiative recombination process between electron-hole pairs in the QW. The difference in carrier concentration is shown in Figure 11.1(a)-(b), where the homojunction in (a) uses a semiconductor with the same E_g on each side of the junction with dissimilar dopants and concentrations. When the homojunction operates in forward bias, carriers diffuse to the bordering side of the junction and result in a wide distribution of carriers across both sides of the junction. The minority carriers can radiatively recombine but are limited by their diffusion length. In the heterojunction design shown in 11.1(b), carriers are confined in the QWs, and as long as the barrier heights are much higher than the thermal energy kT, carrier escape will be low and allow them to radiatively recombine at a faster rate due to a higher concentration in the QWs [140]. Furthermore, the multiple QW structure requires thin barriers such that carrier transport will be sufficient between the QWs.

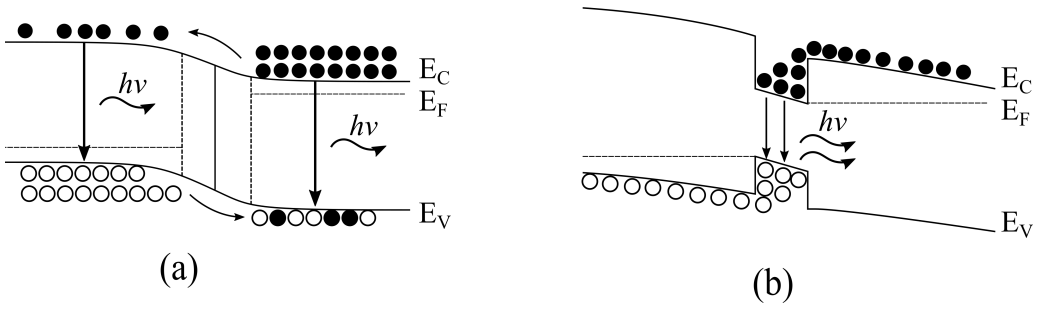

Figure 11.1: Charge carrier distribution in the (a) homojunction and a (b) heterojunction under forward bias conditions.

In an ideal structure, every injected electron leads to an emitted photon according to the E_g of the QW. For the InGaP QW, the turn-on voltage is near 2.0 eV, equivalent to 620 nm, the

wavelength of red light. In the forward bias regime, radiative recombination of every electron-hole pair will lead to a quantum efficiency of unity. The internal quantum efficiency (η_{IQE}) is defined as,

$$\eta_{IQE} = \frac{P_{int}/hv}{I/e}, \tag{11.1}$$

where P_{int} is the internal optical power from emitted photons in the active region, hv is the photon energy at the emission frequency, I is the injection current, and e is the electron charge. Ideally, the η_{IQE} would sum to unity provided that every electron-hole recombination event would lead to the emission of a photon according to the E_g of the QWs.

In mm-scale LEDs, the surface states at the mesa-etched sidewalls are several diffusion lengths away from the active region. As the size of the LED reduces, the surface energy states are within the diffusion length of charge carriers, which increases the non-radiative recombination of electron-hole pairs. Surface recombination plays a significant role in radiative and internal quantum efficiency. The efficiency decreases as the μLED size reduces due to an increase of midgap energy states at the etched sidewalls. The recombination events can be defined by their lifetime, where the sum of the radiative lifetime, τ_r, and the non-radiative lifetime, τ_{nr}, describes the total probability of recombination events in the LED:

$$\tau^{-1} = \tau_r^{-1} + \tau_{nr}^{-1}. \tag{11.2}$$

Since radiative recombination is the desired process in LEDs, the ratio between the radiative lifetime and all recombination events is described by,

$$\eta_{IQE} = \frac{\tau_r^{-1}}{\tau_r^{-1} + \tau_{nr}^{-1}}. \tag{11.3}$$

These expressions show that the radiative lifetime should be the limiting process for the LED to operate within the radiative limit.

11.2.2 Reducing Non-Radiative Recombination by Sidewall Treatments

The practical fabrication of μLEDs includes an etching mechanism to establish and isolate devices across the host wafer. Dry etching is the favored method as it allows for a high anisotropic profile and resolution, and numerous efforts have shown controlled etch profiles with high anisotropy and low surface damage [159–165]. Inductively-coupled plasma reactive-ion etching (ICP-RIE) is a favored dry etch process that uses chemically reactive plasma to remove exposed material by accelerating energized ions towards the material. In ICP-RIE, two radio frequency sources individually control the plasma generation (ICP) and the forward bias of accelerated ions towards the wafer (RF). Decoupling the ICP and RF powers creates a large processing window where the density of the energized ions in the plasma and their acceleration towards the wafer is controlled separately. Chlorine (Cl)-based plasma is used to remove the III-V materials in the AlGaInP epitaxial LED structure.

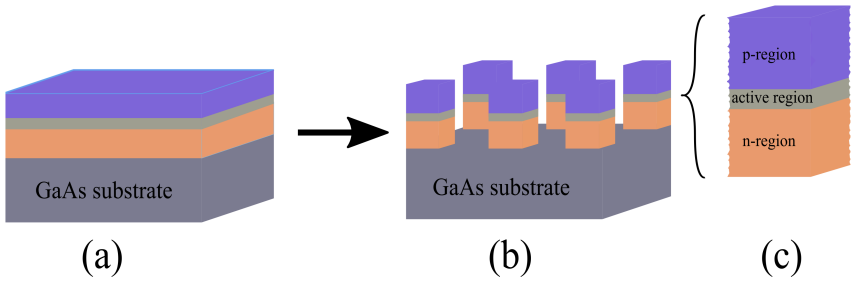

Figure 11.2: Dry etching procedure and sidewall damage where (a) displays the epitaxial layer structure on the host GaAs substrate, (b) displays the dry etch isolation step, and (c) zooms in on the roughened sidewalls due to the dry etch.

Figure 11.2(a)-(c) outlines the process of isolating LEDs according to a specific area through

photolithography and dry etching, where (a) presents the host wafer with the epitaxial structure, (b) presents the isolation of individual LEDs through dry etching and (c) shows the disruption in crystal periodicity at the roughened sidewalls. The damage during the dry etching process leads to defects at the sidewalls of the μLED, inducing surface recombination when the device is in operation. Wide E_g semiconductor regrowth is the primary passivation technique used in this work. Through process development, the top of the LED is protected by a dielectric material, so under the right growth conditions, the III-V material will not grow on top of the dielectric material and cover the top of the LED. This approach provides an avenue for in situ etching of the sidewalls immediately before sidewall regrowth, which avoids the complication of the sidewalls being exposed to air before passivation. Specifically, the in situ etching is accomplished using precursors with halomethane compounds that etch away III-V material under the right reactor conditions. During the process, chlorine radicals etch back nanometers of material at the sidewalls and remove the oxidized material. The etch is performed with a phosphine (PH_3) overpressure to etch back the PH_3-based layers.

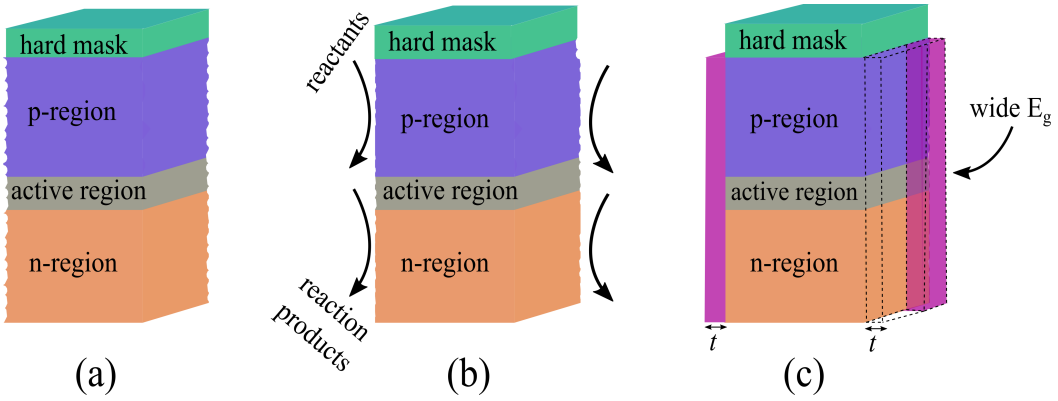

Figure 11.3: Diagram showing (a) LED with sidewall damage, (b) surface cleaning via wet-chemical etching or in situ etching and (c) sidewall regrowth of wide E_g semicondcutor.

The surface cleaning processes are shown in Figure 11.3(a)-(c) where the reactants consist

of wet chemistry or precursor to slightly remove material at the sides of the LED. This process is intended to reduce sidewall damage, as depicted in Figure 11.3(a). The overgrowth material must have a E_g that is wider than the QWs so that any lateral photon emission from the QWs does not parasitically absorb in the sidewall material. Two candidates are explored in this research, namely InGaP and AlInP, as the sidewall material. Although InGaP has the same E_g as the QWs, it was still explored to investigate the quality of sidewall coverage. Additionally, the sidewall material is less than 100 nm thick, which is optically thin and is expected not completely to absorb all internally emitted photons. Figure 11.3(c) displays the overgrowth of a wide E_g material with thickness, *t*. This thickness is targeted at less than 100 nm and uniformly coats all LED surfaces.

11.2.3 Light Extraction and Optical Power Output

The light extraction efficiency (η_{LEE}) describes the efficacy of internal radiative processing and depends on the design and quality of the active region and the η_{IQE}. Ideally, every emitted photon would exit the LED to be used as a useful light source. However, that is not the case in real LED structures. Practical loss mechanisms may occur, such as the absorption of spontaneously emitted photons into the substrate, absorption at the front metal contact, or total internal reflection. The η_{LEE} can be expressed by,

$$\eta_{LEE} = \frac{P_{out}/hv}{P_{int}/hv}, \tag{11.4}$$

where P_{out} is the optical power emitted into space. One main loss mechanism is the TIR of spontaneously emitted photons from the active region as they strike the internal front surface of the LED. The TIR depends on the escape cone angle, as described in Chapter 3. The escape cone is restricted by the dramatic change in the index of refraction between the semiconductor

and air [140]. The escape cone can be broadened using a low-index transparent layer deposited on the LED. Increasing the η_{LEE} enhances the optical power output, which is desired in LED display technology. Related to the optical power output and the η_{LEE} is the external quantum efficiency (η_{EQE}), which is the product of the IQE and extraction efficiency can be expressed as,

$$\eta_{EQE} = \frac{P_{out}/hv}{I/e}. \tag{11.5}$$

The η_{EQE} represents the ratio of the number of useful emitted photons to the number of injected electrons and is dependent on both the η_{IQE} and η_{LEE}. The η_{EQE} in practical LEDs begins to drop from its maximum point in a high current injection regime. This is known as efficiency droop and there are many mechanisms to explain this behavior, including Auger recombination, carrier leakage, defects, and the quantum-confined Stark effect [166–168]. The efficiency droop in LEDs refers to the reduction in efficiency with increasing current densities and can be expressed as,

$$droop = \frac{EQE_{Max} - EQE_J}{EQE_{Max}}. \tag{11.6}$$

The EQE_{Max} and EQE_J represent the maximum EQE value and the EQE at a given current density. Suppressing the slope in which the EQE reduces at a high injection current directly results from effective sidewall passivation and light extraction. Other methods such as front surface texturing are employed in μLED research to improve η_{LEE}. However, these methods require careful engineering to reduce surface recombination at the front of the LED. This work uses a low-index layer on top of the LEDs due to feasible processing without needing surface texturing.

11.3 Chapter Summary

Light management at the surfaces of LEDs is critical to increasing radiative recombination and light extraction efficiency, especially as the device area enters the sub-μm scale. Specifically, surface treatments at the sidewalls along with sidewall passivization through regrowth have the potential to significantly improve the radiative lifetime and recombination in μm-scale LEDs. Wet chemistry and in situ etching aim to remove thin sidewall layers while keeping the anisotropic profile determined by dry etching. These cleaning techniques can be used together or separately. The in situ etch allows immediate overgrowth of a wide E_g material to cover the sidewalls of the LED. This removes the impact of oxidation in Al-containing materials. The overgrowth requires thorough investigation to achieve uniform coverage across the sidewalls. Improving the η_{LEE} is accomplished in many ways, with the simplest being the addition of a transparent, low-index layer situated on top of the LED. This layer will add a step to the index of refraction and increase the internal escape cone of spontaneously emitted photons that strike the front surface of the LED. The process development of the μLEDs and the surface cleaning, regrowth, and low-index layer are discussed in the next chapter.

Chapter 12

Process Development of AlGaInP Micro-LEDs

12.1 Introduction

This chapter involves the process development of the red-emitting μLEDs, including LED chip design, ultraviolet photolithography, dry etching, surface cleaning, and regrowth. The processing steps are optimized through multiple process runs and material characterization. Microscopic imaging helps guide the experiments and relates the effective process parameters with LED quality. Numerous ICP-RIE dry etch recipes led to the optimal conditions capable of achieving vertical and smooth LED profiles. This set the basis for minimizing structural defects. Additional approaches using wet-chemical etching at the sidewalls were explored, and the promising candidate using a buffered oxide etch was identified. As well, in situ etching experiments developed a slow etch recipe using CCl_4 to remove nanometers of material at the sidewalls. The regrowth experiments are based on pre-existing high-quality growth conditions for the ternaries InGaP and AlInP. Microscopic imaging on the regrowth material determined which conditions lead toward uniform sidewall coverage.

12.2 Hard Mask Development and Photolithography

The μLEDs investigated in this work require a photolithography process that achieves a high resolution in sub-μm thick features. The features of the LEDs range between 5 μm, 10 μm, 15 μm, 25 μm, and 50 μm. The dry etching of the LEDs includes Cl-based plasma, so an inert material is chosen as the hard mask to protect the regions of the LEDs. The hard mask materials include SiO_2 and silicon nitride (SiN_x) since both have a slow etch rate in the Cl-based plasma. The flow in Figure 12.1 outlines the process of isolating the LEDs. This figure shows an example of 15 μm x 15 μm square LEDs with 10 μm pitch. Plot (a) represents a top-down diagram of some features on the mask, which is transferred to the hard physical mask, as shown in Appendix A. Figures 12.1(b)-(c) display the exposed photoresist using the patterned mask and the transfer of the pattern through the photoresist once exposed to UV light and developed.

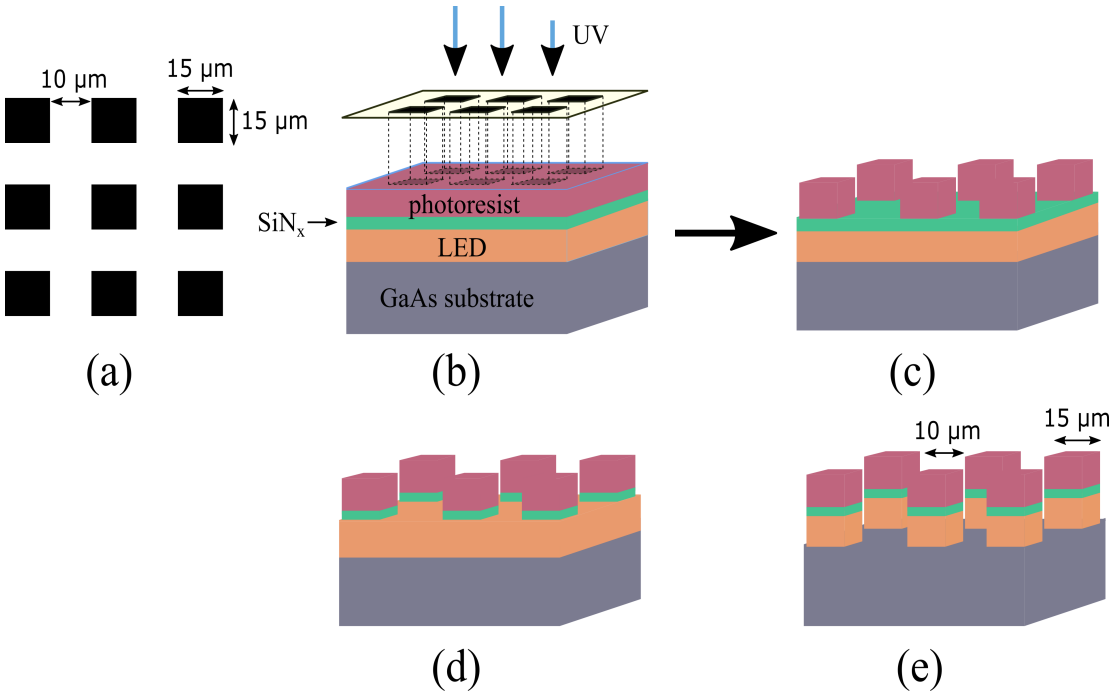

Figure 12.1: Process flow using hard contact lithography where (a) displays a top-view diagram of the hard mask, (b) displays the UV exposure of the mask on the coated wafer, (c) displays the patterned photoresist after exposure and development, (d) displays the dry etched hard mask and (e) displays the dry etched LED, which ideally follows the same shape as the original hard mask pattern.

The III-V mesa development depends on a repeatable lithography process that patterns the hard mask before the III-V dry etching. A positive photoresist, AZ MIR 701, is used due to its high resolution at the μm-scale. Figure 12.2 displays the photoresist profile using a Suss MicroTec MJB4 hard contact mask aligner with a broadband exposure dose equal to 132 mJ/cm^2. The profile has smooth sidewalls with an inclination of less than 10° and is near 1.1 μm thick. Ideally, the mask pattern will be transferred to the hard mask and LED through dry etching. However, optimization is required in the etch conditions to achieve this goal. Therefore, the dry etching conditions for the hard mask and the LEDs are optimized to realize

the highest resolution features using hard contact lithography.

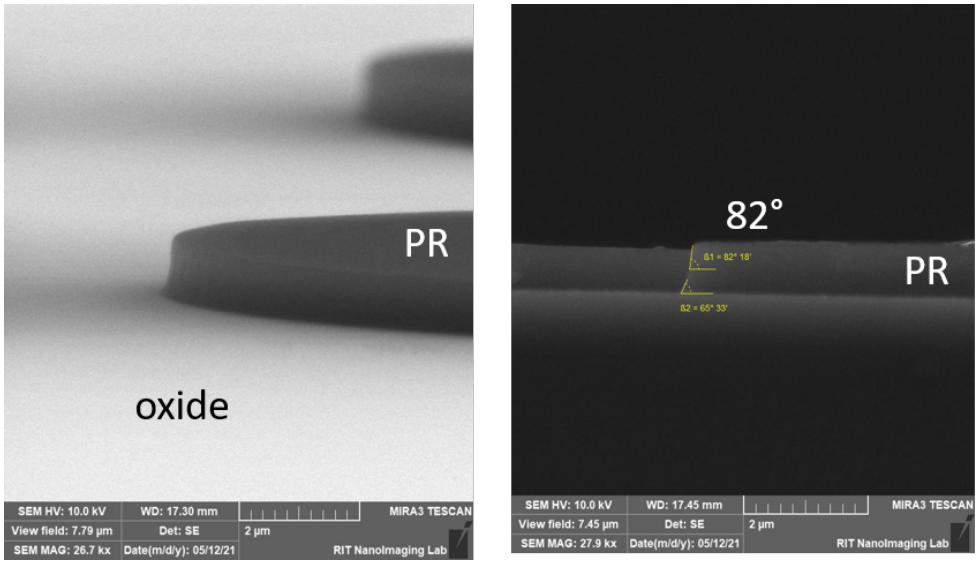

Figure 12.2: AZ MIR 701 photoresist profile using hard contact alignment with an exposure dose of 132 mJ/cm2.

The hard mask (green) is dry etched using a CF_4-based environment and takes on the same profile as the photoresist under the proper dry etching conditions, as illustrated in Figure 12.1(d). The SiN_x and SiO_2 are deposited using PECVD, and the target thickness is 500 nm to ensure complete protection at the tops of the LEDs during III-V dry etching. Figure 12.1(e) displays the completed LEDs with similar dimensions as the hard patterned mask. The 500 nm-thick Si-based films serve as the hard mask during III-V dry etching as the Cl-based plasma offers a highly selective etch to the III-V material. The Si-based masks are dry etched using the ICP-RIE system using fluorine-based plasma. Both hard masks required multiple dry etch recipes and SEM images to determine a recipe that achieves an anisotropic profile with high selectivity.

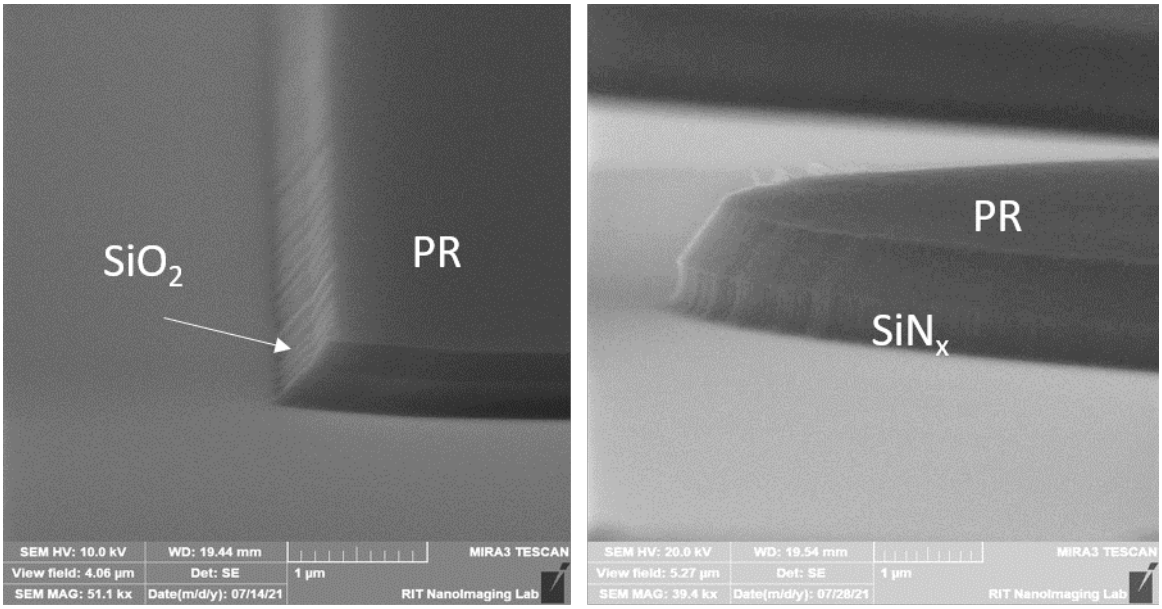

Figure 12.3: Best condition hard mask profile for (a) SiO_2 and (b) SiN_x based on the dry etch recipes in this work.

Figure 12.3 displays tilted SEM images for the best condition hard mask profiles of (a) SiO_2 and (b) SiN_x. The SiO_2 etching determined that the sidewall angle increases with high ICP power and low pressure. However, the selectivity reduces between the SiO_2 and photoresist, and the SiO_2 profile has a sidewall inclination of around 60°. The low selectivity resulted in incomplete etching of the SiO_2 layer before the photoresist was completely removed. On the other hand, the SiN_x profile has a sidewall inclination between 80-90° with selectivity greater than 1, so the photoresist completely protects the respective regions throughout the dry etch. The process parameters for the hard masks are reported Table A.2 in Appendix A.

12.3 Dry Etch Processing of Micro-LEDs

The epitaxial LED structure is dry etched once the wafer has been patterned using the process described above. Due to the broad process window available when performing ICP-RIE, several dry etch recipes were performed on the LED wafers. The dry etching was performed in a PlasmaTherm Apex ICP-RIE tool. Initially, the LED wafers were held at 20°C using chlorine (Cl_2), boron trichloride (BCl_3), and argon (Ar). The recipes explore a combination of conditions based on the tool parameter space. These conditions include the three gases listed above, the ICP power ranging from 0-800 W, the RIE power ranging from 0-200 W, and the pressure ranging from 5-25 mTorr.

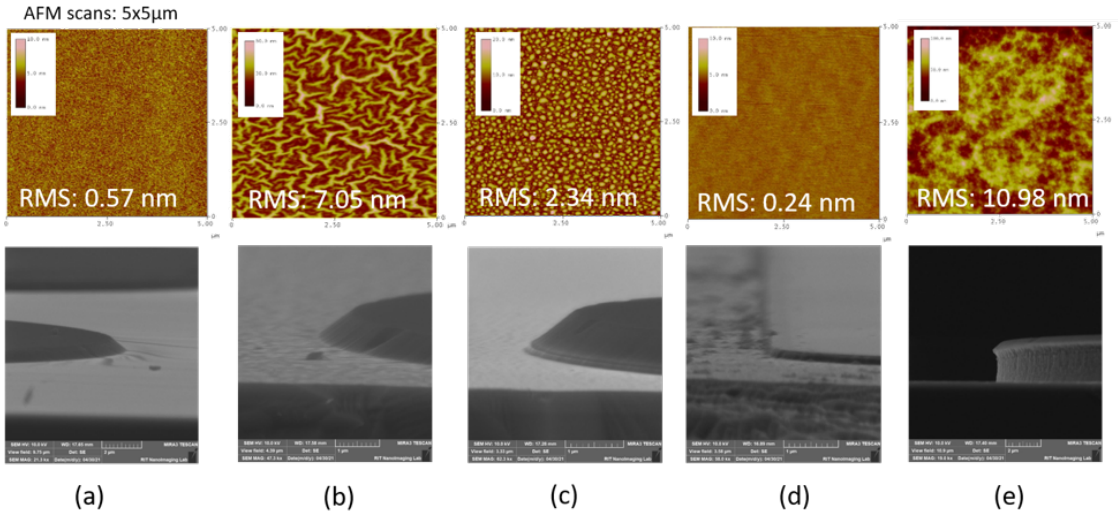

Figure 12.4: Initial ICP-RIE recipes using Plasmatherm at RIT on a type I epi wafer with etch conditions listed in Table 12.1 (a) recipe 1, (b) recipe 2, (c) recipe 3, (d) recipe 4 and (e) recipe 5.

Figure 12.4 displays the AFM and SEM images for the dry etch recipes as reported in Table 12.1 tested on the LED wafer with a SiO_2 hard mask. The surface roughness extracted from AFM correlates to the induced roughness and a high ICP power in runs 2 and 5. Additionally,

the etch rate significantly increases along with a higher ICP and forward bias. Promisingly, etch recipe 5 demonstrated quasi-vertical sidewalls using a BCl_3/Cl_2 plasma with a high ICP and RF power. The trade-off with increasing RF power is that anisotropic profiles are achieved, but surface roughness increases as the ion bombardment at the wafer increases. Therefore, the conditions used in recipe 5 were expanded to optimize the LED profile further.

Table 12.1: ICP-RIE dry etch conditions at 25°C

Parameter	Run 1	Run 2	Run 3	Run 4	Run 5
BCl3 (sccm)	10	0	20	0	20
Cl2 (sccm)	0	20	20	0	10
Ar (sccm)	0	10	20	20	0
ICP (W)	50	800	50	425	800
Bias (W)	50	50	150	250	250
Pressure (mTorr)	5	5	5	5	5
RMS (nm)	0.57	7.05	2.34	0.24	10.98
Etch rate (nm/min)	0	113	234	68	2513

Figure 12.5 displays the AFM and SEM for a second dataset of etch conditions and each recipe is associated with etch conditions in Table 12.2. According to the results from Figure 12.5(a)-(c), the surface roughness reduces with increasing pressure (runs 6-8). Additionally, the anisotropy is low for all recipes with a forward bias of less than 100 W. High anisotropy is linked to increased forward bias and ICP power, while a smooth surface may be achieved by increasing pressure. Increasing the pressure will reduce the mean free path of ions in the plasma, slightly reduce the etch rate, and reduce ion bombardment-induced physical damage to the III-V surface.

Based on the ICP-RIE results above, the recipes achieving low surface roughness and high anisotropic profiles were employed on the LED wafer using a patterned SiO_2 hard mask. The ICP-RIE recipes were performed at elevated temperatures to improve surface roughness through

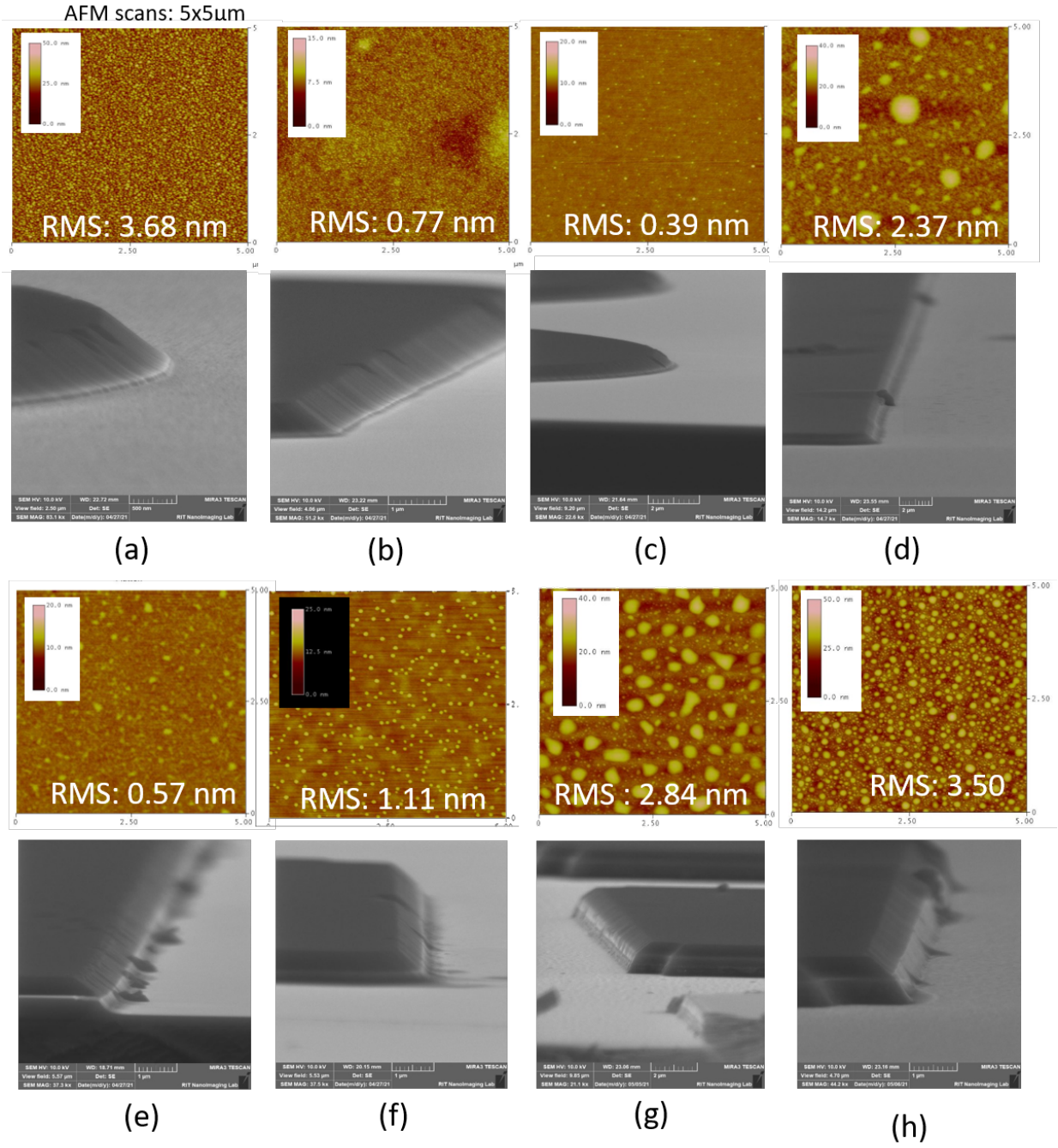

Figure 12.5: ICP-RIE results with conditions listed in Table 12.2 (a) recipe 6, (b) recipe 7, (c) recipe 8, (d) recipe 9, (e) recipe 10, (f) recipe 11, (g) recipe 12 and (h) recipe 13.

Table 12.2: ICP-RIE conditions associated with Figure 12.2 at 25°C

Parameter	Run 6	Run 7	Run 8	Run 9	Run 10	Run 11	Run 12	Run 13
BCl3 (sccm)	15	15	15	15	0	0	0	10
Cl2 (sccm)	0	0	0	0	15	15	20	10
Ar (sccm)	5	5	5	5	5	5	0	8
ICP (W)	450	450	450	450	450	450	300	550
RF (W)	15	15	15	35	15	35	250	130
Pressure (mTorr)	3	5	10	5	5	5	5	5
RMS (nm)	3.68	0.77	0.39	2.37	0.57	1.11	2.84	3.50
Etch rate (nm/min)	20	20	20	76	35	70	459	283

desorption of involatile $InCl_x$ byproducts [169, 170]. A temperature dot study determined the difference in temperature between the heater set point and the carrier wafers resting on the electrode. The Corning glass carrier used in this work has a low thermal conductivity and did not show any change in temperature with a set point of 100°C. For this reason, a 6" Si carrier wafer was used for elevated temperature recipes, which has a higher thermal conductivity. At a set point of 100°C, the temperature dots on the Si wafer confirmed a temperature between 77-82°C. Based on the temperature dot study, a 6-minute temperature stabilization step was added at the beginning of the elevated temperature etch recipes to confirm that the wafers were heated to the appropriate temperature. Figure 12.6 highlights the ICP-RIE etch recipe that demonstrates quasi-vertical and smooth sidewalls for the LEDs using a SiO_2 hard mask. The SEM images are taken at various angles where (a) is a cross-sectional (90° tilt), (b) is a 5° back-tilt from the cross-sectional position (95° tilt), and (c) is a 10° back-tilt from the cross-sectional position (105° tilt). The SiO_2 hard mask was not removed for the SEM images, and it can be seen in the angled region at the top of the mesas.

Numerous ICP-RIE dry etch recipes were conducted on the LED wafers using the SiO_2 hard mask using the PlasmaTherm tool using mid-range ICP and RIE power appears to result in high anisotropy when using a BCl_3/Cl_2 plasma. Increasing pressure and electrode temperature successfully reduce the surface roughness and sidewall damage. The final dry etch recipe

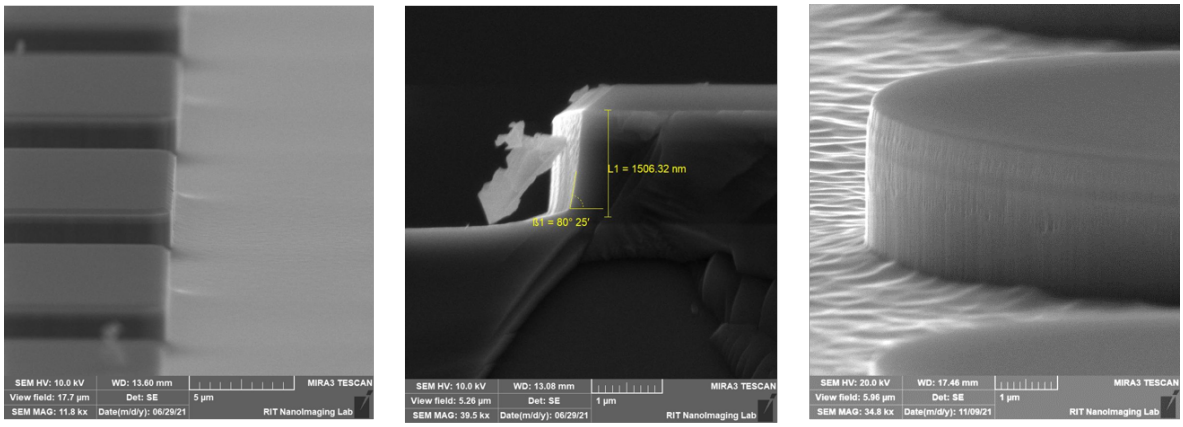

Figure 12.6: ICP-RIE quasi-vertical etch recipe to etch LED structures with different sizes and shapes including (a) 5 μm x 5 μm square (tilted 95°), (b) cross-sectional of 5 μm x 5 μm square and (c) 5 μm circular LED (tilted 95°).

BCl_3 (sccm)	20
Cl_2 (sccm)	10
Ar (sccm)	5
ICP (W)	500
RIE (W)	200
Sample T (°C)	80 ± 3
RMS (nm)	6.1
Etch rate (nm/min)	750
Anisotropy	0.8
Pressure (mTorr)	10

Table 12.3: Quasi-vertical etch recipe

achieving quasi-vertical and smooth sidewalls for the μLEDs is shown in Figure 12.6 and is used the isolate the LEDs throughout this work.

12.4 Surface Cleaning

During the dry etch processing of the LEDs, a slow-etch recipe resulted in an angled mesa profile. This profile is shown in 12.7. Although this recipe is far from the goal of achieving

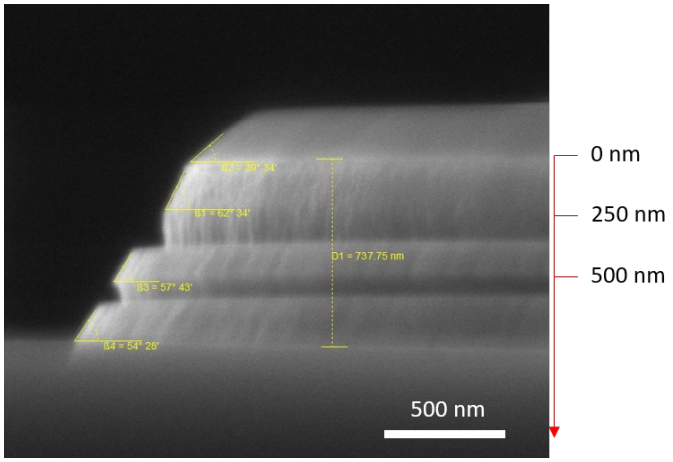

Figure 12.7: SEM image of the LED profile using a slow dry etch recipe.

anisotropic and smooth sidewalls, the particular profile was beneficial when testing different wet chemistries and extracting lateral etch rates (LER). The different regions in the LED structure can easily be distinguished from the SEM, making it suitable to calculate the etch rates and selectivity during wet etching. The wet-etch chemistries explored here include hydrochloric acid (HCl), phosphoric acid (Hl_3PO_4), and hydrofluoric acid (HF), diluted in DI water to investigate the change in etch rate and selectivity. Recently, surface treatment using diluted HF on 12 μm x 12 μm AlGaInP red LEDs showed a 35% boost in EQE after the chemical treatment [171].

Diluted HCl was initially investigated on the LED structures. Figure 12.8(a)-(c) displays results of HCl:H_2O with SEM images (b) 1:20 ratio and (c) 1:40 ratio. Figure 12.8(a) is a chart showing the LER measured from the SEM images taken from Figure 12.8(b)-(c). Figure 12.8(b) highlights smoothed sidewalls compared to the post-dry etch profile. However, a fast LER in the p-type region below the SiO_2 hard mask (top-most layer) is evident. The LER reduces as the H_2O concentration increases. However, the sidewalls do not appear to become smooth, as shown in Figure 12.8(c). The trade-off between smooth profiles and a fast LER makes the diluted HCl wet chemistry an inadequate cleaning procedure before sidewall regrowth.

Two different ratios using HCl:H_3PO_4:H_2O were explored on the dry etched LED mesas to

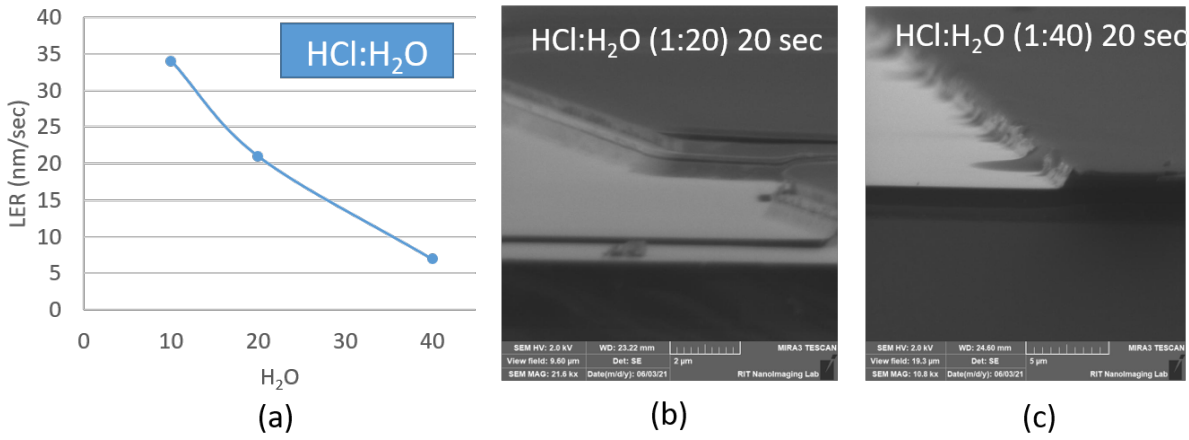

Figure 12.8: Wet etching LED structure for 20 seconds using the chemistry HCl:H_2O with two different ratios of (a) 1:20 and (b) 1:40.

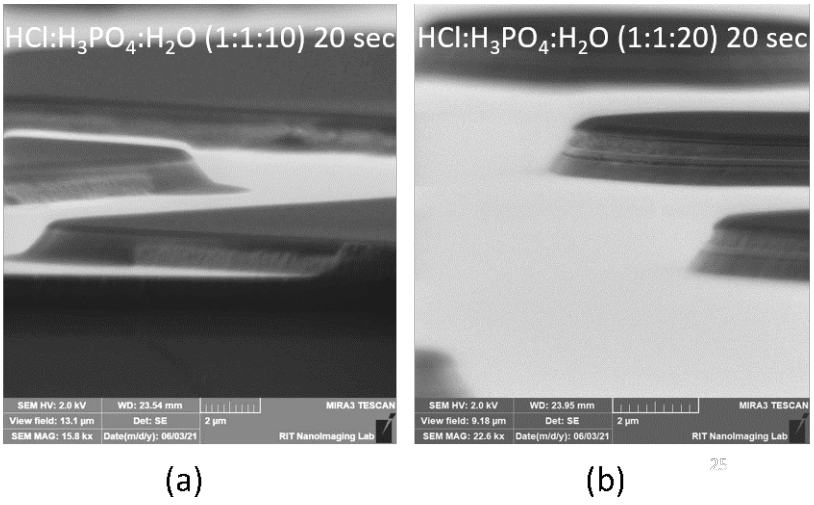

Figure 12.9: Wet etching LED mesa structure for 20 seconds using the chemistry HCl:H_3PO_4:H_2O with two different ratios of (a) 1:1:10 and (b) 1:1:20.

determine LER and sidewall morphology with increasing water concentration. The SEM images in Figure 12.9(a)-(b) show a 1:1 ratio between HCl:H_3PO_4 with increasing H_2O concentration, highlighting smooth sidewalls compared to the post-dry etch profile. For each case, reliable LER measurements determined from the SEM images were unattainable due to a significantly slow etch rate compared to the HCl:H_2O chemistry. With increasing H_2O concentration, this wet chemistry may be suitable for removing less than 100 nm and reducing damage at the sidewalls.

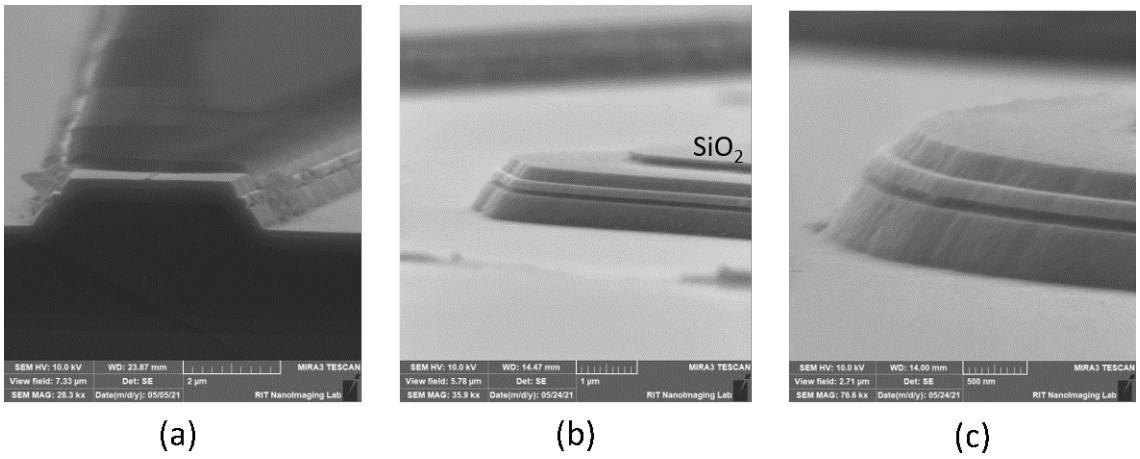

Figure 12.10: (a) SEM image post dry etch on a wagon wheel structure, (b) SEM on the wagon wheel structure in BOE for 5 minutes and (c) zoomed in SEM image (b).

The BOE treatment used in this work consists of a 1:10 ratio HF:H_2O to investigate the improvement in the sidewalls. Figure 12.10(b)-(c) displays the result of a 5 min BOE etch, while Figure 12.10(b)-(c) displays the post-dry etch profile. The BOE significantly reduces the sidewall roughness and removes material build-up along the edges. The SiO_2 hard mask etches away, as seen in Figure 12.10(b). However, a SiN_x hard mask has a slower etch rate in BOE and is a better candidate when using BOE as a surface clean prior to sidewall overgrowth. The AlInP layer appears to have a faster LER than the other layers, but this can be reduced with

a shorter BOE clean in less than 5 minutes.

12.5 Wide Bandgap Overgrowth

The wide E_g overgrowth material for sidewall passivation investigated in this work includes the $In_{0.49}Ga_{0.51}P$ and $Al_{0.52}In_{0.48}P$, both lattice matched to GaAs. In total, eleven combinations of surface treatments and sidewall growth were investigated and labeled according to the alphabet, as seen in Table 12.5. Initially, various surface treatments, including the BOE wet chemical etch and the in situ etch, where combined with the same overgrown material, as seen for conditions A through F. This initial study was followed by surface characterization, as shown below, along with photoluminescence, which is discussed in Chapter 13. The conclusions from the first study trajected the second study following the conditions shown in G through K.

Sample	$Material$	$Thickness(nm)$	V/III	$GT(°C)$	$BOE(min)$	$insitu(min)$
A	$InGaP$	60	110.3	675	N/A	Y
B	$InGaP$	60	110.3	675	N/A	N
C	$InGaP$	60	110.3	675	1	N
D	$InGaP$	60	110.3	675	3	N
E	$InGaP$	60	110.3	675	1	Y
F	$InGaP$	20	110.3	675	3	Y
G	$InGaP$	20	110.3	675	5	Y
H	$InGaP$	20	110.3	700	5	Y
I	$InGaP$	20	198.8	700	5	Y
J	$AlInP$	60	56.5	650	5	Y
K	$AlInP$	60	56.5	700	5	Y

Table 12.4: Overgrowth and surface treatment conditions

Conditions A-F follow the same InGaP passivation growth, which is based on established growth conditions for high-quality InGaP. Samples A and B did not receive a BOE surface treatment after ICP-RIE etch and before loading into the MOVPE reactor. Samples E and C were etched in BOE for 1 minute, while samples F and D were etched for 3 minutes. Samples

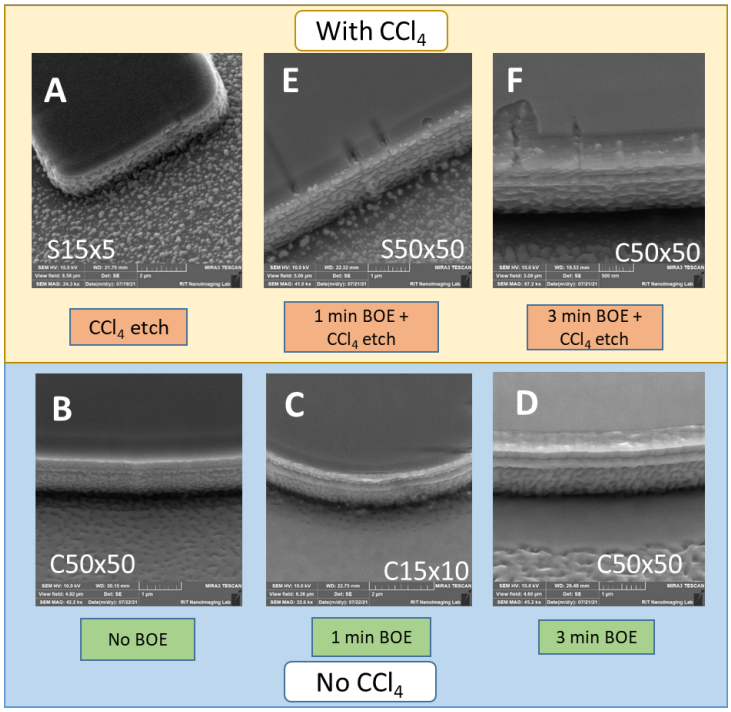

Figure 12.11: SEM images of InGaP overgrown sidewalls of Type II epi material under indicated etch/cleaning regimens for samples A-F.

A, E, and F also received the in situ etch before overgrowth, while samples B, C, and D did not. The in situ etch conditions are consistent across all samples and include the introduction of CCl_4 with a PH_3 overpressure. Samples A, E, and F received a CCl_4 etch after the sample was cooled to 650°C but before the InGaP growth. The etch used a molar ratio of 1.2×10-4 for 143 seconds, targeting 10 nm of sidewall removal. For MOVPE growth, the samples were brought to a bake temperature of 700°C under a PH_3 overpressure and held for 5 minutes. The temperature was lowered to 650°C, where 20 nm of InGaP was grown at 3.12 μm/hr with a V/III ratio of 110. After growth, the sample was cooled under a PH_3 ambient.

The SEM images in Figure 12.11 show sidewall morphology post-overgrowth. In samples with the CCl_4 etch, cracks in the SiO_2 film can be seen, which propagate through into the epi. This cracking was due to the aggressive nature of the Cl-based etching and was eliminated

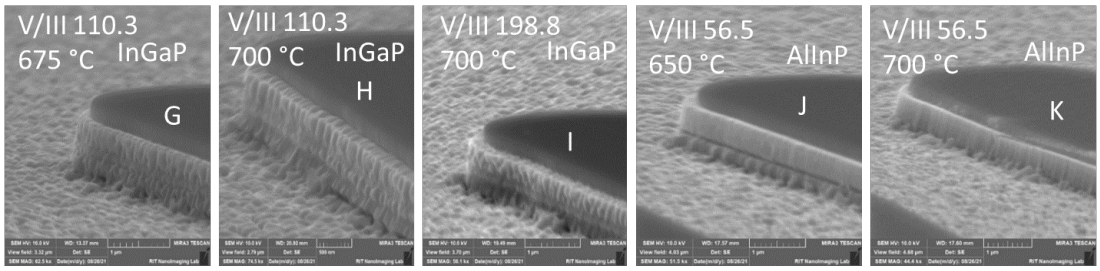

Figure 12.12: SEM images on wagon wheel structures (major flat to the left) on conditions G-K.

by switching to SiN_x. Sidewall morphology of the InGaP in all cases looked somewhat non-continuous and island-like. The island-like nucleation of InGaP may result from both sidewall damage and the nature of the exposed crystal planes. While the overgrowth will require further investigation, the current sample set was still investigated for the efficacy of the passivation using InGaP, as discussed next.

The second set of samples, denoted G-K, was prepared similar to the A-F set. The main change was that SiN_x was used as a hard mask instead of SiO_2. The test conditions centered on the best conditions from the previous set, sample F, which used a 3-minute BOE clean coupled with a CCl_4 etch. Three samples continued with InGaP overgrowth, first repeating condition F (G), then increasing growth temperature (H), and both growth temperature and V/III. Two additional samples used AlInP as the overgrowth material, targeting 60 nm of growth using previously developed conditions with a temperature of 650°C (J) and 700° (K).

SEM images of sidewalls from samples G-K are shown in Figure 12.12. Despite all samples receiving a CCl_4 etch, there is no apparent cracking in the SiN_x hard mask as was observed in the SiO_2 hard mask, suggesting the SiN_x is better suited to protecting the red epi during this cleaning and overgrowth process. Additionally, the sidewalls overgrown with AlInP (J, K) appear much smoother than the InGaP samples, indicating complete wetting and two-dimensional growth on the sidewall. Figure 12.13(a)-(c) compare the SiO_2 and SiN_x hard mask

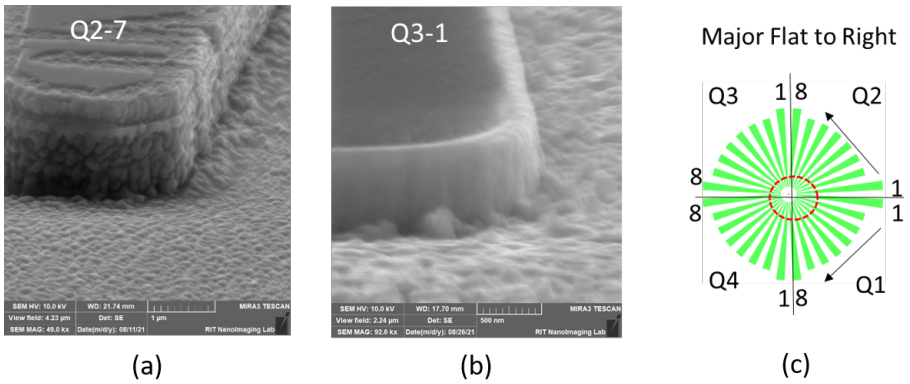

Figure 12.13: Wagon wheel SEM images of (a) SiO_2 mask with cracks from CCl_4 in situ etch and roughened InGaP regrowth (condition F) and (b) SiN_x mask without cracks from CCl_4 in situ etch and smooth sidewalls from AlInP regrowth (condition K). Plot (c) displays the wagon wheel notation.

after the in situ etching. In particular, Figure 12.13(a) shows the roughened InGaP regrowth of condition F with cracking in the SiO_2 caused by the in situ etch. Figure 12.13(b) shows the smooth AlInP regrowth from condition K with a smooth SiN_x mask, confirming the robustness of the SiN_x when exposed to the in situ etch. Figure 12.13(c) displays the wagon wheel notation for reference.

12.6 Micro-LED Fabrication

The processing of the LED wafers shown in Figure 12.1 describes the photolithography and dry etching of the hard mask and LEDs. The size of the LEDs depends on the dimensions of the hard physical mask, which consists of circular and square mesa sizes with spacings ranging from 5 μm, 10 μm, 15 μm, 25 μm, and 50 μm. There is much research that focuses on the use of a transparent conductive oxide (TCO) such as indium tin oxide (ITO), but many challenges surface relating to the high resistivity in ITO and GaP as the top contact layer [172]. Initially, a simple process using ITO top contacts was attempted, but a couple of issues made this approach unsuccessful. Mainly, the poor contact between GaP and ITO and the incomplete passivation

between the ITO and the substrate, which provided an alternative pathway for current to travel, put this top contact scheme at a halt. A more successful and direct approach using lithography and metal deposition allowed the μLEDs to be measured electrically, as discussed in Chapter 13. The design is shown in Figure 12.14(a), where each material is denoted in the key. The contrast between the index of refraction at the top semiconductor and air leads to the TIR of photons that spontaneously emit after radiative recombination in the active region of the LED. Using a low-index layer that is also transparent at the top of the LED will improve light extraction at the top of the LED. Since the LED requires back and top contact for electrical transport, the top grid finger design is often used [173]. Like in solar cells, top metal grids lead to some shadowing loss as photons are blocked from leaving the LED. This leads to a grid finger shadowing percentage loss. Since this is a top-down diagram, the SiN_x hard mask on top of the LED is not drawn. It is important to note that this SiN_x mask remains intact in this top contact design, and a small pocket in the SiN_x is exposed so that a single metal grid finger can contact the top GaP layer. Figure 12.14(b) is a tilted SEM image (10° backward tilt using a cross-sectional stage) that displays the completed fabrication on a 25 μm square LED. In this image, the metal grid finger fills the dry etched pocket in the SiN_x, making electrical contact with the GaP contact layer. The metal grid finger and busbar are completely isolated from the sidewalls and the field (substrate) using a second SiN_x isolating layer. The SiN_x isolating layer is to confirm full passivation of the sidewalls and field in case there are regions of non-uniform III-P growth.

This design consists of two lithography levels: (1) SiN_x pocket dry etch and (2) metal deposition (Figure 12.15(c)). Before starting lithography, 100 nm of SiN_x was deposited via PECVD to completely cover the sidewalls and field on each chip. Level 1 exposes a small triangular region on the tops of the LEDs to dry etch away the SiN_x hard mask. Notably, the

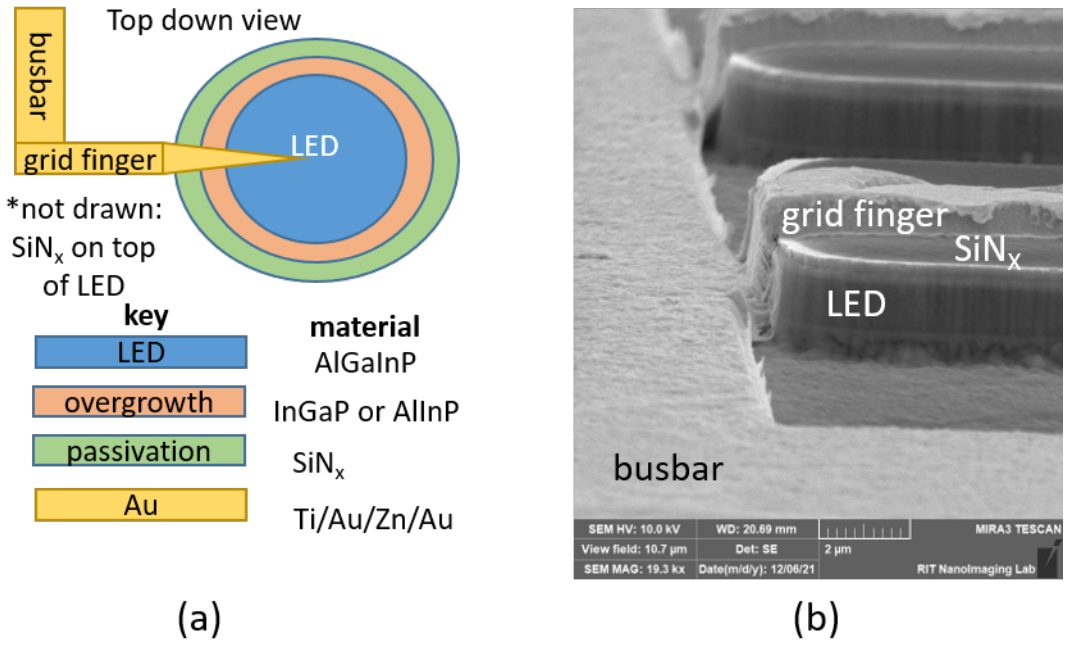

Figure 12.14: Plot (a) is a top-down cartoon diagram displaying the LED design to contact the top GaP contact layer, and plot (b) is a tilted SEM image of a completely fabricated 25 μm LED using the design in the plot (a).

entire SiN_x mask was not removed due to previous studies showing increased damage to the III-V materials when exposed to CF_4 plasma. The exposed region (black triangles) is shown in the GDS image in Figure 12.15(a), and Figure 12.15(b) is a microscope image showing the pocket exposing the GaP layer after dry etching. The second layer exposes regions for patterning the grid fingers and metal grid, as shown in Figure 12.15(c). The grid finger overlays the exposed pocket in the SiN_x mask for a single LED. Figure 12.15(d) offers a microscope image of the developed pattern before evaporating the metal for a square 25x15 μm LED array. For the metal, a 3 nm Ti adhesion layer was thermally evaporated, then the Au (20 nm)/Zn (20 nm)/Au (850 nm) stack was evaporated. The metal was lifted off using an ultrasonic NMP bath heated to 35°C for 25 minutes. The backside contact consists of Ge (20 nm)/Au (20 nm)/Ni (5 nm)/Au (400 nm) stack, and the metal layers were annealed in N_2 for 6 mins at 407°C.

Some images contacting the LEDs are shown in Figure 12.16(a)-(b) where the plot (a) is a

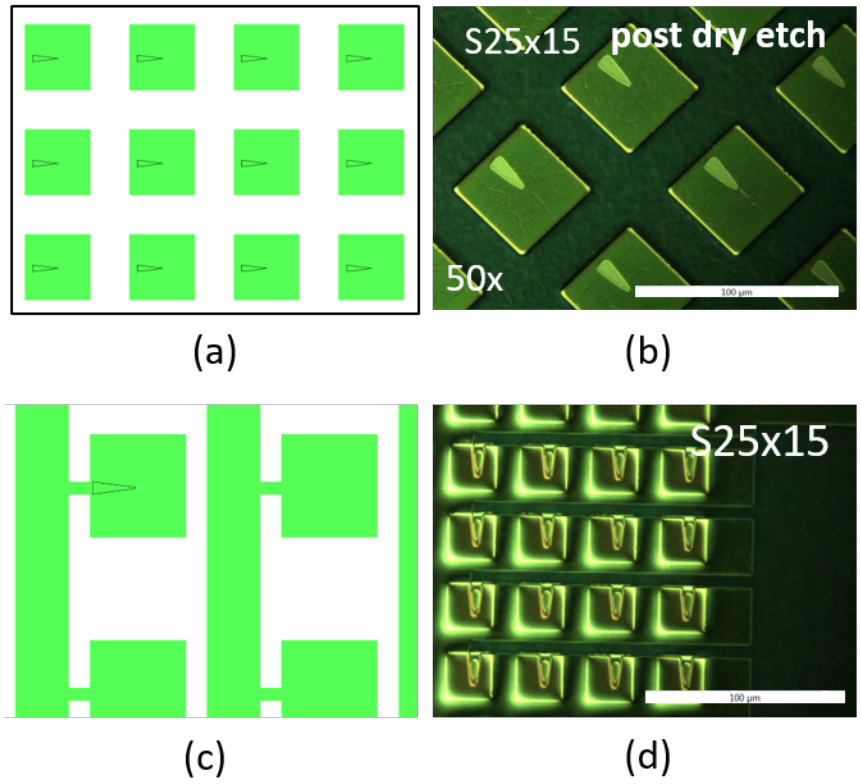

Figure 12.15: Plot (a) is a GDS image of the first lithography layer showing a 25x15 μm square LED array where the small triangles are the pockets to dry etch through the SiN_x. Plot (b) is a microscope image of the square 25x15 μm LED after the SiN_x pocket etch. Plot (c) is a GDS image of the second lithography layer showing a 25x15 μm square LED array where the grid fingers and busbars expose regions for metal evaporation. Plot (d) is a microscope image after layer 2 was developed to show the metal grid design.

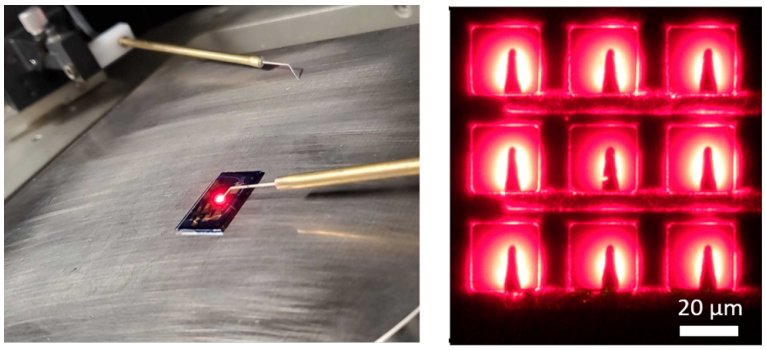

(a) (b)

Figure 12.16: Plot (a) is a picture contacting a 25 μm LED on a chip and plot (b) is a Keyence microscope image contacting a 3x3 array of 15 μm square LEDs.

picture when a single 25 μm LED is in contact and (b) is a microscope image contacting a 3x3 array of 15 μm square LEDs.

While this fabrication process allowed the LEDs to be measured electrically, the metal shadowing reduced the optical power output. Also, current crowding around the metal grid finger is evident and most likely due to the thin GaP contact layer. Future work to update the fabrication process to use transparent conductive oxides while achieving adhesion at the GaP contact layer is required to improve the LOP of the devices.

12.7 Chapter Summary

This chapter involves processing AlGaInP μLEDs to achieve a quasi-vertical profile and smooth sidewalls by optimizing lithography and the dry etching process. The LED dry etching relies on a repeatable hard mask lithography process, developed for both SiO_2 and SiN_x hard masks. The best known dry etching conditions for SiO_2 were developed initially, and later the SiN_x due to its anisotropic and smooth profile, high selectivity, and slow etch rate in BOE. Many iterations of the BCl_3/Cl_2 dry etch performed on the mesas resulted in a quasi-vertical profile with smooth sidewalls. This was accomplished using a mid-range ICP and RIE power. The

elevated electrode temperature allowed the $InCl_x$ byproducts to be completely removed from the surface without redepositing, which led to increased surface roughness. Surface cleaning using both wet-chemical and in situ etching was explored. Specifically, the BOE wet etch resulted in the smoothest profile post-dry etch compared to the diluted $HCl:H_3PO_4:H_2O$ mixtures. The in situ etching allows for small amount of the sidewall material to be removed immediately before overgrowing the wide bandgap semiconductor. Through SEM, the sidewall overgrowth profiles were explored, and the in situ etching using CCl_4 resulted in the SiO_2 cracking. Switching to SiN_x removed this issue and any impacts from regrowth material growing on the tops of the LEDs. Overall, the InGaP sidewall morphology was not as smooth as the AlInP. The AlInP growth condition K also has the most uniform coverage according to the crystalline direction. These results give insight into the sidewall coverage according to the growth conditions.

Chapter 13

Micro-LED Characterization

13.1 Introduction

This chapter involves the optoelectronic analysis of the LEDs with different active region thicknesses. The LEDs undergo various sidewall treatments as described in the previous chapter. These treatments include combinations of BOE sidewall etch and regrowth conditions. The power-dependent photoluminescence (PDPL) measurements provide evidence of the recombination events as higher photoexcitation of carriers saturates the trap-related defects. From this analysis, the slope in PL suggests what combination of sidewall treatments effectively reduces sidewall defects. These PDPL measurements are expanded to a generation rate analysis where the internal quantum efficiency, relative to the material parameters, is modeled. Both analyses show that BOE, in situ etching, and AlInP regrowth are effective at passivating the sidewalls. The InGaP regrowth leads to incomplete sidewall coverage and reduces the optical performance of the LEDs. This result is confirmed when four conditions, including the untreated, A, F, and K, are fabricated into LEDs with top and bottom contacts. Finally, the electroluminescence analysis suggests that the InGaP regrowth is parasitically reducing the LOP potentially due to its narrow bandgap energy relative to the quantum wells and the incomplete passivation.

13.2 Power-Dependent Photoluminescence

PDPL is a valuable tool providing evidence of the recombination events in direct bandgap semiconductor devices. The generation of photoexcited carriers changes according to the laser power density. At low injection, the recombination in the active region of the LED is dominated by mid-gap trapping centers or defects. As the injection level increases, the traps are saturated with carriers, and radiative recombination begins to dominate. The LED that reaches a higher PL intensity at any laser power density indicates a smaller amount of trapping centers, which is dependent on the sidewall passivation.

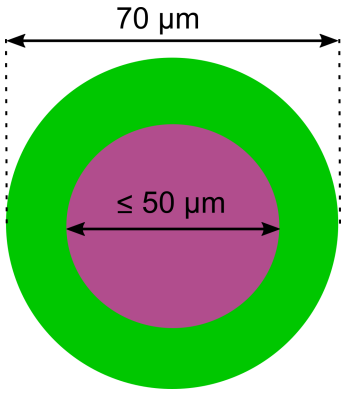

Figure 13.1: Top-down view of the 532 nm laser saturating the LED under test.

PDPL measurements were taken on single 50μm x 50 μm LEDs with conditions A-F using a Horiba micoOS PL system and a 532 nm excitation laser. The laser power density incident on the LED is controlled using neutral density filters and keeping the laser spot size consistent across all measurements. The LED spot size of 70 μm in diameter overfilled the LEDs to avoid the complication in the analysis due to carrier diffusion, which occurs when the excitation spot is smaller than the LED area. The procedure for the PDPL analysis to extract the recombination regimes has been described previously by Walker et al. [174] where PL measurements are taken at different laser intensities, and the integrated PL signal normalized to the incident laser

intensity generates profiles to exhibit recombination regimes. The top-down diagram of the laser saturating the LED is shown in Figure 13.1. The 532 nm laser power is held constant at 380 mW/cm^2 and the neutral density filters reduce the incident power density on the LEDs.

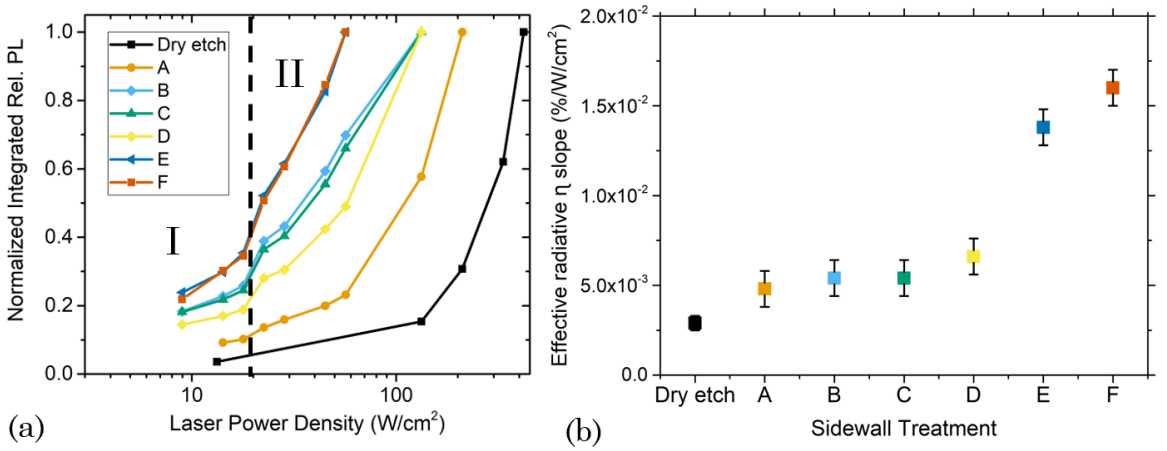

Figure 13.2: For conditions A-F, Plot (a) is the normalized integrated PDPL vs. laser power density and plot (b) is the effective radiative efficiency slope in Regime II for each condition.

Within the 50 μm x 50 μm circular mesa array, five mesas were selected along the diagonal of the array, and PDPL measurements were taken. The non-radiative recombination centers dominate at low excitation levels, and the PL begins to plateau in Regime I, as shown in Figure 13.2(a). The increased excitation level in Regime II increases the PL signal from each LED as the trapping centers become saturated and radiative recombination dominates. Notably, the PL signal at any given laser power density increases for the LEDs with improved sidewall passivation, which is directly related to the sidewall treatments. This is true for all conditions A-F when compared to the dry etched LED with no sidewall treatments (black curve). Conditions E and F saturate at lower injection levels, resulting in the greatest PL signal compared to the other conditions. The slopes extracted from the PL signal trends reveal which sidewall conditions reach the radiative recombination regime faster. The slopes in Regime II for each

condition are shown in Figure 13.2(b), where conditions E and F display the highest slopes. Interestingly, conditions A-D behave similarly and indicate that wet etching alone is not sufficient in reducing sidewall damage before regrowth. Since conditions A-D represent sidewall treatment with either BOE or in situ etching, E and F indicate that some combination of the two treatments is necessary before regrowth to reduce non-radiative recombination events at the sidewalls.

The first round of conditions labeled A-F focused on InGaP regrowth and combinations between BOE and in situ etching to passivate the sidewalls. One consideration is that the sidewall material has the same bandgap energy as the QWs, which may parasitically absorb any radiatively emitted photons at the sidewalls. The results from conditions A-F show that some combination of BOE and in situ etching treatments are crucial to enhancing the PL signal. These results projected another study to explore the use of AlInP in a new set of regrowth samples denoted as conditions G-K. To recall, condition G is a repeat of the best-known condition from the original dataset, condition F. Using AlInP as the regrowth material has benefits beyond InGaP, including its indirect bandgap, which makes it transparent at the QW emission. Single point PL measurements initially gauged the efficacy of the new conditions. The 15 μm x 15 μm LEDs are saturated with the laser in all measurements. Figure 13.3(a) presents the PL signal from one 15 um LED for each condition and plot (b) presents the average and standard deviation across six LEDs for each condition. Both plots show that the AlInP regrowth samples J and K achieve the highest PL signal and condition I is the lowest. Interestingly, the higher growth temperature InGaP conditions (H and I) did not show a higher PL intensity than the standard condition G. The high V/III ratio in condition I led to a film that has a higher group V-rich condition, which red-shifted the PL peak. This may be due to a higher degree of hillock density in the InGaP film due to dislocation [175].

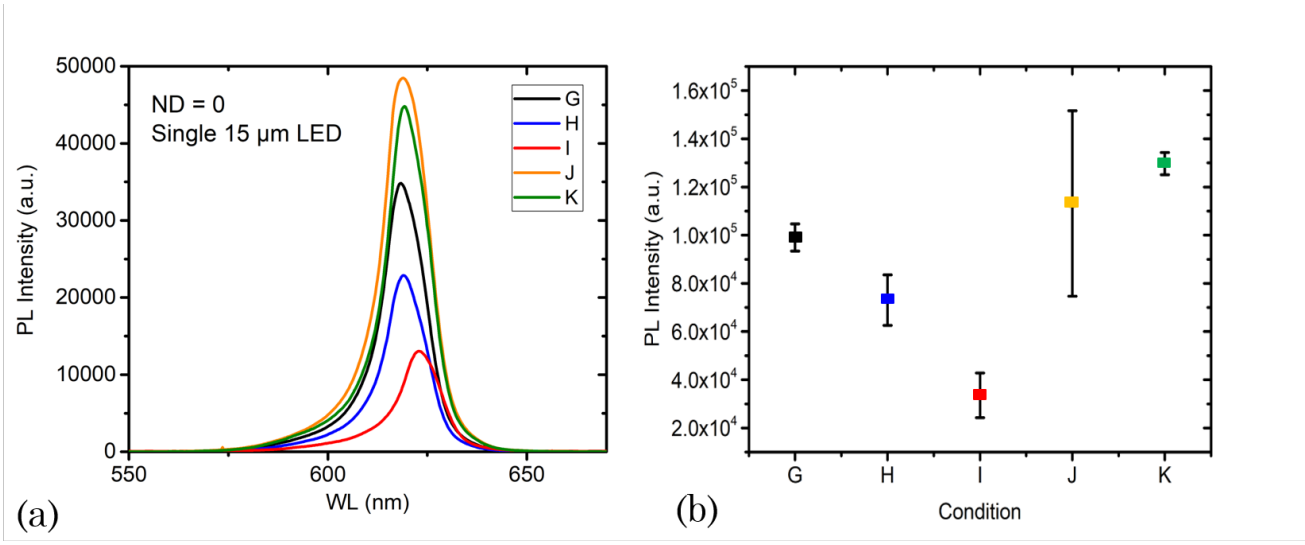

Figure 13.3: Plot (a) is the PL spectra for conditions G-K on a single circular 15 μm x 15 μm LEDs and plot (b) is the average and standard deviation of PL intensity across six LEDs.

PDPL measurements were taken on the six 15 μm x 15 μm LEDs from conditions G-K, and an IQE analysis was conducted on the average PL signal across the six LEDs as a function of laser power density. Based on the PDPL measurements, the IQE can be modeled according to the generation rate, G, and carrier concentration, n [176]. In this analysis, the IQE is expressed in terms of the carrier generation rate, which is based on the recombination events, as shown in Equations (13.1)-(13.2).

$$G = R_{total} = An + Bn^2, \tag{13.1}$$

$$IQE = \frac{Bn^2}{An + Bn^2} = \frac{Bn^2}{G}, \tag{13.2}$$

The generation rate is theoretically expressed in terms of fitting parameters, P_1 (Equation 13.5) and P_2 (Equation 13.6). In these expressions, η is a constant determined by the total

collection efficiency and volume of the active region. The measured integrated PL intensity, I_{PL}, is determined from the PDPL measurements as seen in Equation 13.3. The fitting parameters and modeled generation rate are found in Equations (13.4)-(13.6).

$$I_{PL} = \eta B n^2, \tag{13.3}$$

$$G = \frac{A}{\sqrt{B\eta}}\sqrt{I_{PL}} + \frac{1}{\eta} I_{PL}, \tag{13.4}$$

$$P_1 = \frac{A}{\sqrt{B\eta}}, \tag{13.5}$$

$$P_2 = \frac{A}{\eta}, \tag{13.6}$$

Experimentally, the generation rate can be determined based on the excitation laser source shown in Equation 13.7, where α is the absorption coefficient of the InGaP quantum wells at 532 nm, P_{laser} is the power of the laser with no neutral density filter, R is the front side reflection of the LED, A_{spot} is the excitation area, and hv is the energy of the photon at 532 nm.

$$G = \frac{\alpha P_{laser}(1-R)}{A_{spot} hv} = P_1 \sqrt{\eta}\sqrt{B} n^2 + (\sqrt{B} n)^2. \tag{13.7}$$

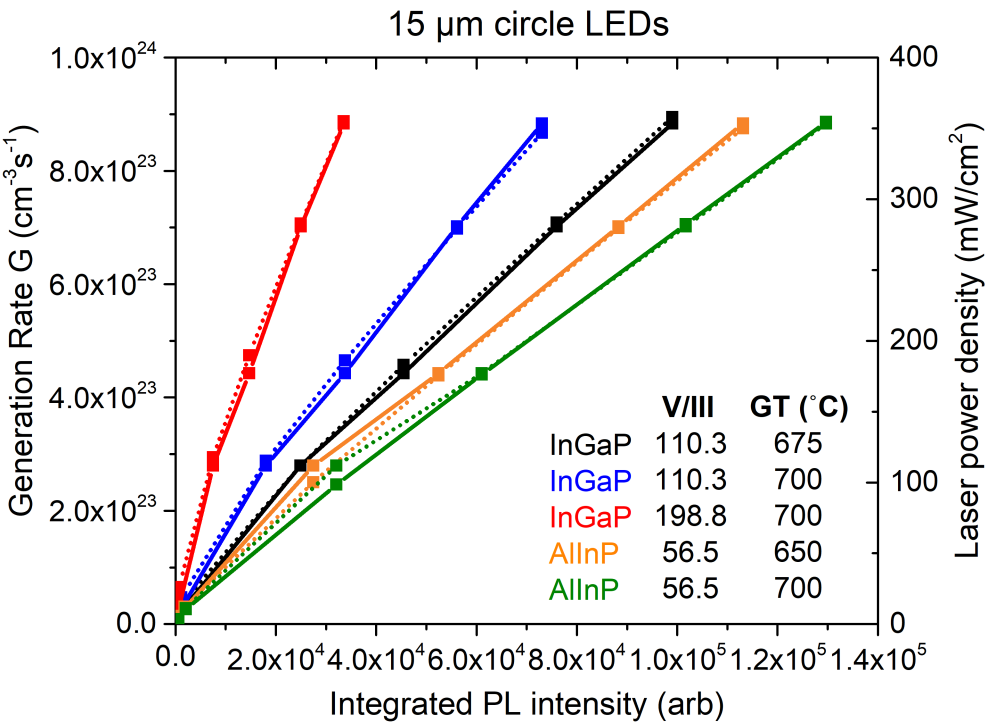

Figure 13.4: Generation rate (G) vs. integrated PL intensity (I_{PL}) for conditions G-K based on PDPL measurements and fitted curves.

Figure 13.4 displays the fitted (dotted curves, Equation 13.4) and experimental (solid curve, Equation 13.7) generation rate versus the measured integrated PL intensity for conditions G-K. The modeled generation curves agree with the experimental curves, and the fitted parameters are listed below in Table 13.2. This plot shows that the AlInP conditions J and K achieve the highest integrated PL signal at any given generation rate. From the fitted results, the radiative recombination coefficient can be solved by manipulating Equation 13.4, which can then be input into Equation 13.2 to solve for the IQE and carrier concentration.

Sample	P_1	P_2	Bn^2	IQE
G	$7.4x10^{20}$	$6.4x10^{18}$	$4.3x10^{23}$	49.1
H	$1.1x10^{21}$	$7.8x10^{18}$	$3.2x10^{23}$	36.3
I	$2.1x10^{21}$	$1.5x10^{19}$	$1.9x10^{23}$	21.5
J	$4.5x10^{20}$	$6.4x10^{18}$	$5.9x10^{24}$	66.5
K	$3.0x10^{20}$	$6.0x10^{18}$	$6.7x10^{24}$	76.0

Table 13.1: Fitting parameters and extracted IQE at 9x10^{23} cm^{-3}

The IQE vs. carrier concentration is shown in Figure 13.5 for conditions G-K. As discovered in the generation rate vs. integrated PL intensity, the AlInP-based regrowth conditions J and K achieve the highest IQE at any given carrier concentration. Specifically, J and K conditions achieve IQE above 50% at a carrier concentration equal to 5x10^{16} cm^{-3}. This result is consistent with the high PL intensity in Figure 13.3 and the smooth sidewalls shown in the SEM image in Figure 12.13. The best-known InGaP-regrowth condition is G, which includes both BOE and in situ etching at a low growth temperature. Condition I achieves the lowest IQE, and its carrier concentration is below 5x10^{16} cm^{-3} due to a low integrated PL intensity as the sidewall passivation is inadequate.

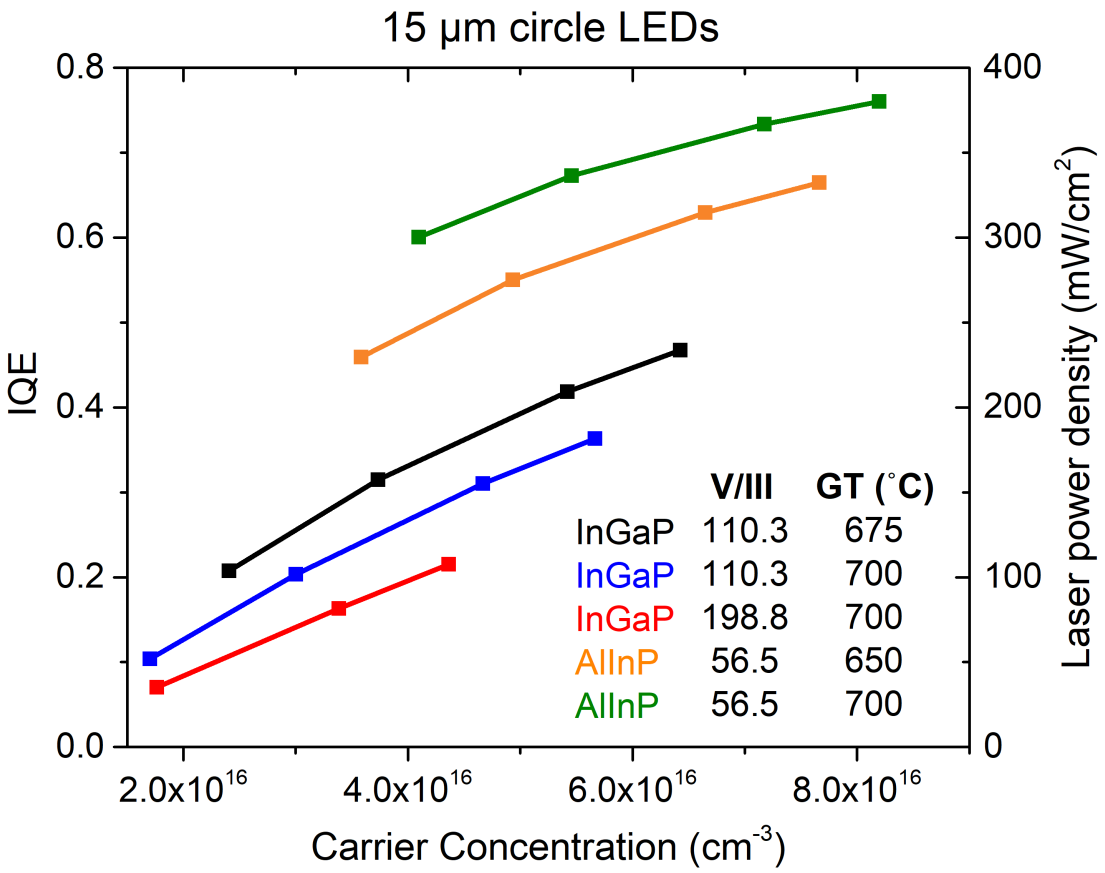

Figure 13.5: Internal quantum efficiency as a function of carrier concentration for conditions G-K.

Using Equation 13.1, the non-radiative SRH recombination coefficient is determined at a given generation rate. Figure 13.6 displays the extracted SRH coefficient at a generation rate equal to 9x10^{23} cm^{-3}s^{-1}. Condition I results in the highest SRH recombination due to the low-level integrated PL signal and reduced carrier concentration at any given laser power density. Condition K also has the lowest SRH coefficient, indicating the best-known sidewall passivation across the treatments explored. SRH coefficients for AlInP reported in literature are between 1x10^{6}-1x10^{8} s^{-1}, and the values reported in this research are within this range [176, 177]. It is worth noting that the values extracted for IQE and SRH depend on the fitting parameters and

result in some open-ended quantitative interpretation, but the trends and comparison across each sample are accurate.

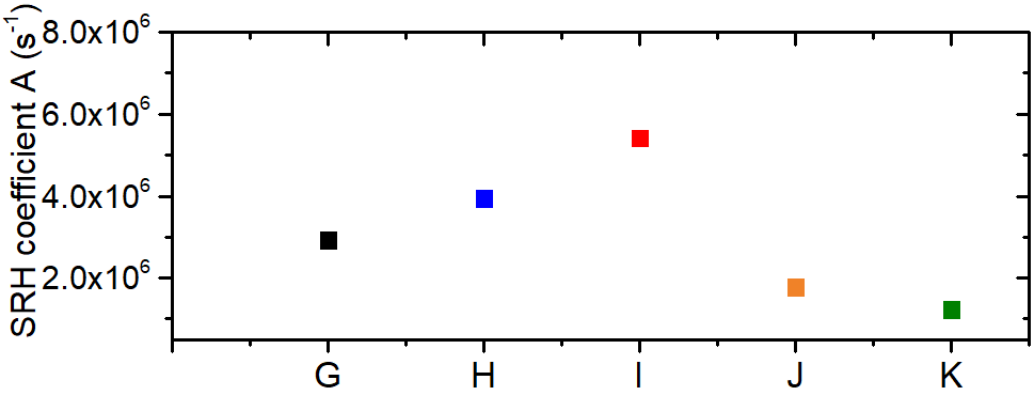

Figure 13.6: SRH recombination coefficient, A, according to different sidewall treatments. B is equal to 1x10^{-10} cm^3/s.

Overall, the PDPL analyses conducted on the LEDs with various sidewall conditions show that both the BOE and in situ etching in conjunction with AlInP passivation are more effective, provided by the higher PL signal, than no treatment. The AlInP regrowth may be better than the InGaP regrowth since it has more conformal and complete coverage along the sidewalls and omit parasitic absorption due to its indirect bandgap. Based on these results, μLEDs of various sizes from 15x15 μm to 50x50 μm were fabricated using the process described in the previous chapter.

13.3 Electrical Analysis

The fabrication process outlined in Chapter 12 was conducted on a range of LED with different sidewall conditions to investigate the electrical performance. These conditions include dry etched (untreated), InGaP and AlInP regrowth. One InGaP regrowth sample did not have surface cleaning, as denoted by condition A. The second InGaP overgrowth sample (condition

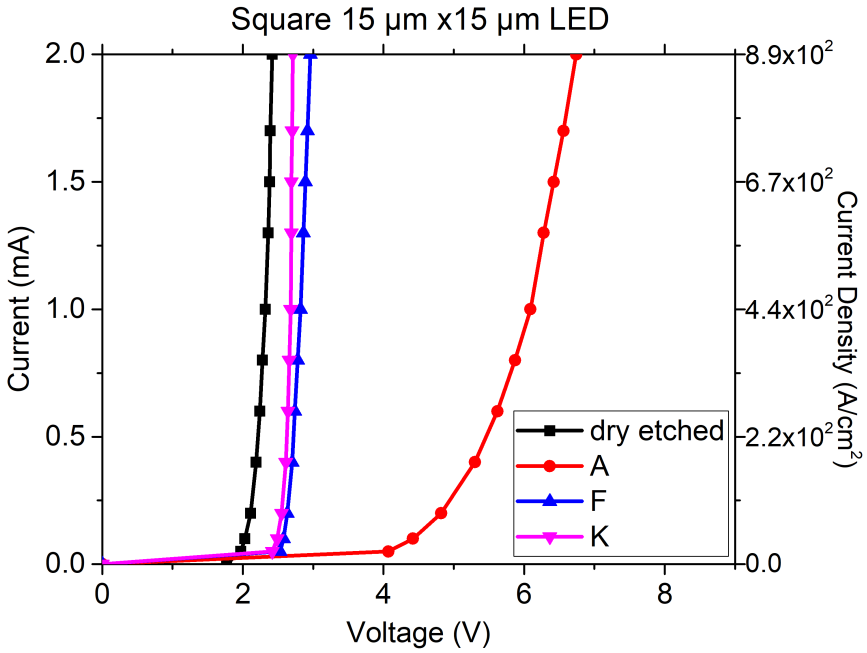

Figure 13.7: Forward bias J-V measurements on 15 μm LEDs with condition A, F, anf K, compared to the untreated LED.

F) and the AlInP overgrowth sample (condition K) received the BOE treatment and in situ sidewall etch before regrowth. Figure 13.7 compares the forward bias IV measurements across each sample. The untreated LED exhibits diode-like behavior at the lowest turn-on voltage near 2.2 V, while condition K and F turn-on voltage are near 2.5 V. This suggests some level of added resistance at the sidewalls from either the sidewall treatments, the regrowth processes, or a combination thereof, and requires additional investigation. Condition A has the lowest turn-on voltage near 4 V, which suggests high parasitic resistance losses for this particular LED under test. A new fabrication approach to reduce the series resistance and measure individual LEDs with different active areas more efficiently is required to understand the influence of regrowth and the impact sidewall treatments have on the resistive properties.

Trends in the reverse bias regime for the untreated and best-known condition K were compared next. Figure 13.8(a)-(b) shows the IV measurements on the untreated and condition K

LEDs as a function of LED size. Specifically, Figure 13.8(a) displays the *ln(I) vs. V* and as the LED size reduces from 50 μm x 50 μm to 15 μm x 15 μm, the current density increases in the reverse bias regime. This increase in current indicates higher surface defects and dependency on the sidewall quality. For the smallest LEDs with size 15 μm x 15 μm, condition K has a lower leakage current in reverse bias compared to the untreated sample. Figure 13.8(b) displays the forward bias IV measurements where the reduction in volume as the LED size reduces results in a higher current density at lower voltage bias. Also, condition K shows a smaller range in voltage as the LED size reduces compared to the untreated sample, indicating control over the quality across various sized LEDs and resistance due to sidewall passivation.

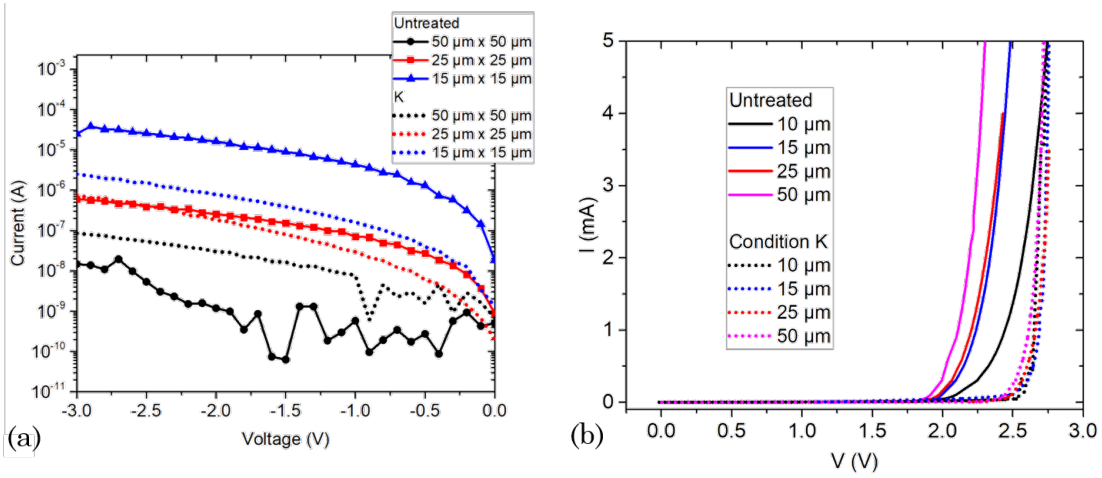

Figure 13.8: Plot (a) reverse bias of the untreated and condition K LED and plot (b) forward bias of the untreated and condition K with various sizes.

To measure the optical power output, an integrating sphere collected photon emission from the μLEDs. A small contact probe is connected to the top grid fingers on the LEDs, causing a mm-sized gap between the window and the surface of the LED. This is displayed in Figure 13.9. The small gap remained consistent across all samples. However, complete photon collection is not possible in this apparatus. This setup allows for fast measuring without the need for wire

bonding.

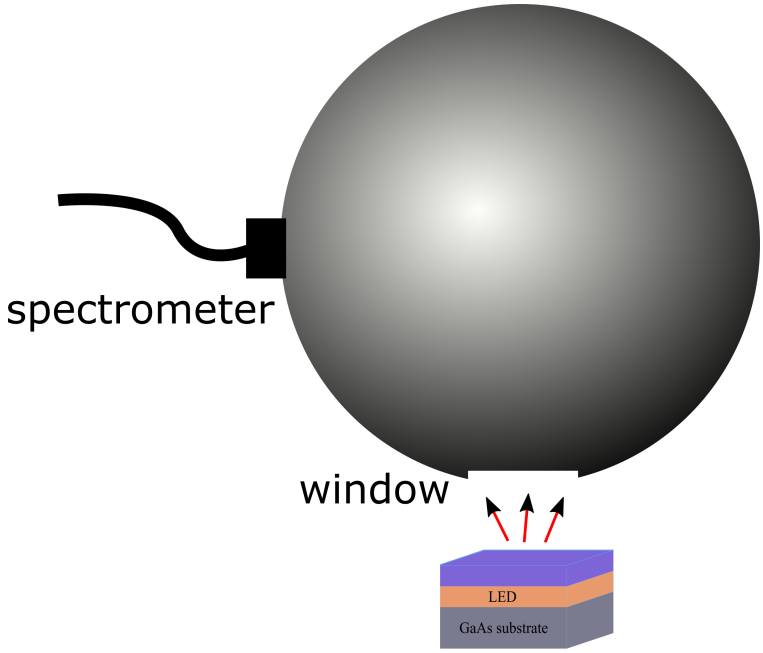

Figure 13.9: Integrating sphere set up to measure EL and optical power output.

Figure 13.10 shows the radiant flux measurements taken on the untreated 25 μm x 25 μm LED at various injection currents and focusing on the emission wavelength at 620 nm. The peak signal is near the characteristic emission wavelength at low injection currents and is measured between 626-628 nm. At high injection currents, the emission becomes broader, and the peak wavelength redshifts. This shift and broadening in emission is due to the internal thermal increase due to excess carriers and continuous current injection.

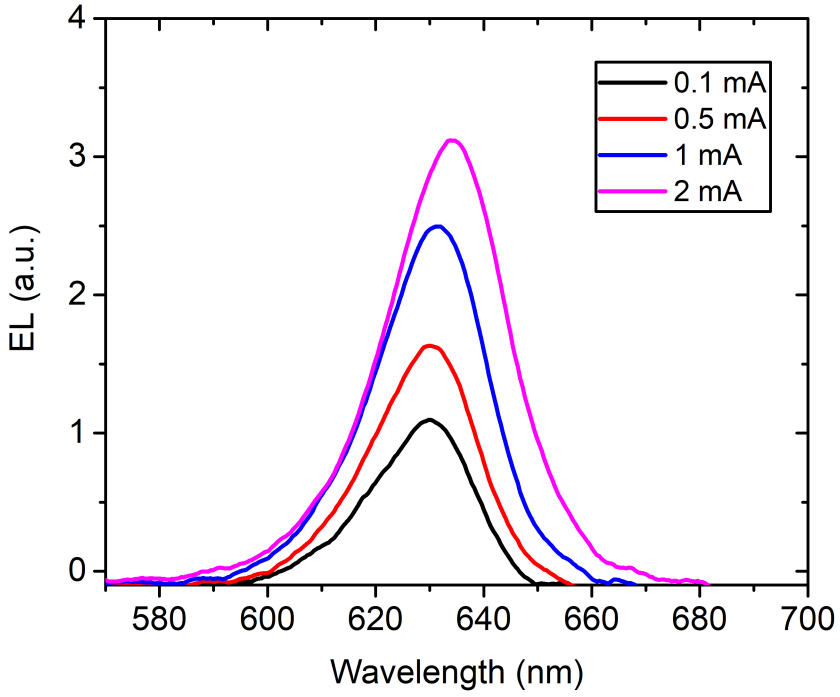

Figure 13.10: Collected radiant flux vs. wavelength for the post dry-etched 25 μm x 25 μm LED.

The optical power output is calculated by integrating the area under the EL emission curves at each injection current within a wavelength range of 550 nm to 700 nm. Figure 13.11 displays the normalized optical power output from low to high injection currents. The signal continues to increase until thermal mechanisms dominate where the signal plateaus near high injection levels above 800 A/cm^2, which is beyond the point of LED operation in display technology.

Focusing on the 15 μm x 15 μm LEDs, Figure 13.12 displays the calculated EQE and efficiency droop for the four LEDs with different surface treatments. Condition K surpasses the other conditions with the highest EQE at low injection current, as determined from the LOP. After this point, the efficiency droop begins to climb as the EQE reduces. At an injection current equal to 1 mA, the droop in EQE is 38% for condition K and over 50% for the other

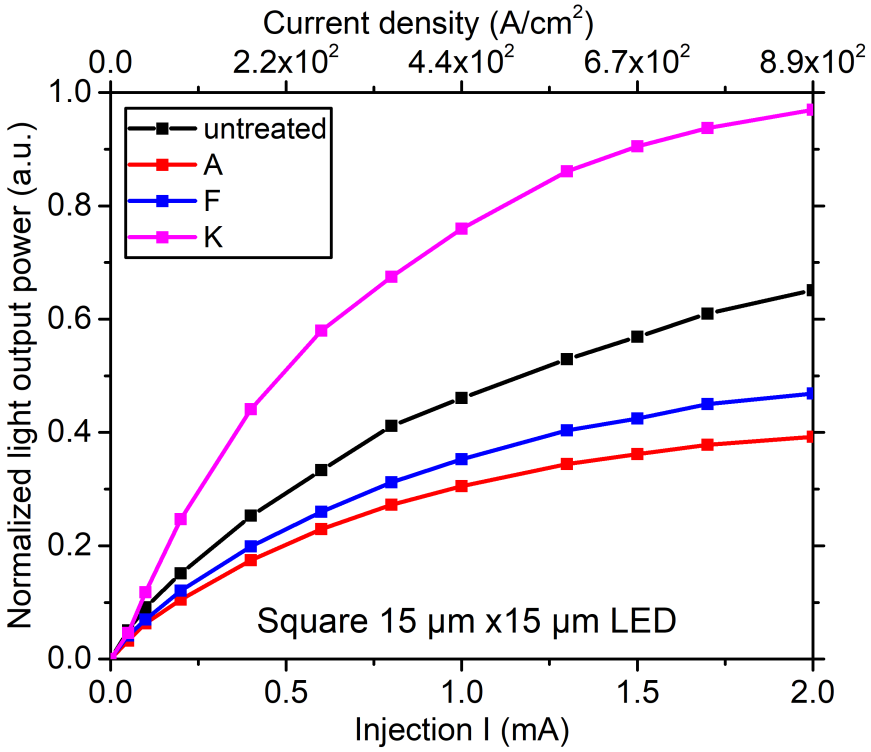

Figure 13.11: Normalized light output power vs. injection current calculated between 550 nm and 700 nm in wavelength.

conditions. Regarding conditions A and F, the LOP and therefore, the EQE, is low potentially due to the parasitic absorption at the sidewalls since InGaP has the same bandgap as the QWs. Additionally, the SEM shown above provides evidence of nonuniform and coalesced growth at the sidewalls, indicating insufficient passivation.

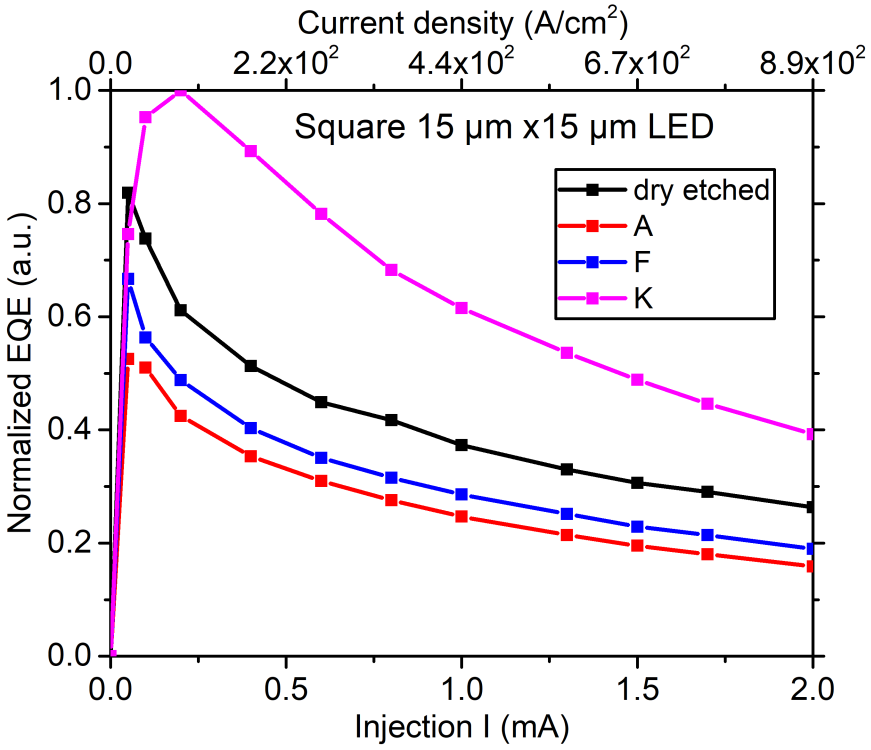

Figure 13.12: Calculated EQE and efficiency droop at the same injection current.

13.4 Chapter Summary

The multiple sidewall treatments presented in this chapter were diagnosed by analyzing the LED material as a function of the active area and determining the efficacy of the surface treatments when compared to each other. The photoluminescence analyses were based on well-established methods reported in literature and allowed the LEDs to be analyzed without

finishing the top and bottom metallization. The best-performing conditions utilized some combination of BOE and in situ etching from these measurements. Moreover, the wide and indirect bandgap AlInP regrowth progressed the PL intensity and, in return, the carrier generation and internal quantum efficiency. Moreover, the SRH coefficient was the lowest on condition K, which supports the previous observations through sidewall quality in SEM and high PL intensity. The PDPL analysis projected a complete fabrication study comparing the best-known conditions to an LED with untreated sidewalls. The electrical measurements indicate that condition K demonstrates the highest optical power output as LED area reduces, which supports the BOE wet etch, the in situ etch, and using AlInP as an overgrowth material rather than InGaP. This is most pronounced in the 15 μm x 15 μm where the sidewalls play a more significant role in recombination. Further, the InGaP overgrowth conditions result in reduced optical power, most likely due to parasitic absorption of laterally emitted photons in the InGaP sidewall and insufficient sidewall passivation. Future work includes repeating these results and designing a new mask outline to address the individual LEDs mounted on a chip efficiently. Further investigation in wide Eg regrowth layers and testing various combinations of the BOE and in situ etch will confirm repeatability. Overall, the outcomes in this research provide evidence that a combination of sidewall treatments is required and provides a promising pathway to continue reducing the non-radiative recombination and improve the μLEDs optical performance.

Chapter 14

Conclusions

Part II of this dissertation involves the design, process development, fabrication, and characterization of red-emitting AlGaInP-based μLEDs with dimensions less than or equal to 50 μm x 50 μm. The challenges with LEDs as the area-to-perimeter ratio increases include disrupting the crystal lattice due to the dry etching required to isolate the devices. Enhanced light emission requires sufficient sidewall passivation to mitigate the midgap energy states and improve radiative recombination. This was achieved by optimizing a fabrication process to result in smooth and anisotropic LED profiles. In particular, the photolithography, hard mask, and III-V dry etching processes were optimized by multiple processing runs and microscopic imaging to examine the profile and material quality. The wet-chemical sidewall treatments show the slow etch rate using a buffered oxide etch, promising to remove less than 100 nm of sidewall material before passivating with a non-active material. The in situ etch technique also provides new combinations of sidewall treatment and allows for wide E_g regrowth without exposing the sidewalls to air. From PDPL, the reduced slope in EQE from condition K, which includes the BOE and in situ etch along with AlInP regrowth, suggests effective sidewall passivation as the perimeter-to-area increases. Condition K led to the highest PL intensity and lowest SRH recombination coefficient, which relates to the complete and uniform sidewall coverage depicted through microscopic imaging. After PDPL measurements determined that some combination

between BOE and in situ etching was required to passivate the LED sidewalls before regrowth, selective conditions were used to electrically characterize the optical power output using an integrating sphere setup. The fabrication process using single grid fingers was developed to measure the LEDs electrically. The reverse bias current was lower for the smallest LEDs using condition K compared to the untreated sample. This result relates to the increased optical power output and EQE from condition K, indicating effective sidewall passivation. Future work includes investigating more combinations of the BOE and in situ etch and new regrowth conditions for the wide E_g AlInP overgrowth layer. A new LED chip design and fabrication process using ITO as a transparent contact will also progress the electrical measurements across the LEDs and determine the best conditions for effective sidewall passivation. The work presented in this research sets a pathway for future investigation to improve the optical performance of red-emitting AlGaInP μLEDs.

Chapter 15

Products

First-Author Peer-Reviewed Journal Publications

1. **D'Rozario, J.R.**, Polly, S. J., Nelson, G.T., Wilt, D. and Hubbard, S. M., "Modeling free-carrier absorption in ultrathin III-V solar cells with light management," Opt. Express 30, 7096-7109 (2022)

2. **D'Rozario, J.R.**, Polly, S.J., Nelson, G.T., Wilt, D., Hubbard, S., "Thin Gallium Arsenide Solar Cells With Maskless Back Surface Reflectors," in IEEE Journal of Photovoltaics, doi: 10.1109/JPHOTOV.2020.3019950 (2020)

Co-Authored Peer-Reviewed Journal Publications

1. Nelson, G.T., **D'Rozario, J. R.**, Hubbard, S.M., "Finite difference time domain simulations of absorption enhancement in thin GaAs solar cells with textured back surface reflectors", Solar Energy Materials and Solar Cells (2022)

Patents

1. *Method of in situ texturing III-V semiconductors using halomethane compounds* - **pending patent**, provisional No. 2022-003, date of application: January 5, 2022

2. *Longpass Distributed Bragg Reflector (LPDBR)*, United States, 2021-020-01 PRV - Provisional 63/211,824, June 17, 2021

Conference Proceedings

1. **D'Rozario, J.R.**, Polly, S. J., Tatavarti, R. and Hubbard, S. M., "Light Management for improved photon absorption in thin-film radiation-tolerant multijunction space photovoltaics," 2022 SPIE Photonics West, paper 11996-11 (2022)

2. **D'Rozario, J.R.**, Polly, S. J., Tatavarti, R. and Hubbard, S. M., "Advancements in Light Management for Thin-Film Space Photovoltaics," 2021 IEEE 48th Photovoltaic Specialists Conference (PVSC), pp. 1266-1269, doi: 10.1109/PVSC43889.2021.9518582 (2021)

3. **D'Rozario, J.R.**, Polly, S., Tatavarti R., Hubbard, S., "Back Surface Reflectors in Thinned Gallium Arsenide Solar Cells" European PV Solar Energy Conference and Exhibition (2020)

4. **D'Rozario, J.R.**, Polly, S.J., Nelson, G.T., Hubbard, S., "Back Surface Reflectors for Thin III-V Multi-junction Space Photovoltaics," Photovoltaic Specialists Conference, pp. 1686-1688, doi: 10.1109/PVSC45281.2020.9300732 (2020)

5. Polly, S.J., **D'Rozario, J.R.**, Nelson, G.T., Tatavarti, R., Hubbard, S. "Longpass Distributed Bragg Reflector for Improved Radiation Tolerance and Current Matching in Multijunction Solar Cells", Photovoltaic Specialists Conference, pp. 1537-1539, doi: 10.1109/PVSC45281.2020.9300621 (2020)

6. Tatavarti, R., Forghani, K., Rowall D., Reddy, R., **D'Rozario, J.R.**, Nelson, G.T., Hubbard, S., "Radiation Hardening of Dual Junction Solar Cells," Photovoltaic Specialists Conference, pp. 2258-2261, doi: 10.1109/PVSC45281.2020.9300545 (2020)

7. **D'Rozario, J.R.**, Polly, S.J., Nelson, G.T. Hubbard, S. "Improved Photoabsorption in Thin Gallium Arsenide Solar Cells using Light Trapping Techniques" 46th IEEE Photovoltaic Specialists Conference Proceedings, pp. 2603-2607, doi: 10.1109/PVSC40753.2019.8980886 (2019)

8. Polly, S.J., Nelson, G.T., **D'Rozario, J.R.**, Tatavarti, R., Hubbard, S.M. "Radiation Effects

in Thinned GaAs Photovoltaics Incorporating DBRs for Improved Radiation Tolerance of Multijunctions," 46th IEEE Photovoltaic Specialists Conference Proceedings, pp. 2818-2821, doi: 10.1109/PVSC40753.2019.8980875 (2019)

9. McClure, E., **D'Rozario, J.R.**, Polly, S.J., Hubbard, S.M. "Gallium Arsenide Solar Cell Growth on Polycrystalline Germanium Substrates by Aluminum-Induced Crystallization," 46th IEEE Photovoltaic Specialists Conference Proceedings, pp. 1029-1033, doi: 10.1109/PVSC 40753.2019.8981323 (2019)

10. Nelson, G.T., **D'Rozario, J.R.**, Polly, S.J., Tatavarti, S.R., Hubbard, S.M. "Modeling of practical light management for absorption enhancement in III-V multi-junction and quantum-dot solar cells." IEEE 7th World Conference on Photovoltaic Energy Conversion (WCPEC) (A Joint Conference of 45th IEEE PVSC, 28th PVSEC & 34th EU PVSEC), pp. 2913-2917, doi: 10.1109/PVSC.2018.8547395 (2018)

11. Polly, S. J., Nelson, G., **D'Rozario J.R.**, McClure, E., Tatavarti, R., Hubbard, S.M., "Incorporation of Photonic Structures for Improved Radiation Tolerance of Lattice Matched Triple Junction Solar Cells," in 2018 IEEE 7th World Conference on Photovoltaic Energy Conversion (WCPEC), pp. 2924-2927, doi: 10.1109/PVSC.2018.8547668 (2018)

Appendix A

Appendix A

A.1 Solar Cell Process Development

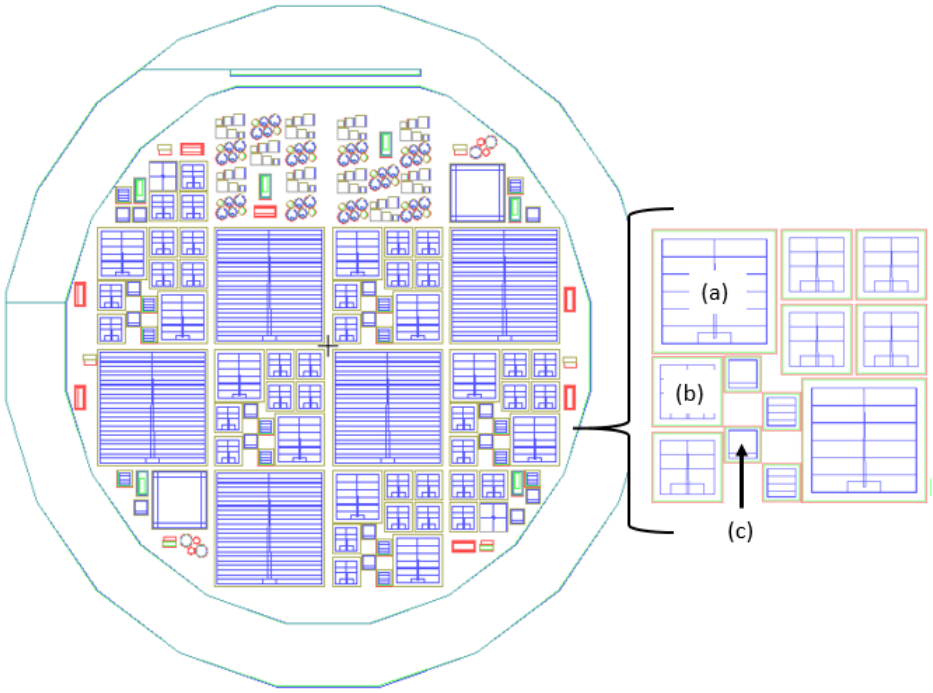

Figure A.1: Mask layout for the top-top contact design. The active solar cell areas are (a) 0.2025 cm^2, (b) 0.06 cm^2, and (c) 0.0125 cm^2.

The top-top contact design mask was made with various cell areas, with the largest being the 1 cm^2 area. The three layers consist of top metal, solar cell isolation, and backside metal, as shown in Figure A.1 (expanded portion). A different color represents each layer: the top metal

is blue, the solar cell isolation is green, and the back metal is red. The cell sizes vary from 0.06 cm^2 , 0.2025 cm^2, and 1 cm^2. Figure A.2(a)-(b) displays the tilted SEM on a fabricated solar cell using a top-top contact design with and without color correction to denote the different regions. The backside metal, shown by the region marked as (1) in A.2(b), is completely isolated from the active region of the solar cell, as shown by region (3). The green region marked as (2) is the exposed TTC layer, which carriers laterally travel through and are collected at the backside contact.

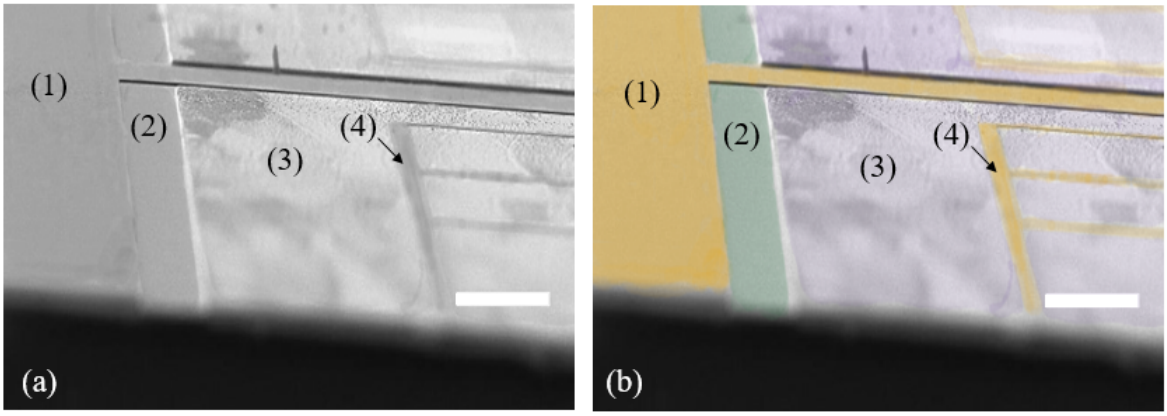

Figure A.2: Tilted 35° SEM of a thin-film GaAs solar cell with the top-top contact design with (a) as taken SEM image and (b) color SEM with color correction to denote the back Au contact (1), TTC layer (2), GaAs cell (3), and top Au contact (4). SEM was taken at 20 kV and the scale bar represents 100 μm.

This mask includes transfer length measurement (TLM) pads patterned on the TTC layer so that the contact and sheet resistivity can be measured for the back contact. The TLM measurement uses a four-point probe system where two probes measure current, and the other two probes for voltage across metal squares deposited on the semiconductor surface. The metal area for the different pads remains the same, while the distance between each pad reduces. The distances vary from 35 μm to 10 μm, as shown in Figure A.3. The total resistance between the two metal pads is,

$$R_{\mathrm{T}} = 2R_{\mathrm{C}} + \frac{R_{\mathrm{S}}}{W}L \tag{A.1}$$

where $\mathrm{R_C}$ is the resistance at the metal/semiconductor interface, and the semiconductor resistance is the second term. For the case where the distance between the two pads is zero, the total resistance would be equal to twice the contact resistance. Thus, the contact resistance can be determined by extrapolating to $\mathrm{L} = 0$. Moreover, the sheet resistance can be determined by taking the slope from the fitted data.

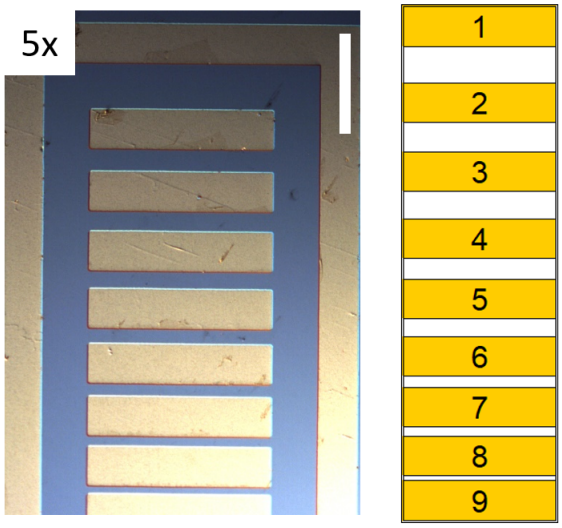

Figure A.3: Microscope image of the electroplated Au TLM pad (left) and a cartoon diagram showing the reduction in spacing between pads 1 through 9 (right). The white scale bar in the microscope image is 100 μm.

Figure A.4(a) displays the parameters extracted from the TLM measurement performed on the (a) front side n-type contact and the (b) backside p-type contact for the top-top contact design. The contact resistivity is within the range of low resistance for 1-sun illuminated J-V measurements.

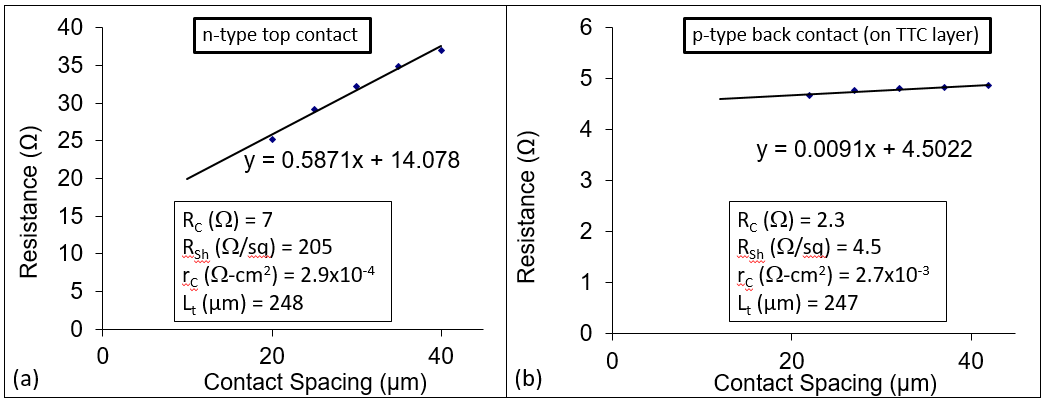

Figure A.4: TLM results from the (a) n-type top contact and (b) p-type bottom contact on the TTC layer for the top-top contact design.

A.2 Free-Carrier Absorption Modeling

The optical modeling performed in Chapter 6 relies on appropriate optical data to represent the different semiconductor and dielectric materials used in the GaAs solar cell and back surface reflector. Figure A.5(a)-(b) displays the measured materials used in the solar cell structure. These measurements were performed using a spectroscopic ellipsometer (RC2, J.A. Woollam Co., Inc.). The GaAs optical data was taken directly from the CompleteEase Software.

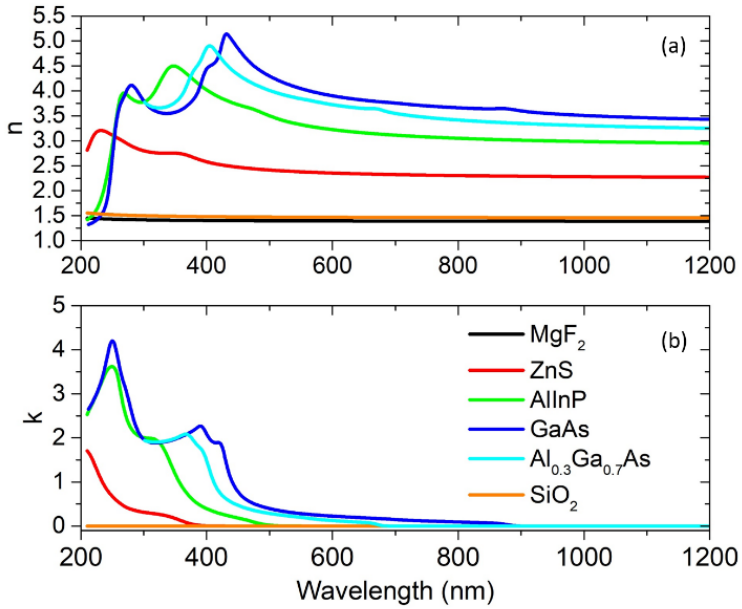

Figure A.5: Optical constants (a) index of refraction, n and (b) extinction coefficient, k measured using an RC2 spectroscopic ellipsometer from J.A. Woollam Co.

Using the open-source Python 3 extension, Rayflare, the Pol method established in the Stanford Stratified Structure Solver (S4) was used [118, 124] and convergence tests were conducted for a series of Fourier orders in the XY plane of the grating layer. The number of Fourier components used in the calculation was specified through a convergence test to maximize accuracy while maintaining decent computation time.

Figure A.6 compares the GaAs absorption from 650 nm to 920 nm and the absorption in the back layer, using Fourier orders from 100 through 225. The absorption converges at higher Fourier orders, highlighting the maximum deviation less than 2% between 169 and 225 orders at 880 nm near the GaAs band edge. Furthermore, the maximum deviation across all wavelengths less than 0.5% shows stability in the optical measurements when using 169 orders.

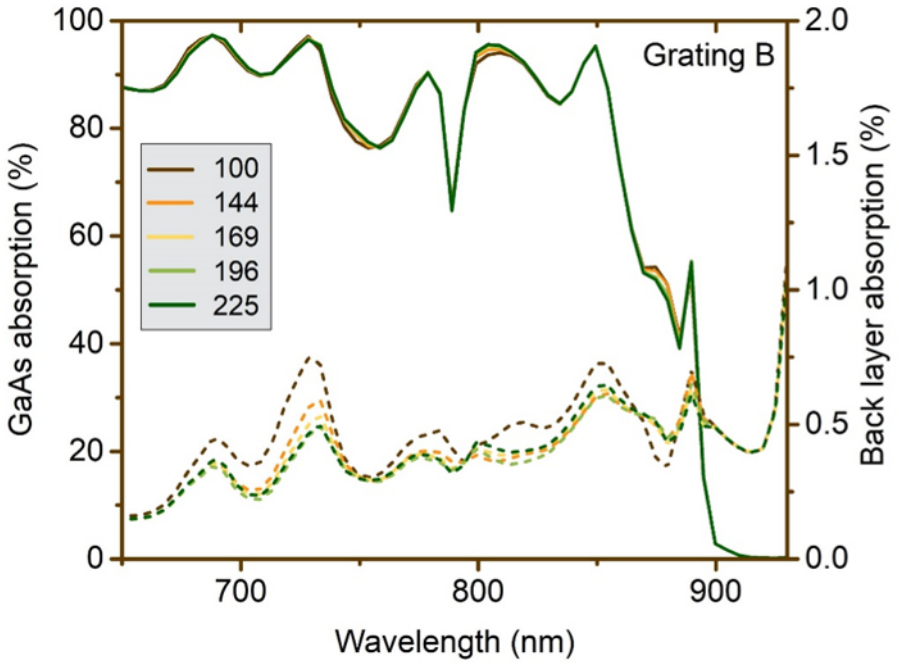

Figure A.6: GaAs absorption and Grating B absorption near the GaAs band edge using Fourier orders of 100 through 225 in the grating layer.

The two primary responses, the J_{SC} and FCA in the back layer, are shown in Figure A.7, highlighting the convergence at higher Fourier orders. The maximum deviation for J_{SC} and FCA between 169 and 225 orders was less than 0.01% and 0.05%, respectively. These convergence tests validate the use of 169 orders, which resulted in nearly a 3-fold reduction in the computation time for the simulations conducted in this research.

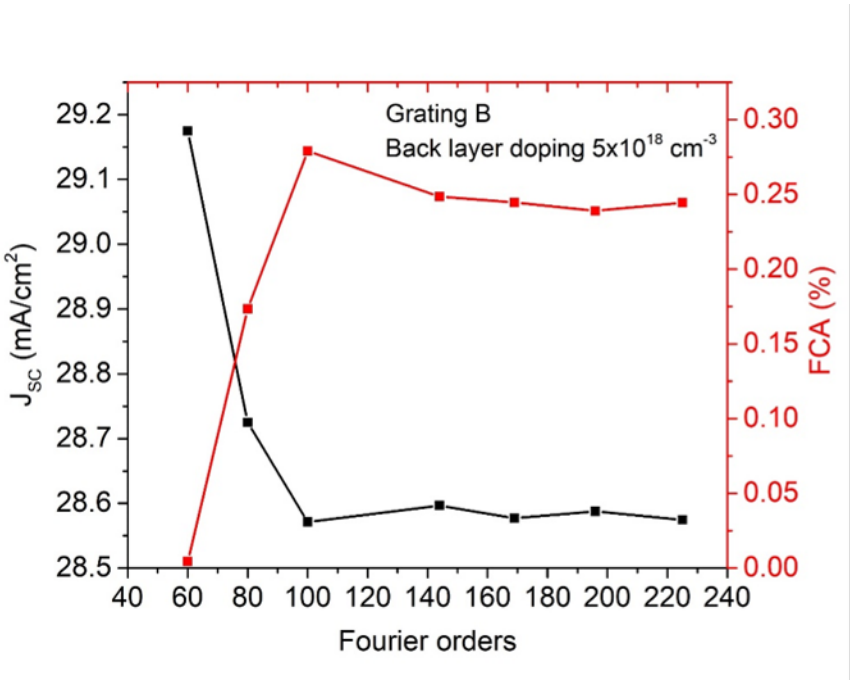

Figure A.7: J_{SC} and normalized FFCA in Grating B for Fourier orders 60 through 225 in the grating layer.

A.3 Micro-LED Process Development

Hard masks were created for patterning SiO_2 or SiN_x on the epi wafers for ICP-RIE and overgrowth experiments. The mask is designed for the 100 mm red-emitting LED structures. In this mask, the features shown in Figure A.8 present the set of mesas sizes and spacings condensed into 2 cm x 2 cm chips for individual experiments in etching and overgrowth. The feature set is comprised of circular and square mesas in grids of 25 by 25 with sizes of 5 μm, 10 μm, 15 μm, 25 μm, and 50 μm, and spacings of 5 μm to 15 μm with 5 μm steps, and again with 25 μm and 50 μm. Figure A.8(a) displays four of the 25 total square mesa arrangements with different sizes and spacing. Finally, Figure A.8(b) displays a wagon wheel structure with continuously varying lines and spaces from 5 μm to 50 μm with a total inner radius of 100 μm

and outer diameter of 1000 μm. In each cardinal direction, two features extend from the circle, and the two that extend the farthest (shown on the right) are always aligned pointing towards the major flat of the wafer for consistent orientation in imaging. The wagon wheel structure is intended to allow observation of crystallographic growth along varying planes from the host substrate.

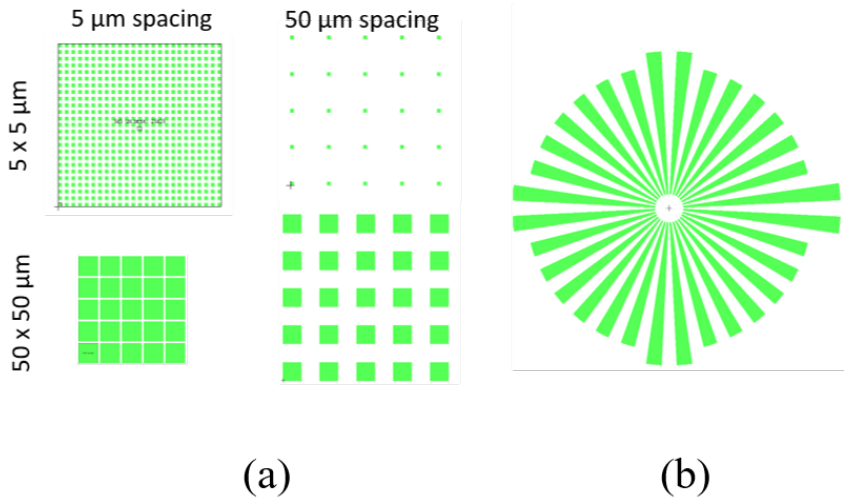

Figure A.8: GDS mask layout of (a) various sized square mesas and (b) wagon wheel structure.

A photograph of this mask is shown in Figure A.9(a) and Figure A.9(c) are Nomarski micrographs of the hard masks to show square mesas of different sizes and spacing and the wagon wheel structure.

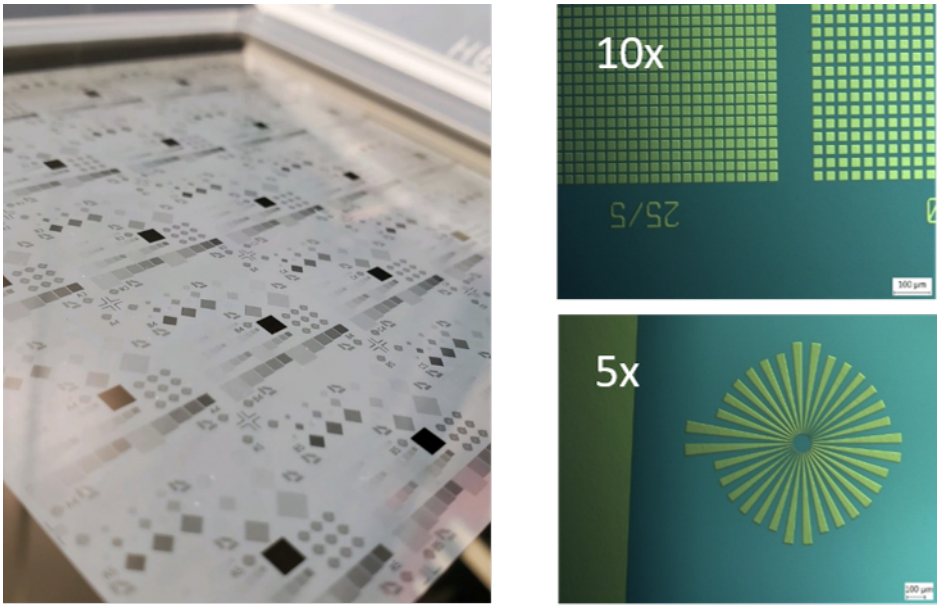

Figure A.9: Pictures of physical hard masks for (a) ICP-RIE mesa etching and (b) Nomarski images on square mesa features and a wagon wheel structure.

A.4 Hard Mask Processing

In Part II of this dissertation, the LED mesa development depends on a repeatable lithography process that patterns the hard mask (namely, SiO_2 or SiN_x) prior to the III-V dry etching. Chapter 12 discusses the optimized photoresist profile using a Suss MicroTec MJB4 hard contact mask aligner with a broad band exposure dose equal to 132 mJ/cm^2. The positive AZ MIR 701 photoresist profile has smooth sidewalls with an inclination of less than 10° and is near 1.1 μm in thickness. The lithography process, including photoresist bake temperatures, is shown in Table A.1.

Both hard masks required multiple dry etch recipes and SEM images to determine a recipe that achieves an anisotropic profile with high selectivity. The dry etch recipes are included in

Table A.1: Process parameters for patterning the hard mask with AZ MIR 701 photoresist.

Process	*Parameter*	*Time (sec)*
Spin coat	2500 rpm	40
Soft bake	95 °C	60
Exposure	132 mJ/cm^2 (broad band)	
Post-exposure bake	115 °C	60
Develop	Microposit MF CD-26	60
Post-develop hard bake	120 °C	60

Table A.2. From the SiO_2 etching, it was determined that the sidewall angle increases with high ICP power and low pressure. However, the selectivity reduces between the SiO_2 and photoresist. The SiN_x profile has a sidewall inclination between 80-90° with selectivity greater than 1, whereas the SiO_2 profile has a sidewall inclination around 60° and etches slower than the photoresist. In both profiles, the photoresist etches in the fluorine-based plasma and results in an angled profile. The angled photoresist profile is not a concern since it will be removed prior to III-V dry etching. Lastly, the wet-etch rates in 10:1 BOE for SiO_2 and SiN_x are 90 nm/min and 20 nm/min, respectively. The slow BOE etch rate in SiN_x is useful for sidewall cleaning, as discussed in Chapter 12.

Table A.2: Dry etch process parameters for patterning the hard masks.

Hard mask	SiO_2	SiN_x
CF_4 (sccm)	50	45
O_2 (sccm)	0	5
ICP (W)	500	350
RIE (W)	100	50
Pressure (mTorr)	35	50
Material etch rate (nm/min)	75	155
Photoresist etch rate (nm/min)	150	112
Selectivity (material/photoresist)	0.5	1.4
Material etch rate (nm/min)	60-65	80-90

References

[1] Jenny Nelson. *The Physics of Solar Cells*. Imperical College Press, 2003.

[2] Jong-Hyun Ahn and Jae-Hyun Kim. Series in display science and technology micro light emitting diode: Fabrication and devices micro-led technology.

[3] K. Thyagarajan and Ajoy Ghatak. *Lasers Fundamentals and Applications*. Springer Science+Business Media, second edi edition, 2011.

[4] Tahir Iqbal Awan, Anam Ahmad, Saliha Bibi, Aqsa Tehseen, and Almas Bashir. Nanomaterials. *Chemistry of Nanomaterials*, pages 225–269, 2020.

[5] Chao Zhao, Zhaonan Li, Tianyi Tang, Jiaqian Sun, Wenkang Zhan, Bo Xu, Huajun Sun, Hui Jiang, Kong Liu, Shengchun Qu, Zhijie Wang, and Zhanguo Wang. Novel iii-v semiconductor epitaxy for optoelectronic devices through two-dimensional materials. *Progress in Quantum Electronics*, 76:100313, 3 2021.

[6] Martin A. Green, Yoshihiro Hishikawa, Ewan D. Dunlop, Dean H. Levi, Jochen Hohl-Ebinger, and Anita W.Y. Ho-Baillie. Solar cell efficiency tables (version 52). *Progress in Photovoltaics: Research and Applications*, 26:427–436, 7 2018.

[7] Taesoo D. Lee and Abasifreke U. Ebong. A review of thin film solar cell technologies and challenges, 2017.

[8] Vidur Raj, Tuomas Haggren, Wei Wen Wong, Hark Hoe Tan, and Chennupati Jagadish. Topical review: Pathways toward cost-effective single-junction iii-v solar cells, 4 2022.

[9] Mark J. Kerr, Andres Cuevas, and Patrick Campbell. Limiting efficiency of crystalline silicon solar cells due to coulomb-enhanced auger recombination. *Progress in Photovoltaics: Research and Applications*, 11:97–104, 3 2003.

[10] Tom Tiedje, Eli Yablonovitch, George D. Cody, and Bonnie G. Brooks. Limiting efficiency of silicon solar cells. *IEEE Transactions on Electron Devices*, 31:711–716, 1984.

[11] Masafumi Yamaguchi. Radiation-resistant solar cells for space use. *Solar Energy Materials and Solar Cells*, 68:31–53, 2001.

[12] Spectrolab: A boeing company. https://www.spectrolab.com/company.html.

[13] Space solar cells / coverglass interconnected cells (cic) -solaero. https://solaerotech.com/products/space-solar-cells-coverglass-interconnected-cells-cic/.

[14] Microlink devices, inc. http://mldevices.com/.

[15] Raja Arumugam Senthil, Jayaraman Theerthagiri, S.K. Khadheer Pasha, Madhavan Jagannathan, Andrews Nirmala Grace, and Sivakumar Manickam. Multijunction solar cells based on iii–v and ii–vi semiconductors. *Oxide Free Nanomaterials for Energy Storage and Conversion Applications*, pages 307–328, 1 2022.

[16] Arto Aho, Riku Isoaho, Marianna Raappana, Timo Aho, Elina Anttola, Jari Lyytikäinen, Arttu Hietalahti, Ville Polojärvi, Antti Tukiainen, Jarno Reuna, Leo Peltomaa, and Mircea Guina. Wide spectral coverage (0.7–2.2 ev) lattice-matched multijunction solar cells based on algainp, algaas and gainnassb materials. *Progress in Photovoltaics: Research and Applications*, 29:869–875, 7 2021.

[17] Zachary Shible Bittner. Development and characterization of novel iii-v materials for high efficiency photovoltaics. *Thesis. Rochester Institute of Technology*, 2018.

[18] S. R. Messenger, G. P. Summers, E. A. Burke, R. J. Walters, and M. A. Xapsos. Modeling solar cell degradation in space: A comparison of the nrl displacement damage dose and the jpl equivalent fluence approaches. *Progress in Photovoltaics: Research and Applications*, 9:103–121, 2001.

[19] Mitsuru Imaizumi, Tetsuya Nakamura, Tatsuya Takamoto, Takeshi Ohshima, and Michio Tajima. Radiation degradation characteristics of component subcells in inverted metamorphic triple-junction solar cells irradiated with electrons and protons. *Progress in Photovoltaics: Research and Applications*, 25:161–174, 2017.

[20] R. Tatavarti, A. Wibowo, V. Elarde, F. Tuminello, R. Pastor, T. Giannopoulos, M. Osowski, R. Chan, C. Youtsey, G. Hillier, and N. Pan. Large-area, epitaxial lift-off, inverted metamorphic solar cells. *Conference Record of the IEEE Photovoltaic Specialists Conference*, pages 001941–001944, 2011.

[21] Shin Ichiro Sato, Takeshi Ohshima, and Mitsuru Imaizumi. Modeling of degradation behavior of ingap/gaas/ge triple-junction space solar cell exposed to charged particles. *Journal of Applied Physics*, 105, 2009.

[22] George Thomas Nelson IV. Native and radiation-induced defects in iii-v solar cells and photodiodes. *Thesis. Rochester Institute of Technology*, 2019.

[23] P.C. Colter, G. Kinsey, N.H. Karam, R.R. King, C.M. Fetzer, J.H. Ermer, Hojun Yoon, K.M. Edmondson, D.D. Krut, H.L. Cotal, and A.P. Stavrides. High-efficiency space and terrestrial multijunction solar cells through bandgap control in cell structures. pages 776–781, 2003.

[24] F Dimroth, C Baur, M Meusel, S Van Riesen, and A W Belt. 5-junction 111-v solar cells for space applications. 2003.

[25] L. C. Hirst, M. K. Yakes, J. H. Warner, M. F. Bennett, K. J. Schmieder, R. J. Walters, and P. P. Jenkins. Intrinsic radiation tolerance of ultra-thin gaas solar cells. *Applied Physics Letters*, 109, 2016.

[26] Tomoyuki Inoue, Kentaroh Watanabe, Kasidit Toprasertpong, Hiromasa Fujii, Masakazu Sugiyama, and Yoshiaki Nakano. Enhanced light trapping in multiple quantum wells by thin-film structure and backside grooves with dielectric interface. *IEEE Journal of Photovoltaics*, 5:697–703, 2015.

[27] Dong Yang, Zhaopeng Xu, Fei Bian, Haiyan Wang, Jiazhuang Wang, and Lu Sun. Broadband enhancement of dielectric light trapping nanostructure used in ultra-thin solar cells. *Optics Communications*, 411:65–69, 2018.

[28] Shi Liu, Weiquan Yang, Jacob Becker, Ying Shen Kuo, and Yong Hang Zhang. Non-lambertian reflective back scattering and its impact on device performance of ultrathin gaas single-junction solar cells. *IEEE Journal of Photovoltaics*, 5:832–839, 2015.

[29] Nicolas Vandamme, Hung Ling Chen, Alexandre Gaucher, Benôt Behaghel, Aristide Lemaître, Andrea Cattoni, Christophe Dupuis, Nathalie Bardou, Jean Franc¸ois Guillemoles, and Stephane Collin. Ultrathin gaas solar cells with a silver back mirror. *IEEE Journal of Photovoltaics*, 5:565–570, 2015.

[30] Stéphane Collin, Benoît Behaghel, Romaric De Lépinau, Andrea Cattoni, Nathalie Bardou, Hung-Ling Chen, Julie Goffard, and Christophe Dupuis. Multiresonant light trapping in ultra-thin gaas and cigs solar cells. 2017:PW3A.2, 2017.

[31] Zhenqiang Ma, Dong Liu, He Ding, and Xing Sheng. Thin-film iii–v single junction and multijunction solar cells and their integration onto heterogeneous substrates. *Inorganic Flexible Optoelectronics*, pages 177–207, 2019.

[32] Emily D Kosten, Jackson H Atwater, James Parsons, Albert Polman, and Harry A Atwater. Highly efficient gaas solar cells by limiting light emission angle. *Light: Science Applications*, 2013.

[33] J. Bhattacharya, N. Chakravarty, S. Pattnaik, W. D. Slafer, R. Biswas, and V. Dalal. Comparison of optical properties of periodic photonic-plasmonic and randomly textured back reflectors for nc-si solar cells. *Journal of Non-Crystalline Solids*, 358:2313–2318, 2012.

[34] N. J. Ekins-Daukes, N. P. Hylton, A. Mellor, B. Bläsi, S. A. Maier, Y. Al-Saleh, N. Tucher, H. Hauser, C. Wellens, T. Thomas, E. Oliva, and O. Höhn. Nanoparticle scattering for multijunction solar cells. *Photonics for Solar Energy Systems VI*, 9898:989809, 2016.

[35] Jianling Xiao, Kezheng Li, Juntao Li, Jindong Song, Emiliano R. Martins, Rongbin Su, Hanlin Fang, and Thomas F. Krauss. Paths to light trapping in thin film gaas solar cells. *Optics Express*, 26:A341, 2018.

[36] Lu Xu, Yuan Yao, Noah D. Bronstein, Lanfang Li, A. Paul Alivisatos, and Ralph G. Nuzzo. Enhanced photon collection in luminescent solar concentrators with distributed bragg reflectors. *ACS Photonics*, 3:278–285, 2016.

[37] Chung Yu Hong, Mu Min Hung, Tung Ting Yang, Yi Chin Wang, Yu Chen Lin, and Peichen Yu. Photovoltaic characteristics of gaas solar cells with selective filters. *2015 IEEE 42nd Photovoltaic Specialist Conference, PVSC 2015*, pages 2–4, 2015.

[38] Sergey Eyderman, Alexei Deinega, and Sajeev John. Near perfect solar absorption in ultra-thin-film gaas photonic crystals. *Journal of Materials Chemistry A*, 2:761–769, 2014.

[39] Aixue Shang and Xiaofeng Li. Carrier depletion and electrical optimization of gallium arsenide plasmonic solar cell with a rear metallic grating. *Applied Physics Letters*, 106, 2015.

[40] Martin A. Green. The path to 25cell evolution. *Prog. Photovolt: Res. Appl.*, 17:183–189, 2009.

[41] Alongkarn Chutinan, Catherine Wei Wei Li, Nazir P. Kherani, and Stefan Zukotynski. Wave-optical studies of light trapping in submicrometre-textured ultra-thin crystalline silicon solar cells. *Journal of Physics D: Applied Physics*, 44, 2011.

[42] Chog Barugkin, Thomas Allen, Teck K Chong, Thomas P White, Klaus J Weber, and Kylie R Catchpole. Light trapping efficiency comparison of si solar cell textures using spectral photoluminescence. 2015.

[43] Patrick Campbell and Martin A. Green. Light trapping properties of pyramidally textured surfaces. *Journal of Applied Physics*, 62:243–249, 1987.

[44] Yan Wang, Lixia Yang, Yaoping Liu, Zengxia Mei, Wei Chen, Junqiang Li, Huili Liang, Andrej Kuznetsov, and Du Xiaolong. Maskless inverted pyramid texturization of silicon. *Scientific Reports*, 5:1–7, 2015.

[45] Patrick Campbell and Martin a Green. High performance light trapping textures for monocrystalline silicon solar cells. *Solar Energy Materials*, 65:369–375, 2001.

[46] Quiebras Ximello N. Wet chemical textures for crystalline silicon solar cells, 2013.

[47] Alexandre Gaucher, Andrea Cattoni, Christophe Dupuis, Wanghua Chen, Romain Cariou, Martin Foldyna, Lolc Lalouat, Emmanuel Drouard, Christian Seassal, Pere Roca-Cabarrocas, and Stéphane Collin. Ultrathin epitaxial silicon solar cells with inverted nanopyramid arrays for efficient light trapping. *Nano Letters*, 16:5358–5364, 2016.

[48] Chetan Singh Solanki and Hemant Kumar Singh. *c-Si solar cells: Physics and technology.* 2017.

[49] Martin A. Green and Mark J. Keevers. Optical properties of intrinsic silicon at 300 k. *Progress in Photovoltaics: Research and Applications*, 1995.

[50] Robert F Pierret. Semiconductor device fundamentals. *New York*, page 792, 1996.

[51] Daniel Neves Micha, Oliver Höhn, Eduard Oliva, Vera Klinger, Andreas W. Bett, and Frank Dimroth. Development of back side technology for light trapping and photon recycling in gaas solar cells. *Progress in Photovoltaics: Research and Applications*, 27:163–170, 2019.

[52] Julia R D'Rozario, Stephen J Polly, George T Nelson, and Seth M Hubbard. Thin gallium arsenide solar cells with maskless back surface reflectors. *IEEE Journal of Photovoltaics*, 10:1681–1688, 2020.

[53] MaartenA facile light-trapping approach for ultrathin GaAs solar cells using wet chemical etching van Eerden, Gerard J. Bauhuis, Peter Mulder, Natasha Gruginskie, Marco Passoni, Lucio C. Andreani, Elias Vlieg, and John J. Schermer. A facile light-trapping approach for ultrathin gaas solar cells using wet chemical etching. *Progress in Photovoltaics: Research and Applications*, 28:200–209, 2020.

[54] George T. Nelson, Julia D'Rozario, Stephen J. Polly, Rao Tatavartiy, and Seth M. Hubbard. Modeling of practical light management for absorption enhancement in iii-v multijunction and quantum-dot solar cells. pages 2913–2917. IEEE, 6 2018.

[55] Larkin Sayre, Eduardo Camarillo Abad, Phoebe Pearce, Pierre Chausse, Pierre Marie Coulon, Philip Shields, Andrew Johnson, and Louise C. Hirst. Ultra-thin gaas solar cells with nanophotonic metal-dielectric diffraction gratings fabricated with displacement talbot lithography. *Progress in Photovoltaics: Research and Applications*, pages 1–13, 2021.

[56] Hung Ling Chen, Andrea Cattoni, Romaric De Lépinau, Alexandre W. Walker, Oliver Höhn, David Lackner, Gerald Siefer, Marco Faustini, Nicolas Vandamme, Julie Goffard, Benoît Behaghel, Christophe Dupuis, Nathalie Bardou, Frank Dimroth, and Stéphane Collin. A 19.9absorber and a silver nanostructured back mirror. *Nature Energy*, 4:761–767, 2019.

[57] A. Mellor, N. P. Hylton, S. A. Maier, and N. Ekins-Daukes. Interstitial light-trapping design for multi-junction solar cells. *Solar Energy Materials and Solar Cells*, 159:212–218, 2017.

[58] Jeronimo Buencuerpo, Myles Steiner, and Adele Tamboli. Optically-thick 300 nm gaas solar cells using adjacent photonic crystals. *Optics Express*, 28:13845–13860, 2020.

[59] William Shockley and Hans J. Queisser. Detailed balance limit of efficiency of p-n junction solar cells. *Journal of Applied Physics*, 32:510–519, 1961.

[60] Eric Y. Chen, Sean J. Babcock, and Richard R. King. Predicted performance of high-efficiency photovoltaics with energy-selective front reflectors for photon recycling enhancements. *Conference Record of the IEEE Photovoltaic Specialists Conference*, pages 1737–1742, 2019.

[61] Lin Zhu, Yuji Hazama, Anurag Reddy, Kentaroh Watanabe, Yoshiaki Nakano, Masakazu Sugiyama, and Hidefumi Akiyama. Modeling and design for low-cost multijunction solar cell via light-trapping rear texture technique: Applied in ingap/gaas/ingaas triple junction. *Progress in Photovoltaics: Research and Applications*, 28:251–265, 2020.

[62] M. A. Steiner, E. E. Perl, J. F. Geisz, D. J. Friedman, N. Jain, D. Levi, and G. Horner. Apparent bandgap shift in the internal quantum efficiency for solar cells with back reflectors. *Journal of Applied Physics*, 121, 2017.

[63] Thorsten Trupke, Jianhua Zhao, Aihua Wang, Richard Corkish, and Martin A. Green. Very efficient light emission from bulk crystalline silicon. *Applied Physics Letters*, 82:2996–2998, 5 2003.

[64] Owen D. Miller, Eli Yablonovitch, and Sarah R. Kurtz. Strong internal and external luminescence as solar cells approach the shockley-queisser limit. *IEEE Journal of Photovoltaics*, 2:303–311, 2012.

[65] Tianyao P. Xiao and Eli Yablonovitch. Ultra-high luminescence efficiency as a technology enabler: solar cells, thermophotovoltaics, and optoelectronic refrigerators. page 18, 2018.

[66] Daniel Neves Micha, Oliver Höhn, Eduard Oliva, Vera Klinger, Andreas W. Bett, and Frank Dimroth. Development of back side technology for light trapping and photon recycling in gaas solar cells. *Progress in Photovoltaics: Research and Applications*, 27:163–170, 2019.

[67] Alexandre W. Walker, Oliver Höhn, Daniel Neves Micha, Benedikt Bläsi, Andreas W. Bett, and Frank Dimroth. Impact of photon recycling on gaas solar cell designs. *IEEE Journal of Photovoltaics*, 5:1636–1645, 2015.

[68] M. A. Steiner, J. F. Geisz, I. García, D. J. Friedman, A. Duda, and S. R. Kurtz. Optical enhancement of the open-circuit voltage in high quality gaas solar cells. *Journal of Applied Physics*, 113, 2013.

[69] Eli Yablonovitch. Statistical ray optics. *Journal of the Optical Society of America*, 72:899, 2008.

[70] Natasha Gruginskie, Gerard Bauhuis, Peter Mulder, Elias Vlieg, and John Schermer. Photon recycling in thin-film gaas solar cells. *VII Congresso Brasileiro de Energia Solar - CBENS 2018*, 0, 2018.

[71] G. J. Bauhuis, P. Mulder, E. J. Haverkamp, J. C.C.M. Huijben, and J. J. Schermer. 26.1 *Solar Energy Materials and Solar Cells*, 93:1488–1491, 2009.

[72] Zachary C. Holman, Stefaan De Wolf, and Christophe Ballif. Improving metal reflectors by suppressing surface plasmon polaritons: A priori calculation of the internal reflectance of a solar cell. *Light: Science and Applications*, 2:0, 2013.

[73] George T. Nelson, Julia D'Rozario, Stephen J. Polly, Rao Tatavarti, and Seth M. Hubbard. Modeling of practical light management for absorption enhancement in iii-v multijunction and quantum-dot solar cells. *2018 IEEE 7th World Conference on Photovoltaic Energy Conversion, WCPEC 2018 - A Joint Conference of 45th IEEE PVSC, 28th PVSEC and 34th EU PVSEC*, pages 2913–2917, 2018.

[74] C.B. Honsberg and A.M. Barnett. Light trapping in thin film gaas solar cells. *In Conference Record of the IEEE Photovoltaic Specialists Conference (Vol. 1, pp. 262–267). Publ by IEEE. https://doi.org/10.1364/oe.26.00a341*, pages 262–267, 2002.

[75] Andres Otto. Excitation of nonradiative surface plasma waves in silver by the method of frustrated total reflection. *Physics*, 410:398–410, 1968.

[76] Yao Shan, Guohang Hu, Maria Luisa Grilli, Hongbo He, Meiping Zhu, Yuanan Zhao, and Jianda Shao. Measuring ultrathin metal coatings using spr spectroscopic ellipsometry with a prism-dielectric-metal-liquid configuration. *Optics Express*, 27:7912, 2019.

[77] Thomas S. Wilhelm, Zihao Wang, Mohadeseh A. Baboli, Jian Yan, Stefan F. Preble, and Parsian K. Mohseni. Ordered al x ga 1- x as nanopillar arrays via inverse metal-assisted chemical etching. *ACS Applied Materials and Interfaces*, 10:27488–27497, 2018.

[78] Jennifer Hydrick, James G. Fiorenza, Lukas Chrostowski, Jizhong Li, Ji-Soo Park, Wei Shi, Yiheng Lin, Ting-Chang Chang, Guangrui (Maggie) Xia, Mark Greenberg, and Zigang Duan. Monolithic integration of algaas distributed bragg reflectors on virtual ge substrates via aspect ratio trapping. *Optical Materials Express*, 7:726, 2017.

[79] A. Datas and P. G. Linares. Monolithic interconnected modules (mim) for high irradiance photovoltaic energy conversion: A comprehensive review. *Renewable and Sustainable Energy Reviews*, 73:477–495, 2017.

[80] Cheng Wei Cheng, Kuen Ting Shiu, Ning Li, Shu Jen Han, Leathen Shi, and Devendra K. Sadana. Epitaxial lift-off process for gallium arsenide substrate reuse and flexible electronics. *Nature Communications*, 4:1–7, 2013.

[81] Z. Cevher, P. A. Folkes, H. S. Hier, B. L. Vanmil, B. C. Connelly, W. A. Beck, and Y. H. Ren. Optimization of the defects and the nonradiative lifetime of gaas/algaas double heterostructures. *Journal of Applied Physics*, 123, 2018.

[82] Makoto Konagai, Mitsunori Sugimoto, and Kiyoshi Takahashi. High efficiency gaas thin film solar cells by peeled film technology. *Journal of Crystal Growth*, 45:277–280, 12 1978.

[83] Sudersena Rao Tatavarti, Zachary S. Bittner, A. Wibowo, Michael A. Slocum, George Nelson, Hyun Kum, S. Phillip Ahrenkiel, and Seth M. Hubbard. Epitaxial lift-off (elo) of ingap/gaas/ingaas solar cells with quantum dots in gaas middle sub-cell. *Solar Energy Materials and Solar Cells*, 185:153–157, 2018.

[84] G. J. Bauhuis, P. Mulder, E. J. Haverkamp, J. J. Schermer, E. Bongers, G. Oomen, W. Köstler, and G. Strobl. Wafer reuse for repeated growth of iii-v solar cells. *Progress in Photovoltaics: Research and Applications*, 18:155–159, 2010.

[85] Venkat Selvamanickam, Carlos A Favela, Sicong Sun, and Venkat Selvamanickam. Novel epitaxial lift-off for flexible , inexpensive gaas solar cells. *2020 IEEE 46th Virtual Photovoltaic Specialists Conference (vPVSC)*, pages 3–5, 2020.

[86] Cassi A. Sweet, Joshua E. McNeely, Brian Gorman, David L. Young, Aaron J. Ptak, and Corinne E. Packard. Engineering controlled spalling in (100)-oriented gaas for wafer reuse. *2015 IEEE 42nd Photovoltaic Specialist Conference, PVSC 2015*, pages 1–4, 2015.

[87] Sunghyun Moon, Kangho Kim, Youngjo Kim, Junseok Heo, and Jaejin Lee. Highly efficient single-junction gaas thin-film solar cell on flexible substrate. *Scientific Reports*, 6:1–6, 2016.

[88] Hung Ling Chen, Andrea Cattoni, Nicolas Vandamme, Julie Goffard, Aristide Lemaitre, Amaury Delamarre, Benoit Behaghel, Kentaroh Watanabe, Masakazu Sugiyama, Jean Francois Guillemoles, and Stephane Collin. 200nm-thick gaas solar cells with a nanostructured silver mirror. *2017 IEEE 44th Photovoltaic Specialist Conference, PVSC 2017*, pages 1–4, 2017.

[89] Daniel Neves Micha, Oliver Höhn, Eduard Oliva, Vera Klinger, Andreas W. Bett, and Frank Dimroth. Development of back side technology for light trapping and photon recycling in gaas solar cells. *Progress in Photovoltaics: Research and Applications*, 27:163–170, 2019.

[90] Martin A. Green. *Solar Cells: Operating Principles, Technology, and Systems Applications*. Prentice-Hall, Inc., solid stat edition, 1982.

[91] Eunseong Moon, Inhee Lee, David Blaauw, and Jamie D. Phillips. High-efficiency photovoltaic modules on a chip for millimeter-scale energy harvesting. *Progress in Photovoltaics: Research and Applications*, 27:540–546, 2019.

[92] Juho Kim, Jeongwoo Hwang, Kwangsun Song, Namyun Kim, Jae Cheol Shin, and Jongho Lee. Ultra-thin flexible gaas photovoltaics in vertical forms printed on metal surfaces without interlayer adhesives. *Applied Physics Letters*, 108, 2016.

[93] Alan S. Teran, Eunseong Moon, Wootaek Lim, Gyouho Kim, Inhee Lee, David Blaauw, and Jamie D. Phillips. Energy harvesting for gaas photovoltaics under low-flux indoor lighting conditions. *IEEE Transactions on Electron Devices*, 63:2820–2825, 2016.

[94] R.F. Wolffenbuttel. Low-temperature intermediate au-si wafer bonding; eutectic or silicide bond. *Sensors and Actuators A: Physical*, 62:680–686, 7 1997.

[95] Kentaroh Watanabe, Tomoyuki Inoue, Kasidit Toprasertpong, Amaury Delamarre, Hassanet Sodabanlu, Jean Francois Guillemoles, Masakazu Sugiyama, and Yoshiaki Nakano. Optical analysis of the photon recycling effect in ingaas/gaasp multiple quantum well solar cell with light trapping structure. *2017 IEEE 44th Photovoltaic Specialist Conference, PVSC 2017*, pages 1–5, 2018.

[96] Julia R. D'Rozario, George Nelson, Steve J. Polly, and Seth M. Hubbard. Improved photoabsorption in thin gallium arsenide solar cells using light trapping techniques. *2019 IEEE 46th Photovoltaic Specialists Conference (PVSC), Chicago, IL, USA,*, pages 2603–2607, 2019.

[97] Peng Lian, Tao Yin, ZunTu Xu, Hongdong Zhao, Deshu Zou, Guo Gao, Jinyu Du, Changhua Chen, Changbao Tao, Jianxing Chen, Guangdi Shen, Qing Cao, Xiaoyu Ma, and Lianhui Chen. High-quality carbon-doped gaas/algaas material growth in mocvd and its application for optoelectronic devices. *Semiconductor Lasers III*, 3547:278, 1998.

[98] Christine Bryce and Dimitrios Berk. Kinetics of gaas dissolution in h2o2 -nh4oh-h2o solutions. *Industrial and Engineering Chemistry Research*, 35:4464–4470, 1996.

[99] Hairen Tan, Laura Sivec, Baojie Yan, Rudi Santbergen, Miro Zeman, and Arno H.M. Smets. Improved light trapping in microcrystalline silicon solar cells by plasmonic back reflector with broad angular scattering and low parasitic absorption. *Applied Physics Letters*, 102, 2013.

[100] Zeyu Li, E. Rusli, Martin Foldyna, Junkang Wang, Wanghua Chen, Ari Bimo Prakoso, Chenjin Lu, and Pere Roca i Cabarrocas. Nanostructured back reflectors produced using polystyrene assisted lithography for enhanced light trapping in silicon thin film solar cells. *Solar Energy*, 167:108–115, 2018.

[101] Zhipeng Huang, Nadine Geyer, Peter Werner, Johannes De Boor, and Ulrich Gösele. Metal-assisted chemical etching of silicon: A review. *Advanced Materials*, 23:285–308, 2011.

[102] Thomas S. Wilhelm, Cody W. Soule, Mohadeseh A. Baboli, Christopher J. O'Connell, and Parsian K. Mohseni. Fabrication of suspended iii-v nanofoils by inverse metal-assisted chemical etching of in0.49ga0.51p/gaas heteroepitaxial films. *ACS Applied Materials and Interfaces*, 10:2058–2066, 2018.

[103] Ho-Yuen Cheung, Hao Lin, Fei Xiu, Fengyun Wang, Senpo Yip, Johnny C Ho, and Chun-Yuen Wong. Mechanistic characteristics of metal-assisted chemical etching in gaas. 2014.

[104] Thomas S. Wilhelm, Alex P. Kolberg, Mohadeseh A. Baboli, Alireza Abrand, Kris A. Bertness, and Parsian K. Mohseni. Communication—black gaas with sub-wavelength nanostructures fabricated via lithography-free metal-assisted chemical etching. *ECS Journal of Solid State Science and Technology*, 8:Q134–Q136, 2019.

[105] Stephen Jade Polly. Design and implementation of quantum dot enhanced next generation photovoltaic devices. *Thesis. Rochester Institute of Technology*, 2015.

[106] H.J. Hovel and J.M. Woodall. Theoretical and experimental evaluations of gaalas - gaas solar cells. *In Proceedings of the IEEE Photovoltaic Specialists Conference*, 1973.

[107] J. T. Verdeyen. *Laser Electronics*. Prentice-Hall International, 1989.

[108] Natasha Gruginskie, Federica Cappelluti, Gerard Bauhuis, Alberto Tibaldi, Gemma Giliberti, Peter Mulder, Elias Vlieg, and John Schermer. Limiting mechanisms for photon recycling in thin-film gaas solar cells. *Progress in Photovoltaics: Research and Applications*, pages 3–5, 2020.

[109] Donald A. Clugston and Paul A. Basore. Modelling free-carrier absorption in solar cells. *Progress in Photovoltaics: Research and Applications*, 5:229–236, 1997.

[110] Marc Rudiger, Johannes Greulich, Armin Richter, and Martin Hermle. Parameterization of free carrier absorption in highly doped silicon for solar cells. *IEEE Transactions on Electron Devices*, 60:2156–2163, 2013.

[111] Chin Yi Tsai. Interband and intraband absorption coefficients of silicon: Theoretical frameworks and formulations. *IEEE Journal of Selected Topics in Quantum Electronics*, 26:1–10, 2020.

[112] K. A. Bulashevich, V. F. Mymrin, S. Yu Karpov, D. M. Demidov, and A. L. Ter-Martirosyan. Effect of free-carrier absorption on performance of 808 nm algaas-based high-power laser diodes. *Semiconductor Science and Technology*, 22:502–510, 2007.

[113] E. A. Avrutin and B. S. Ryvkin. Theory of direct and indirect effect of two-photon absorption on nonlinear optical losses in high power semiconductor lasers. *Semiconductor Science and Technology*, 32, 2017.

[114] Joachim Piprek and Z. M. Li. Evaluating two-photon absorption effects on pulsed high-power laser operation. *Proceedings of the International Conference on Numerical Simulation of Optoelectronic Devices, NUSOD*, 2018-Novem:89–90, 2018.

[115] Srini Krishnamurthy, Zhi Gang Yu, Leonel P. Gonzalez, and Shekhar Guha. Temperature- and wavelength-dependent two-photon and free-carrier absorption in gaas, inp, gainas, and inasp. *Journal of Applied Physics*, 109, 2011.

[116] D. A. Veselov, Yu K. Bobretsova, A. Y. Leshko, V. V. Shamakhov, S. O. Slipchenko, and N. A. Pikhtin. Measurements of internal optical loss inside an operating laser diode. *Journal of Applied Physics*, 126, 2019.

[117] Xin Xiao, Hongfei Jiao, Jinlong Zhang, Xinbin Cheng, and Zhanshan Wang. Study of algaas/gaas low loss semiconductor coatings for precision measurement. *Proc. SPIEC 11617, International Conference on Optoelectronnic and Microelectronic Technology and Application*, page 119, 2020.

[118] Phoebe Pearce. Rayflare: flexible optical modelling of solar cells. *Journal of Open Source Software*, 6:3460, 9 2021.

[119] Hiroyuki Fujiwara. *Spectroscopic Ellipsometry: Principles and Applications*. 2007.

[120] Y. V. Flores, M. P. Semtsiv, M. Elagin, G. Monastyrskyi, S. Kurlov, A. Aleksandrova, J. Kischkat, and W. T. Masselink. Thermally activated leakage current in high-performance short-wavelength quantum cascade lasers. *Journal of Applied Physics*, 113, 2013.

[121] Moshe Levy, Yoram Karni, Noam Rapaport, Yaroslav Don, Yuri Berk, Dan Yanson, Shalom Cohen, and Jacob Oppenheim. Development of asymmetric epitaxial structures for 65laser diodes in the 9xx-nm range. *High-Power Diode Laser Technology and Applications VIII*, 7583:1–10, 2010.

[122] M. Sotoodeh, A. H. Khalid, and A. A. Rezazadeh. Empirical low-field mobility model for iii-v compounds applicable in device simulation codes. *Journal of Applied Physics*, 87:2890–2900, 2000.

[123] Sadao Adachi. Gaas, alas, and al x ga 1 x as: Material parameters for use in research and device applications. *Journal of Applied Physics*, 58:R1–R29, 1985.

[124] Victor Liu and Shanhui Fan. S 4: A free electromagnetic solver for layered periodic structures. *Computer Physics Communications*, 183:2233–2244, 2012.

[125] Emily D. Kosten, Brendan M. Kayes, and Harry A. Atwater. Experimental demonstration of enhanced photon recycling in angle-restricted gaas solar cells. *Energy and Environmental Science*, 7:1907–1912, 2014.

[126] L. Li, S. Gan, B. K. Han, H. Qi, and R. F. Hicks. The reaction of carbon tetrachloride with gallium arsenide (001). *Applied Physics Letters*, 72:951–953, 1998.

[127] A Rebey, A Bchetnia, and B El Jani. Etching of gaas by ccl and vcl in a metalorganic vapor-phase epitaxy reactor, 1998.

[128] S. Arakawa, M. Itoh, and A. Kasukawa. In-situ etching of semiconductor with cbr4 in mocvd reactor. pages 71–74, 2001.

[129] T. J. de Lyon. Minority carrier lifetime and photoluminescent response of heavily carbon-doped gaas grown with gas source molecular-beam epitaxy using halomethane doping sources. *Journal of Vacuum Science Technology B: Microelectronics and Nanometer Structures*, 10:846, 3 1992.

[130] M A Steiner, J F Geisz, R C Reedy, and S Kurtz. Direct comparison of inverted and non-inverted growths of gainp solar cells: Preprint, 2008.

[131] Nathan P. Wells, Travis U. Driskell, Andrew I. Hudson, Stephen D. Lalumondiere, William T. Lotshaw, David V. Forbes, and Seth M. Hubbard. Carrier quenching in ingap/gaas double heterostructures. *Journal of Applied Physics*, 118, 2015.

[132] Ho Kwan Kang, Chul Gi Ko, Keun Man Song, Wonkyu Park, Sang-Hyuk Park, Chang Zoo Kim, Hogyoung Kim, and Dong Hwan Jun. Te doping in the gaas tunnel junction for gainp/gaas tandem solar cells. *Semiconductor Science and Technology*, 26:075009, 2011.

[133] Julia D'Rozario, Steve Polly, Rao Tatavarti, and Seth Hubbard. Novel in situ texturing for light management in thin-film iii-v space photovoltaics. *Applied Physics Letters (under review)*, 2022.

[134] Ryan M. France, Pilar Espinet-Gonzalez, Brian B. Haidet, Kunal Mukherjee, Harvey L. Guthrey, Harry A. Atwater, and Don Walker. Development of lattice-mismatched gainasp for radiation hardness. *IEEE Journal of Photovoltaics*, 10:103–108, 1 2020.

[135] M. Sukeerthi and Siva Kotamraju. Study of degradation in 3j inverted metamorphic (imm) solar cell due to irradiation-induced deep level traps and threading dislocations using finite element analysis. *Physica E: Low-Dimensional Systems and Nanostructures*, 127, 3 2021.

[136] Stephen J. Polly, George Nelson, Julia D'Rozario, Elisabeth McClure, Rao Tatavarti, and Seth M. Hubbard. Incorporation of photonic structures for improved radiation tolerance of lattice matched triple junction solar cells. *2018 IEEE 7th World Conference on Photovoltaic Energy Conversion, WCPEC 2018 - A Joint Conference of 45th IEEE PVSC, 28th PVSEC and 34th EU PVSEC*, pages 2924–2927, 2018.

[137] Stephen J. Polly, George T. Nelson, Julia R. D'Rozario, Rao Tatavarti, and Seth M. Hubbard. Radiation effects in thinned gaas photovoltaics incorporating dbrs for improved radiation tolerance of multijunctions. pages 2818–2821. IEEE, 6 2019.

[138] Roger E. Welser, Stephen J. Polly, Mitsul Kacharia, Anastasiia Fedorenko, Ashok K. Sood, and Seth M. Hubbard. Design and demonstration of high-efficiency quantum well solar cells employing thin strained superlattices. *Scientific Reports*, 9, 12 2019.

[139] David Wilt, George T. Nelson, Julia R. D'Rozario, Seth M. Hubbard, and Stephen J. Polly. Modeling free-carrier absorption in ultrathin iii-v solar cells with light management. *Optics Express, Vol. 30, Issue 5, pp. 7096-7109*, 30:7096–7109, 2 2022.

[140] E. Fred. Schubert. *Light-emitting diodes*. Cambridge University Press, 2006.

[141] M. Ajmal Khan, Noritoshi Maeda, Masafumi Jo, Yuki Akamatsu, Ryohei Tanabe, Yoichi Yamada, and Hideki Hirayama. 13 mw operation of a 295-310 nm algan uv-b led with a p-algan transparent contact layer for real world applications. *Journal of Materials Chemistry C*, 7:143–152, 2019.

[142] Kosuke Oiwa, Yusuke Ozawa, Kent Nagumo, Seiya Nishimura, Yasushi Nanai, and Akio Nozawa. Remote blood pressure sensing using near-infrared wideband leds. *IEEE Sensors Journal*, 2021.

[143] Ansara Noori, Parvez Mahbub, Miloš Dvořák, Arko Lucieer, and Mirek Macka. Radiometric analysis of uv to near infrared leds for optical sensing and radiometric measurements in photochemical systems. *Sensors and Actuators, B: Chemical*, 262:171–179, 6 2018.

[144] Jule Buehler, Florian Sommerfeld, Tobias Meurle, Katharina Hoenes, and Martin Hessling. Disinfection properties of conventional white led illumination and their potential increase by violet leds for applications in medical and domestic environments. *Advances in Science and Technology Research Journal*, 15:169–175, 2021.

[145] Hideki Hirayama, Noritoshi Maeda, Sachie Fujikawa, Shiro Toyoda, and Norihiko Kamata. Recent progress and future prospects of algan-based high-efficiency deep-ultraviolet light-emitting diodes. *Japanese Journal of Applied Physics*, 53, 10 2014.

[146] Seung Hyun Kim, Parsian K. Mohseni, Yi Song, Tatsumi Ishihara, and Xiuling Li. Inverse metal-assisted chemical etching produces smooth high aspect ratio inp nanostructures. *Nano Letters*, 15:641–648, 2015.

[147] J. Y. Lin and H. X. Jiang. Development of microled, 3 2020.

[148] S. X. Jin, J. Li, J. Z. Li, J. Y. Lin, and H. X. Jiang. Gan microdisk light emitting diodes. *Applied Physics Letters*, 76:631–633, 1 2000.

[149] Brandon Mitchell, Volkmar Dierolf, Tom Gregorkiewicz, and Yasufumi Fujiwara. Perspective: Toward efficient gan-based red light emitting diodes using europium doping, 4 2018.

[150] Ya Ju Lee, Chia Jung Lee, and Chih Hao Chen. Determination of junction temperature in ingan and algainp light-emitting diodes. *IEEE Journal of Quantum Electronics*, 46:1450–1455, 2010.

[151] Joseph Flemish, Zhongmin (Frank) Ren, Wouter Soer, Robert Armitage, Hossein Lofti, Rajiv Pathak, Hee Jin Kim, Srinivasa Banna, Willem Sillevis-Smitt, Jia Cheng Tan, Yiongxiang Melvin Tio, Reigh Distor, Shimin Lim, and Kheng Boo Lim. Microled architectures for low-power display applications. page 7. SPIE-Intl Soc Optical Eng, 3 2022.

[152] Jeong-Tak Oh, Sang-Youl Lee, Yong-Tae Moon, Ji Hyung Moon, Sunwoo Park, Ki Yong Hong, Ki Young Song, Chanhyoung Oh, Jong-In Shim, Hwan-Hee Jeong, June-O Song, Hiroshi Amano, and Tae-Yeon Seong. Light output performance of red algainp-based light emitting diodes with different chip geometries and structures. *Optics Express*, 26:11194, 4 2018.

[153] Dening Zou, Yuqing Zhou, Xin Zhang, Wei Zhang, and Ying Han. High temperature oxidation behavior of a high al-containing ferritic heat-resistant stainless steel. *Materials Characterization*, 136:435–443, 2 2018.

[154] Sancan Han, Chenchao Xu, Huijin Li, Shaogang Liu, Huiwen Xu, Yuankun Zhu, Anle Fang, and Xianying Wang. Algainp-based micro-led array with enhanced optoelectrical properties. *Optical Materials*, 114, 4 2021.

[155] M. Zaknoune. Nonselective wet chemical etching of gaas and algainp for device applications. *Journal of Vacuum Science Technology B: Microelectronics and Nanometer Structures*, 16:223, 1 1998.

[156] Junchi Yu, Tao Tao, Bin Liu, Feifan Xu, Yao Zheng, Xuan Wang, Yimeng Sang, Yu Yan, Zili Xie, Shihao Liang, Dunjun Chen, Peng Chen, Xiangqian Xiu, Youdou Zheng, and Rong Zhang. Investigations of sidewall passivation technology on the optical performance for smaller size gan-based micro-leds. *Crystals*, 11:1–9, 2021.

[157] Jong-Hee Kim. Selective etching of algaas/gaas structures using the solutions of citric acid/h[sub 2]o[sub 2] and de-ionized h[sub 2]o/buffered oxide etch. *Journal of Vacuum Science Technology B: Microelectronics and Nanometer Structures*, 16:558, 2002.

[158] Jae Won Seo, Hwa Sub Oh, Joon Seop Kwak, Hyun Don Song, Kyung Wook Park, Duk Hyun Park, Seong Wook Ryu, and Young Ho Park. Improved light-extraction efficiency of the aigalnp-based light-emitting diodes fabricated using a chemical wet etch of n-aigainp layer. *Journal of the Korean Physical Society*, 55:314–317, 2009.

[159] G. J. Sonek and J. M. Ballantyne. Reactive ion etching of gaas using bcl//3. *Journal of Vacuum Science and Technology B: Microelectronics and Nanometer Structures*, 2:653–657, 1984.

[160] C. V. J. M. Chang. Reactive ion etching of alingap and gaas in sicl4/ch4/ar-based plasmas. *Journal of Vacuum Science Technology B: Microelectronics and Nanometer Structures*, 12:536, 1994.

[161] T. Yoshikawa. Smooth etching of various iii/v and ii/vi semiconductors by cl2 reactive ion beam etching. *Journal of Vacuum Science Technology B: Microelectronics and Nanometer Structures*, 14:1764, 5 1996.

[162] J. Hong, J. W. Lee, C. J. Santana, C. R. Abernathy, S. J. Pearton, W. S. Hobson, and F. Ren. Plasma etching of ingap, alinp and algap in bcl3 environments. *Materials Science and Engineering B*, 41:247–252, 1996.

[163] G. T. Edwards, D. I. Westwood, and P. M. Smowton. Selective etching of algainp laser structures in a bcl3/cl 2 inductively coupled plasma. *Semiconductor Science and Technology*, 21:513–519, 2006.

[164] Katherine Booker, Yahuitl Osorio Mayon, Christopher Jones, Matthew Stocks, and Andrew Blakers. Deep, vertical etching for gaas using inductively coupled plasma/reactive ion etching. *Journal of Vacuum Science Technology B*, 38:012206, 2020.

[165] Younes Boussadi, Névine Rochat, Jean Paul Barnes, Badhise Ben Bakir, Philippe Ferrandis, Bruno Masenelli, and Christophe Licitra. Investigation of sidewall damage induced by reactive ion etching on algainp mesa for micro-led application. *Journal of Luminescence*, 234, 2021.

[166] Jixiang Ding. Suggestions on efficiency droop of gan-based leds. volume 729. Institute of Physics Publishing, 2 2020.

[167] Houqiang Fu and Yuji Zhao. Efficiency droop in gainn/gan leds, 2018.

[168] Joong-Yeon Cho, Kyeong-Jae Byeon, Jin-Seung Kim, and Heon Lee. Improved algainp vertical emitting light-emitting diodes using direct printing. *Optics Letters*, 38:1573, 2013.

[169] Rob W. van der Heijden, Mischa S. P. Andriesse, Carl-Fredrik Carlstrom, Emile van der Drift, Erik-Jan Geluk, A. F. Karouta, Peter A. Nouwens, Y. Siang Oei, Tjibbe de Vries, and Huub W. M. Salemink. Deep dry etching process development for photonic crystals in inp-based planar waveguides. volume 5450, page 523. SPIE, 9 2004.

[170] S. C. McNevin. Chemical etching of gaas and inp by chlorine: The thermodynamically predicted dependence on cl2 pressure and temperature. *Journal of Vacuum Science Technology B: Microelectronics and Nanometer Structures*, 4:1216, 9 1986.

[171] Byung Oh Jung, Wonyong Lee, Jeomoh Kim, Myungshin Choi, Hui Youn Shin, Minho Joo, Sukkoo Jung, Yoon Ho Choi, and Moon J. Kim. Enhancement in external quantum efficiency of algainp red -led using chemical solution treatment process. *Scientific Reports*, 11:1–9, 2021.

[172] Chih Hung Yen, Yi Jung Liu, Kuo Hui Yu, Pei Ling Lin, Tzu Pin Chen, Li Yang Chen, Tsung Han Tsai, Nan Yi Huang, Chong Yi Lee, and Wen Chau Liu. On an algainp-based light-emitting diode with an ito direct ohmic contact structure. *IEEE Electron Device Letters*, 30:359–361, 2009.

[173] Sheng Hang, Chia Ming Chuang, Yonghui Zhang, Chunshuang Chu, Kangkai Tian, Quan Zheng, Tingzhu Wu, Zhaojun Liu, Zi Hui Zhang, Qing Li, and Hao Chung Kuo. A review on the low external quantum efficiency and the remedies for gan-based micro-leds, 4 2021.

[174] A. W. Walker, S. Heckelmann, C. Karcher, O. Höhn, C. Went, M. Niemeyer, A. W. Bett, and D. Lackner. Nonrad iative lifetime extraction using power-dependent relative photoluminescence of iii-v semiconductor double-heterostructures. *Journal of Applied Physics*, 119, 2016.

[175] al TaeWan Kim, Bing Wang, Cong Wang, David A Kohen, Jeong Woo Hwang, Jae Cheol Shin, and Jürgen Michel. Mocvd-regrown ga-rich ingap films on sige virtual substrates for si-based iii-v optoelectronic device applications ga-rich ingap films on sige virtual substrate.

[176] Q. Dai, M. F. Schubert, M. H. Kim, J. K. Kim, E. F. Schubert, D. D. Koleske, M. H. Crawford, S. R. Lee, A. J. Fischer, G. Thaler, and M. A. Banas. Internal quantum efficiency and nonradiative recombination coefficient of gainn/gan multiple quantum wells with different dislocation densities. *Applied Physics Letters*, 94:3–6, 2009.

[177] Andrew C. Espenlaub, Daniel J. Myers, Erin C. Young, Saulius Marcinkevičius, Claude Weisbuch, and James S. Speck. Evidence of trap-assisted auger recombination in low radiative efficiency mbe-grown iii-nitride leds. *Journal of Applied Physics*, 126, 11 2019.